DIAGNOSIS OF THE FLUX EMANATING FROM THE INTERMEDIATE FOCUS OF AN EXTREME ULTRAVIOLET LIGHT LITHOGRAPHY SOURCE

BY

JOHN R. SPORRE

DISSERTATION

Submitted in partial fulfillment of the requirements
for the degree of Doctor of Philosophy in Nuclear Engineering
in the Graduate College of the
University of Illinois at Urbana-Champaign, 2013

Urbana, Illinois

Doctoral Committee:

Professor David N. Ruzic, Chair
Professor James F. Stubbins
Professor George H. Miley
Professor James G. Eden

ABSTRACT

The implementation of extreme ultraviolet (EUV) light lithography as the solution for next generation lithography needs, stands at a critical point. Having already missed the last several projected insertion nodes, it is necessary to rapidly solve the current issues with the light source that prevent it from being cost effective. To this extent, this dissertation seeks to understand one primary issue with EUV light lithography tools, the transport of energetic species that can damage post-intermediate focus optics and increase the cost of tool ownership.

In this paper, the effects of chamber pressure, buffer gas mass, and pinch gas mass on debris transport will be explored using the XTREME XTS 13-35 EUV light source. Utilizing the Sn Intermediate Focus Flux Emission Detector (SNIFFED), three triple Langmuir probes, as well as a set of Si witness plates placed along the mock-up collector optic and at the intermediate focus, it will be shown that the interaction between high energy electron and photons, energetic ions, and energetic neutrals with the buffer gas has a considerable impact on the creation and transport of non-EUV photon debris to the intermediate focus.

The creation of an EUV light emitting plasma results in the propagation of three separate observable plasmas: one initiated by the high energy electrons decoupled from the plasma core, one caused by the energy retarded fast electrons coupled with the expansion of the high energy ions, as well as the expansion of the lower energy core of the EUV emitting plasma into the surrounding buffer gas. The generated plasmas are typically in the range of 3-6 eV with densities on the order of 10^{13} cm^{-3}. It will be shown

that electron temperatures and densities generally peak at 12 mTorr using Ar buffer gas and a N_2 fueled pinch. While electron temperatures greatly increase up to 11±2 eV with He buffer gas, and drop down to 6±1 eV for Ar buffer gas, the larger species with more electrons, and less ionization potential, have the highest density. In general there is very little effect observed in changing the pinch species used, except to change the arrival time of the second and third plasmas.

It will be shown that the propagation and scattering of the energetic pinch species results in the energizing of the buffer gas as well. With increased energy, and the consequent ionization, these buffer gas species sputter the chamber walls and introduce any contaminant there into the chamber atmosphere. If the pressure is not high enough, these species (oxygen and carbon) readily reach the intermediate focus and deposit on any surface after it. Furthermore, the presence of these expanding plasmas can contribute to a negative charge flux of $\sim$-0.25±0.1x10^{11} e-cm^{-2} impending upon the intermediate focus facing surface, though the chamber pressure largely determines the amount of ions and electrons reaching the surface. The interaction between the intermediate focus facing components and the charged flux can lead to sputtering, or further deposition as the ions are accelerated through the built up sheath into the surface (depending on the suppression of the energetic ions and neutrals ejected from the EUV emitting plasma). The excitation of the buffer gas species also results in the transport of neutral atoms over 100 eV to the intermediate focus. This is largely affected by the chamber pressure (peak flux was observed at 6 mTorr with an arrival time of ~700 μs), buffer gas mass (40 AMU had the highest measured flux with an arrival time of ~800 μs), and pinch gas species (40 AMU pinch gas mass had the highest energy deposition into 40 AMU buffer gas, though arrival

time was the same for all species. Furthermore, deposition rates at the intermediate focus were shown to peak at 2 mTorr with a rate of $1.5\pm0.3x10^{-4}$ nm/pulse and a total film concentration of oxygen and carbon totaling greater than 90%. Increasing pressure reduces deposition rate because of increased buffer gas suppression of depositing metals from the electrode, as well as increased etching by the higher density generated plasmas. Increasing buffer gas mass species were theoretically shown to decrease the deposition rate at the intermediate focus, though Sn and Cu particulates increased with increasing buffer gas mass due to arcing between the electrodes and resulting sputtering. Ultimately the understanding of the importance in choosing buffer gas mass, pinch gas mass, and chamber pressure are emphasized in regards to the transport of debris from the EUV emitting plasma to the intermediate focus. The implementation of extreme ultraviolet (EUV) light lithography as the solution for next generation lithography needs, stands at a critical point. Having already missed the last several projected insertion nodes, it is necessary to rapidly solve the current issues with the light source that prevent it from being cost effective. To this extent, this dissertation seeks to understand one primary issue with EUV light lithography tools, the transport of energetic species that can damage post-intermediate focus optics and increase the cost of tool ownership.

In this paper, the effects of chamber pressure, buffer gas mass, and pinch gas mass on debris transport will be explored using the XTREME XTS 13-35 EUV light source. Utilizing the Sn Intermediate Focus Flux Emission Detector (SNIFFED), three triple langmuir probes, as well as a set of Si witness plates placed along the mock-up collector optic and at the intermediate focus, it will be shown that the interaction between

the photons, energetic ions, and energetic neutrals with the buffer gas has a considerable impact on the creation and transport of non-EUV photon debris to the intermediate focus.

The creation of an EUV light emitting plasma also develops three separate observable plasmas that propagate through the chamber: one created by the photoionization of buffer gas species with the 93 eV photons, one that is caused by charge exchange with the energetic ejected ions and electrons from the EUV plasma, as well as one found by the expansion and incorporation of the EUV emitting plasma into the surrounding buffer gas. The generated plasmas are typically in the range of 3-6 eV with densities on the order of 10^{13} cm^{-3}, with the energetic ion/electron plasma typically generating the highest temperatures. It will be observed that electron temperatures and densities generally peak at 12 mTorr using Ar buffer gas and a N_2 fueled pinch. While electron temperatures greatly increase up to 11 eV with He buffer gas, and drop down to 6 eV for Ar buffer gas, the larger species with more electrons has the highest density. In general there is very little effect observed in changing the pinch species used, except to change the arrival time of the second and third plasmas.

It will be shown that the propagation and scattering of the energetic pinch species results in the energizing of the buffer gas as well. With increased energy, and the consequent ionization, these buffer gas species sputter the chamber walls and introduce any contaminant there into the chamber atmosphere. If the pressure is not high enough, these species (oxygen and carbon) readily reach the intermediate focus and deposit on any surface after it. Furthermore, the presence of these ionized species can contribute to a negative charge flux of $\sim$-0.25±0.1x10^{11} e-cm^{-2} impending upon the intermediate focus

facing surface, though the plasma density largely determines the amount of ions and electrons reaching the surface. This can lead to sputtering, or further deposition as the ions are accelerated through the built up sheath into the surface. The excitation of the buffer gas species also results in the transport of neutral atoms over 100 eV to the intermediate focus. This is largely affected by the chamber pressure (peak flux was observed at 6 mTorr with an arrival time of ~700 μs), buffer gas mass (40 AMU had the highest measured flux with an arrival time of ~800 μs), and pinch gas species (40 AMU pinch gas mass had the highest energy deposition into 40 AMU buffer gas, though arrival time was the same for all species. Furthermore, deposition rates at the intermediate focus were shown to peak at 2 mTorr with a rate of $1.5\pm0.3\text{x}10^{-4}$ nm/pulse and a total film concentration of oxygen and carbon totaling greater than 90%. Increasing pressure reduces deposition rate because of increased buffer gas suppression of depositing metals from the electrode, as well as increased etching by the higher density generated plasmas. Increase buffer gas was theoretically shown to decrease the deposition rate at the intermediate focus, though Sn and Cu particulates increased with increasing buffer gas mass due to arcing between the electrodes and resulting sputtering. Ultimately the understanding of the importance in choosing buffer gas mass, pinch gas mass, and chamber pressure are emphasized in regards to the transport of debris from the EUV emitting plasma to the intermediate focus.

To My Family, Friends, and Those Who Gave Me a Chance

ACKNOWLEDGMENTS

Many individuals have been instrumental in the development of this work, as well as the development of myself as a scholar and an individual. I would like to thank my good friend and advisor Professor David N. Ruzic, without whom my interest in plasmas would never have evolved. The time spent together both in and out of lab will always be cherished, and looked back upon with great fondness. I would like to thank Dr. Erik Antonsen for his initial encouragement to go for a Ph.D., as well as providing too many short man jokes to even remember (Erik is short). Many thanks go to my closest friends Dave Lartonoix and Gabe Chavez, who helped get me into shape, dress better, and have lent an open ear for me to vent. Many thanks also to my very good friend Robert Lofgren, whose strange ability to speak nearly flawlessly using movie quotes still astounds me. Furthermore, I would like to thank my former undergrads Pi Zonooz and Dan Organ, without their assistance none of this would have been possible. Lastly, I would like to thank the pillars of my life, my parents, and my grandparents. Without this solid base in my life I know I would not be where I am today. I'd also like to thank Netflix for providing a mindless diversion amongst the weeks and weeks of writing.

The works shown here would not have been possible without funding from various sources. I would like to thank accordingly, SEMATECH, the Intel Corporation, and XTREME Technologies who each allowed the Center for Plasma-Material Interactions to develop such wonderful tools as the SNIFFED apparatus to measure debris coming from the intermediate focus.

TABLE OF CONTENTS

CHAPTER 1

INTRODUCTION

The creation of the integrated circuit in the 1950s spawned the development of a unique industry solely devoted to developing computation capabilities for society. The resulting demand for faster, smaller, and less power hungry components was an inevitable consequence of increasing need by consumers to perform more varied and intensive computational tasks. In 1965, Gordon Moore forecasted the resulting technological advancements that would occur in the decades following the creation of the integrated circuit. Moore stated, in an effort to emphasize the future role of integrated circuits in the world, that the number of *cost effective* transistors on a die would double approximately every two years [1]. As shown in figure 1.1, this projection has remarkably held true.

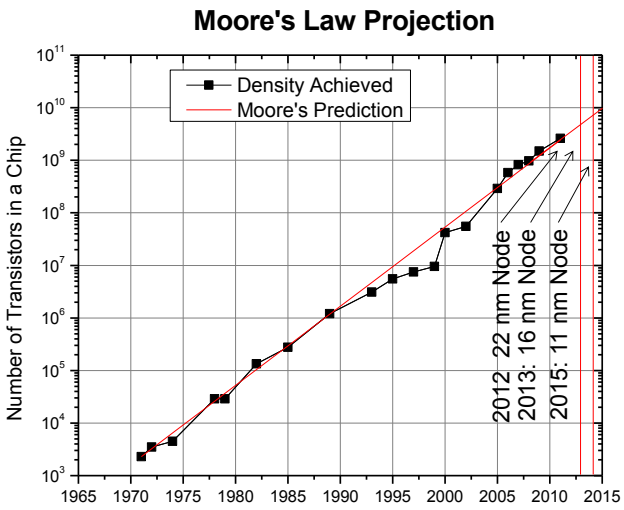

Figure 1.1: The number of transistors on a die has doubled nearly every 24 months. This trend will not continue forever, but until the physical limits imposed by silicon are reached, efforts are being made in finding technology to extend this trend into the future. Data obtained from [2]

As it stands in 2013, industry is currently producing integrated circuits at a 22 nm half-pitch (half the distance between smallest printed feature sizes on a wafer) using 193 nm light sources with processes called double patterning and immersion lithography. While there currently exist solutions to go beyond 22 nm flash half pitch sizes on the International Technology Roadmap for Semiconductors, there exists a need to develop a new wavelength of radiation for the lithography exposure step. While continued use of 193 nm excimer laser technology is fundamentally capable of creating resolutions for the 16 nm and 11 nm nodes, the cost effectiveness of such solutions does not meet requirements. While there are several possible next generation technology options being pursued, extreme ultraviolet (EUV) light lithography, which uses a 13.5 nm wavelength, presents a promising solution to the issue of improving resolution while keeping costs to a minimum. With its origins beginning in the 1980s, EUV lithography has been widely researched and presents a possible solution to the problems that exist

for expanding to sub-10 nm features [3].

As with all advancements in technology, however, there are problems to overcome before EUV lithography can be implemented. The absorption of 13.5 nm light into nearly all substances requires the use of vacuum systems, reflective optics (as opposed to transmissive), reflective masks (the component that contains the information to be printed on the wafer), as well as a degree of contamination control never before approached with prior lithography technology. The fact that a simple transparent pellicle cannot be used to inhibit the transportation of debris (anything that is not in band EUV radiation) also becomes an issue when one considers the ejecta of the 30 eV, 10^{-19} cm^{-3} plasma used to emit the desired wavelength. This energetic debris is thus capable of reaching and destroying the collector optics used to focus the EUV light on the intermediate focus.

The ability to mitigate this debris is a critical facet of maintaining low cost of ownership for high volume manufacturing. The plasma sources generate energetic Sn ions and neutrals with energies typically in the range of 1-10 keV, but are capable of energies above 50 keV. If not mitigated, these energetic atoms can sputter or be deposited onto the collector optics, consequently resulting in the loss of EUV light reflectivity and an increase in total cost to print a computer chip. As shown in figure 1.2, without using debris mitigation techniques, a discharge-produced plasma EUV emitting light source can deposit Sn at a rate of 3.9×10^{-4} nm/pulse. It is possible to reduce this rate, by four orders of magnitude, to 3.2×10^{-8} nm/pulse with buffer gas and a foil trap in place, however even this rate results in too little tool uptime for high volume

manufacturing [4]. Considering that a manufacturing tool can run upwards of 7 kHz, it would take only 6.2 hours of operation to deposit 5 nm of Sn on the surface of the collector, and a consequent 70% reduction in EUV light reflectivity. Even though the source to collector debris transport issue has largely been resolved, focus must be placed on understanding the debris transport mechanisms from the source to the intermediate focus location where only clean EUV photons are allowed to be transmitted.

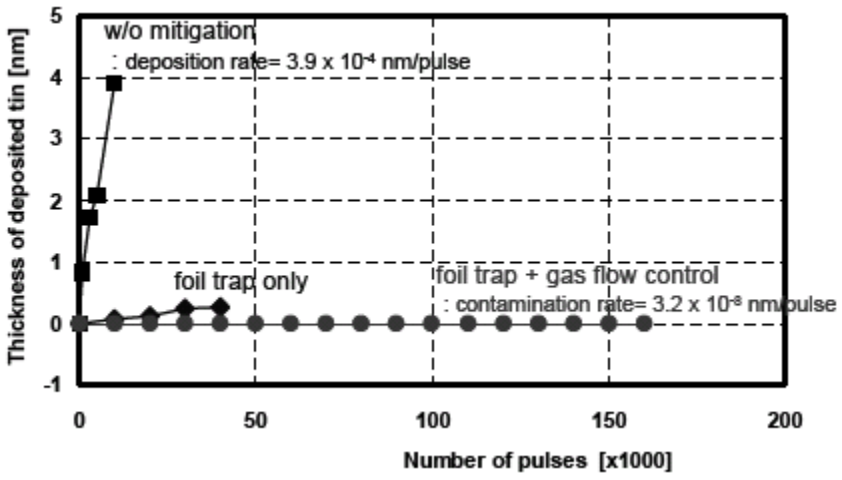

Figure 1.2: Shown are the Sn deposition rates of a typical z-pinch Sn-fueled EUV source. It was observed that without debris mitigation in place, 3.9×10^{-4} nm/pulse Sn deposition was observed. Utilizing a foil trap and buffer gas, this amount was reduced by four orders of magnitude to 3.2×10^{-8} nm/pulse. Figure reprinted from [4].

Not allowing contamination to reach the intermediate focus is paramount to the success of EUV lithography as a next generation tool. In order to prevent the energetic ions, neutrals, and contaminant species from reaching the intermediate focus it is first necessary to understand how such species are transported after their creation in the dense warm EUV light emitting plasma. As such, the *focus of this thesis will be placed on understanding the mechanisms by which debris is transported to the intermediate focus,*

how debris is created en route to the IF, and how traditional source-collector debris mitigation techniques change the emanating flux that is observed.

CHAPTER 2

BACKGROUND

2.1 Introduction

One of the most critical process steps in the creation of a computer chip occurs when the desired design information is transferred onto the substrate surface. This step proceeds through the use of lithography, and has been the driving force behind computer chip performance advancements since their creation in 1958 [5]. While the lithography step can be substituted with methods such as imprint lithography, ion beam milling, or directed self-assembly (all in developmental non-production stages of research), the most widely used and functional technology is optical lithography. In this chapter, the fundamental concepts of optical lithography will be presented and discussed. The next generation candidate for optical lithography, EUV light lithography, will be explored, and the shortcomings of EUV plasma debris mitigation will also be presented in light of the topic of this thesis.

2.2 Optical Lithography

A schematic diagram of an optical lithography system is diagramed in figure 2.1. Each optical lithography system is conceptually the same in that it contains five different components: the source of radiation, the condenser optics, a mask, the projection optics, and a substrate [6]. In the past, radiation sources such as high-pressure mercury arc lamps, excimer lasers, and even tabletop X-ray sources have been used to provide

desired wavelengths needed to achieve required resolution characteristics [7-9]. Consumer demand has driven the wavelength from 436 nm (g-line) to 365 nm (i-line), down to 248 nm (KrF excimer lasers) and 193 nm (ArF excimer lasers) in order to accommodate Moore's law and push the cost effective size of the integrated circuit even smaller [5, 10]. The second component, the condenser lens, collects the light from the radiation source and then manipulates it to form a plane wave that is diffracted off of the mask. The mask is the device that contains the image that will be printed on the substrate surface. The last component, the projection lenses, reduces the formed image by a factor of 4 or 5 and transposes it onto a photosensitive "resist" layer deposited onto the substrate [11]. Each of these components has an effect on the resulting resolution that is achievable for a given technology step, and while conceptually each optical lithography chain is the same, individual technologies vary greatly for different wavelengths being utilized.

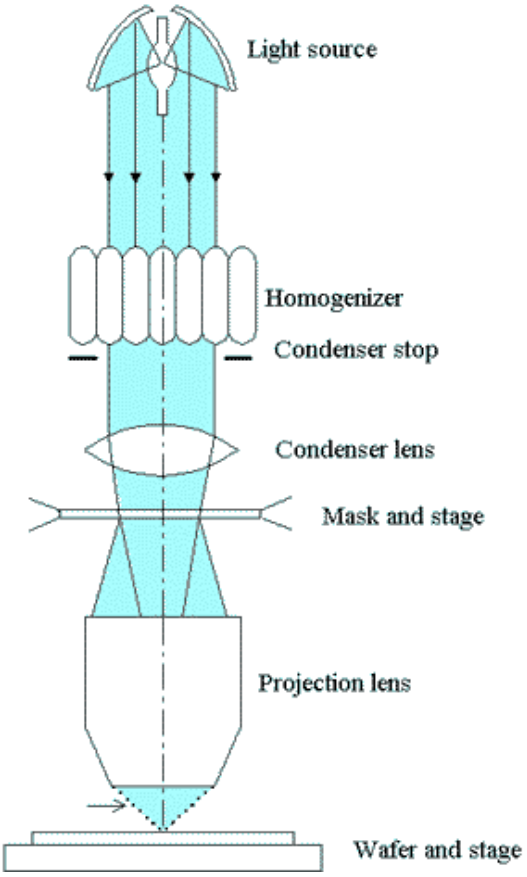

Figure 2.1: A schematic diagram of a generic optical lithography system consisting of the radiation source, the collector optics, the mask, the projection optics, and the wafer. Figure taken from [6].

The desired image is printed onto the substrate by using one of two exposure methods: stepping or scanning. The first technique exposes the whole mask and reduces the image five times before it is projected onto the substrate. The wafer is then moved to reprint the image at the next location. The second method moves the mask together with the wafer, only exposing a small portion of the mask at a time, until the entire reticle has been printed onto the wafer. After exposing one integrated circuit onto the mask, the wafer is moved to a new location and the process is repeated. The light that is projected onto the wafer causes a chemical reaction that either strengthens ("negative" resist) or weakens ("positive" resist) the photoresist deposited on the wafer.

After exposure, a chemical wash is utilized to remove the weakest resist material while the remaining material serves to protect areas from the etching and deposition processes. Because the development on the photoresist is dependent on the wavelength being used, it is not surprising that the limiting step in developing denser and more intricate features is the optical lithography step.

2.2.1 Resolution and depth of focus

While it is understood that decreasing radiation wavelength improves the density of circuits that can be placed on a wafer, the real cost tradeoffs are better understood in relation to two parameters: resolution and depth of focus. The resolution of an optical lithography system defines the smallest feature that can be printed onto the wafer. The mathematical definition is given by equation 1.1, where R is the smallest resolvable half-pitch feature, k_1 is a constant that is defined by the optical train, λ is the wavelength of light being used, and NA is the numerical aperture of the lens system within the optical lithography tool [12]. NA aperture is defined in equation 1.2, where n is the refractive index of the medium between then final lens and the wafer, and θ is the half-angle formed by the rays that are incident on the wafer.

$$R = k_1 \frac{\lambda}{NA} \tag{1.1}$$

$$NA = n \sin(\theta) \tag{1.2}$$

A quick look at the equation for resultion immediately shows that decreasing wavelength, increasing numerical aperture, or decreasing k_1 are all viable methods for improving feature sizes. For any given wavelength of radiation, it is thus possible to

create smaller features by simply manipulating the resist material and or the optical components that focus the light. The limits on these improvements are confined by physics and chemistry, but in general the NA of lithography systems can range anywhere from 0.3 to 1.35 and k_1 is typically larger than 0.25 [13, 14]. Unfortunately, however, the depth of focus, provides a restriction on how improvements to resolution are achieved. The depth of focus is defined as the distance over which the projected image remains in focus. Because there is a finite thickness of photoresist deposited onto the wafer, a system with too little depth of focus would not adequately expose the deepest parts of the photo resist and a highly anisotropic feature would not be formed. The depth of focus, defined in equation 1.3, has three different parameters: k_2 is a tool based constant, and the NA and λ are the same terms found in equation 1.2.

$$DOF = k_2 \frac{\lambda}{NA^2} \tag{1.3}$$

Because switching wavelengths generally comes at the cost of retooling an entire optical lithography line (and consequently building a new fab building to house the new equipment), industry has generally sought to extend the use of a particular optical train by manipulating NA, and the parameters k_1 and k_2 as much as possible. Given the tradeoff between resolution and depth of focus, however, it is clear that there is a limit to such extensions of technology. At some point it is no longer more cost effective to delay the implementation of a new wavelength of radiation.

2.2.2 Alternative techniques

Optical lithography, despite its mainstream understanding and implementation, is not the only option when it comes to patterning wafers. There are several other non-photon based techniques that have the potential to be used in the next generation of computer chip manufacturing. The first technique of interest is electron beam lithography. This technique is similar to optical lithography, but instead of exposing the resist with photons, electrons are used. There are still condenser and illumination optics, but the lenses are replaced with electromagnetic diverters that serve to focus and planarize the electron flux on the surface. Furthermore, electron sensitive resists are utilized to print features. Ultimately, given the size of an electron, this technique has the capability of creating feature sizes that border the fundamental tunneling limits of Si-based feature design. Unfortunately, because each line is printed linearly, this technique suffers from being too slow to produce high volume manufacturing with a low cost of ownership. This technique can be used, however, for making the masks that optical lithography uses [15, 16].

Another technique of interest is nanoimprint lithography. Nanoimprint is the nanoscale equivalent to using a stamp to print an image onto a piece of paper. Instead of ink, the imprint is created into a form of resist. This process is capable of achieving feature sizes down to 14 nm half-pitch, but suffers from printing defects that originate during the physical contact step, as well as being too slow for high volume manufacturing [17, 18].

Maskless optical lithography is another promising technique. Instead of getting information off of a permanent mask fixture, an on-the-fly mask is created using a digital mirror array. These systems are not capable of necessarily containing all mask information on a given pass (mirror size limitations), but could be used in direct-write mode with applications such as mask development or even laser milling of substrate surfaces [19, 20]. High resolution arrays do exist, however, which could possibly lead to high volume manufacturing applications for the flat panel display industry [21]. Ultimately though, these processes are not fast enough to meet the requirements needed for main stream high volume manufacturing.

2.3 Extreme Ultraviolet Light Lithography

Currently, industry is utilizing various techniques to extend the use of 193 nm light utilized in excimer laser lithography systems. Excimer lasers were originally proven experimentally in 1975 and have since been implemented as the predominant radiation source for optical lithography [22]. The extensions (to increase NA and reduce the k_1 factor) include immersion lithography, double patterning, phase shift masks, and off-axis illumination. The first technique, immersion lithography, improves resolution by increasing the index of refraction between the last lens and the wafer. A liquid is placed between the last lens and the substrate surface preventing complete internal reflection that occurs with a gap of air alone. Initial efforts focused on the use of high purity water as the gap material. Unfortunately in order to reach the 32 nm node by 2011, higher index of refraction materials were required to increase the NA up to 1.6. These

materials are generally not as inert as water posing safety risks, and furthermore This technique alone did not meet the speed needs of high volume manufacturing [23]. The second technique, double patterning, utilizes multiple patterning periods to partially expose the photo resist in areas not to be removed and full exposure in sub-wavelength regions to be etched. This technique, unlike immersion lithography, does not affect the numerical aperture, but instead affects the k_1 factor; consequently there is no effect on the depth of focus using immersion lithography. Another advantage of this process is that presently installed infrastructure does not need a large amount of modification. The downsides of this technique include stitching errors and a reduction in wafer throughput because of the doubling of exposure steps required [23-25]. Another extension technique, phase shift masks, utilizes variations in mask thickness to alter the phase of the light exposure and increase contrast during the exposure process. Unfortunately the complex algorithms required to construct the masks makes this technique difficult to implement on a wide scale [26-28]. The last technique being employed is off-axis illumination. This technique collects the zeroth and first order light from a source to improve resolution of the shorter wavelength spacing between these orders. Because this technique affects utilized wavelength it improves upon the resolution as well as the depth of focus [29, 30]. While all of these techniques enable the use of 193 nm light to print sub 32 nm features, they all come at a cost in processing time and ultimately increase the cost of ownership required to manufacture computer chips. The ultimate solution to these problems is a reduction in wavelength, which is where the introduction of EUV light lithography is most appealing.

Cost estimations created by the ITRS, pictured in figure 2.2, reveal the primary reason that EUV light lithography is an attractive next step in optical lithography [31]. In an industry where public success is determined by financial profit, the fiscal bottom line is the ultimate determiner in technology implementation. While initial capital costs for the implementation of EUV light lithography are large, due to having to create an entirely new fabrication facility, these are outweighed by the per-wafer cost advantages in the long term.

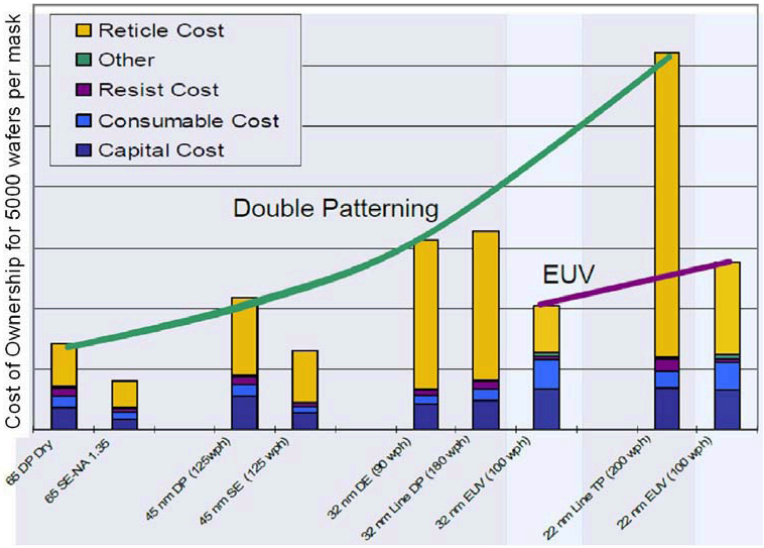

Figure 2.2: The long term cost improvements of implementing EUV lithography in place of implementing 193 nm extensions. Figure taken from [31].

EUV light lithography utilizes 13.5 nm light to pattern features on a wafer. This is over an order of magnitude smaller wavelength than currently used 193 nm (DUV) i-line lithography techniques. The advantage of this wavelength improvement allows for improvement of resolution without the inverse square diminishing returns of 193 nm extensions. Unfortunately, because EUV lithography is absorbed into most materials (including air) by the photoelectric effect, a simple transition from light source to light

source is not a viable option [32]. As such, all EUV lithography steps require high vacuum to prevent absorption of the light into atmospheric pressure gases. Furthermore, all of the optics must be reflective instead of transmitting, and new EUV sensitive resists are required. Of most importance to this thesis, however, is the fact that there does not exist a usable transparent pellicle that can protect the collector optics from the EUV light emitting plasma. Ultimately these technological hurdles have delayed EUV lithography's introduction into use for the 32 and 22 nm nodes, pushing its eventual implementation off to the 13 nm node or beyond – if at all.

2.3.1 EUV plasma

One of the primary hurdles preventing the implementation of EUV technology is the non-EUV light ejecta that leaves the EUV light emitting plasma. The current industry used fuel for EUV light emission, Sn, requires 8+ and 12+ ionization states to be achieved [33]. To generate these ionization states, a plasma with electron temperatures of approximately 30 eV, and densities on the order of 10^{20} cm^{-3} are required [34, 35]. A considerable amount of energy is deposited into the atoms to create the plasma, with less than 6% actually being converted into useable EUV light. The remaining energy goes into the generation of heat, out of band radiation, and high energy ions and neutrals.

An EUV plasma can be formed by one of two methods: laser or electric discharge. A more detailed examination of these two processes will proceed in section 2.3.3, but presently the basic fundamentals will be presented. The first method, laser produced

plasma generation, uses a high power laser (> 10^{10} W/cm^2) that liberates and then accelerates electrons from the surface of an ~30 μm Sn droplet; the liberated electrons heat the plasma and the optimal density is achieved as the droplet expands [36]. The second method operates by creating a Sn plume of gas between two rotating disk electrodes. The potential across the electrodes discharges across the plume, providing current to heat and compress the plasma through magnetic confinement. A third device, used for the purposes of the experiments in this dissertation, is a Z-pinch discharge. This device operates using Lorentz forces as illustrated in figure 2.3 [37, 38]. The ionization process begins by pre-ionizing a gas in a cylindrical cathode. A large capacitor bank is allowed to rapidly discharge across the plasma, creating a current in the Z-direction (thus the namesake). The plasma is then compressed and heated by the induced magnetic field and the opposing electric fields created in the plasma. After the plasma generates enough energy to emit EUV light, the confinement is relaxed to prepare for the next "pinch". Unfortunately, during this relaxation period, the magnetic confinement is inadequate to maintain compression and highly energetic ions are allowed to expand into the chamber [39].

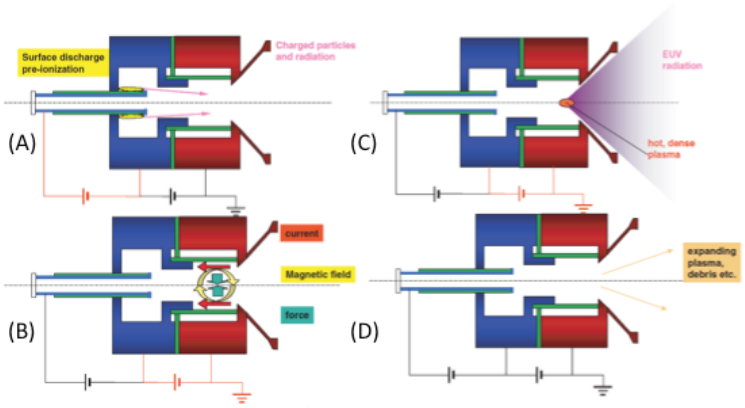

Figure 2.3: A diagram of a z-pinch plasma-producing device. A) A preionized plasma is formed by electrons being emitted off the surface of a metal cavity. B) A large 20 kA current is discharged through the preionized plasma. The induced magnetic field compresses the plasma causing it to heat up and have density increase. C) Once the plasma has reached a critical density and temperature around 30 eV, EUV light is emitted in 2π sr. D) When the current flow relaxes, the magnetic confinement is weakened and the energetic atoms within the plasma are ejected in the same direction as the light, though not isotropically. Figure taken from [39].

2.3.2 EUV fuels

Three different EUV emitting fuels have been considered for high volume manufacturing: Li, Xe, and Sn. The characteristic emission outputs of these fuels are presented in figure 2.4. Li was first to be considered due to its tight bandwidth around 13.5 nm, ±0.135 nm [40, 41]. Furthermore, because Li is a low Z material, its ions are likely to cause less damage when ejected from the plasma. Although it has a conversion efficiency of 2.5%, which is comparable to the other two fuels, Li has the fatal flaw of being extremely condensable and very reactive with other materials [41-43].

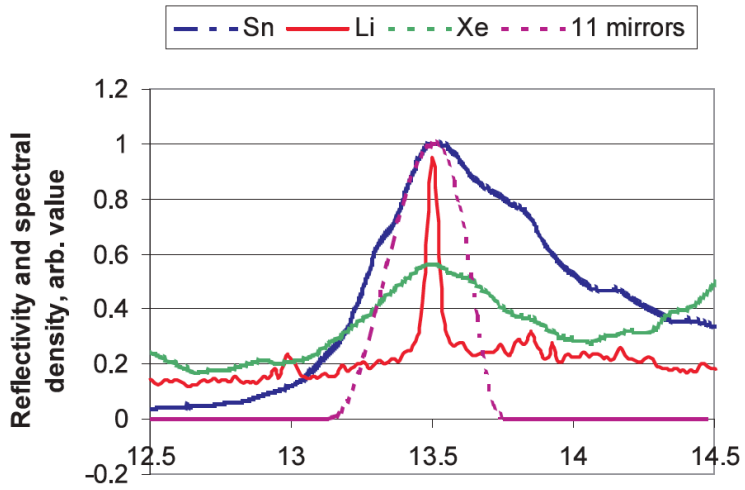

Figure 2.4: The spe ctral density plots of Li, Sn, and Xe are presented. Each plot is normalized to unity and does not represent the absolute amount of EUV emission. These plots reveal why Li is ideal as a mono-energetic light emitter, and why Xe and Sn are more ideal for their output. The 11-mirrors line is a computational calculation suggesting the reflectivity of the Sn line at a given wavelength with 11 mirrors being used. Figure taken from [40].

Consequently, Xe was chosen as the next fuel because it was a noble gas, preventing it from reacting with or condensing on anything in the EUV plasma chamber. Unfortunately, Xe has two drawbacks. First, Xe has a mass of 131 amu, which causes considerable sputtering damage when, and second Xe suffers from the fact that its conversion efficiency is less than 1% [44, 45]. The non-ideal conversion efficiency is caused by only the 10+ ionization state participating in EUV light emission. Because of the low conversion efficiency, the only method for high volume manufacturing involves increasing the operating frequency and power input, which results in increases in thermal lodes impinging upon the collector optics. Unfortunately these high thermal loads increase layer diffusion and cause warping of the collector optics, which results in unusable reflection efficiency [46].

Sn was the fuel finally settled on for high volume manufacturing purposes. Sn fuel exists as a happy medium between these two fuels, and is currently the fuel being

used in EUV lithography tools. Sn has the advantage of utilizing both its 8+ and 10+ ionization states for creating EUV light, and as such its conversion efficiency can theoretically be increased to 6%, though current practice is limited to less than 4% [47-49]. Unfortunately Sn suffers the same condensability issues exhibited with Li, though it is less reactive. As such, a great deal of effort has been placed on developing methods for cleaning Sn off of the collector optics [50]. Ultimately, however, Sn is the only current likely candidate for high volume manufacturing because it is the optimum balance between advantages and disadvantages.

2.3.3 EUV sources and collector optics

As mentioned previously, proposed high volume EUV light emitting sources come in two varieties: laser produced plasma, and gas discharge produced plasma. Although both techniques operate entirely differently, the ultimate goal of creating an EUV light emitting plasma is achieved.

Laser produced plasma are generated using a laser focused onto a small droplet. The laser liberates electrons at the surface of incidence. The electrons are accelerated into the bulk of the droplet via momentum exchange, causing heating, ionization, and expansion of the droplet, which consequently forms into a plasma. The kinetic energy of the electrons is proportional to the energy deposited by the laser, and as such it is required to have greater than 10^{10} W/cm^2 fluence. The droplets are generated by a high backpressure gas, which extrudes molten Sn through a small orifice. The droplet generator, as shown in figure 2.5, produces droplets at a rate of several hundred

kilohertz with diameters of 10 – 150 μm [51]. The created EUV light is collected using a normal incidence collector optic, illustrated in figure 2.6, and then focused onto the intermediate focus [52]. The mirrors used to collect the light are called "normal incidence" mirrors due to the fact that the light is normally incident on the surface of the collector. Laser produced plasma sources have two primary methods of debris mitigation. The first method is the use of mass-limited droplets, which provide only as much fuel as is required to create EUV light. Furthermore, the liquid density has been found to be less efficient that that formed by the use of a pre-pulse laser, which has the sole purpose of expanding the droplet before the most powerful EUV plasma producing CO_2 laser. The increase in conversion efficiency is due to the fact that at higher densities, the droplet is too optically dense for EUV light to be emitted from the center of the droplet [53].

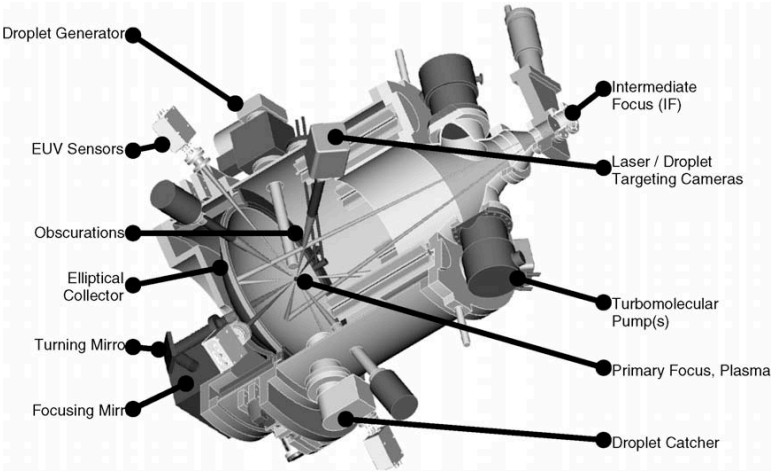

Figure 2.5: A diagram of a laser produced plasma assembly shows the various components of a Cymer laser produced plasma assembly. A liquid drop generator ejects molten Sn droplets into the chamber where a laser is used to create an EUV plasma from behind the collector optic. The light is collected, using a normal incidence mirror, and projected onto the intermediate focus. Figure taken from [51].

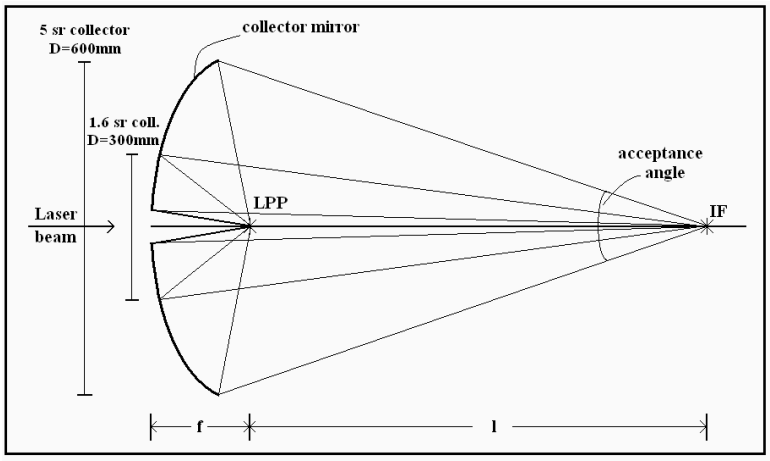

Figure 2.6: A schematic diagram of how laser produced plasma collector optics collect EUV light. laser produced plasma mirrors are normal incidence and placed directly behind the EUV source. A laser is fired through a hole in the collector to allow for the production of EUV light from a Sn droplet. Figure taken from [52].

The second method, rotating disk electrode produced plasma, uses a more efficient electric discharge process. There are effectively two different styles of gas discharge produced plasmas sources that are presently being investigated for EUV applications. The first method, briefly discussed in section 2.3.1 utilizes a electrodynamics properties of a Z-pinch gas discharge. The second method utilizes a rotating disk electrode that is immersed in molten Sn as shown in figure 2.7. A several kilovolt potential is applied between the cathode and anode, which are constantly replenished by the molten Sn bath in which they are partially submersed. An excimer laser ablates a plume of Sn that travels between the two electrodes. When the density of the gas between the electrodes is high enough, an electric discharge forms, and current flows through the Sn plume, creating EUV light [54]. While electric discharges are the most efficient method of producing EUV light, the plasma's proximity to the surface leads to introduction of additional debris that can reach the collector optics –

increasing cost of ownership and tool down time. Grazing incidence mirrors are used to collect the light from gap discharges, as shown in figure 2.8 [55]. Unfortunately, due to the geometric limitations of gas discharge produced plasma sources, the grazing incidence mirrors do not collect as much light as the mirrors used for laser produced plasma applications. Unlike the normal incidence collector optics, grazing incidence collector optics do not require multilayer structures, but do require a two bounce reflection process.

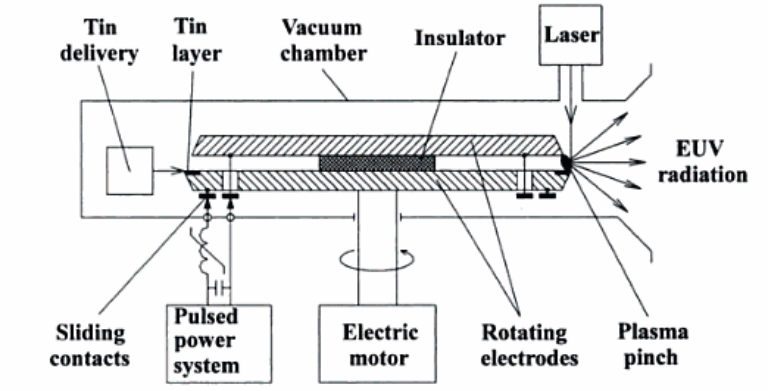

Figure 2.7: A rotating disk electrode source is one of a few different types of gas discharge produced plasmas. The two disks rotate, and are coated in a thin Sn layer which replenishes the fuel. A laser is fired externally that causes a plume of Sn gas to gap the two electrodes. The potential on the electrodes is then discharged across the gap creating EUV light. Figure taken from [54].

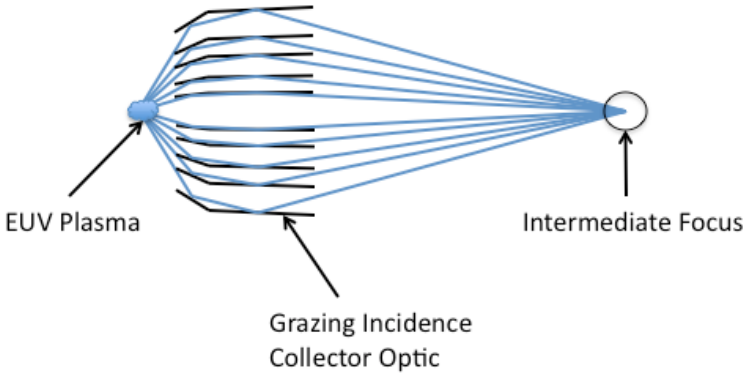

Figure 2.8: The gas discharge produced plasma source grazing-incidence collector optic. Unlike laser produced plasma normal incidence mirrors, grazing incidence mirrors collect light between the source and the intermediate focus. Grazing incidence mirrors often utilize a two-bounce collection technique in order to increase the amount of light collected while being able to reduce the physical footprint of the collector.

Normal incidence collector optics have a multilayer surface that has an additional capping layer to prevent oxidation. The chosen materials for the multi-layer mirror structure are typically alternating bilayers of high and low Z, in order to maximize the constructive interference of the light being reflected off of the surface. The sizing of the layers is determined by Bragg diffraction, $n\lambda=2d\sin(\theta)$, where n is an integer, λ is the wavelength of light, d is the multilayer spacing, and θ is the angle of incidence. The typical materials chosen for these layers are 4.5 nm of Si and 2.4 nm of Mo. These materials are chosen for their high contrast and low absorption of EUV light. The segmented length of 6.9 nm is chosen because it is nearly half the wavelength of 13.5 nm light, thus optimizing Bragg diffraction [32, 56, 57]. Typically 40-50 bi-layers are fabricated for one mirror. Additional layers do not increase reflectivity and only add to fabrication costs. Having more bi-layers than necessary does, however, allow for a certain amount of surface erosion to occur before the mirror is considered non-viable. One concern with all collector optics is the oxidation of the outer layer; an oxidized layer

of Si or Mo reduces EUV light reflectivity and increases out of band radiation reflection. As such, an approximately 2 nm thick layer of Ru is deposited on the outermost surface. Ru is chosen for its high reflectivity and high oxidation resistance [58]. Diffusion amongst the bi-layers is also a concern, and much research has been invested in Gibbsean segregation alloys, and other diffusion barriers [59, 60].

Unlike normal incidence mirrors, grazing incidence mirrors do not typically require the use of multilayer structures. Instead, a simple layer of highly polished Ru is coated onto a stainless steel substrate for the same reasons it is ideal as a capping layer on normal incidence mirrors [58]. Multilayer layer structures have been studied however. The primary goal with these systems is to resist reflectivity loss due to mirror degradation and increased surface roughness caused by energetic species bombardment [61].

Ultimately, the two major differences between the normal incidence mirrors and the grazing incidence mirrors exists in their construction. The first major difference exists because normal incidence mirrors require the use of a multi-layer mirror structure where grazing incidence mirrors do not. The effects of diffusion and inter-layer mixing due to energetic debris damage are more relevant to normal incidence mirrors than grazing incidence mirrors. While energetic debris is still very detrimental to grazing incidence mirrors, it is manifested in the development of surface roughness, which causes scattering and diffusion of the light being reflected. In concept, it is easier to create a grazing incidence mirror, though it is more difficult to maintain its reflectivity when exposed to the energetic debris created by the EUV plasma; surface roughness is

heavily detrimental to surface reflectivity of grazing incidence collectors. Normal incidence mirror fabrication is a very difficult process given the necessity of highly uniform nanoscopic layers on a large curved surface. A second major difference between the two techniques is the amount of light that can be collected. Fundamentally the normal incidence mirror is more efficient due to its collection of a large solid angle. The normal incidence mirror incorporates several shells that do not completely collect all of the light being generated due to material spacing. There exists a finite distance between each mirror that needs to be maintained, and it is impossible to reflect the smallest angles directly in front of the plasma. These shells also increase the complexity of fabrication and cooling. Thermal loads are of great concern for both mirror types, as heating of the mirrors can cause warping, and diffusion of the materials of which the mirrors are composed. Furthermore, both mirrors are strongly affected by the presence of deposited EUV fuel contaminants, which have the potential of changing the composition of the mirror surface.

Issues regarding collector optic lifetime arise primarily due to its placement near the EUV source. As was mentioned previously, highly energetic ions and neutrals are ejected from the EUV emitting plasma upon relaxation of current that confines the plasma through the development of magnetic fields. The requirement to reflect 13.5 nm light also causes surface roughness changes of 0.5 nm to adversely affect the reflectivity of the mirror surface, especially for grazing incident collectors. Other concerns in collector optic performance are caused by the diffusion of the mirrors due to thermal loads, as well as oxidation and ion implantation. If the layers are altered by

deposited/implanted EUV fuel, the reflectivity of the mirror will be lowered and the cost of ownership of the entire tool will be increase. As such, it is illuminating to discuss the creation and attempted mitigation of such energetic debris.

2.4 Extreme Ultraviolet Light Source Debris

The lifetime of a collector optic is of paramount importance to EUV lithography tool manufacturers due to the direct impact on tool cost. While the collectors themselves cost hundreds of thousands of dollars to develop, the downtime required replacing them once they no longer reflect enough light takes up to eight hours [62]. Each hour of downtime is equivalent to several millions of dollars in lost revenue to the fabrication facility. As mentioned in section 2.3, three different factors have an impact on mirror lifetime: the thermal load, the deposited contamination of EUV fuels and other contaminants, as well as the energetic debris flux incident on the plasma facing surface. Because the collector optics are positioned in proximal distance to the EUV plasma, the debris (anything that isn't EUV) developed in the plasma is going to impact the collector optic if complete mitigation of debris is not possible.

The plasma that emits EUV light also radiates infrared light, ultraviolet light, as well as light in the visible spectrum. Because the collector optics are only optimized to reflect EUV light, the out of band radiation will be partially absorbed (though parts of the spectrum will also be reflected which is not desirable). The absorbed energy creates a thermal load on the collector optics that is increased with the scaling of the EUV source power and size of collector optic surface. Energetic atoms that are not mitigated

will also deposit their energy into the bulk of the collector. Ultimately the effects of the increase in temperature of the collector optic lead to inter-layer diffusion and strain development between layers. Inter layer diffusion, especially relevant to multi-layer mirror surfaces, diminishes the effectiveness of Bragg diffraction and reduces the ideal reflection of EUV. By inducing strain on the layers (caused by different material layers having different coefficients of expansion) inter-layer defects will be created that will have a malevolent effect on the mirror surfaces that need to be smooth.

Deposition of condensable energetic fuel and chamber contaminants is a second concern to EUV lithography cost of ownership in light of industry's shift to condensable Sn fuel. The materials chosen to reflect EUV light off of the mirror surface are chosen because they have electrical properties that are ideal for reflecting a certain bandwidth of light. Sn, unfortunately, readily absorbs EUV light and its presence on the collector optic surface increases the reflection of out of band radiation and leads to EUV light absorption. The fact that the EUV plasma does not uniformly deposit Sn also presents a concern to grazing incidence collector optics. This type of collector optic suffers greatly from increases in surface roughness and non-uniform deposition of an EUV absorbing film leads to significant losses in reflectivity.

The last major influence on collector optic lifetime is the effect of energetic debris interactions with the mirror surface. The energies required to ionize the EUV fuels sufficiently has the side effect of generating high-energy ions and neutrals as well. These energetic atoms have been measured with energies up to 50 keV [63]. If left unmitigated, the energetic flux can induce one of two main processes two occur:

implantation or sputtering. Implantation into the mirror can create substrate-doping defects that affect the optical parameters of the mirror, cause inter-layer scattering, reducing the effectiveness of Bragg diffraction, and can even cause EUV absorption that increases thermal concerns. Surface sputtering leads to an increase in surface roughness, which can reduce the reflectivity of the mirror and increase cost of ownership. While the previously described thermal concerns and EUV fuel deposition can be handled with water cooling and cleaning techniques respectively, the complete mitigation of energetic atoms is extremely difficult. The reason it is so difficult is the need for cost effective operation. The mirrors must be placed close to the EUV plasma to collect as much light as possible using the smallest, and most cost effective mirror possible. Furthermore, the debris mitigation techniques cannot have a noticeable impact on the collection and transmittance of EUV light. While it is common to use a buffer gas around the plasma to retard the species energies through scattering processes, there is a tradeoff between the allowable buffer gas pressure and the attenuation of EUV light. Ultimately, it is such tradeoff considerations that drive the research and progress within EUV lithography as it is sought to be the next generation of optical lithography.

2.5 Aim of Present Work

While many challenges still hinder the path to high volume implementation of EUV lithography, heroic efforts to increase light source power have yielded potential tool implementation in the upcoming years. While it is (albeit not

financially) possible to implement EUV lithography as it stands now, the ability to keep costs at a minimum is paramount to the successful implementation of EUV lithography. In order to achieve cost-effectiveness, however, optimization of every aspect of the lithography tool is required. As mentioned previously, one primary concern is the extension of collector optic lifetime in addition to the production of only clean EUV photons at the intermediate focus point of the EUV light source. While considerable effort has been invested into understanding the transport of debris from the EUV plasma to the collector surface, much focus is still required to completely understand how these utilized mitigation techniques affect transport of debris to the intermediate focus.

It is to this gap in knowledge that this work seeks to provide a bridge. Through the utilization of the detectors that will be presented in chapter 3, an in depth understanding of the debris transport mechanisms will be presented. Furthermore, the secondary generation of plasma and its consequences will be detailed and connected to carbon contamination observed at the intermediate focus. Ultimately, through the variation of different pinch gas mass, buffer gas mass, as well as buffer gas pressure, an analysis of the effects of debris mitigation on debris transport will be presented. These measurements will shed light upon the reason why current EUV light source suppliers have chosen to increase chamber pressures up to 1 Torr (much larger than the maximum 22 mTorr in the presented results) and introduced high flow gas filters at the intermediate focus. Lastly, the theoretical analysis of the transport processes will provide an understanding of what exactly

allows high-energy species to reach the intermediate focus without proper mitigation techniques in place.

2.6 Previous Works

While a great deal of research is been focused on investigating the creation and transport of debris from the EUV plasma to the collector optics, almost no research has been done on directly investigating the progressive transport to the intermediate focus. Through an extensive literary search, only one source was found to even consider how Sn is transported throughout an EUV REDPP source chamber. In a doctoral thesis by Kurt Gielissen for the Eindhoven University of Technology, results demonstrate that there are three different types of particles emitted from REDPP sources: micro particles, slow atomic/ionic debris, and fast ionic debris[64]. In this work, micro particles are described as the particles formed at the electrode surface and are ejected micron-sized particles due to the incident laser pulse used to create the gaseous Sn plume. The slow atomic/ionic debris is a result of second plasma created after the pinch plasma has diffused away from the chamber. Lastly, the fast ionic debris (>10 keV) is a direct consequence induced areas of high inductance within the sausage instability of a pinch plasma. In these areas the applied voltage can be greater than 10x that which is applied across the rotating disk electrodes, resulting in the acceleration of 10+ ions up to 100 keV. Ultimately, Gielissen demonstrated that Sn contamination can be reflected off of collector optic Ru surfaces while also depositing material through a splashing process, by which the micro particles reach the surface and collapse or reflect off of it depending on

the temperatures. Out of line of sight Si witness plates also observed Sn deposition (~25% as much as direct line of sight) that was attributed to the anisotropic slow atomic/ionic debris evolution through the chamber as well as reflected sputtering from other locations in the chamber. Furthermore, SRIM modeling revealed that while normal incidence mirrors sputter ~10 ions per incident Sn atom no matter the energy, grazing incidence mirror sputtering yields strongly depended on incident energy. Ultimately, however, the method by which highly energetic ionized debris reached the intermediate focus was not discussed.

Professor Ruzic has modeled the transport of neutral species in an investigation of fusion devices[65]. In this paper, it is discovered that scattering of neutral species is dominated by two reactions: ionization and elastic scattering. In areas of low plasma density, the driving scattering process is elastic scattering. Where plasma density is increased, ion-neutral scattering events are predominant. In these reactions, the neutral species' direction and energy are changed during ionization. Further investigation into the transport of neutral species of specified energy (E<1 keV) down a 1mTorr pipe revealed that at such low pressures, the mean free path between scattering collisions resulted in the dominant neutral collision being with the tube walls. As such, because this investigation dealt with the re-molecularization of neutral species, the density of neutral *atoms* decreased exponentially with the length of the tube being the primary independent variable.

Further intermediate transport research has been performed at CPMI prior to the development of SNIFFED [66]. In these experiments the collector optic was

installed, and intial witness plate, ion and neutral flux, and Faraday cup measurements were taken at a location on the opposing wall (from the pinch) outside of the collector shells. At this location, it was observed that a charged positive flux was present through the first 4 ⌠s after the formation of EUV light. This resulting flux, if assumed to be singly charged equated to $\sim 3x10^{11}$ ions/mm^2. An additional concern to contamination issues is the presence of Carbon contamination observed at these locations. It was observed that an unmasked Si surface facing the chamber would have a deposited film that is roughly 50% C, 20% Si, 30% O. A similar unmasked sample that was loosely covered (to prevent photon/ion irradiation but to allow gas dispersal to the surface) showed ratios of 20/25/55 for C/Si/O respectively. This is in comparison to the masked samples, which had a surface composition of 8/32/60 for C/Si/O. The carbon contamination was concluded to be a result of EUV-photon carbon molecule cracking near the surface of the Si. These results were concluded after exposing multilayer mirror samples at a grazing incidence directly to the pinch, and performing EUV reflectivity measurements. As shown by Shin in [67], the resulting reflectivity measurements did not correspond the anticipated reflectivity loss due to surface roughening alone (at the time the measurements were taken using a Xe fuel). The reflectivity measurements in fact showed a series of resonance absorption peaks that could be modeled with up to 100 nm of C contamination after 2.8 million pinches.

CHAPTER 3

EXPERIMENTAL SETUP

3.1 Introduction

Familiarization with the experimental apparatus is requisite to comprehending obtained results. The first section of this chapter details the XTREME XTS 13-35 gas discharge EUV emitting light source. The following sections detail the XTREME commercial EUV emission diagnostic (XCEED), XCEED's debris mitigation capabilities, as well as the diagnostics that are critical to analyzing the process through which debris is transported to the intermediate focus. The order of these subjects is chosen to provide a conceptual progression from the creation of EUV light to the qualification and quantification of debris emitted at the intermediate focus.

3.2 XTS 13-35 Z-Pinch EUV Emitting Source

The XTS 13-35 EUV light source (fig. 3.1) was originally developed by XTREME Technologies, GmbH, to produce 35 W, in 2π sr, of 13.5 nm light (2% bandwidth) when operating at the maximum frequency of 1 kHz using Xe gas as the EUV emitting fuel [68]. With Xe, an approximate conversion efficiency of 0.55% was achieveable [69]. While the light is not generated in a way that is currently being explored for high volume manufacturing (the laser produced plasma and rotating

disk electrode sources), it does serve as an adequate replacement that mimics the same processes occurring in these other two types of sources.

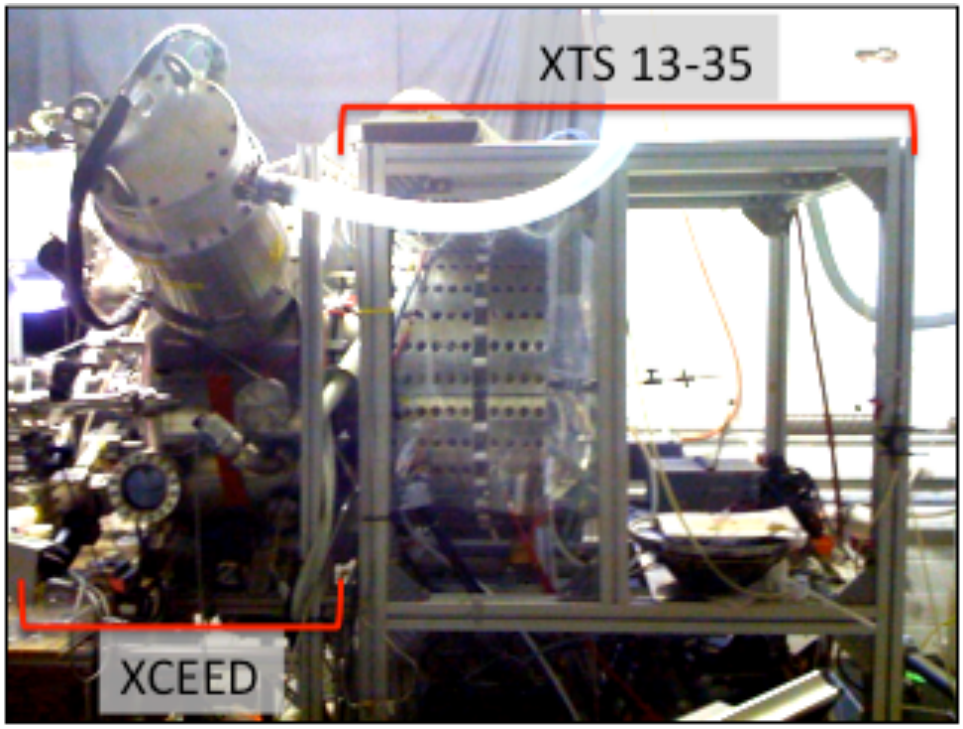

Figure 3.1: The XTS 13-35 EUV source is shown coupled with the XCEED chamber. The XTS 13-35 source is capable of creating 35 W of EUV light in 2π sr with operation frequency of 1000 Hz. The XCEED chamber is used to measure EUV emission, energetic flux, and to test mitigation techniques.

The XTS 13-35 utilizes the fundamental physics of the z-pinch, conceptually described in chapter 2, to compress a pre-ionized gas and generate EUV light. For the purposes of this experiment, and to mimic the Sn fuel used in commercial tools, the W cathode was replaced with a solid Sn cathode. The highly ionized N_2 gas used ablates the Sn from the electrode and introduces it into the pinch plasma. The capacitor bank of the XTS 13-35 is charged to 2.5 kV and is discharged with a current approaching 20 kA over a period of approximately 0.1 μs to create the 30 eV, 10^{20} cm^{-3} plasma necessary to produce EUV using the ablated Sn atoms. The

cylindrical pinch plasma expands radially from the source emitting EUV, out of band radiation, as well as energetic ions and neutrals.

3.3 XCEED

The XTREME commercial EUV emission diagnostic (XCEED) was developed to allow experimental investigations of the XTS 13-35 generated plasma. XCEED is a large vacuum chamber that couples directly to the XTS 13-35 source via a vacuum tight ISO flange fitting. Originally developed in 2004, the chamber was designed with the intent to allow the characterization of energetic debris, EUV exposure experiments. For the scope of this research, several diagnostics were utilized at these ports to better understand the

3.3.1 Chamber design

The XCEED chamber itself consisted of a 46 cm radius cylinder that extended a length of 35.6 cm. The chamber was coupled to the XTS 13-35 source using an ISO250 port. Three other such ISO250 ports were equally spaced around the cylinder for uniform pumping capabilities. The critical experimental access ports are the nine 2-3/4" flanges positioned along the horizontal plane that extends through the center of pinch. These ports are placed in direct line-of-sight to the EUV plasma pinch point and located every 5^{o} along a 0.72 cm radius around the pinch from 10^{o} to 45. In total there are 47 different ports that provide access to the XCEED chamber, making it a versatile portal to investigate ongoing processes in the EUV plasma expansion.

A mockup collector optic was mounted inside of the XCEED chamber, for the intermediate focus measurement experiments but not the ion/neutral species energy measurements. The mock-up was used to simulate the specular reflection of photons from the plasma source to the intermediate focus. For this chamber, the intermediate focus was simulated at 0.72m from the EUV plasma source at the 0° port. The mock-up collector optic consisted of two stainless steel shells. The outer shell was 0.44m in diameter and designed to reflect 30° light while the inner shell was 0.13m in diameter and designed to reflect 10° light. While stainless steel shells aren't capable of reflecting EUV light, the purpose of this dissertation was to investigate debris transport. These shells do, however, serve to simulate the reflection and transport of energetic debris emanating from the EUV emitting plasma. The brackets that support the shape of the shells obscured direct line of sight from the EUV plasma source to the intermediate focus.

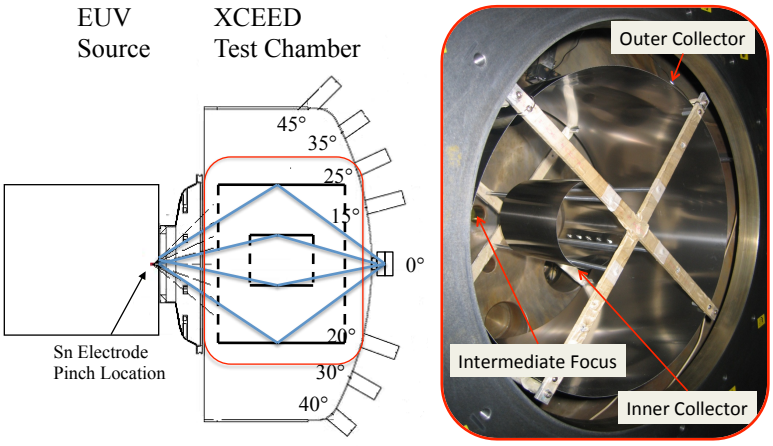

Figure 3.2: Shown is the mock-up collector optic as positioned in the XCEED chamber. The inner shell is designed to specularly reflect 10° light, while the outer shell is designed to reflect light from 30° away from normal.

3.3.2 Pressure and gas regulation

The XCEED pressure regulation system is composed of three types of pumps in series. The first stage is a rough pump capable of removing gas at approximately 7 l/s (N_2 rated). This pump was chosen to handle the multitude of reactive gases that were used for various experiments performed within the XCEED chamber, though no reactive gases were used for the purpose of these experiments. Utilizing only this pump, it is possible to achieve a base pressure $8x10^{-1}$ Torr.

The second stage of pumping consists of a Roots blower. Again the dry feature of the blower allows for the added ability to handle reactive gases that would cause problems with typical oil-based pumps. When placed in operation with the first stage of pumping, the achievable steady state base pressure of the XCEED system is approximately $3x10^{-3}$ Torr. Although this pressure is adequate to operate the XTS 13-35 source for low pinch-gas flow rates, gas purity and high gas flow requirements require the use of turbomolecular pumps.

Two magnetically levitated turbomolecular pumps, capable of a pumping rate of 5000 l/s, are the last stage of pumping. These two pumps are attached to the ISO250 flanges located on the upper half of the XCEED chamber. One of the pumps is attached in conjunction with a manually adjustable variable flow gate valve. An ultimate base pressure of $1x10^{-6}$ Torr was achievable using all three stages of pumping with a 24-hour bake out period.

Gas is introduced into the chamber using two 1000 sccm rated (N2 calibrated) mass flow controllers. The first injection point is through the solid Sn cathode, where pre-ionization of the pinch gas occurs. The second entry point is

located between the electrodes and a collimated tungsten foil trap. The gas injected through the electrode will be referred to as "pinch gas," and the gas injected between the foil trap and the electrodes will be referred to as "buffer gas" for the purposes of this dissertation. The utilized relative gas flow rates and corresponding conversion ratios, relative to the calibrated N_2 gas factors, are listed in table 3.1.

Table 3.1: Ar buffer gas operating conditions and corresponding flow rates and achieved chamber pressures.

Gas Flow Rate (SCCM)	Gas Species	MFC Setpoint (0-5 V)*	Gas Flow Ratio	Gauge Conversion
100	Ar	0.36	1.4	1.3
200	Ar	0.72	1.4	1.3
500	Ar	1.8	1.4	1.3
1000	Ar	3.6	1.4	1.3
100	He	0.34	1.45	0.3
200	He	0.68	1.45	0.3
100	Ne	0.34	1.46	0.18
200	Ne	0.68	1.46	0.18
100	N_2	0.5	1	1

[1]Based on a 1000 sccm MFC

3.4 Debris Mitigation Techniques

The XCEED chamber and the XTS 13-35 source are equipped with two different primary debris mitigation techniques. The first method of debris mitigation is the aforementioned collimated tungsten foil trap. When energetic species are scattered, they pick up an angular (in spherical coordinates) velocity component that causes them to collide with the filaments. The tungsten can withstand the high heat loads and is relatively resistant to sputtering, sparing the much more delicate collector optics. The second form of debris mitigation consists of buffer gas being injected between the EUV plasma and the collimated foil trap to

increase the scattering collisions. Several other secondary forms of debris mitigation including heterogeneous fuel mixing, electric field lines, and magnetic field lines are easily implemented into the XCEED chamber, but are not relevant to the scope of the research presented [70].

3.4.1 Collimated foil trap debris mitigation tool

A collimated foil trap is a piece of equipment that is created out of thin tungsten foils. The foils are arranged in such a manner that channels are radially projected out from the z-pinch location. A secondary series of rings are placed in a similar fashion that results in the formation of the rectangular channels. By maintaining this shape, although a large amount of material is used to create the foil trap, there is very little influence on the visual cross section between the light source and the collector optics. Ultimately the foil trap's purpose lies in the fact that many collisions occur not only within the pinch itself, but also in the relatively dense gas that has expanded due to z-pinch destabilization. When collisions occur, the scattered energetic species no longer travel radially from the pinch, and are thus unable to traverse the ~ 5 cm length of the foil trap channels without undergoing gas scattering. As such, the scattered energetic species collide with the tungsten walls of the channel instead of the nearby collector optics. While it is still possible for unscattered and lowly scattered species to still make their way – with all of their energy – to the collector optics, the foil trap is able to mitigate a considerable amount of debris emanating from the pinch. Furthermore, area directly in front of the EUV plasma in the Z-direction is occluded to prevent the highest energy species

from reaching the intermediate focus. Since the z-pinch is cylindrical, upon expansion most of the species are likely to travel in the direction of the cylinder, the center of the foil trap.

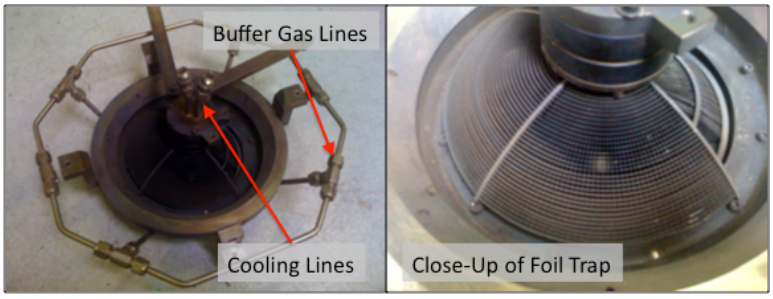

Figure 3.3: The collimated foil trap utilizes gas scattering to deflect energetic debris into the sides of the foil trap instead of on the collector optics. A buffer gas placed between the source and the foil trap aids in this scattering process.

3.4.2 Buffer gas curtain

The second phase of primary debris mitigation, the buffer gas curtain, coupled with the foil trap in order to increase the effectiveness of gas scattering. A shower ring of 6 mm stainless steel tubing, placed around the edges of the foil trap, injects gas into the gap between the EUV plasma and the collimated foil trap. The choice of gas, in a high-volume manufacturing tool, is determined based on the tradeoff between EUV absorption and high mass (atom size). Currently laser produced plasma sources utilize hydrogen gas, while rotating disk electrodes use argon as the buffer gas. Because surface roughness is more critical to grazing incidence mirrors, the larger and more massive species is required. The buffer gas species used in these experiments were varied to isolate the effects of buffer gas on debris transport.

3.5 Diagnostics

Several different diagnostics were utilized in an effort to understand what and how much non-EUV light debris reaches the intermediate focus of an EUV light lithography tool. The various diagnostics, and the purpose of their implementation, are diagrammed in the following three sections. The first diagnostic discussed is the Sn Intermediate focus flux emission detector. This detector, truly a combination of four different detectors, is capable of analyzing ion and electron flux, energetic charged and neutral particle flux, residual gas composition, as well as measuring erosion and deposition rates. The second discussed diagnostic, an energetic ion and neutral analyzer, is used to quantify the energetic ejecta coming from the EUV plasma. Lastly, a set of triple Langmuir probes are used to characterize the propagation and development of plasma throughout the EUV lithography tool. When combined, these detectors allow for a quantified observation of debris transport from development to ejection at the intermediate focus.

3.5.1 Sn intermediate focus flux emission detector (SNIFFED)

The Sn Intermediate Focus Flux Emission Detector (SNIFFED) apparatus, pictured in figure 3.4, was developed to measure the non-photon flux exiting the intermediate focus. It consists of four different diagnostics placed along a ring positioned to intersect the 10^{o} specular reflection. Each of these diagnostics seeks to analyze a certain aspect of expected emission. The first diagnostic, a shielded Faraday cup, is used to measure the charge and arrival time of any type of charge flux. The outer shield is electrically isolated from the interior cup, to allow charge

discrimination between ions and electrons, with a 2 mm orifice for charge flux measurements. The second diagnostic, a dual quartz crystal microbalance, measured any ongoing erosion or deposition during the operation of the EUV source. One of the crystals is covered for the duration of the measurement process to account for changes measurements due to thermal considerations. The third diagnostic, a residual gas analyzer, provided an analysis of contaminant gas species. The gas analyzer used for these experiments, was capable of measuring up to 100 amu species, high enough to measure molecular compounds and any atomic species used in the EUV source chamber. The fourth diagnostic is a set of dual microchannel plates equipped with two charged plates for charged particle deflection. These dual microchannel plates, when biased at -2500 V, create a measureable electron signal when impacted by energetic ions or neutrals greater than 100 eV. The charged particle deflectors allow for the analysis of the charged versus neutral energetic flux and combine to allow for the detection of any energetic species that might cause energetic impact damage to down line optics. Based on time-of-flight analysis, the microchannel plates also allow for a determination of the timing between plasma formation and flux arrival time. In order to prevent arcing between the plates, the SNIFFED chamber is maintained at $5x10^{-7}$ Torr. When coupled with the Faraday cup, it is possible to know a relative flux measurement of ions.

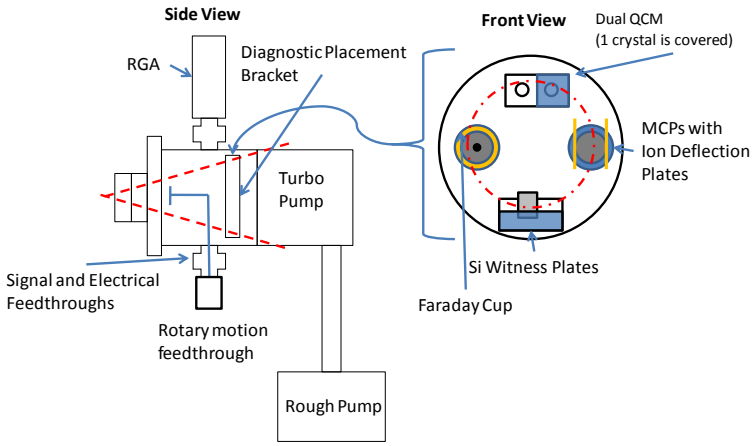

Figure 3.4: Shown are the detectors utilized in the Sn Intermediate Focus Flux Emission Diagnostic (SNIFFED). The dual quartz crystal monitor measures deposition or erosion, the microchannel plates (MCPs) with charged particle deflection measure the energetic atomic flux, and the Faraday cup provides a quantitative analysis of the charged species leaving the intermediate focus. Each of these detectors is positioned on the annulus that is formed by the 10^{o} reflection angle. The residual gas analyzer (RGA), provides a compositional analysis of any contaminant gases present.

3.5.2 Ion and neutral atom energy analyzers

In order to adequately understand the debris coming from a EUV source, it is necessary to be able to measure both the energetic charged and neutral fluxes. In order to measure the positive ion flux, a spherical sector electrostatic energy analyzer was developed at the Center for Plasma-Material Interactions by Keith Thompson in 2004 [71-73]. This detector is a Comstock model AC-902B Spherical Sector Energy Analyzer that is placed within a custom vacuum chamber designed to be attached to EUV sources for measurement. The setup of this detector is shown schematically in figure 3.5.

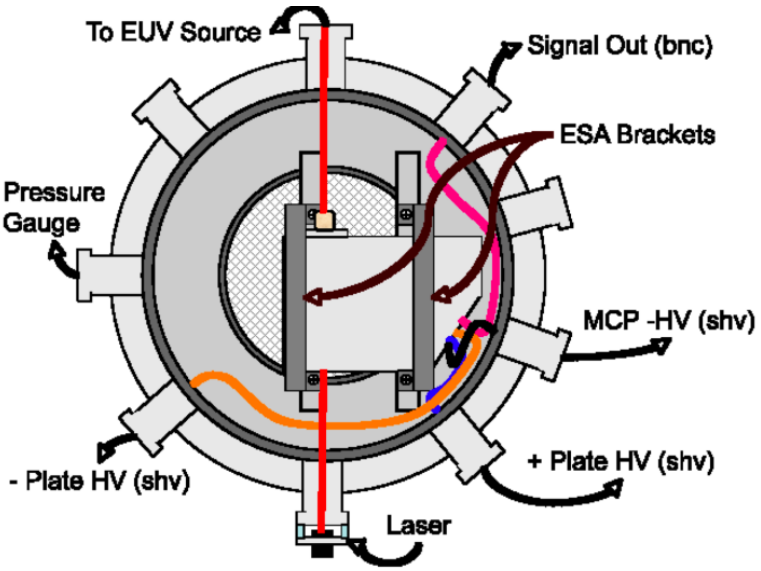

Figure 3.5: A cartoon figure diagramming the ESA chamber shows how the ESA is positioned with respect to the EUV source debris. Various high voltage ports allow for the selection of a given E/q ratio, and allow for the measurement of ion flux.

The detector consists of two plates that are spherical in shape and extend 160^{o} from the entrance to the exit point. The inner and outer plates are placed at a negative and positive potential in order to curve ions along the path using the Lorentz force. The ions that are allowed to traverse the entire path are chosen based on their energy to charge ratio. As shown in equation 3.1, the energy (E) to charge (q) ratio can be selected by placing a certain difference in voltage (ΔV) across the plates with inner and outer radii r_1 and r_2. For the purpose of these measurements, a positive and a negative polarity 3kV, 300 W power supply was used to isolate singly charged ions up to 14 keV.

$$\frac{E}{q} = \frac{\Delta V}{\left(\frac{r_2}{r_1} - \frac{r_1}{r_2}\right)} \tag{3.1}$$

The energy resolution of the detector, ΔE, is dependent on the energy (E) of the ion being observed, the mean sphere radius (R), the angle over which the ion

travels (φ), the direct distance between the entrance and the exit of the detector (δ), and lastly is dependent on the diameter of the entrance orifice (ω). The relationship between these characteristics is shown in equation 3.2. The manufacturer provided each of these equations, though the formulations are relevant to all spherical analyzers. Values relating to the AC-902B detector are shown in table 3.2.

$$\frac{\Delta E}{E} = \frac{\omega}{[R(1-\cos\varphi)+\delta\sin\varphi]} \tag{3.2}$$

Table 3.2: Various design characteristics of the ESA used in these experiments.

Parameter	Value
r_1	4.88 cm
r_2	6.02 cm
R	5.47 cm
φ	160°
δ	1.07 cm
ω	2 mm

Having an understanding of how the AC-902B isolates energetic ions, it is now possible to understand how the detector counts the number of ions that traverse the spherical sector. Immediately after the exit orifice is a pair of microchannel plates. Microchannel plates are fabricated from lead glass, and contain tens of thousands of tiny 10-100 μm pores that act as electron multipliers [74]. When an ion, or any energetic atom, impinges upon the microchannel plate surface, an electron cascade is created that is further multiplied through the length of the plate. This electron multiplication process is diagramed in figure 3.6. A second plate is placed within two millimeters of the first and a potential is applied to accelerate the electrons from the first plate to the second plate. The second

microchannel plate further multiplies the electron cascade to the point that an electrical signal can be measured. In total, the electron multiplication is on the order of 10^7 times larger than the original cascade created by the first plate.

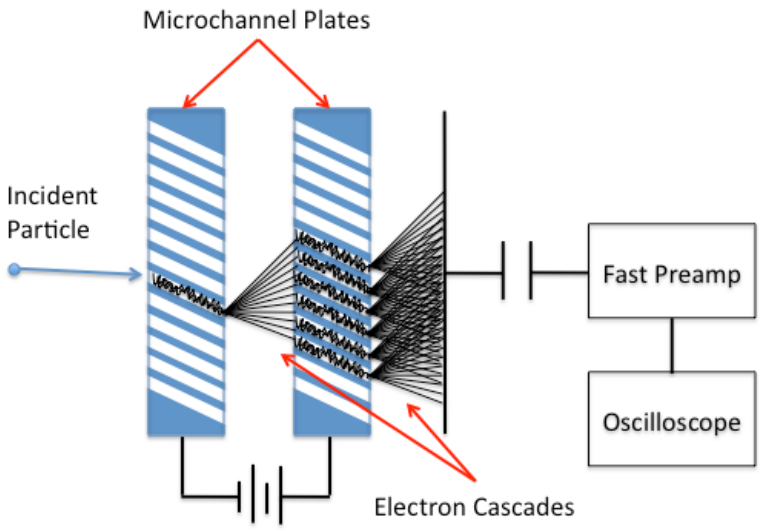

Figure 3.6: Microchannel plates consist of tiny electron amplifying pores that create an electron cascade when hit with an ion, a neutral atom, or photons. These plates are used to measure the energetic ion and neutral fluxes emitted by EUV sources.

To quantify the signal produced, an Ortec fast preamp model 9326 is used to increase the signal output to the point that an approximately 100 mV a 5-10 ns wide signal is created. This signal is monitored using an Agilent 8102B oscilloscope that has a 1 GHz resolution. When observed on the oscilloscope, the microchannel plate signal to noise ratio is approximately 20-30. The histogram function of this oscilloscope allows for a cumulative summation of the total number of signals observed after the formation of the EUV plasma. Each time a trigger is sent to the oscilloscope, a count is added to a column of the histogram so that over a period of time, a summation of the total number of counts observed at a certain time period can be observed. The histogram plot that results is a function of the time period

being observed, as well as the trigger point (-40 mV), which is manually set within the oscilloscope's function settings. A measurement is taken for 2 minutes from the range of 0-50μs and the summed hits are converted into measured ion flux using a process which is detailed in [72].

While the spherical sector energy analyzer is able to measure ions, neutral species are not subject to the electrostatic bending forces and simply pass straight through the alignment orifice in the back of the ion energy analyzer. In order to measure energetic neutrals, a neutral energy detector was developed. The neutral detector diagnostic is essentially the same as the ESA assembly without the use of the energy sector discriminator. The setup consists of a set of Chevron style dual microchannel plates, which are placed behind the ESA in direct line of sight to the EUV source. In this setup, the ESA acts as an ion diversion device that allows two different signals to be observed by the neutral detector. The first measurement involves leaving the diverting plates of the ESA set at ground so they have no influence on the beam reaching the neutral detector. The beam thus measured contains both neutral and charged species and is termed the "total" signal. The second measurement places a 6 kV potential difference across the diverting plates and is capable of preventing all ionized debris from reaching the neutral detector as shown in figures 3.7 and 3.8. Even though the ion diverting plates are only capable of isolating singly ionized 14 keV ions for ion measurements, the potential placed across the plates is enough to divert much higher energetic ions just enough to be extinguished against the walls of the plates.

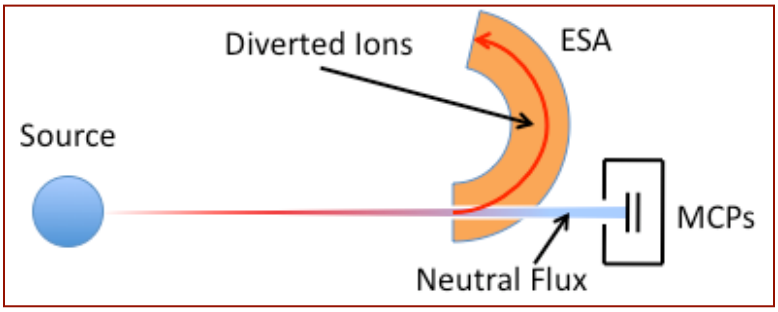

Figure 3.7: The ESA is used as an ion diverter for neutral detector measurements. This results in a neutral only flux being measured by the microchannel plates. The subtraction on the total and neutral flux estimates the energetic ion flux.

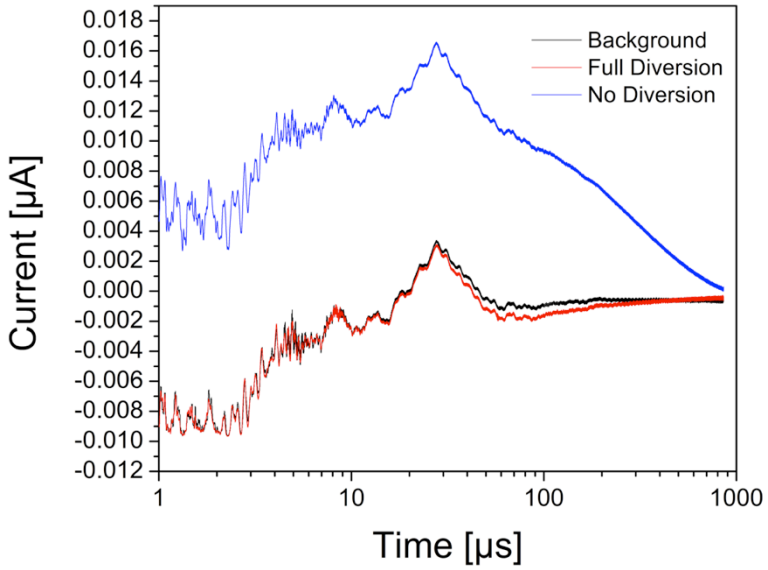

Figure 3.8: Faraday cup measurements proving the effectiveness of the ESA's ability to mitigate ions is shown. The black line shows the measurement with no mitigation, where as the red line shows full mitigation in use. The green line is the background measurement taken with all ion and photon beams being blocked. There is only marginal separation between full diversion and background, which occurs later than 30 μs after pinch formation and is due to variation in the signal.

Because the debris travels through the alignment orifice of the ESA, this orifice is the smallest orifice to be consider when calculating flux measurements. Original designs of the neutral detector incorporated a set of deflection plates placed perpendicularly to the beam of charged particles, yet complete deflection of ions was not capable due to the shielding effects of the intermixed ions. Without

much higher voltages, than were capable with cost effective power supplies, it was not possible to completely get rid of the ions.

The physical assembly of the neutral detector consists of a stainless steel enclosure, which is grounded to the chamber wall as shown in figure 3.9. This enclosure is designed to reduce the amount of electromagnetic noise experienced by the charging and discharging of capacitors typical of Z-pinch devices. There is a hole in the front plate, allowing for the transmission of the debris. The microchannel plate assembly is the same as that used in the ion energy sector analyzer, and behaves equally given that microchannel plates are momentum exchange devices independent of charge. Lastly, there is a capacitor connected to the rear plate of the microchannel plates that is attached to a BNC port on the chamber. The same Ortec fast preamp is used to modulate the resulting signal so that noise is less of a factor when measuring the signal. The resulting signal is once again monitored with the oscilloscope's histogram function to measure the signal from the start of the EUV formation to the end of species arrival.

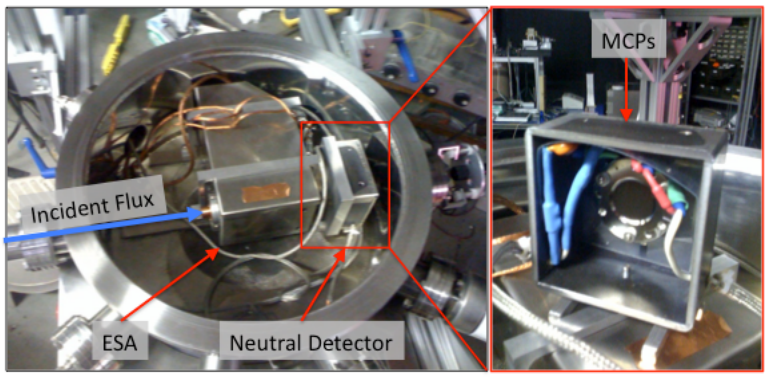

Figure 3.9: Shown are the ion energy sector analyzer and the neutral detector as they are positioned in the vacuum chamber. The neutral detector is positioned behind the alignment orifice so that energetic ions can be removed using the deflection capabilities of the ion analyzer.

3.5.3 Triple Langmuir probe plasma diagnostic

It was shown in the preliminary results that decaying charged flux was reaching the intermediate focus above 1000 sccm Ar buffer gas flow rate. As such it is believed that at these conditions, a secondary diffuse plasma is also being created. Because these operating conditions resulted in the most effective debris mitigation, it is necessary to confirm the existence of, and understand, the properties of this plasma. Typically, with steady state plasmas, it is possible to use a Langmuir probe to analyze the ion density, electron density, as well as electron temperature. Unfortunately, the transient and rapid nature of the EUV plasma expansion requires a different approach to accurately characterize the plasma. To this extent a Langmuir triple probe will be utilized to analyze the temporal fluctuations in the electron temperature and density. This technique will be able to analyze the secondary plasma that is developed either through photoionization or through electron excitation. As shown in figure 3.10, the probe will be placed inside of the inner most collector optic as well as outside of the collector shell, where the highly energetic pinch ions cannot reach.

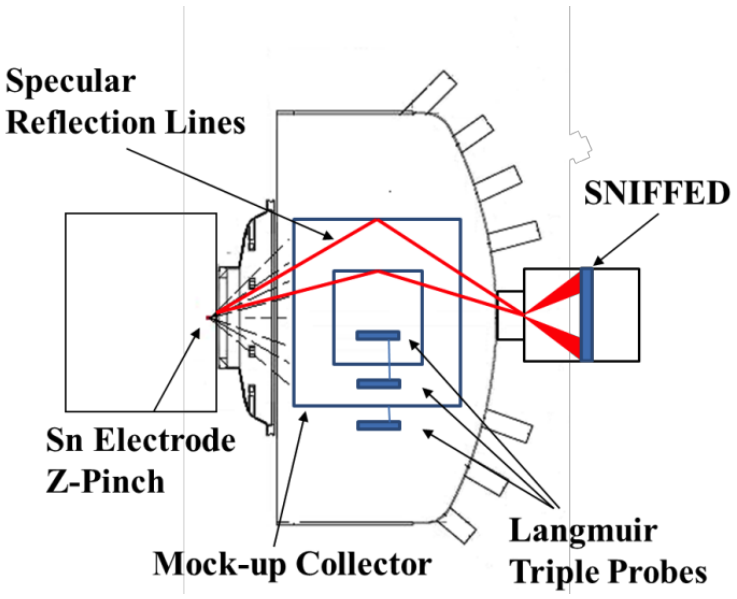

Figure 3.10: Langmuir triple probe measurements will be taken at three different locations relative to the mock-up collector optic as diagrammed above. These probe measurements will analyze the diffuse plasma that is formed after a z-pinch plasma is created. The three different locations will analyze differences in the plasma relative to where the collector optic cylinders are located.

Triple probes operate by placing one probe at the floating potential (V_2) of the plasma, while applying a positive (relative to the floating potential) bias to another probe (V_1). The third probe (V_3) is biased negatively relative to the floating potential to be located in the ion saturation curve of a typical plasma current-voltage curve. The electron temperature (Te) of a plasma can be determined if the plasma follows the following three assumptions: (1) The electron temperature is Maxwellian, (2) the mean free path of electrons is larger than the sheath size, (3) the sheath size is smaller than the distance between the three probes. If V_{dx} is defined as the difference between the V_x (x = 1 or 3) and the floating potential, the electron temperature can be solved for iteratively with equation 3.3:

$$\frac{1}{2} = \frac{1 - \exp\left(-eV_{d2}/kT_e\right)}{1 - \exp\left(-eV_{d3}/kT_e\right)} \tag{3.3}$$

If V_{d3}>>kTe, then the equation can be directly solved for Te. Utilizing this determined quantity, the electron density can be determined directly from equation 3.4, where M is the mass of the ionized species, i_{sat} is the ion saturation current measured from probe three, A_x is the probe surface area, n_e is the electron density, and t is the time.

$$n_e(t) = \frac{i_{sat}(t)}{0.61 e A_x}\sqrt{\frac{M}{T_e(t)}} \tag{3.4}$$

Ultimately the electron temperature and densities of diffuse plasma at the various presented debris mitigation schemes will be measured.

3.6 Experimental Procedure

In order to analyze the processes by which debris is transported from the EUV plasma to the intermediate focus, a series of experiments were orchestrated to isolate the variations in debris transport due to chamber pressure, buffer gas mass, and pinch gas mass. These experiments are outlined in table 3.3. For each of the experiments (excluding Si witness plate deposition experiments that will be described shortly), a collimated buffer gas foil trap was placed between the EUV plasma and the rest of the chamber. This trap is utilized as a primary source of debris mitigation and functions most effectively when chamber pressure is high

enough to induce gas scattering, which causes high-energy species to deposit their energy into the tungsten filaments instead of the fragile collector optics.

Table 3.3: Diagrammed are the experimental conditions to diagnose the methods by which debris is transported to the intermediate focus. Experiments 1-5 explore the effects of chamber pressure, experiments 2,6-7 explore the effects of buffer gas mass, and experiments 8-10 explore the effects of pinch gas mass on debris transport.

Exp. Number	Pinch Gas Flow Rate (SCCM)	Pinch Gas Species	Buffer Gas Flow Rate (SCCM)	Buffer Gas Species	Chamber Pressure (mTorr)	Pinch Freq. (Hz)
1	100	N_2	0	-	0.3	20
2	100	N_2	200	Ar	3	20
3	100	N_2	1000	Ar	6	20
4	100	N_2	1000	Ar	12	20
5	100	N_2	1000	Ar	22	20
6	100	N_2	200	He	3	20
7	100	N_2	200	Ne	3	20
8	100	Ar	200	Ar	2	20
9	100	He	200	Ar	2	20
10	100	Ne	200	Ar	2	20

For each of these experiments, microchannel plate, Faraday cup, residual gas analyzer, Langmuir triple probe, and quartz crystal microbalance data sets were acquired. Two individual sets of data were taken using the microchannel plates: with and without charged particle deflection. The histogram measurements (similar to the method used to take ion/neutral data as diagrammed in section 3.5.2) were summed over a period of three minutes with a detector bias of -2000 V. The histogram discriminator was set at -20 mV, which was well below the ± 5 mV noise signal. For charge deflection, two electrically isolated 2.3 cm copper plates were placed at the entrance of the SNIFFED apparatus. A charge differential of 6000 kV

was placed across gap of 4 cm with capability of completely deflecting 50 keV Ar^+ ions as shown in figure 3.12.

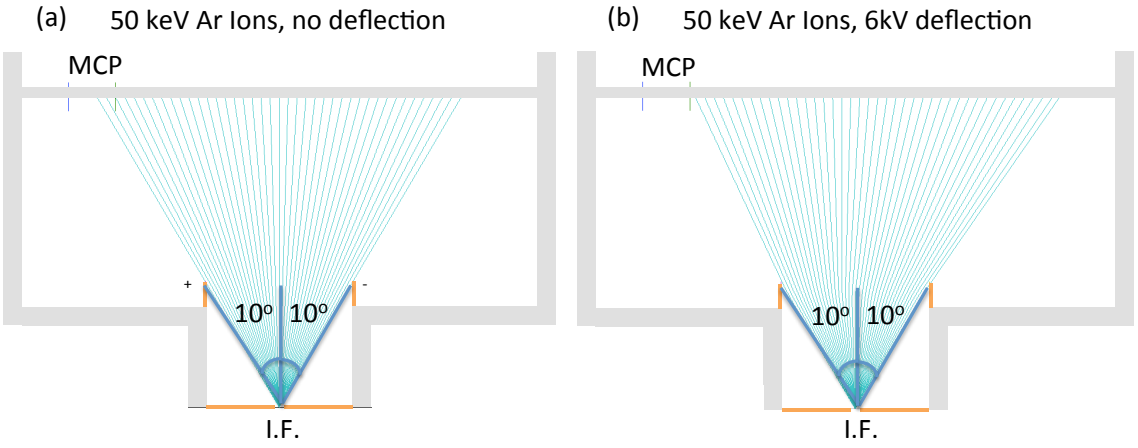

Figure 3.11: Two 2.3 cm copper plates separated by 4 cm provide ion deflection capabilities to measure the neutral flux emitted at the intermediate focus. (a) Without ion deflection enabled the microchannel plates are exposed to the ion and neutral flux emitted at 10^o incident angle from the interemediate focus. (b) With a 6kV potential placed across the two plates, 1+ Ar ions up to 50 keV are deflected enough to not reach the microchannel plate entrance orifice.

Residual gas analyses were subsequently taken and cross-calibrated to the pressure measured in the chamber. A degas procedure was utilized at the beginning of each experiment to make sure that all contaminants were removed from the filament, to remove contaminant influence on the results.

An average of 128 samples was taken for each Faraday cup measurement (one data set with 10 µs/div and one with 100 µs/div for near an broad spectrum analysis respectively). Three individual data sets were taken for each resolution measurement: +100 V bias, no bias, and -100 V bias. The voltage drop across a 15 Ω was measured using two 10:1 voltage probes using the 1 MΩ terminator option on the oscilloscope.

The bias voltage was applied to the electrically isolated outer cup, which had an entrance orifice diameter of 2 mm.

Langmuir triple probe measurements of electron temperature and electron density were carried out as described in section 3.5.3. Six nine-volt batteries applied a 54 V bias across a 122 Ω resistor to determine I_{sat}, Te, and n_e. During the experiment, the plasma characteristics were taken at each of the three chamber locations for the given operating parameters. An average of 128 samples was taken to determine the temporal changes of plasma characteristics.

Lastly, while the other measurements were being taken, the frequency of the exposed quartz crystal was monitored relative to the covered quartz crystal (to account for temperature variations in crystal frequency). In total, the measurements were taken over a one hour period – ample time to measure changes in the crystal mass even at the smallest amount of change. The crystal was initially coated in Sn to increase the Sn sticking coefficient as it was believed before these experiments that this would be one of the predominant species to deposit at the intermediate focus.

As mentioned previously, a set of Si witness plates was installed throughout the chamber to analyze what and how much deposition was occurring at various locations. The placement of these samples is diagrammed in figure 3.13. While deposition/erosion rates were readily observable using the quartz crystal monitor using the conditions diagrammed above, in order to analyze deposition quantities using Si witness plates, a larger deposition rate was required. In order to achieve measureable thicknesses on the

witness plates, the collimated foil trap was removed and pinch frequency was altered. These modified conditions are outlined in table 3.4. Unfortunately, because of the un-optimized operation using modified pinch gases, it was not possible to take Si witness plate measurements for He and Ne pinch gases. The lack of the collimated foil trap resulted in the direct arcing of current from the cathode to the nearest protrusion of the anode instead of a proper pinch being formed. It is believe that this is either due to a lack of pressure buildup behind the foil trap or the lack of a forward facing ground surface to help stabilize the pinch source. It was visually observed that no such arcing occurred with the foil trap in place. After the pinch exposure was complete, the coated Si witness plates were analyzed using profilometry (to determine step height), x-ray photoelectron spectroscopy (to determine surface composition), as well as scanning electron microscopy (to determine surface morphology). The x-ray photoelectron spectroscopy and scanning electron microscopy analyses were only performed for each sample on experiment two; only the intermediate focus location samples were analyzed for each of the other experiments.

Table 3.4: Shown are the modified z-pinch operating parameters for Si witness plate exposure.

Exp. Number	Pinch Gas Flow Rate (SCCM)	Pinch Gas Species	Buffer Gas Flow Rate (SCCM)	Buffer Gas Species	Exposure Time (min)	Pinch Freq. (Hz)
1	100	N_2	0	-	150	20
2	100	N_2	200	Ar	150	25
3	100	N_2	1000	Ar	150	40
4	100	N_2	1000	Ar	150	40
5	100	N_2	1000	Ar	150	40
6	100	N_2	200	He	150	40
7	100	N_2	200	Ne	150	40

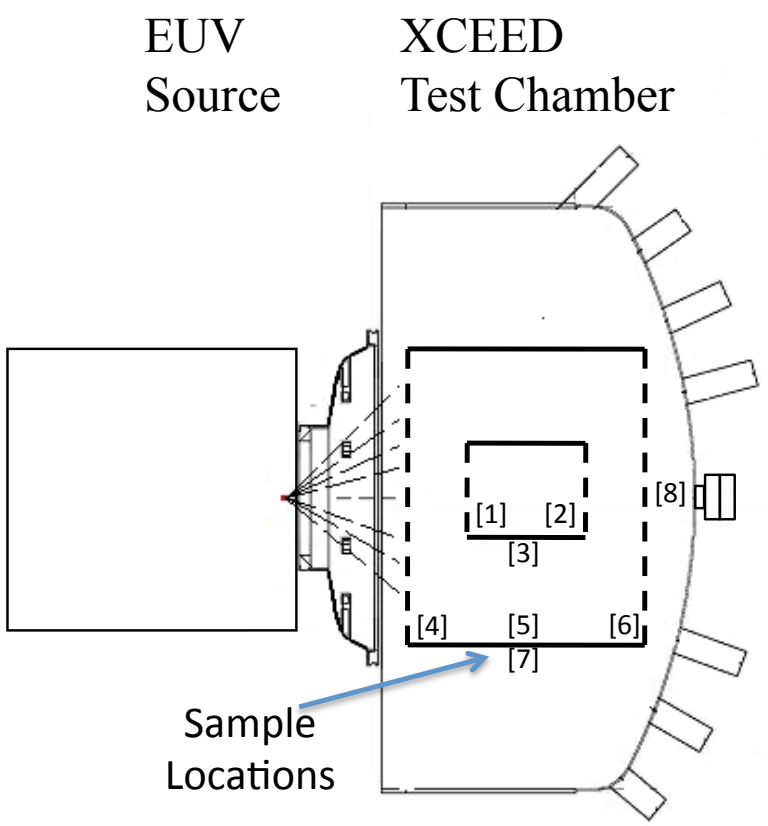

Figure 3.12: Shown are the 8 different locations of Si witness plates. Each sample was placed along the horizontal plane (with respect to looking at pinch from the front of the chamber) that bisected the collector optic. Locations 1,2,4-6 are located on the inside of their respective collector shells, locations 3 and 7 are located on the outside of the shells, and location 8 is at the location of the intermediate focus.

Using the SNIFFED apparatus, Langmuir triple probes, and Si witness plates, a better understanding of the ongoing processes in debris transport are better understood. These diagnostics enable a quantitative analysis of the energetic charged and neutral flux, composition of the debris, gaseous contaminants, as well as contamination rates. Coupling these measurements with variations in the buffer gas mass, chamber pressure, and pinch gas mass furthermore provided the ability to determine which components contributed to observations made during data analysis.

CHAPTER 4

THEORY

4.1 Introduction

Having a theoretical understanding of experimentally observed phenomena not only provides confirmation of proposed hypotheses, but also further develops an understanding of observations not previously anticipated. In order to adequately understand the transport of energetic debris from the EUV plasma source to the intermediate focus, a theoretical model was developed using the Monte Carlo method. The model functions by creating a test atom, giving it an initial trajectory and energy, and subjecting it to gas-scattering collisions and wall-scattering collisions.

The intricacies of these scattering will be discussed in the following sections, but it is prudent to discuss the manipulation of energy within this model. Each gas-scattering collision proceeds by elastic scattering. The inter-atomic potentials between two participating species is pre-determined using Leonard-Jones (attractive well) and Abrahamson potentials (repulsive force), allowing for the use of classical Newtonian physics to be accurately applied. The net result of a collision results in no net energy loss in the total system, but there is a change in energy from the incident species to the target species. At this point, the model creates a new atom with initial energy/direction to test later, and proceeds to carry out the flight path of the initial incident atom. Wall-scattering collisions are handled using the

Stopping and Range in Matter (SRIM) code developed by Ziegler and Biersack [75]. While a more in depth discussion will follow, the SRIM code models the stopping power of an ion as it traverses through a defined structure. The code takes the input of an incident ion mass, angle, and energy and outputs the number and type of sputtered atoms, the angles at which they leave the surface, as well as the possible backscattering of the incident atom. Using this information, the probability of deposition or backscattering is determined. Furthermore, by running the code thousands of times, the angular distribution of the backscattered atoms and their average energy can be determined to calculate a new backscattered trajectory and energy loss term for the incident atom in a scattering collision. These terms are important to the understanding of how energetic atoms traverse through the EUV lithography tool, and how it differs from the specular reflection of light.

It will be shown in the following sections that the pressure of the chamber, the buffer gas species, and created energetic species emanating from the EUV plasma all have an effect on debris transport to the intermediate focus. It will be shown that for the pressures used in experimentation, 0.3-22 mTorr, there is a transition from wall collision dominant interactions to gas collision dominant interactions. It is between these extreme conditions where scattering of energetic species to the intermediate focus is optimized because there is enough gas scattering to prevent the large energy reduction/implantation caused by interactions with wall surfaces. Above a critical point the increase in gas collisions suppresses the transport of energetic species because they're either redirected into

the wall, or the elastic scattering collisions reduce the energy of the high-energy plasma species to thermal levels.

The last detail of the model involves the end point determination for each test atom. The model stops carrying out the test when the atom either deposits onto a surface, reaches a maximum number of steps (set at 10000), survives past a maximum period of time (set at 1s, which is well beyond any arrival time observed experimentally), has a net energy reduction to room temperature (0.025 eV), or reaches the intermediate focus. The intermediate focus is modeled larger than its actual size (10 cm vs. 1 mm) due to the small fraction of species that actually make the end goal. This is simply a way of getting results in a sensible time period, and the values are reduced by an r^{-2} term to compensate for the inflated measurement. In an experimental setting, approximately 10^{16} ions are generated (assuming 9 mm^3 plasma size, 10^{20} ions/cm^2) each pulse. Unfortunately, it takes on the order of 1 hour to model 10^6 test atoms, and as such it is simply not possible to completely model every species generated and ejected by the EUV plasma.

A representative end point tally for 10000 Sn atoms into Ar buffer gas at each of the pressure trials is given in table 4.1. A majority of the species are deposited into either the collector optics or the outer chamber walls. With increases in pressure, the increased energy transfer results in an increase in the number of species that thermalized. For each of these conditions, and any tests run with this model in general, the max step and max time end point conditions were set sufficiently high to not result in the removal of a test atom from the chamber before

a real interaction triggered the end of a test atom's life. Increasing pressure reveals the transition from primarily wall collision to gas atom collision interactions. Because of the higher gas collision probability, nearly 88.8% of the test atoms were thermalized before they deposited onto a surface.

Table 4.1: Shown is a tally of the end of life conditions accounting for a representative set of 10000 Sn test atoms in Ar buffer gas.

Pressure (mTorr)	Made I.F.	Implanted	Max Time	Max Steps	Thermalized	Total Species
0.3	0.32%	99.67%	0%	0%	0.01%	10000
2	0.71%	98.61%	0%	0%	0.68%	10000
6	0.34%	83.63%	0%	0%	16.03%	10000
12	0.02%	42.79%	0%	0%	57.19%	10000
22	0.00%	11.20%	0%	0%	88.80%	10000

Each of these Sn test atoms generates new species either by buffer gas collisions or sputtering material off of walls. The resulting tallies of these species are shown in table 4.2 (only buffer gas collisions were considered in this representative case). A larger fraction of thermalized species is observed relative to the initial Sn test atoms due to the fact that in general scattered species will have a lower energy than their collision inducing pinch species. It is also important to note that as pressure increases, more scattering collisions occur, and consequently more species are generated. Nearly a factor of 60 times more species are scattered at 22 mTorr than at 0.3 mTorr.

Table 4.2: Shown is a tally of the end of life conditions for the energized Ar buffer gas atoms created by gas scattering with the 10000 Sn test atoms.

Pressure (mTorr)	Made I.F.	Implanted	Max Time	Max Steps	Thermalized	Total Species
0.3	1.03%	90.18%	0.00%	0.00%	8.79%	6305
2	0.52%	57.96%	0.00%	0.00%	41.52%	48201
6	0.06%	21.48%	0.00%	0.00%	78.46%	172737
12	0.00%	7.24%	0.00%	0.00%	92.75%	309629
22	0.00%	2.95%	0.00%	0.00%	97.05%	385047

4.2 Geometry Considerations

The first step in modeling any physical phenomena is determining the number of dimensions and consequent coordinate system to employ. Given the scattering collisions required to properly understand the transport of debris from the energetic plasma to the intermediate focus, and the consequent effect of energy and incident angle on scattering angles and sputtering yields, it was determined that in order to properly model the on going phenomena, a three dimensional model was required. Furthermore, given the highly linear vector based calculations, it was also determined that the Cartesian coordinate system was the most computationally appropriate coordinate system. The modeled geometry is diagrammed in figure 4.1, and the exact dimensions utilized are provided in table 4.1. The brackets were measured and modeled with no thickness, but a width of 0.038 m.

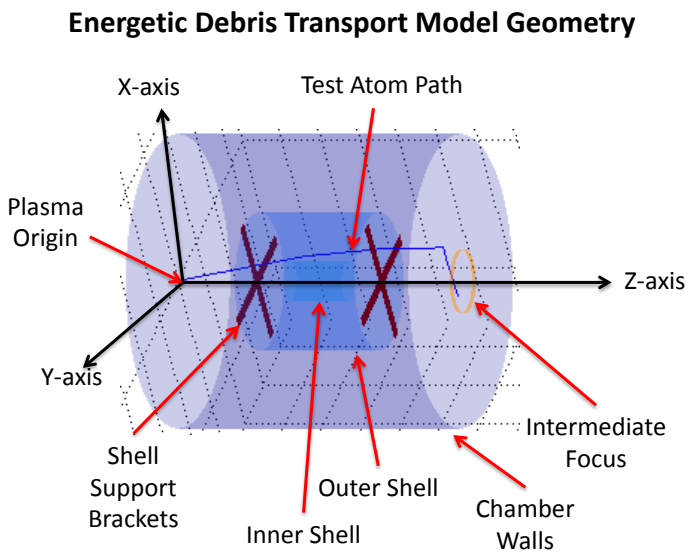

Figure 4.1: Shown is the chamber geometry utilized to model the transport of energetic atoms from the EUV plasma after the creation of EUV light. It consists of the two shells included to act as a mock-up collector optic, the brackets that support these shells and block direct line of sight between the plasma and the intermediate focus, as well as the modeled size of the intermediate focus. The outer chamber shell is modeled as a perfect cylinder, which is assumed to not differ much from the actual chamber.

Table 4.3: The dimensions of the modeled chamber and mock-up collector optic components are provided.

Shell Name	Radius (m)	Length (m)	Distance[1] (m)
Inner Shell	0.064	0.15	0.285
Outer Shell	0.216	0.305	0.2075
Chamber Walls	0.46	0.72	0
Intermediate Focus	0.1	0	0.72

[1]From the plasma to the nearest edge

4.3 Initial Energy Determination

To properly model species coming from the Z-pinch plasma, an energy analysis of the emitted ions and neutrals was performed using the detectors described in section 3.5.2. An analysis of the energetic flux was performed for each pinch gas species utilized: He, Ne, N_2, and Ar. The detectors were positioned at the

0^o port with a travel distance of 1.92 m from the EUV plasma and a minimum orifice diameter of 2 mm. The resulting ion and neutral energy analyses for each species are plotted in figures 4.2-4.5. Although there are discrepancies between the ion flux measured using the neutral detector and those measured using the electrostatic energy analyzer, for the most part they agree well. The discrepancies most likely lie in the fact that the neutral detector analysis requires the assumption of a singular species to convert arrival time to energy. The energy to charge capabilities of the electrostatic energy analyzer allow for a determination of appropriate species, and consequently it is more capable of determining detector efficiency at a given energy. One interesting occurrence that will be later mentioned in the data analysis, is the fact that for each of the measurements C^+ was one of, if not the, most predominant species leaving the plasma. This is a result of chamber contamination as well as the alumina tube used to electrically isolate the pre-ionization circuit from the Z-pinch circuitry. The pinch gas is preionized in this tube, and consequently sputtering of the surface results in the presence of carbon in the EUV plasma emission. The remaining measured species are electrode materials (Cu, Mo, Sn), leak contaminants (O, Ar), or the utilized pinch gas species. The high-energy components observed with the neutral detector are not verifiable with the electrostatic energy analyzer because of breakdown concerns above an E/q ratio of 14 keV/q. Furthermore, ionized species above 3+ are not measureable at higher energies because they fall into the noise range of the measurement, where the electrostatic discharge of the Z-pinch causes false signals to be observed.

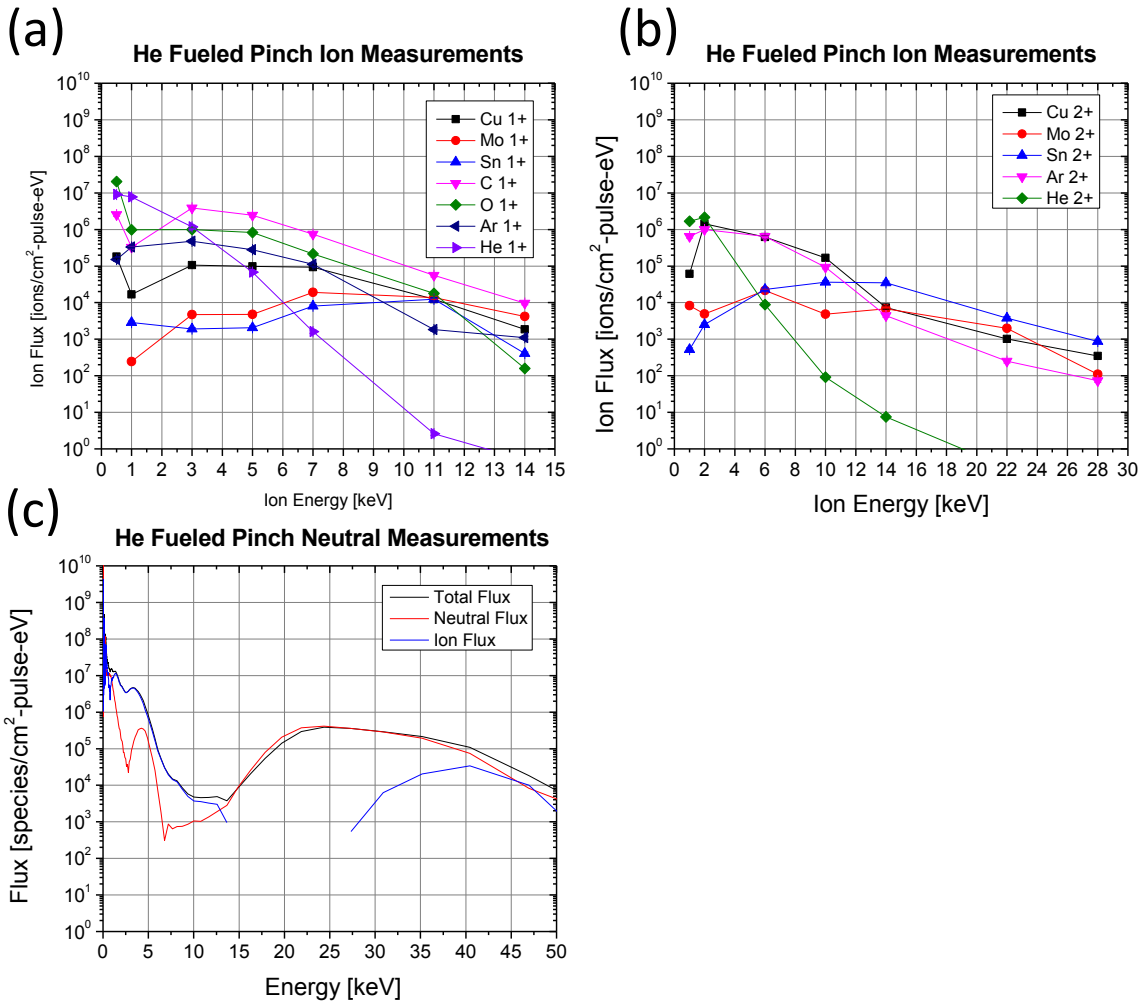

Figure 4.2: Shown are the (a) 1+ ion, (b) 2+ ion, and (c) neutral species measurements for a He fueled pinch. The detectors were 1.92 m away from the pinch. The straight-line plots are taken from the neutral energy detector, with the "ion flux" representing the mathematical subtraction of neutral flux from total flux. The maximum 1+ ion measurement, using the ESA, was at 14 keV; the maximum 2+ ion measurement was at 28 keV. The error of the "total flux", "neutral flux", and "ion flux" is approximately 9.6% based on the calibration of the detector. Error bars are plotted for the other ion energy measurements and are approximately 28% based on the calibration of the energetic ion analyzer.

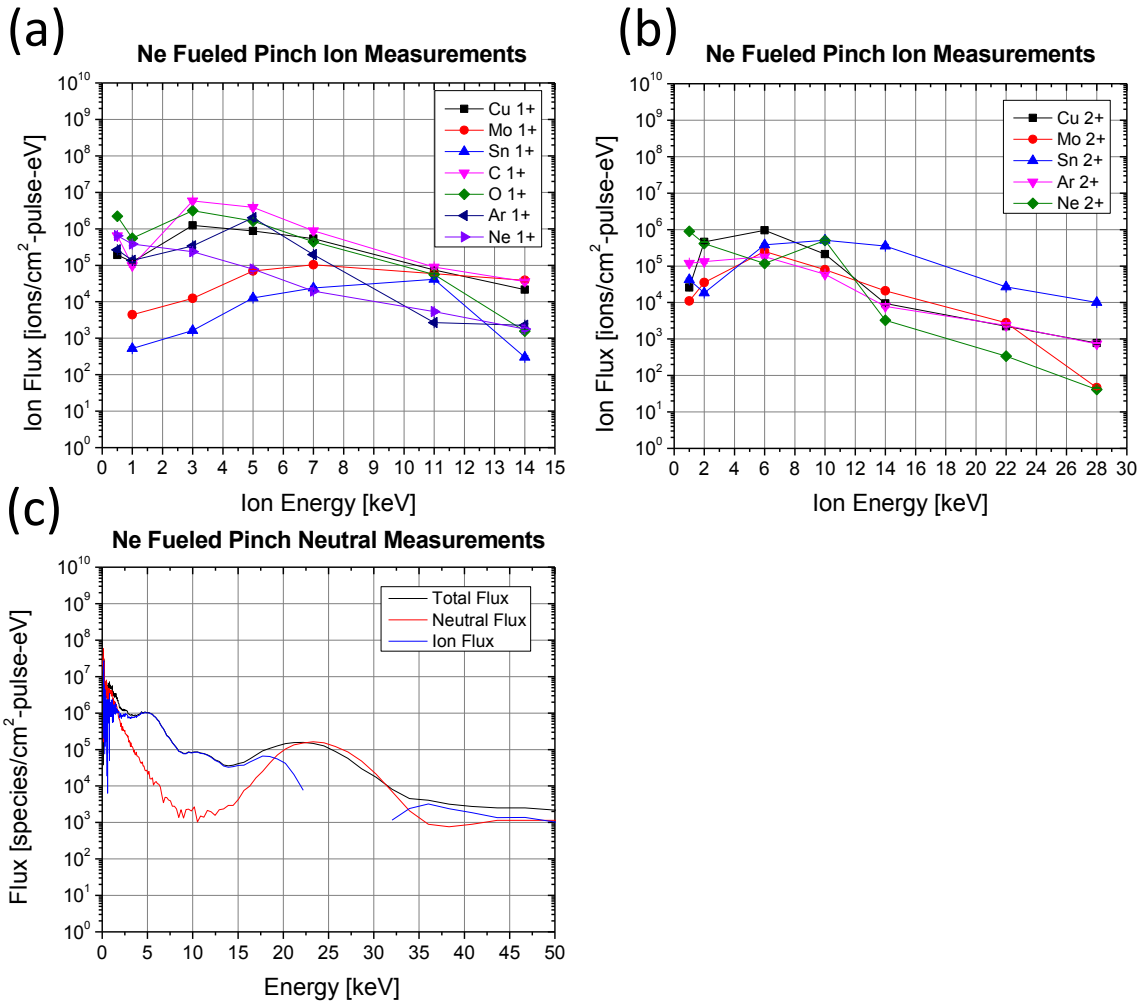

Figure 4.3: Shown are the (a) 1+ ion, (b) 2+ ion, and (c) neutral species measurements for a Ne fueled pinch. The detectors were 1.92 m away from the pinch. The straight-line plots are taken from the neutral energy detector, with the "ion flux" representing the mathematical subtraction of neutral flux from total flux. The maximum 1+ ion measurement, using the ESA, was at 14 keV; the maximum 2+ ion measurement was at 28 keV. The error of the "total flux", "neutral flux", and "ion flux" is approximately 9.6% based on the calibration of the detector. Error bars are plotted for the other ion energy measurements and are approximately 28% based on the calibration of the energetic ion analyzer.

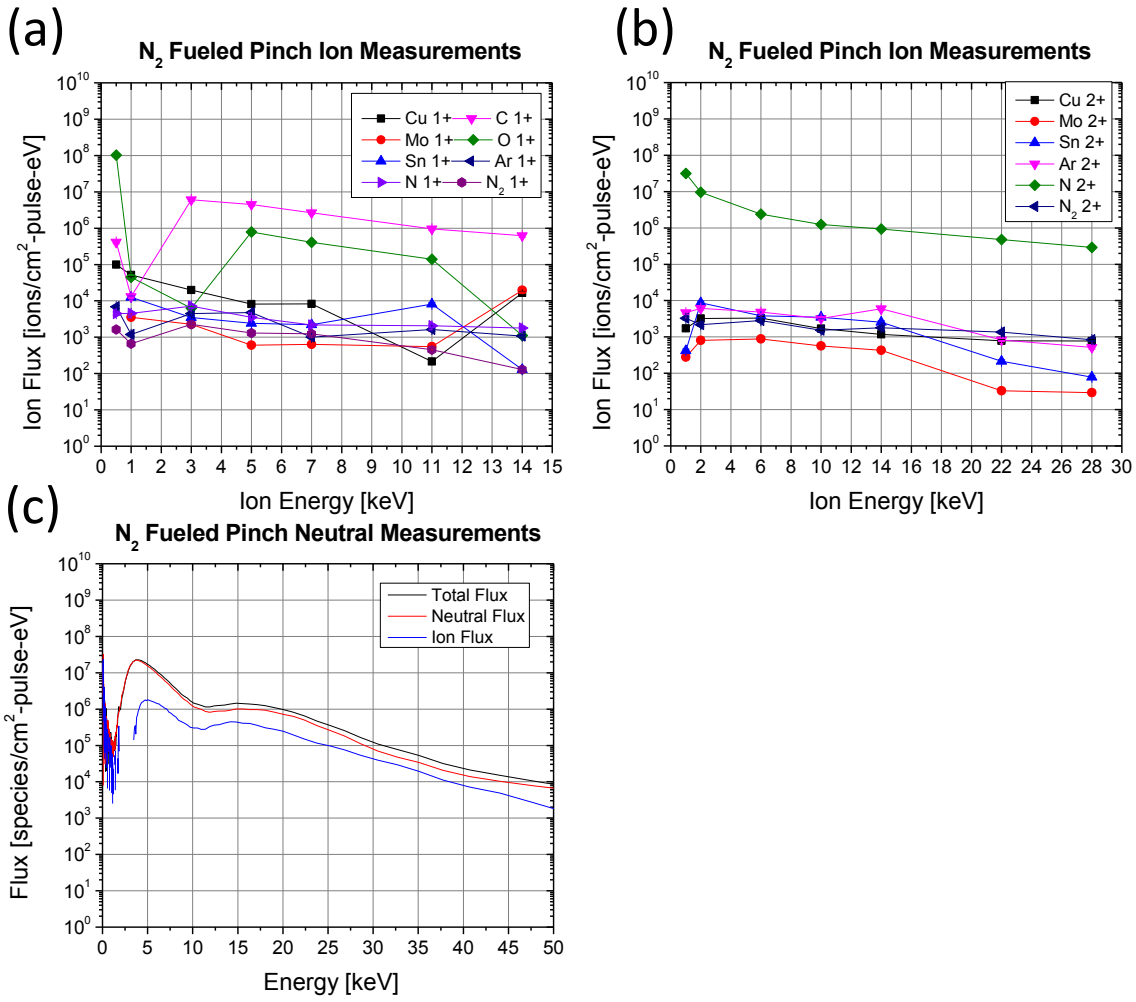

Figure 4.4: Shown are the (a) 1+ ion, (b) 2+ ion, and (c) neutral species measurements for a N_2 fueled pinch. The detectors were 1.92 m away from the pinch. The straight-line plots are taken from the neutral energy detector, with the "ion flux" representing the mathematical subtraction of neutral flux from total flux. The maximum 1+ ion measurement, using the ESA, was at 14 keV; the maximum 2+ ion measurement was at 28 keV. The error of the "total flux", "neutral flux", and "ion flux" is approximately 9.6% based on the calibration of the detector. Error bars are plotted for the other ion energy measurements and are approximately 28% based on the calibration of the energetic ion analyzer.

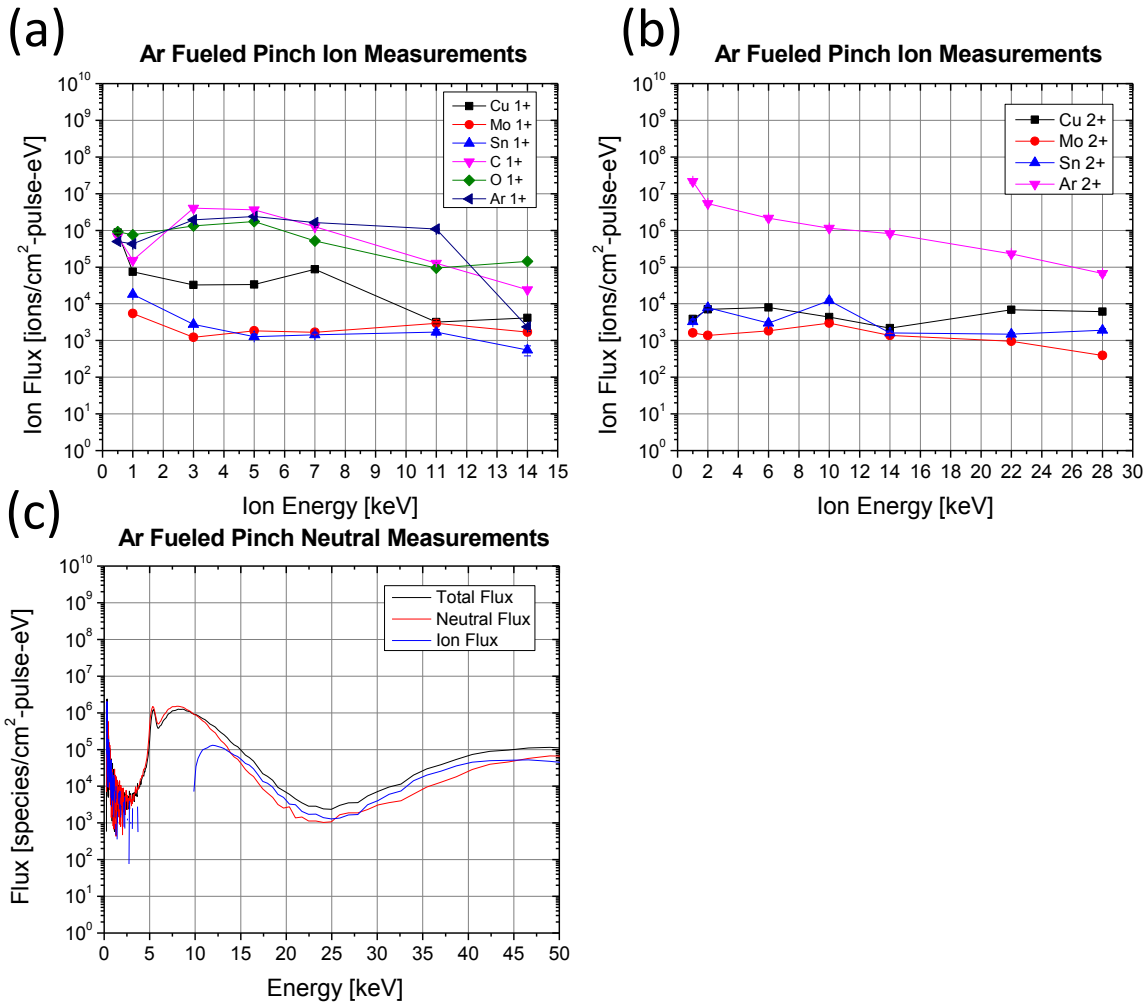

Figure 4.5: Shown are the (a) 1+ ion, (b) 2+ ion, and (c) neutral species measurements for an Ar fueled pinch. The detectors were 1.92 m away from the pinch. The straight-line plots are taken from the neutral energy detector, with the "ion flux" representing the mathematical subtraction of neutral flux from total flux. The maximum 1+ ion measurement, using the ESA, was at 14 keV; the maximum 2+ ion measurement was at 28 keV. The error of the "total flux", "neutral flux", and "ion flux" is approximately 9.6% based on the calibration of the detector. Error bars are plotted for the other ion energy measurements and are approximately 28% based on the calibration of the energetic ion analyzer.

The "total flux" measurements from each of these spectra are utilized for the determination of a test atoms initial energy. For the model, each total flux curve was normalized to determine the probability of an atom being at a given energy. A random energy from 0 to 50 keV is initially chosen, and a random number between 0-1 is created. If the random number is lower than the probability provided by the

normalization, the energy initially selected is chosen; if the random number is larger than the probability calculated, the process is repeated. The validity of this process is shown in figure 4.6, which shows the test energy spectrum and number of chosen species for a given pre-normalization curve (this is not a curve actually used in determining energy for the test atoms used to describe experiments in this dissertation, only one to test the ability to accurately reproduce a provided energy curve). Increasing the number of test atoms tightens the fit, with a perfect alignment occurring at infinity. While this technique does take considerable time to produce an initial energy value for an atom, it is a one off process that does not take up considerable processing time compared to the entire model's operation.

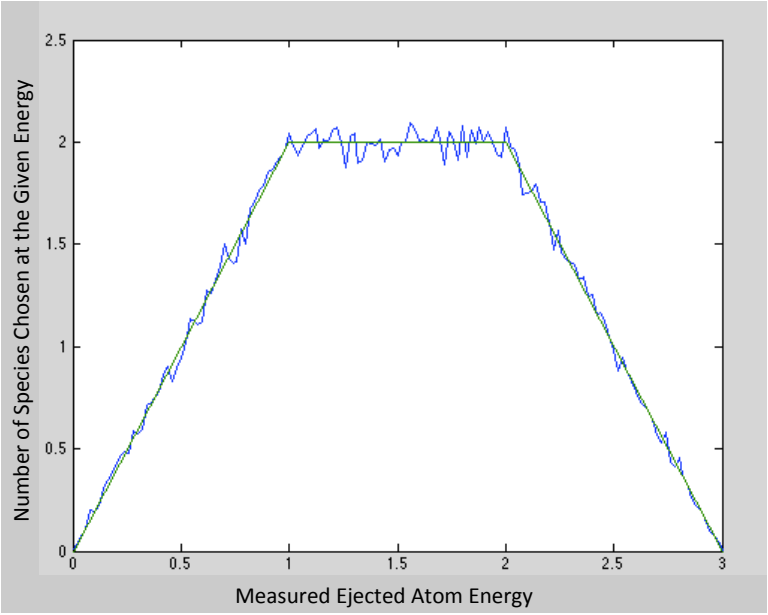

Figure 4.6: Shown is a fictional atom energy curve (solid straight line) that is used to test the function used for determining test atom initial energy values. The resulting chosen energies for 10^6 test atoms are plotted along side of this curve. The selected energies clearly adhere to the provided fictional energy curve.

4.4 Initial Direction Determination

The second step in modeling each test atom is to assign an initial direction vector. It was observed previously that measurements of the angular ion distribution appeared to adhere to a cosine distribution. This is to be expected given the cylindrical electrode format, and is observed in figure 4.7 for a Xe fueled Z-pinch plasma.

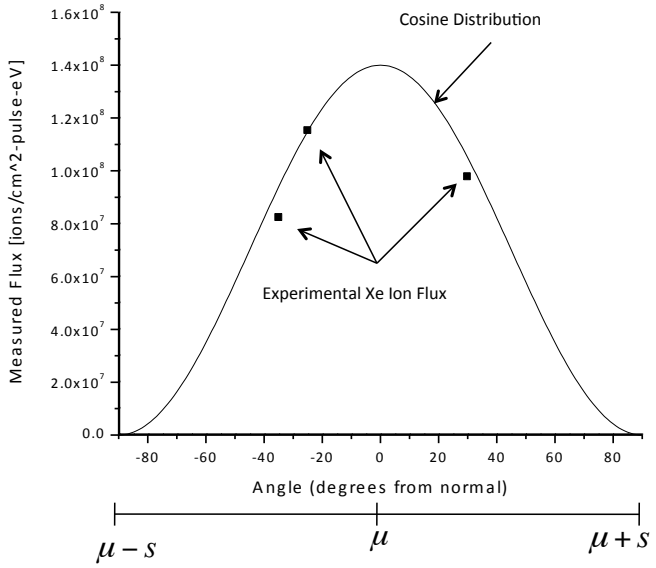

Figure 4.7: Shown is the angular measurement of the total ion flux from the Xe fueled XTS 13-35 source. Accounting for error, the measurements appear to adhere to a cosine distribution – a function of the cylindrical electrode geometry. Test atoms' initial directions are consequently determined by using a random generator that adheres to a cosine distribution in three dimensions.

The initial assumption is made that there is not a correlation between energy atom energy and angle direction. In reality high-energy species are forward directed due to the electric fields created by the Z-pinch and the direction of the instabilities that create high inductive zones for massive ion acceleration. Lower energy species are directed outward due to their large amount of intra-plasma/off

wall scattering as well as not remaining in the linearly directed fields. For the purposes of the model, however, it is not believed that the difference is large enough to be of concern. The random direction code consequently proceeds by initially selecting a random angle from 0 to $\pi/2$, and a random number from 0 to $1/s$ (s is to be defined shortly). The random number is compared to the resulting probability calculated by equation 4.1, the raised cosine distribution function, for the random angle chosen. In this equation, f is the probability distribution function, μ is the centroid of the cosine distribution, $\mu+s$ is the rightward boundary of the function, and $\mu-s$ is the leftward boundary (the corresponding values are also plotted in figure 4.6 for reference) [76].

$$f\left(x,\mu,s\right)=\frac{1}{2s}\left[1+\cos\left(\frac{x-\mu}{s}\pi\right)\right] \tag{4.1}$$

If the randomly chosen number is less than the probability calculated by equation 4.1, the chosen angle is accepted and assigned to the value of φ in spherical coordinates. The assumption of azimuthal symmetry allows for a random value from 0 to 2π to be chosen for θ. Common conversions from spherical coordinates then convert the angular values into a Cartesian coordinate based vector.

As with the constrained random energy generator, 10^6 test atoms were simulated to test the correctness of this randomization method. The resulting plots of φ and θ are shown in figures 4.7 and 4.8 respectively. It is evident that the chosen randomization method correctly results in the desired cosine distribution to mimic the angular spectra from the cylindrical Z-pinch plasma.

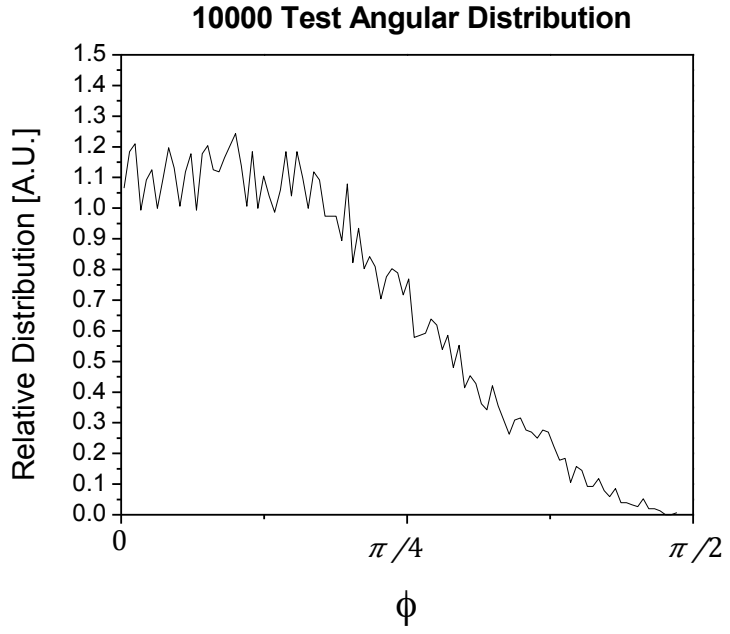

Figure 4.8: Shown are the accumulated relative values of 10^6 tests of the random direction generator. The plotted results are those of the calculated φ value. The shape of the curve closely mimics that of a cosine distribution curve as designed.

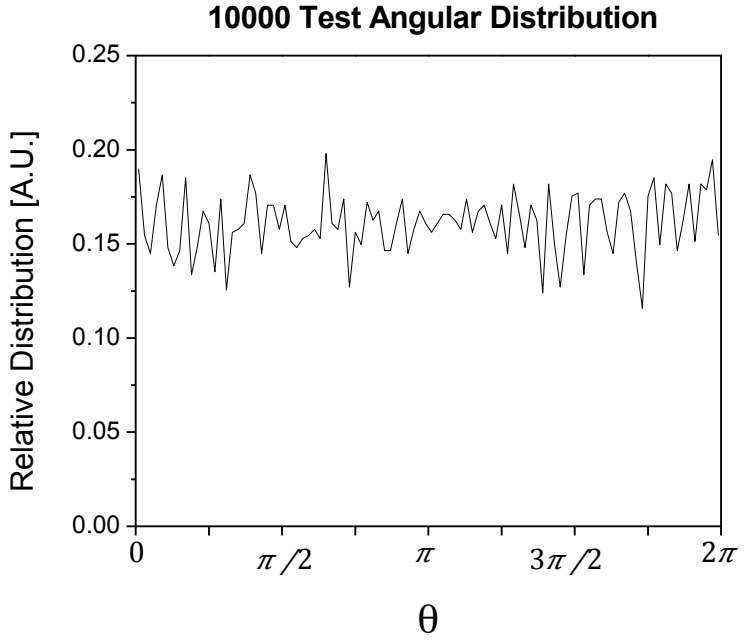

Figure 4.9: Shown are the number of atoms at a given angle, θ, for 10^6 iterations. The plotted results are those of the calculated θ value. The shape of the curve closely mimics that of a cosine distribution curve as designed.

4.5 Collisions

The debris transport model starts by running a loop that determines the test atoms new location based on possible collisions with walls and buffer gas atoms. Initially, a time step of 10^{-6} s is assigned to determine a default distance travelled if no collisions occur. The distance is determined by equation 4.2, where $\mathbf{r_p}$ is the previous location vector, $\mathbf{r_n}$ is the new location vector, $\mathbf{v_p}$ is the velocity vector (as derived from the energy and mass of the test atom), and t is the timestep.

$$\overline{r}_n - \overline{r}_p = \overline{v}_p t \tag{4.2}$$

The model then proceeds to calculate the nearest distance to a surface where wall collision interactions need to proceed. The code calculates whether or not a gas atom collision occurred while traversing the shorter of the two distances; if a collision did occur, the new location is noted. In the case of either a wall collision or a gas atom collision, the new location of the test atom is set at the point of the collision, and the trajectory and energy of the atom is adjusted. The main loop then repeats itself, moving the test atom from collision to collision until an endpoint is reached. If no collisions occurred during the time step, the energy and direction remain the same, since any long-distance attractive or repulsive forces are negated to maintain computational simplicity for speed. For the pressures utilized in these experiments, however, it is assumed that the contributions of these forces are negligible when compared to the other scattering events that occur in relatively short distances.

4.5.1 Wall collision calculations

The first step in determining the new direction and location of a test atom that has undergone a wall collision is determining the point of intersection with the nearest wall surface. Given the default (collisionless) projected location (x_p,y_p,z_p), and the initial location (x_o,y_o,z_o), a three dimensional parametric equation is derived as a function of t (eqs. 4.3-4.5). In these equations, it is important to note that t=0 represents the starting location and t=1 represents the projected location.

$$X(t) = (x_p - x_o)t + x_o \tag{4.3}$$

$$Y(t) = (y_p - y_o)t + y_o \tag{4.4}$$

$$Z(t) = (z_p - z_o)t + z_o \tag{4.5}$$

$$X(t)^2 + Y(t)^2 = R^2 \tag{4.6}$$

The wall collision code is then broken into three collision-determining parts: collisions with cylinder surfaces, collisions with the near pinch and near intermediate focus planar walls, and collisions with the brackets that support the collector optics. The value of t is calculated for each of these surfaces, and a list is compiled to determine the smallest positive value of t for each of the surfaces (smallest t value is the nearest surface with which a collision occurred). To determine if a collision occurred with cylindrical shell surfaces, equation 4.6 is solved with R equal to the radius of the cylinder for which the value of t is being computed. The solution to equation 4.6 is described by the quadratic equation given

in equations 4.7-4.8a-d. If more than one solution exists for t, the smallest value greater than 0 is used. If only negative values exist, the test atom will not penetrate the shell in question and the resulting t value is set to a value of 2 to rule it out as a possible collision.. This is repeated for each of the three cylinder surfaces, compiling a list of all the t values calculated. As a last restriction, the code goes through the t values listed for each of the shells and determines whether or not the corresponding value of Z(t), from equation 4.5, resides within the distances assigned to the shells. If the location of the test atom at t does not reside within the length of the shell, t is set as 2 to signify that a collision didn't actually occur.

$$0 = t^2\left[\left(y_p - y_o\right)^2 + (x_p - x_o)^2\right] + t\left[2x_o(x_p - x_o) + 2y_o(y_p - y_o)\right] + \left[x_o^2 + y_o^2 - R^2\right] \quad (4.7)$$

$$t = \frac{-b \pm \sqrt{b^2 - 4ac}}{2a} \quad (4.8a)$$

$$a = \left[\left(y_p - y_o\right)^2 + \left(x_p - x_o\right)^2\right] \quad (4.8b)$$

$$b = \left[2x_o\left(x_p - x_o\right) + 2y_o\left(y_p - y_o\right)\right] \quad (4.8c)$$

$$c = x_o^2 + y_o^2 - R^2 \quad (4.8d)$$

The next step, in determining which wall the test atom possibly passes through, is to consider the planar walls where the plasma and intermediate focus are located. In this case, equation 4.5 is solved for t with the value of Z(t) set to either 0 (where pinch is located) or 0.72 (where the intermediate focus is located). In this case, it is not necessary to test weather or not the test atom resides within the radius defined by the outer shell, for it would have collided with this shell and

the results would have been recorded in the previous step. If there is any z-component of movement, there will be a positive solution for t and a negative solution for t. As before, only the positive solution is chosen. If there is no z-component of movement, however, the value of t is once again set to 2 so that it will not be chosen as the nearest impact surface.

Lastly, a set of t values is computed for the collector optic structural brackets. The code first solves for t using equation 4.5, with Z(t) set as the distance from the plasma for each sets of brackets. The resulting value of t is then used to compute X(t) and Y(t) using equations 4.3 and 4.4. If the calculated values lie within the confines of the bracket's dimensions, the positive value of t is kept. If it does not lie within these confines, again the value of t is set to -1 so that it will not be chosen as the nearest wall impact.

The compiled list of t values is analyzed to determine which wall, if any, the test atom collides with. The smallest positive value of t is the nearest surface in the path of the test atom, and the resulting Cartesian coordinate is recorded as the point of intersection with the collector. If no positive values of t exist or if all the values of t are greater than 1, no wall collision occurred in the path from the starting point to the projected location. Even if a wall collision did occur, the code will still continue to test for a gas atom collision in the new shorter travel distance. To help visually explain the wall selection process, a two-dimensional diagram and representative t-table are shown in figure 4.10; support brackets are not included in this diagram to aid in simplicity.

x0	y0	z0
0	-0.46	0
xp	yp	zp
0	0.46	0.72

	t val
z pin	-1.00
z if	1.00
r in	0.43
r out	-1.00
r cham	1.00

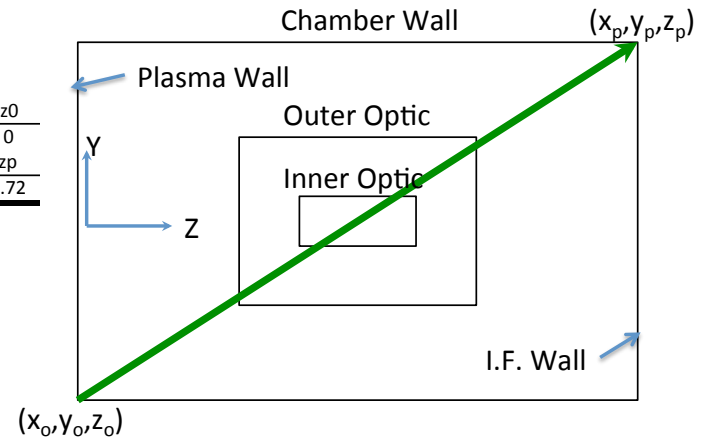

Figure 4.10: The test atom is located on the bottom-most center of the chamber wall and is projected to end up at the upper-most center of the chamber wall. The t values are computed for all surfaces and shown in the table at left. The Zpin (plasma wall) value is -1 because it would require the test atom to move backwards to penetrate that surface. The Zif and Rcham (intermediate focus wall and chamber cylinder) values are obviously 1 because the test atom is projected to be there without any collisions. The Rout (outer collector optic) value is -1 because the test atom will never collide with the outer collector optic. Lastly, the value of Rin (inner collector optic) is chosen because it is the smallest t value between 0 and 1. A second solution to the t value for this shell was found, but the smaller of the two values was used, which corresponds to the nearest surface that the test atom would collide with.

Proceeding with the assumption that the test atom was found to participate in a wall collision, and that a gas atom collision did not occur in the process of reaching the wall, it is now necessary to understand how the incident atom will interact with the surface. For this model, there are two possible consequences of the incident atoms interaction with the surface: deposition and reflection. With each of these possibilities, there also exists the potential for sputtering to occur, which will be explained in section 4.7. When an energetic atom impacts a surface, it is possible that the atom will not penetrate the outer surface potential because it is too low of energy, or it could possibly traverse a few monolayers of the surface and backscatter back out of the surface. The description of this process is complicated and very difficult to analytically describe with a single equation, and is certainly not describable by the specuclar reflection properties enjoyed by photons. For the

purposes of the debris transport model, it is very important to be able to simulate this process, so a set of scattering properties were calculated using the SRIM code developed by Ziegler and Biersack [75].

This SRIM code takes the inputs of ion mass, surface composition, ion energy, and angle of incidence, and calculates how the ion will interact with the surface. SRIM itself is a Monte-Carlo simulation that models the reaction of surface atoms to the displacement and momentum transfer caused by an incident ion. An output file is created at the end of the simulation, which contains energy, direction, and mass information about each of the atomic species that leaves the surface due to sputtering. This can include species that are sputtered out of the surface by backscattering of the ion as it penetrates the outer surface potential, or the incident ion itself. The incident ion is monitored to determine whether it is deposited into the surface or backscattered away from the surface, and its final energy and direction (or location in the surface if it is deposited) is noted as well. The directional cosines of each of relevant species are provided as well.

The debris transport model requires the ability to analyze the reflection of several species (He, Ne, N, Cu, Ar, Mo, and Sn) off of a Sn coated stainless steel substrate, for a wide variety of incident energies and angles. Consequently, for each incident atom species, a table can be created containing the deposition probability, backscattering probability, sputtering probability, ratio of sputtered atoms per incident sputtering ion, average backscattered atom energy, and average sputtered atom energy as shown in figures 4.11-4.15. It is clear in these figures that ion

energy is only a major influence on the sputtering yield and the average energy of the sputtered species. For all other parameters the predominant determining factor is the angle at which the incident ion collides with the surface being sputtered.

Since one single SRIM analysis does not account for all possible atom-surface interactions, 1000 individual runs were performed for each energy and angle condition to average out case by case variations. The surface composition of interaction was constructed as a 5 nm layer of Sn deposited on top of a stainless steel substrate. The Sn layer is included to account for the fact that most of the mock-up collector optic surfaces were covered by more than a few nanometers of Sn (as well as other electrode materials) at the end of each hour long experiment. Even at only 5 nm, SRIM modeling suggests that almost no stainless steel species are capable of being sputtered out of the Sn surface. This is further verified by the lack of stainless steel species observed in the film deposition on top of Si witness plates using x-ray photoelectron spectroscopy. For each of the 1000 tests, the surface morphology is retained. While this is one of the drawbacks of SRIM, it would not be a practical feature given the macroscopic scale of this debris transport model anyways.

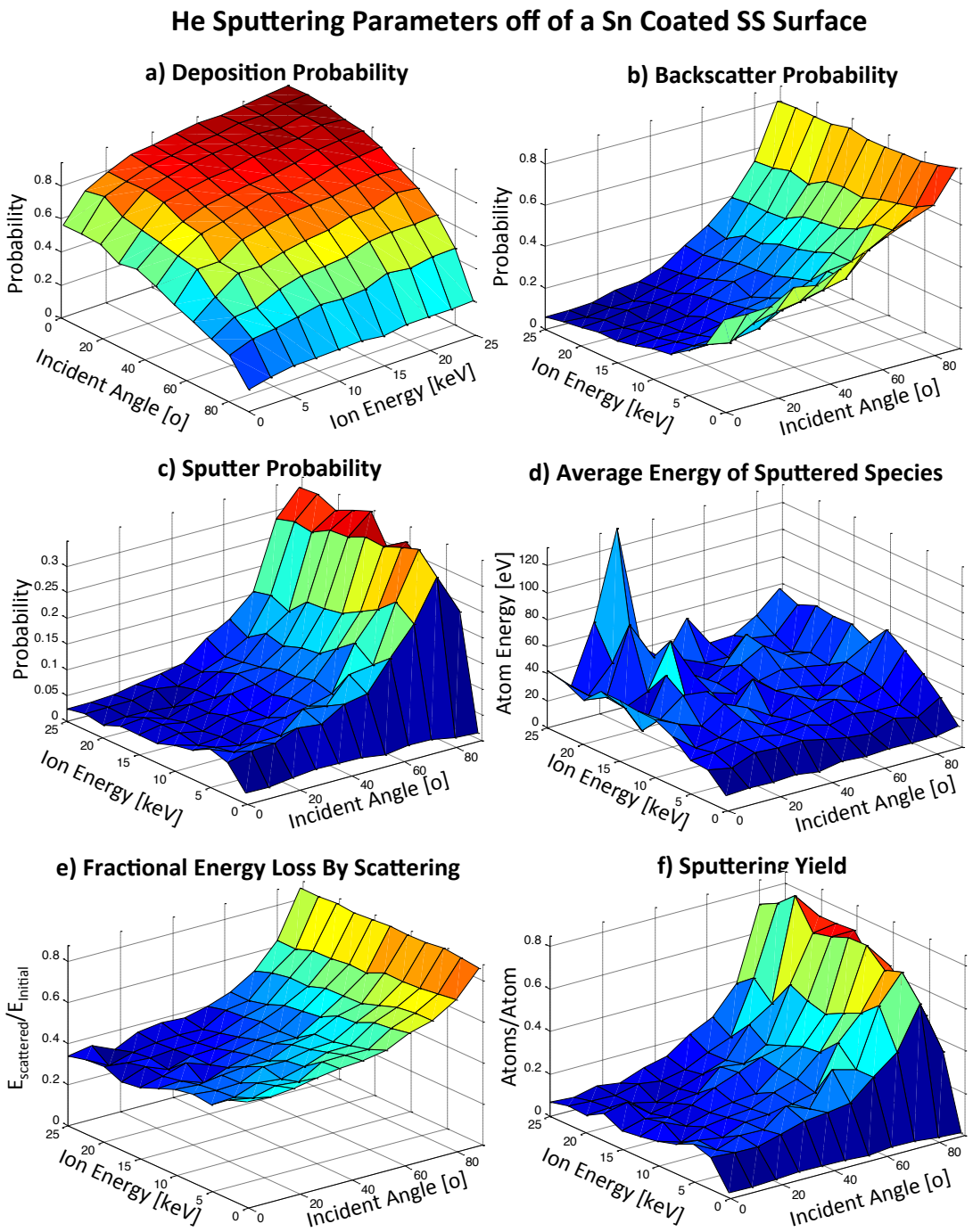

Figure 4.11: Shown are a representative set of measured probabilities for (a) deposition, (b) reflection, and (c) sputtering of a He ion reflecting off of a 5 nm Sn coated stainless steel surface. If sputtering occurs, an average number of sputtered species (f) with average energy (d) are created. The incident ion that interacted with the surface will on average lose a significant portion of its energy though, as shown in (e).

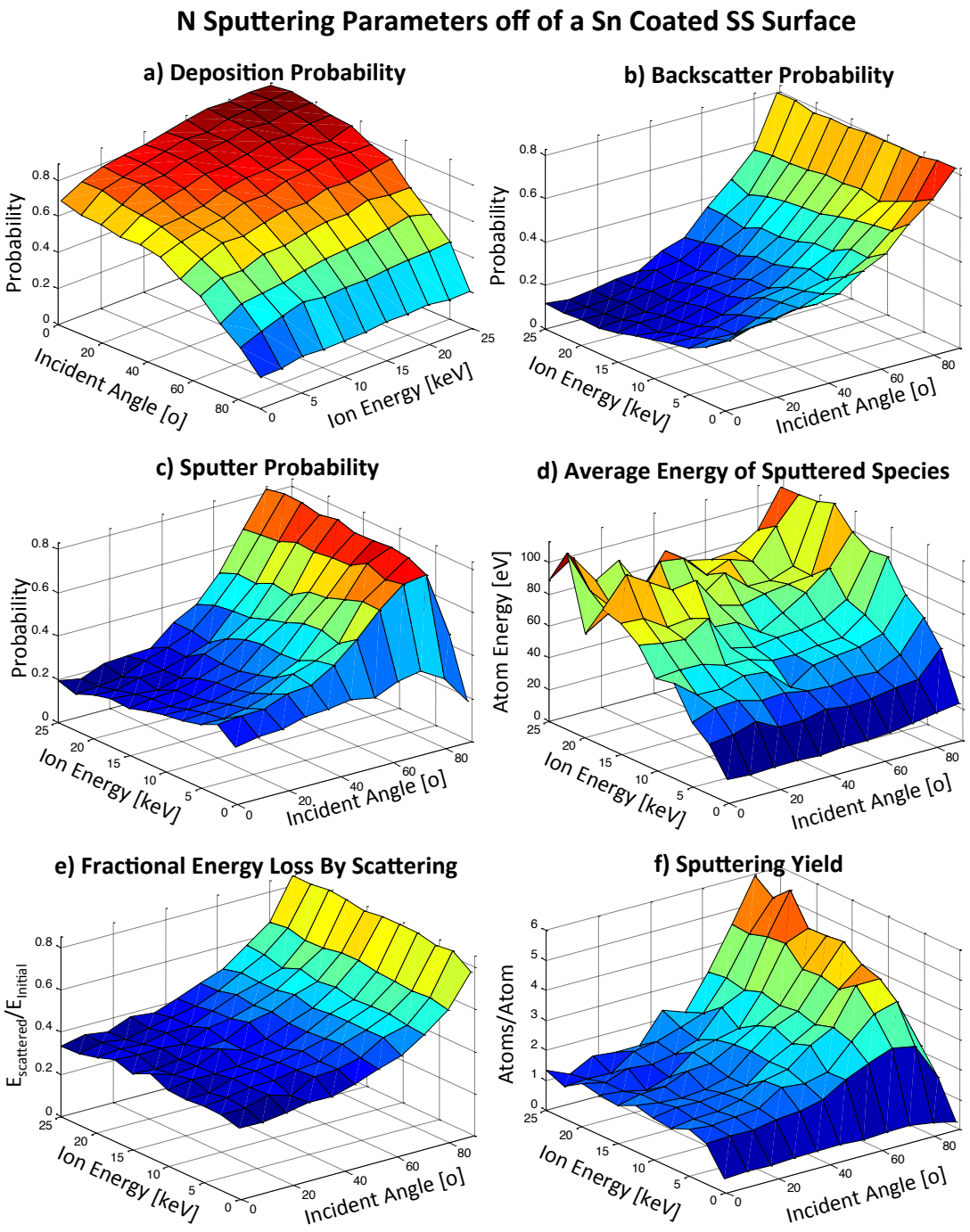

Figure 4.12: Shown are a representative set of measured probabilities for (a) deposition, (b) reflection, and (c) sputtering of a N ion reflecting off of a 5 nm Sn coated stainless steel surface. If sputtering occurs, an average number of sputtered species (f) with average energy (d) are created. The incident ion that interacted with the surface will on average lose a significant portion of its energy though, as shown in (e).

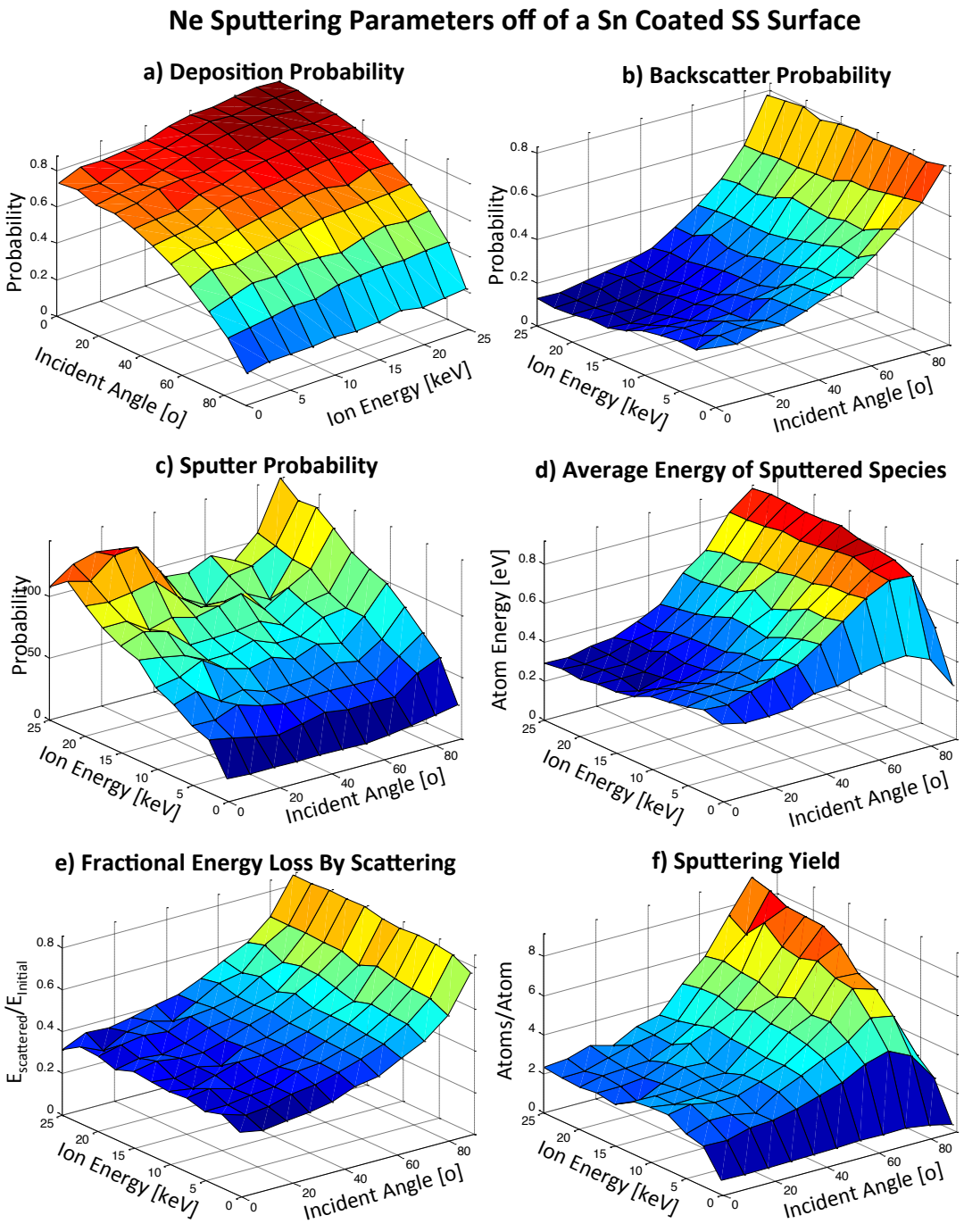

Figure 4.13: Shown are a representative set of measured probabilities for (a) deposition, (b) reflection, and (c) sputtering of an Ne ion reflecting off of a 5 nm Sn coated stainless steel surface. If sputtering occurs, an average number of sputtered species (f) with average energy (d) are created. The incident ion that interacted with the surface will on average lose a significant portion of its energy though, as shown in (e).

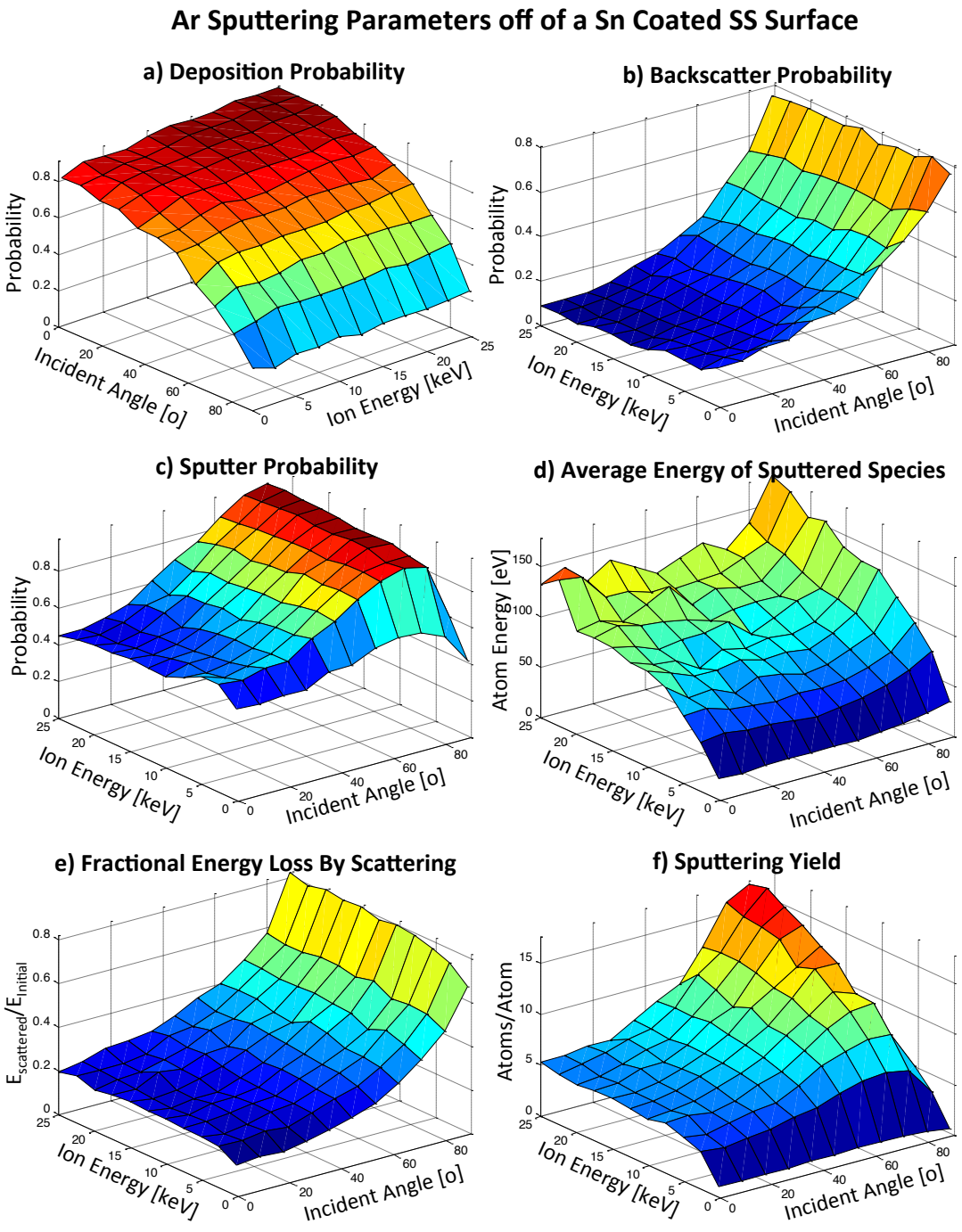

Figure 4.14: Shown are a representative set of measured probabilities for (a) deposition, (b) reflection, and (c) sputtering of an Ar ion reflecting off of a 5 nm Sn coated stainless steel surface. If sputtering occurs, an average number of sputtered species (f) with average energy (d) are created. The incident ion that interacted with the surface will on average lose a significant portion of its energy though, as shown in (e).

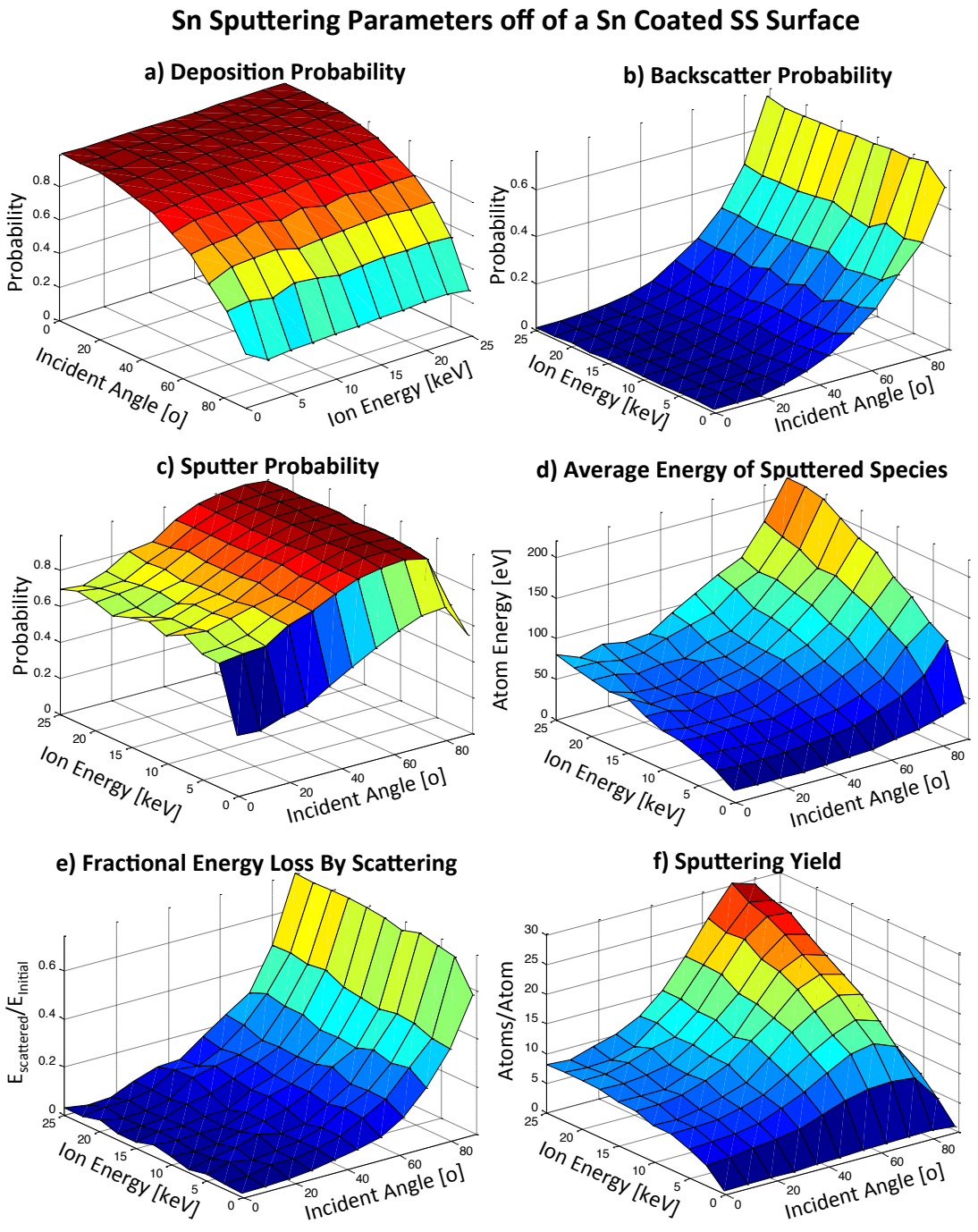

Figure 4.15: Shown are a representative set of measured probabilities for (a) deposition, (b) reflection, and (c) sputtering of an Sn ion reflecting off of a 5 nm Sn coated stainless steel surface. If sputtering occurs, an average number of sputtered species (f) with average energy (d) are created. The incident ion that interacted with the surface will on average lose a significant portion of its energy though, as shown in (e).

The SRIM code also provides a way of estimating the backscatter direction of incident atoms that do not deposit on the surface. A backscattered or sputtered atom's new direction can be characterized by two angles. As shown in figure 4.16, a test atom collides with a surface at an angle of incidence $\theta_{incident,}$ with respect to the surface normal vector. The backscattered direction can be described as a function of the angles $\theta_{scattered,}$ and $\theta_{straggle.}$ While these angles are complexly coupled to intra-surface scattering, they can adequately be described by a cosine distribution fit. Furthermore, the geometry of the problem lends itself readily to the spherical coordinate system. As such, it is simple to convert from the Cartesian vector coordinates provided by SRIM, to the two characterizing angles.

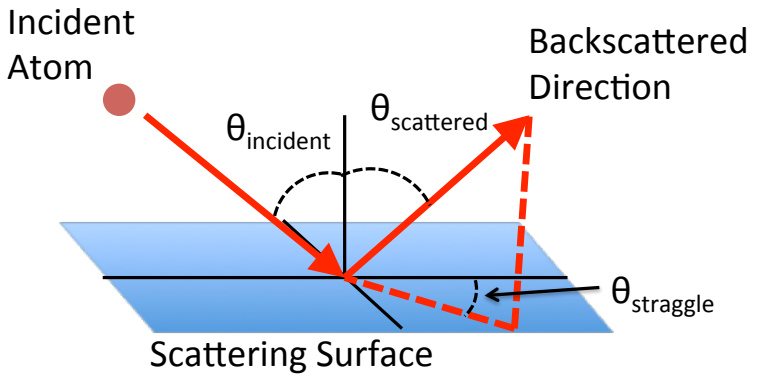

Figure 4.16: The SRIM code allows for the designation of the incident atom's mass, energy, and angle relative to the surface normal. A backscattered atom will leave the surface with an angle of $\theta_{scattered}$ from the surface normal, and an angle of $\theta_{straggle}$ away from the plane that is comprised of the incident vector and the surface normal vector. These two angles are able to be approximated using cosine distribution functions.

Determining the new direction vector begins by calculating the scattering and straggling angles for each of the backscattered species at a given condition (designated mass, incident angle, and surface composition, 1000 runs). Two

histograms are then created with 20 bins (chosen experimentally to adequately provide proper fitting data) to get a hit count for $\theta_{scattered}$ from [0, π] and $\theta_{straggle}$ from [–π, π] (the limits of both angles). To fit the histograms to a cosine distribution function, the value of μ (see equation 4.4) is incremented across the range of the angle being fit (grid size of 100). At the same time, for each value of μ, the value of s is increased from 0 to its maximum value, again with a grid of 100 incremental values. For each combination of μ and s, the sum of the squares of the difference between the normalized cosine distribution function and normalized angle histogram is calculated. At the end of the analysis, the lowest sum is determined as the best fit, and the values of μ and s for both the scatter and straggle angles are added to a table for the given energy and incident angle. Figures 4.17 shows a representative histogram fit for both the straggling (4.17a) and scattering (4.17b) angles of 1000 10.15 keV Ar ions impinging on a 5 nm Sn covered stainless steel surface at an incidence angle of 44.5^{o}. The true process of surface scattering is a very complex series of events that is not completely accurately described by a cosine distribution. With enough energy, a soon to be backscattered atom will actually penetrate the outer atom layers. The collisions it undergoes within this surface can scatter the incident atom back out through the surface. These collisions are inherently complex and result in the presence of scattering angles where the fitted cosine distribution drops to negligible probabilities. This is an unfortunate "error" to the backscatter modeling process, though it is believed to be a minor variance in comparison to the changes involved with angle and energy. The process is repeated for energies from 0.25-50 keV (staggered increments to group this range into 10

different values) and incident angles from 0°-89° (again 10 evenly spaced groupings), to provide a quick reference table for the debris transport model. The ability to correlate the scattering angles to the cosine distribution, and not have to run SRIM for each collision, alleviates a considerable amount of computation time, and still provides a decent estimate of what is occurring when an atom interactions with a surface.

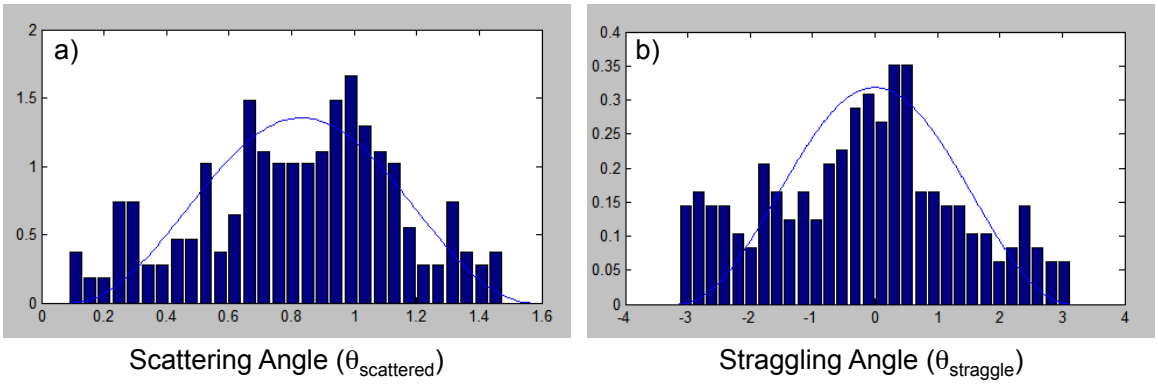

Figure 4.17: The cosine distribution fits for the (a) straggling and (b) scattering angles of the backscattered angles are shown. The SRIM code was run for 1000 ions using a 10.15 kV Ar ion at an incidence angle of 44.5° on a 5 nm Sn covered stainless steel surface. The scattering process can sometimes involve temporary submersion of the incident atom into the inner layers of the surface (with enough energy) after which a collision redirects it out of the surface. This accounts for the species that are observed where the modeled cosine distribution falls to negligible values.

The last part of the wall collision calculations involves determining the backscatter direction vector based on the acquired cosine distributions coefficients for a test atom with known mass, energy, and angle. Because the coefficients are only calculated for a discrete number of conditions, it is first necessary to linearly extrapolate values for a given energy value and angle of incidence. This was achieved using a four-point estimate system. The three closest points of data to the

desired energy and angle values are determined and a vector is created from each of the two furthest (of these three points) points to the closest point. The cross product of these two vectors is taken to create an orthogonal vector, which defines the plane in which these three points lie. Lastly, using the equations of the plane, an extrapolated fit is made given the desired energy and angle. This extrapolation is done for each cosine distribution function parameter, and an appropriate cosine distribution randomization (see section 4.4) is performed to determine the scatter and straggle angle of the simulated test atom's backscatter.

With the required angles determined, keeping in mind that the determined angles are measured off of the XYZ axis, all that is necessary is to determine the rotation required to transfer the vector into the frame of reference of the collision surface. Given the normalized vector of rotation (eq. 4.9), the tensor matrix of the rotation vector (eq. 4.10), the cross product matrix of the rotation vector (eq. 4.11), and the identity vector (eq. 4.12), it is possible to use equation 4.13 to create a rotation matrix. In this equation, θ is the angle of rotation and the other terms are defined by the previous three equations. The first axis of rotation, for applying $\theta_{scattered}$, is defined as the normalization of the cross product of the incident and surface normal vectors. The second required vector of rotation, for $\theta_{straggle}$, is simply the normalized surface normal vector. With the rotation matrix solved for, rotating the original vector $\mathbf{v_{old}}$ about $\mathbf{v_{rotation}}$ is completed using equation 4.14 to create the newly directed vector $\mathbf{v_{new}}$. This function is performed twice for the scattering and straggling angle rotations to create the new direction vector for the test atom that has undergone a wall scattering collisions.

Lastly, the energy for backscattered atoms is derived from the SRIM generated table, an adjustment is made to the test atom variable, and a collision is accordingly noted. It is important to mention that the same process for determining the scattering and straggling angles, and resulting energy, is carried over to the species that are sputtered out of the surface. The only difference between the two processes is that the scattering angle of the sputtered species is modeled as a random number from [0,2π) because there is no directionality to the species that are backscattered out of the surface layer. The probability of sputtering is determined from the SRIM tables and four-point estimate process, as is the number of sputtered atoms that should be expected per sputter inducing incident ion. If sputtering is observed using the model (this feature can be turned on and off to provide a tradeoff between the accuracy of the model and processing time)

$$\overline{v}_{rotation} = \left\langle v_{rx}, v_{ry}, v_{rz} \right\rangle \tag{4.9}$$

$$\overline{v}_{rotation} \otimes \overline{v}_{rotation} = \begin{bmatrix} v_{rx}^2 & v_{rx}v_{ry} & v_{rx}v_{rz} \\ v_{rx}v_{ry} & v_{ry}^2 & v_{ry}v_{rz} \\ v_{rx}v_{rz} & v_{ry}v_{rz} & v_{rz}^2 \end{bmatrix} \tag{4.10}$$

$$\left[\overline{v}_{rotation}\right]_x = \begin{bmatrix} 0 & -v_{rz} & v_{ry} \\ v_{rz} & 0 & -v_{rx} \\ -v_{ry} & v_{rx} & 0 \end{bmatrix} \tag{4.11}$$

$$I = \begin{bmatrix} 1 & 0 & 0 \\ 0 & 1 & 0 \\ 0 & 0 & 1 \end{bmatrix} \tag{4.12}$$

$$R = I\cos\theta + \sin\theta\left[\bar{v}_{rotation}\right]_x + \left(1-\cos\theta\right)\bar{v}_{rotation}\otimes\bar{v}_{rotation} \quad (4.13)$$

$$\bar{v}_{new} = R_{straggling}\left[R_{scattering}\bar{v}_{old}\right] \quad (4.14)$$

4.5.2 Gas-atom collision calculations

The first step in handling gas-atom collisions is the determination if and where such a collision occurs. Because only elastic gas scattering collisions are considered in the debris transport model, the mean free path between collisions can be determined by equation 4.15, where λ is the mean free path, n is the density of the buffer gas species, and σ is the elastic scattering cross section. The buffer gas density is determined using the ideal gas law as given by equation 4.16, assuming a temperature of 295 K. The probability of traveling a distance d_o without undergoing a elastic scattering collision is then given by P_o as given in equation 4.17. The value of d_o is selected as either the distance the test atom travels before a wall collision, or the distance it would travel in the default time step, whichever distance is shorter. Initially, a random value between 0 and 1 is chosen and compared to the probability of survival. If the random value is larger than the value determined in equation 4.17, a collision is deemed to have occurred. The actual distance travelled before the collision is determined using the cumulative distribution function (equation 4.18), where P_x is a random value between 0 and the maximum value of the survival probability in the total distance originally tested (given by $1-P_o$).

$$\lambda = \frac{1}{n\sigma} \quad (4.15)$$

$$P = nRT \tag{4.16}$$

$$P_o = e^{-\frac{d_o}{\lambda}} \tag{4.17}$$

$$r_o = -\lambda \ln(1 - P_x) \tag{4.18}$$

Classical scattering theory is utilized to determine the collision parameters resulting in a new direction and energy for the incident and scattered species, as diagrammed in figure 4.18[77]. Energy (eq. 4.19) and angular momentum (eq. 4.21) are conserved in the elastic collision center of mass (COM) problem within the coordinate system (r,φ). Here, E_{com} is the total center of mass energy of the binary system, V(r) is the interatomic potential between the two atoms, μ is the reduced mass as defined by equation 4.20, b is the impact parameter, υ is the incident atom velocity.

$$E_{com} = V(r) + \frac{1}{2}\mu\left(r'^2 + r^2\varphi'^2\right) \tag{4.19}$$

$$\mu = \frac{m_1 m_2}{m_1 + m_2} \tag{4.20}$$

$$\upsilon b = r^2\varphi' \tag{4.21}$$

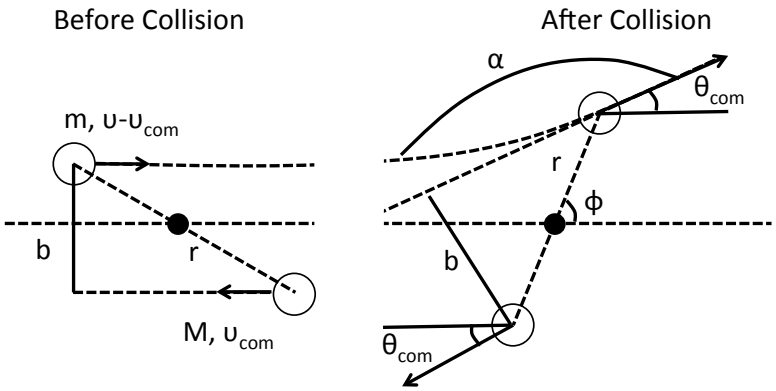

Figure 4.18: A center of mass diagram of the collision between an atom with mass m and υ-υ_{com} incident on a resting mass M with a velocity of -υ_{com}. The resulting collision has a nearest impact point of r_o and scattering angle of θ_{com}.

Restructuring equation 4.19 with the addition of equation 4.21, it is possible to derive an equation for the rate of change of r, r' (eq. 4.22). Setting r'=0 in equation 4.23 describes the relationships between impact parameter, system energy, interatomic potential, relative masses, and incident ion velocity, under the constrictions of equation 4.23.

$$r' = \left(\frac{2}{\mu} \left[E_{com} - V(r) \right] - \frac{\upsilon^2 b^2}{r^2} \right)^{\frac{1}{2}} \tag{4.22}$$

$$b^2 = r_o^2 \left(1 - \frac{V(r_o)}{E_{com}} \right) \tag{4.23}$$

Combining equations 4.22 and 4.19 results in the equation of motion for the incident atom, equation 4.24. The center of mass scattering angle (θ_{com}) can be solved for, equation 4.25, with the understanding that $[\varphi(r=\infty) - \varphi(r=r_o)]=\alpha/2$, where $\pi=\alpha+\theta_{com}$. Because the integral at $r=r_o$ equals infinity, considerations are required to amend for classical scattering's deficiencies. If one integrates from $r=r_o+\varepsilon$ instead, where ε is a small number, then $[\varphi(r=\infty) - \varphi(r=r_o+\varepsilon)+\Delta\varphi]=\alpha/2$, where

$\Delta\varphi = \varphi(r=r_o+\varepsilon) - \varphi(r=r_o)$. θ_{com} is then defined as $\theta_{com}=\pi - \Delta\varphi - \alpha/2$, and equation 4.26 is formed.

$$\frac{d\varphi}{dr} = \frac{\upsilon b}{r^2}\left[\frac{2}{\mu}\left[E_{com} - V(r)\right] - \frac{\upsilon^2 b^2}{r^2}\right]^{\frac{1}{2}} \tag{4.24}$$

$$\theta_{com} = \pi - 2b\int_{r_o}^{\infty} \frac{dr}{r^2\left[1 - V(r)/E_{com} - b^2/r^2\right]^{\frac{1}{2}}} \tag{4.25}$$

$$\theta_{com} = \pi - 2\Delta\varphi - 2b\int_{r_o+\varepsilon}^{\infty} \frac{dr}{r^2\left[1 - V(r)/E_{com} - b^2/r^2\right]^{\frac{1}{2}}} \tag{4.26}$$

It is clear that as ε gets smaller, $\Delta\varphi = \varphi(r=r_o+\varepsilon) - \varphi(r=r_o) = \varepsilon\, d\varphi/dr$. This suggests that a small linear interpolation can be used to evalute for the value of $\Delta\varphi$, and consequently allow for the solution of $\theta_{com.}$ The resulting value of $\Delta\varphi$ is shown in equation 4.27, resulting in the now computationally solvable equation 4.28.

$$\Delta\varphi = \frac{\varepsilon b}{\left(r_o + \frac{\varepsilon}{2}\right)^2\left[1 - \frac{V\left(r_o+\varepsilon/2\right)}{E_{com}} - \frac{b^2}{\left(r_o+\varepsilon/2\right)^2}\right]^{\frac{1}{2}}} \tag{4.27}$$

$$\theta_{com} = \pi - 2\left[\Delta\varphi + b\int_{r_o+\varepsilon}^{L} \frac{dr}{r^2\left[1 - V(r)/E_{com} - b^2/r^2\right]^{\frac{1}{2}}} + \sin^{-1}(b/L)\right] \tag{4.28}$$

The first step in solving equation 4.28 is to determine the value of the interatomic potential V(r), as a function of impact parameter size. The interatomic potential between each species was determined using a combination of the repulsive Abrahamson potential coupled with an attractive well determined based

off of the Lennard-Jones potential with a fitting parameter to couple the two different potentials [78]. The fitting parameter is determined roughly by trying to match the slopes of the rise visually. In reality, for the energies being examined in this paper, this ad hoc fitting process adds very little error to the measurement. The resulting potential is described by equation 4.29 and the fitting parameters given in table 4.2.

$$V(r) = Ae^{-Br} + 4\varepsilon\left[\left(\frac{\sigma}{r}\right)^{x} - \left(\frac{\sigma}{r}\right)^{6}\right] \tag{4.29}$$

Table 4.4: The six fitting parameters for the Abrahamson type potential with attractive well for use in equation 4.28 to calculate elastic scattering interactions.

Reaction	ε (eV)	σ (A)	A (eV)	B (A^{-1})	X	Source
N-He	0.0026	3.12	632.72	3.98	6.5	[79, 80]
N-Ne	0.0049	3.24	2310.29	3.79	7	[79, 80]
N-Ar	0.0092	3.51	3449.99	3.71	6.2	[79, 80]
Sn-He	0.0191	2.70	2695.16	3.85	6.5	[79-81]
Sn-Ne	0.0248	2.81	9840.96	3.65	8	[79-81]
Sn-Ar	0.0465	3.09	14695.64	3.58	7	[79-81]
Mo-He	0.0026	2.65	2369.97	3.85	7	[79, 80, 82]
Mo-Ne	0.0273	2.76	8653.60	3.66	7	[79, 80, 82]
Mo-Ar	0.0512	3.04	12922.54	3.58	6.5	[79, 80, 82]
Cu-He	0.0146	2.42	1805.23	3.87	6.2	[79, 80, 83]
Cu-Ne	0.0357	2.53	6591.52	3.67	6.5	[79, 80, 83]
Cu-Ar	0.0670	2.81	9843.21	3.59	6.5	[79, 80, 83]
Ar-He	0.0031	2.95	1276.62	3.90	6.2	[79, 80]
Ar-Ne	0.0058	3.07	4661.38	3.70	6.5	[79, 80]
Ar-Ar	0.0108	3.35	6960.90	3.63	6.5	[79, 80]
He-He	0.0009	2.56	234.13	4.17	6.1	[79, 80]
He-Ne	0.0016	2.67	854.89	3.98	6.5	[79, 80]
Ne-Ne	0.0031	2.79	3121.50	3.78	6.5	[79, 80]

The interatomic potentials, plotted for each of the possible gas scattering interactions in figure 4.19, are then used to computationally calculate equation 4.28.

A grid of E_{com} from 1-50000 eV is first created, with 10 points per each decade, and a corresponding grid of impact parameters is created in increments of 0.1 from 0-10. The value of r_o is then solved for each energy/impact parameter pair using Newton's method and equation 4.23 in conjunction with the derived interatomic potentials. Finally, the complete equation is integrated using Simpson's rule with an ε of 10^{-4} with an impact parameter of 6000 divisions per angstrom. The resulting table was used as a look up table for gas scattering reactions to determine

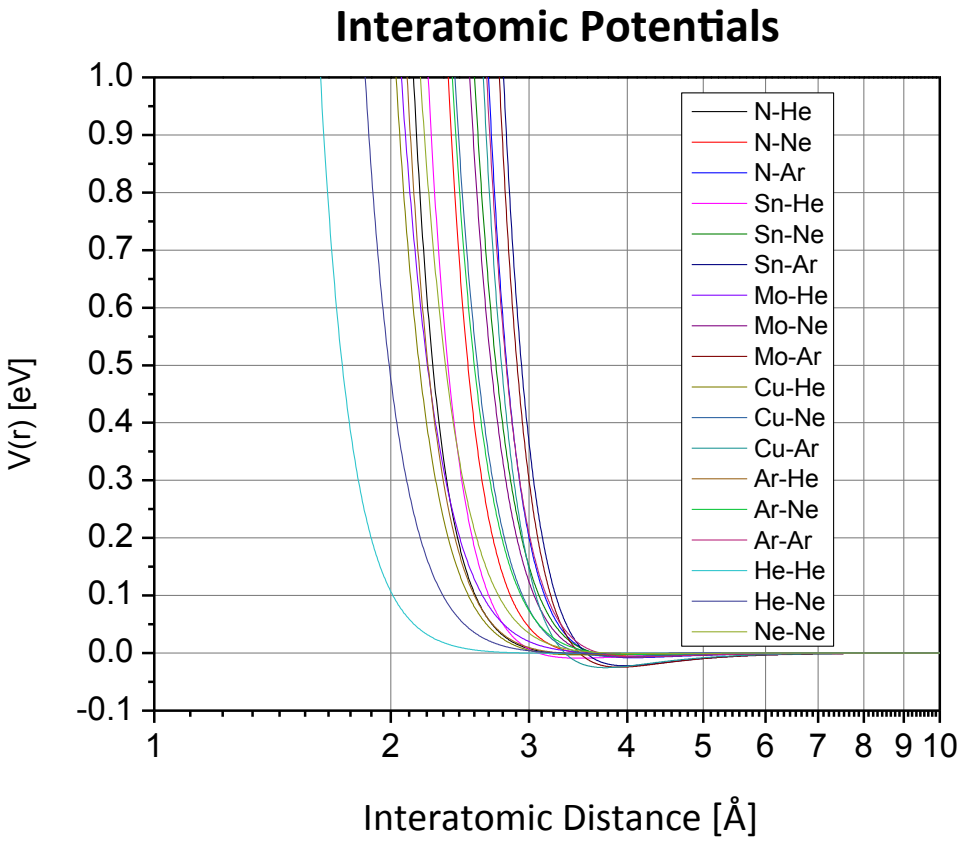

Figure 4.19: Shown are the interatomic potentials for each possible reaction used in the debris transport model. Smaller atoms have closer atomic potentials due to their smaller size. Very close interaction distance results in a strongly repulsive force, but at a certain distance of separation the atoms are actually attractive to one another.

A representative set of center of mass scattering angles is shown in figure 4.20. It is evident in the Sn-Ar atom-atom interaction that as energy is increased, the scattering angle is reduced for a given impact parameter. The decrease in interaction potential also results in a reduction of the elastic scattering cross section, meaning that at higher energies gas atom collisions are less likely. For very low energies, the scattering angle becomes negative at a finite separation point. In this impact parameter range, a quasibound state forms and the incident species is actually backscattered [84]. For the majority of the collisions in this model, due in part to the limitation of species to greater than 0.25 eV for computational speed, the energies are far too great to experience the rainbow scattering phenomenon.

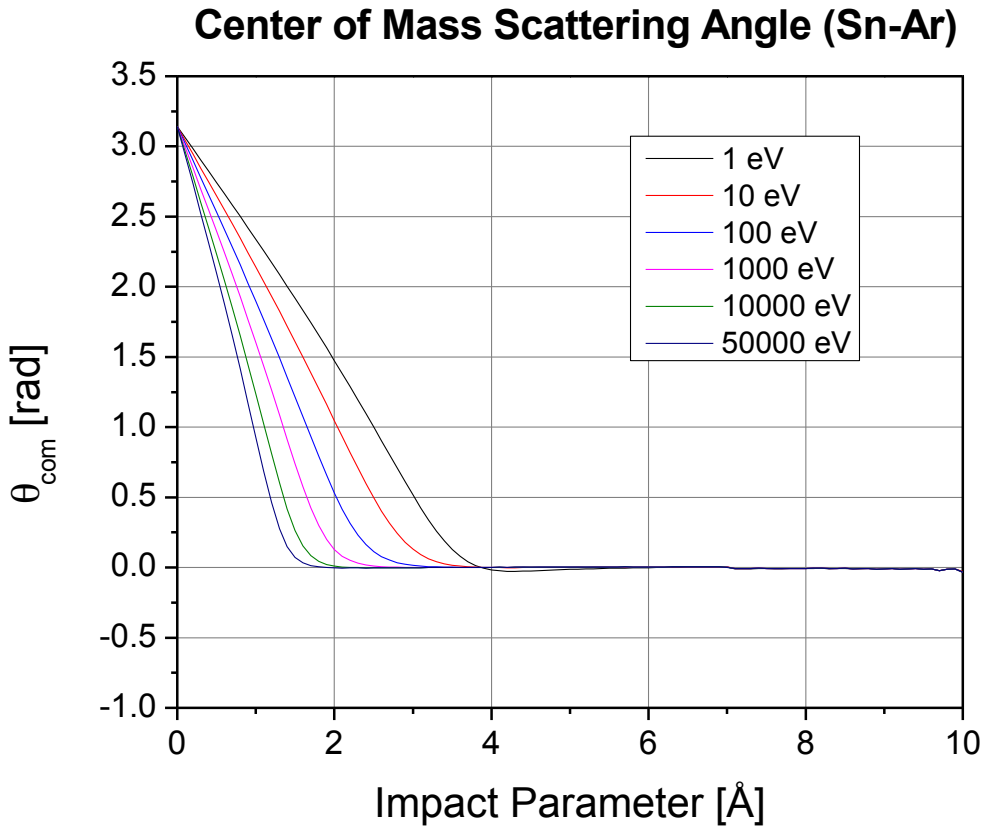

Figure 4.20: A representative set of center of mass scattering angles is provided for a Sn-Ar collision. As the energy of the incident atom is increased, the maximum impact value (the value at which less than 1% scattering occurs), the scattering is more forward peaked and rainbow collisions do not occur.

Having calculated the interatomic potentials and center of mass scattering angles for each of the possible atomic collisions, it is time to return to the elastic scattering cross section. As mentioned previously, the value of the cross section is necessary for determining mean free path – the parameter critical in determining the likelihood of a collision over a certain distance. If one considers the maximum impact parameter, the furthest distance over which a collision will occur, to be the distance beyond which less than 1^{o} of scattering will occur, it is possible to calculate a maximum impact parameter for each possible collision. The total elastic

scattering cross section is simply $\sigma=\pi b_{max}^2$. Since the values of b_{max} are calculated as a function of energy, the scattering cross section is a function of energy; the values for each of the interaction species as a function of energy are plotted in figure 4.21. As energy is increased from the origin, an immediate exponential decay in cross section is observed as the interatomic potential falls off exponentially. Consequently, less energetic species are more likely to be scattered in addition to being scattered at a greater angle. The scattering cross sections are all within two orders of magnitude from $2x10^{-16}$ to $2x10^{-14}$, with the N-Ar interaction having the largest cross section and He-He having the smallest. The discreteness of the data is a consequence of using only ten points per decade of energy to calculate the interatomic potentials of each possible interaction. A linear fit between each data point allows for the determination of mean free paths across the non-discrete energy spectrum required in the debris transport model.

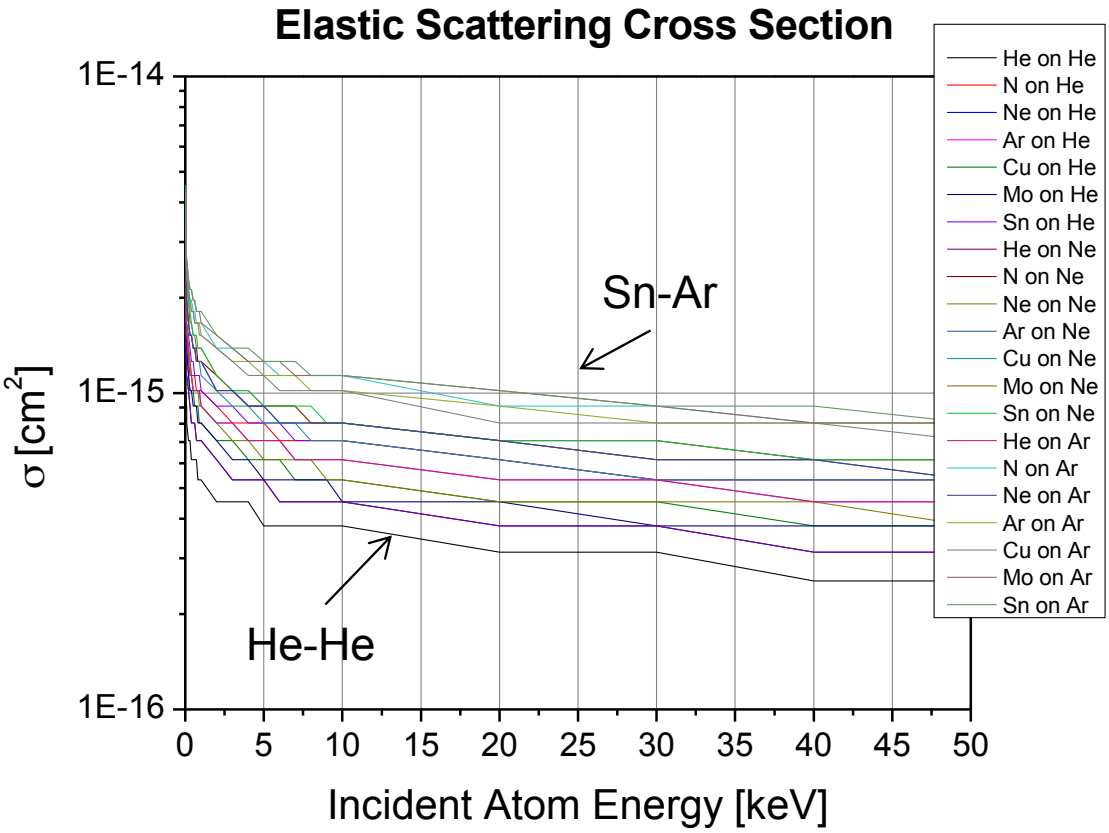

Figure 4.21: Shown are the elastic scattering cross sections for each possible gas scattering reaction. Because the interatomic potential increases as energy is reduced, an increase in energy results in a lower cross section. The likelihood of a scattering event is nearly five times greater for most of the species in consideration.

The last task to complete with the gas scattering interaction is the determination of the energies and directions of the incident and scattering species in the lab frame. Using figure 4.22 as a reference, the velocities of each of the individual species can be written as shown in equations 4.30-4.36.

$$\bar{v}_1 = v_1 \hat{x} \tag{4.30}$$

$$\bar{v}_2 = -\frac{m}{M} v_2 \hat{x} \tag{4.31}$$

$$\bar{v}_1' = v_1 \cos(\theta_{com}) \hat{x} + v_1 \sin(\theta_{com}) \hat{y} \tag{4.32}$$

$$\vec{v}_2' = -\frac{m}{M}v_2\cos(\theta_{com})\hat{x} + -\frac{m}{M}v_2\sin(\theta_{com})\hat{y} \tag{4.33}$$

$$\vec{V}_1 = \left(1+\frac{m}{M}\right)v_1\hat{x} \tag{4.34}$$

$$\vec{V}_1' = \left(\cos(\theta_{com})+\frac{m}{M}\right)v_1\hat{x} + \sin(\theta_{com})v_1\hat{y} \tag{4.35}$$

$$\vec{V}_2' = \frac{m}{M}\left(1-\cos(\theta_{com})\right)v_1\hat{x} - \sin(\theta_{com})v_1\hat{y} \tag{4.36}$$

If ε is the total energy of the center of mass frame and E the total energy of the lab frame, the energies of each individual species pre and post collision can be defined by equations 4.37 and 4.38.

$$E = \frac{1}{2}m(V_1)^2 = \frac{1}{2}m(V_1')^2 + \frac{1}{2}M(V_2')^2 \tag{4.37}$$

$$\varepsilon = \frac{1}{2}m(v_1)^2 + \frac{1}{2}M(v_2)^2 = \frac{1}{2}m(v_1')^2 + \frac{1}{2}M(v_2')^2 \tag{4.38}$$

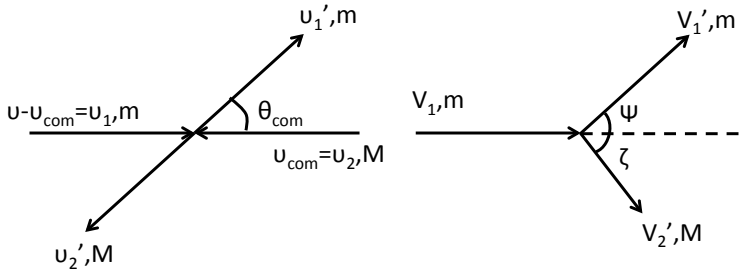

Figure 4.22: In the center of mass frame (a), both the incident and the scattering particle travel towards and away from each other at the same angle. In switching to the lab frame (b), however, each particle takes on its own identity, requiring the determination of the individual angles and velocities.

Combining the two energy equations reveals the relationship, as shown in equation 4.39, between the lab frame energy and the center of mass frame energy, which will always be less than the lab frame energy. Furthermore, it is possible to define the individual energies in terms of the total energies as shown in equations 4.40-3.43.

$$E = \left(\frac{m+M}{mM}\right)\varepsilon \tag{4.39}$$

$$\varepsilon_1 = \varepsilon_1^{'} = \left(\frac{M}{m+M}\right)\varepsilon \tag{4.40}$$

$$\varepsilon_2 = \varepsilon_2^{'} = \left(\frac{m}{m+M}\right)\varepsilon \tag{4.41}$$

$$E_1^{'} = \left(\frac{m^2 + 2mM\cos\left(\theta_{com}\right) + M^2}{\left(m+M\right)^2}\right)E \tag{4.42}$$

$$E_2^{'} = \left(\frac{2mM\left(1-\cos\left(\theta_{com}\right)\right)}{\left(m+M\right)^2}\right)E \tag{4.43}$$

The values of E_1' and E_2' are the post-scattering energies of the scattered species, and the values needed to determine the exit velocity of the test atom in question, and the newly created scattered species in the debris transport model. The different lab frame scattering angles are deduced by geometry in addition to the equations of path, and are as follows:

$$\tan\left(\psi\right) = \frac{\sin\left(\theta_{com}\right)}{\cos\left(\theta_{com}\right) + \frac{m}{M}} \tag{4.44}$$

$$\tan(\zeta) = \frac{\sin(\theta_{com})}{1-\cos(\theta_{com})} \tag{4.45}$$

With the newly directed species' energies and directions determined, the last remaining step in modeling the gas scattering collisions involves taking the direction from the xy-plane to the plane of reference where the atom is located in the model. The actual collision point between the two species is determined by two parameters. The first is the impact parameter defined by b = sqrt(P)b_{max}, where P is a random value in the range of [0,1]. This defines where along the radius the collision occurred, providing information on the scattering angle relative to the two species. In order to determine final directions, however, it is necessary to the azimuthal location of the impact at the given radius b. This is done at random from a value of [0,2π). The two calculated vectors of the scattered species are then rotated, in the same manner as the wall scattering event, until they are in the original three-dimensional location facing the appropriate direction.

4.6 Model Output

The bulk of the analysis is handled outside of the debris transport model. In order to do this, the entire data for each atom species is saved. Each individual test atom has a history of location, energy, incidents (such as scattering events), time of event, direction, as well as information about its birth type (pinch species, sputtered species, or gas scattered species), and additional information about the side of the shell off of which it may have scattered. Information about each progressive generation of species (determined before running the codes) is also saved, which can result in files

containing hundreds of thousands of test atoms in addition to the amount of data kept for each atom. While attempts were made to output commonly useable CSV file outputs, the data writing/loading process was computationally too intensive for practical application, and as such the output file is kept in matlab format.

The IFPlotter.m program provides plotting capabilities for the problem being modeled. This program takes an input of the test atoms to be plotted and the dimensions of the chamber conditions, and plots the resulting path of the test atom as it progresses through the chamber. A sample plot of a 10 keV Sn atom travelling through a 10 mTorr Ar environment is shown in figure 4.23. This figure shows the results of following the evolution of the second generation (the scattered species by the first test atom) as the scattered argon species travel through the chamber.

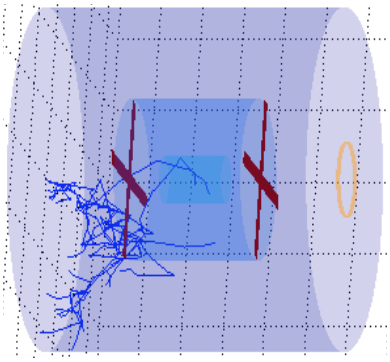

Figure 4.23: Shown is a 10 keV Sn atom's path through the 10 mTorr Ar gas evironment in the chamber. The fingers that appear are the plots of the secondly scattered Ar species. No wall sputtering occurred in this trial.

It is furthermore possible, in the debris transport model, to track multiple generations of species. A plot of the five different generations created by a single 10 keV Sn test atom are shown in figure 4.24e. The collision of energetic species with stagnant background species energizes the background gas, which leads to species

reaching the intermediate focus, as well as other components. Obviously, the computational time increases with an increase in number of generations. In this example case, over 2500 secondary species were generated as a result of a single species being introduced into the chamber.

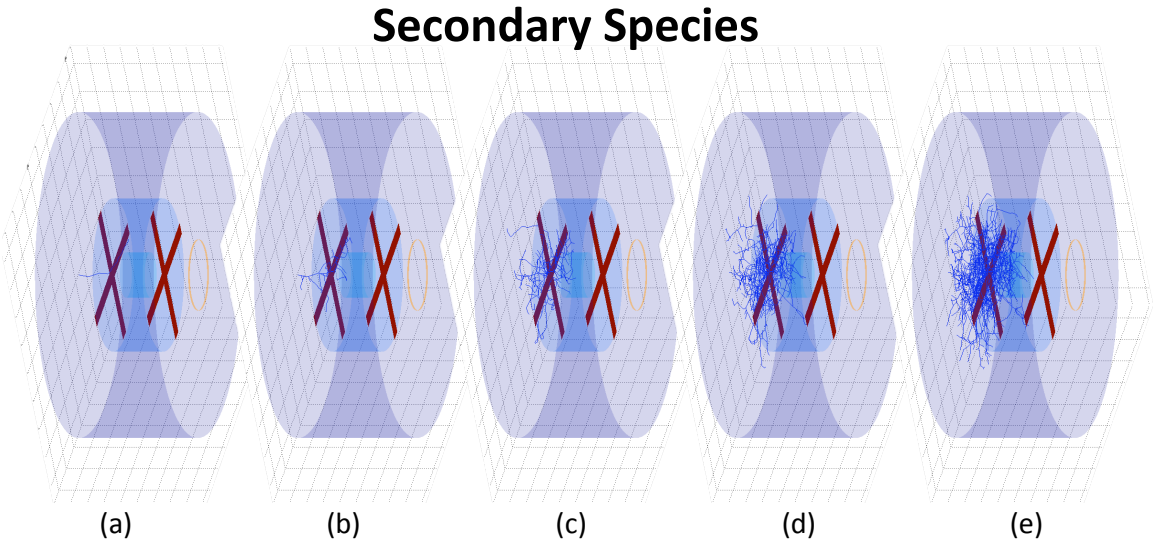

Figure 4.24: It is possible to keep track of the different generations of species. A new generation is created during a scattering event or gas scattering collision. In this figure, The initial test atom (a) creates scattering events which create generation (b). These go on to create additional scattering events and generation (c). It is continued up to generation (e) as shown. All of these events were caused by just the initial introduction of an energetic 10 keV Sn ion into Ar at 10 mTorr.

The effects of chamber pressure are made quite evident by the model, when visualized with IFPlotter. As shown in figure 4.25, as gas pressure is increased, back scattering of the pinch-generated atoms occurs more readily as the mean free path is decreased. The model diagrams this well, as shown in figure 4.26, showing the decreased depth penetration of Sn atoms as they leave the pinch.

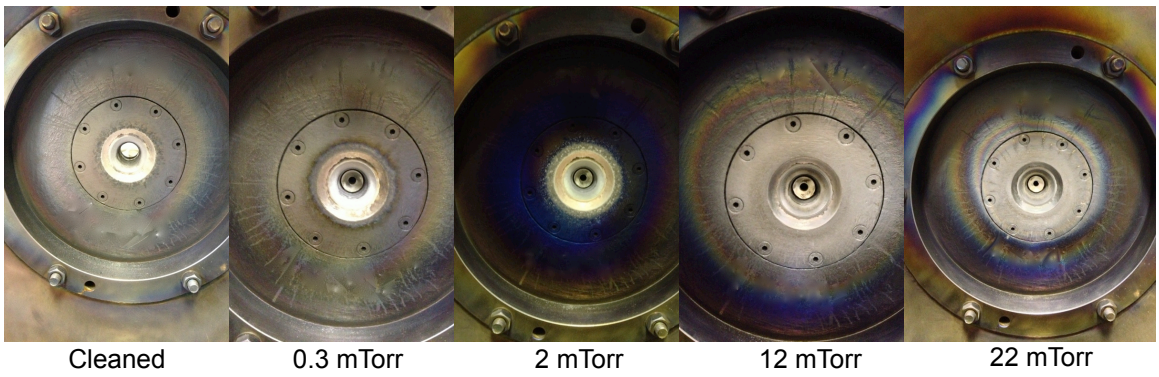

Figure 4.25: Shown are pictures of the electrode area after the operation of each experiment for nearly two hours. As pressure is increased from 0.3 to 2 mTorr, increased plasma density within the chamber causes the removal and cracking of pump oil from the chamber walls. This increases carbon deposition near the electrode surface. Further increases in pressure backscatter Sn around the electrode, as evidenced by the metallic hue.

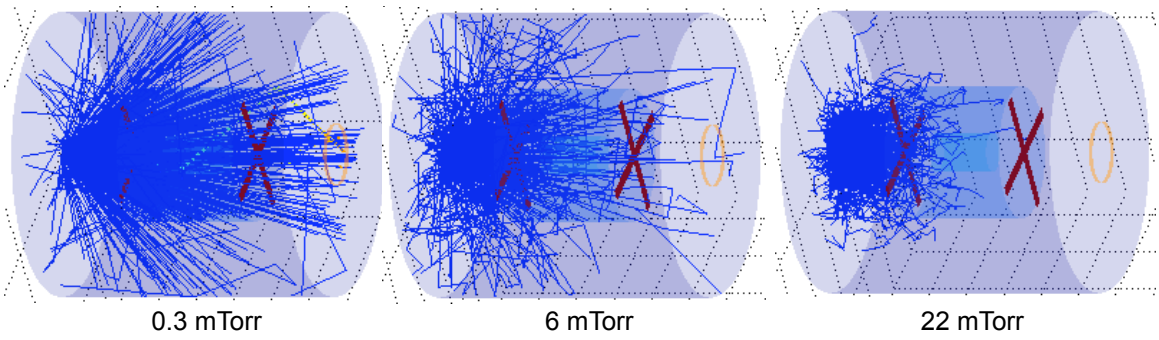

Figure 4.26: Shown are the flight paths for 100 Sn atoms (random energy from 0-25 keV), at increasing pressures. At 0.3 mTorr, the scattering collisions are predominately wall collisions, while at 22 mTorr most collisions are only with gas atoms. The increased collision rate, coupled with the increased energy transfer to the buffer gas, results in less penetration of the electrode materials into the deepest parts of the chamber.

When switching the mass of the buffer gas, it is observed that at 2 mTorr, the higher the buffer gas, the higher the amount of gas scattering. This is a result of the increased scattering cross section (reduces mean free path), and the increased mass of the buffer gas atom. Elastic scattering is most effective at transferring energy between the incident atom and the buffer gas atom when their masses are near equal. As such, for the 118 AMU Sn atoms, argon is the closest in mass and

consequently more efficiently transfers energy and increases scattering throughout the chamber.

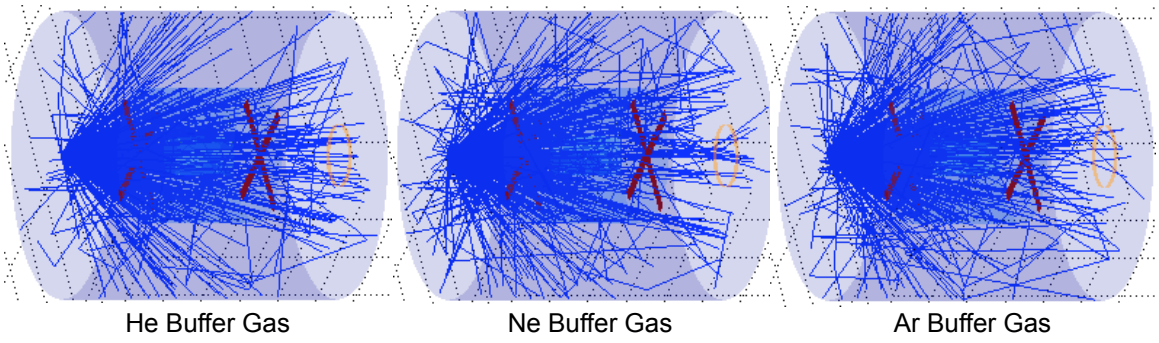

Figure 4.27: Shown are the flight paths of 100 Sn atoms in a 2 mTorr chamber, using three different buffer gasses. Increasing the mass of the buffer gas increases the effectiveness of gas scattering and results in more species being scattered around the chamber befor reaching walls.

When changing the pinch gas from He to Ne to Ar, there is a net effect on the energy transfer (will be discussed more thoroughly in chapter 5) between the accelerated pinch gas atoms and the surround buffer gas. With He there is much more gas scattering because there is very poor energy transfer between He and Ar gasses, and the resulting large scattering angles determined in the elastic scattering equations. The resulting flight paths are shown in figure 4.28.

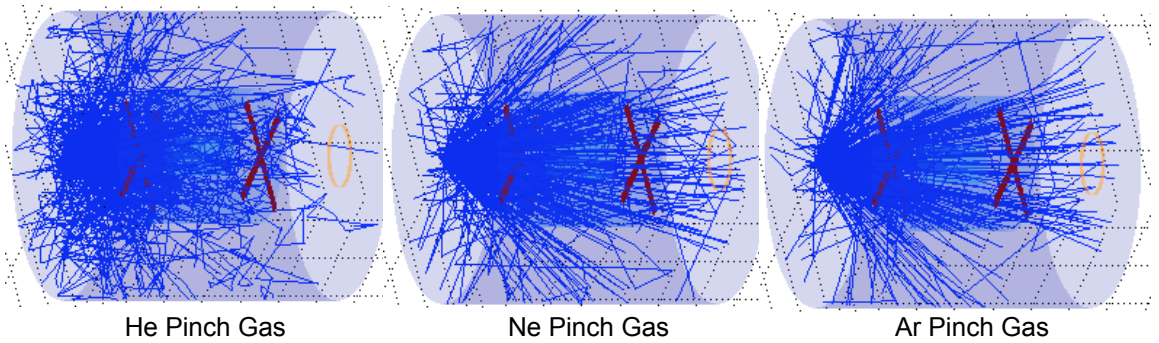

Figure 4.28: The lower massed He gas atoms scatter more readily than the higher massed species due to the increased effectiveness of elastic scattering between a low mass species and a high mass species. Furthermore, the energy transfer between the low mass species and the high mass buffer gas atoms is poor, and the He species survive in the chamber for a longer period of time.

The effective results of these primary interactions determine the effect of pressure, buffer gas mass, and pinch gas mass on the transport of debris fromt the EUV emitting plasma to the intermediate focus of the EUV lithography tool. These theoretical results are used to help explain the experimentally observed phenomenon that will be explained in the next chapter. Ultimately it will be seen that the interaction between the pinch species and the buffer gas are the primary cause of the generation of debris and how it is distributed throughout the chamber.

4.7 Calibration

A calibration factor is utilized to account for discrepancies between the model and the experimental output. This calibration factor is determined by making a comparison between the model's output measurements and the energetic buffer gas flux measurements made with the microchannel plates installed in SNIFFED. The results presented in this section will be further detailed in chapter 5, but are presented here as well to explain the calibration factor.

The data used calibrate the model is measured in units of hits. Microchannel plates are sensitive to the mass and energy of the incident flux, and as such knowledge of both factors is required to convert the hit flux, measured using the microchannel plates, to that of a quantified ion/neutral flux. Since neither value can be determined for these experiments, since each measured atom travels a different distance the time of flight analysis is rendered unusable, the model's atom and energy output needs to first be converted to a hits value that would be observed if the microchannel plates were to measure the atoms created by the model.

Converting the theoretically determined atomic flux to a hit flux allows for a calibration factor to be generated that adjusts the model to the experimentally obtained results. The process of this conversion is as follows.

10000 test atoms were modeled for each experiment, using the pinch gas species as the primary species of interest. The resulting number of energetic buffer gas atoms reaching the intermediate focus for each experiment provides a theoretical measurement of the energetic atomic flux reaching the intermediate focus. This number, for comparison sake to actual measurements, is downscaled by a factor of 0.001^2/0.1^2 to convert from the modeled intermediate focus area (made larger to collect more data) to the area of the actual intermediate focus orifice. Obviously the assumption is made here that the flux is uniform in this region. Furthermore, to account for the sensitivity of the microchannel plates to the atomic mass they are calibrated with, the buffer gas mass is divided by 131 AMU (Xe) and multiplied by the scaled flux measurement. The microchannel plates also have varying efficiency based on the energy of the arriving species, so the running total is multiplied by the detector efficiency at the average arrival energy theoretically determined (actual detector efficiency curves are available in [72]. The calculated value is then divided by the number of test atoms run in the model (10000), and multiplied by the total number of these species measured using the ion and neutral energy analyzer (7.48×10^{11} for N). This converts the theoretical measurement to a value that is comparable to the total measured flux reaching the intermediate focus in a given pulse. Lastly, the value thus far calculated is divided by the microchannel plate base calibration (204 atoms/hit). At this point the number of atoms

theoretically reaching the intermediate focus is converted to the "hit" count that would be observed using a set of microchannel plates.

Dividing the experimental hit count by the theoretical hit count creates an individual factor of difference. This process was repeated for each of the data points measured using the microchannel plate, and the average of these factors is the determined calibration factor. Each of the individual factors are diagrammed in table 4.5, with the average coming out to a factor of 158. In order to provide comparison between the model and the experimental data for 10000 trials on a per atom basis, this factor of 158 is multiplied by the number of measured total atoms created by the pinch ($7.48x10^{11}$ atoms) and divided by the number of test atoms used to create the theoretical measurement (10000 atoms) to create the calibration factor of $1.18x10^{10}$ actual atoms/test atom for use with 10000 test atom runs. The same calibration factor can be scaled to other run counts by applying a factor of 10000 / x test atoms. This calibration factor can be used with any species modeled, and as such is also applicable to the Sn deposition modeling that will be presented.

Table 4.5: The individual difference factors from model to experiment with the model data scaled to $7.5x10^{11}$ atoms.

Experiment	Theoretically flux [hits/cm^2]	Experimental flux [hits/cm^2]	Difference Factor
1	284	45580	160.2
2	4170	663387	159.1
3	5512	890032	161.5
6	159	46290	290.8
7	827	148483	179.4
8	6842	1253516	183.2
9	3090	283870	91.9
10	3181	409935	128.8
		Average:	158

The calibration factor serves as a way to account for error in measurements using the ion and neutral energy analyzers as a method for calculating total flux at the intermediate focus. The measurements presented in section 4.3 were only taken at the 0 degree port, and the relative flux at other angles was assumed to behave like a cosine distribution. In reality the extremely energetic species are forward peaked, and the lesser energy ions/neutrals have a much more uniform distribution. This induces error in the total flux measurements listed, and since this is a value used in the determination of the theoretical measurement it also induces an offset in the theoretical results. The calibration factor accounts for this flux difference (which in the case of the buffer gas measurements would create more scattering collisions and consequently a larger than anticipated flux at the intermediate focus), allowing a true comparison between the theoretical and experimentally measured results. Ultimately, the average factor difference shown in table 4.5 suggests that the total number of species measured using the ion and neutral energy analyzers is actually off by a factor of 157.7. Furthermore, the calibration factor accounts for the fact that only one generation of scattered buffer gas species was followed. Increasing the number of generations increases the computation time by several order of magnitude just to measure three generations. In general this can result in an underestimation by a factor of 6-12, and as such, this offset is also included in the calibration factor.

The resulting calibrated flux measurements are plotted in figure 4.29a-c. The relative trends observed theoretically match those observed experimentally, which lends credence to the thought that the calibration factor is required to account for the difference in total energetic emitted flux from the EUV plasma measured using the ion and neutral energy analyzer from the actual flux emitted. Since the calibration factor is only based off of one pinch gas condition, variations in pinch gas can cause variations in the energetic ion/neutral output of the EUV plasma. It is believed that the variation observed in figure 4.29c, where theory overestimates the He and Ne flux and underestimates the Ar flux, is actually caused by the variation in measured relative fluxes. This cannot easily be verified because there is no direct species determination at energies above 28 keV, where no ion measurements can be taken and neutral only measurements don't shed light on the composition of the flux.

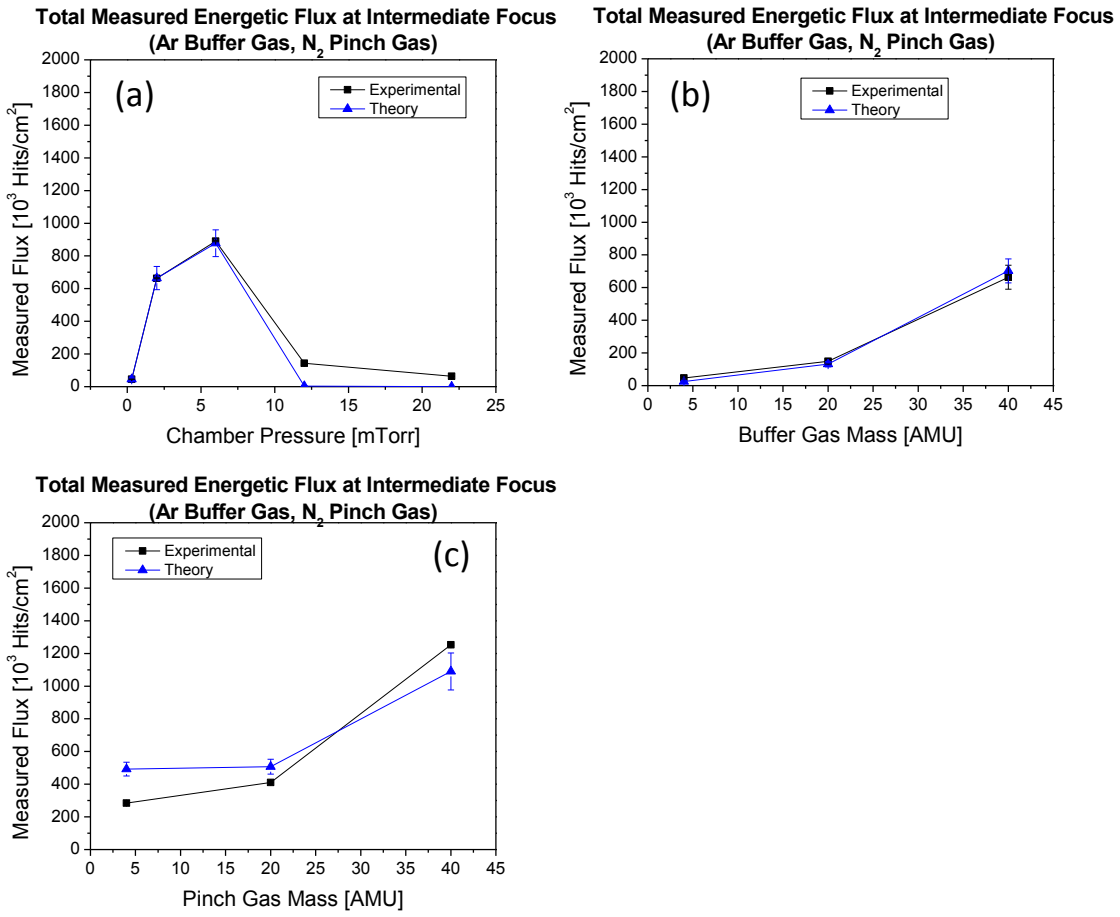

Figure 4.29: Shown are the comparisons between experimental and theoretical flux measurements at the intermediate focus. The trends are preserved, suggesting that the unified calibration factor of 1.18×10^{10} actual atoms/test atom is simply a measure of the underestimation of the total measured flux emitted from the EUV plasma.

CHAPTER 5

RESULTS AND DISCUSSION

5.1 Introduction

In order to understand the mechanisms of debris transport from the EUV emitting plasma source to the intermediate focus, a series of three different experiments were developed. These experiments seek to understand the effects of pressure, buffer gas species, as well as pinch gas species by altering the buffer gas pressure, buffer gas mass, and pinch gas mass respectively. By changing these parameters it is possible to isolate the origins of the observed charged and neutral energetic debris. The results in this section will consequently be presented in three different groupings based on the effect of buffer pressure (0.3,2,6,12,22 mTorr), buffer gas mass (4,20,40 Amu), and pinch gas mass (4,20,40 Amu). Each of these conditions was analyzed using the SNIFFED apparatus, Si witness plates, as well as by a set of three Langmuir triple probes. The SNIFFED apparatus is capable of measuring various flux characteristics at the intermediate focus, the Si witness plates monitor debris transport throughout the chamber, while the Langmuir triple probes provide an analysis of the development and diffusion of primary and secondary plasmas created by the EUV emitting plasma. The advantage of the "symmetrical" triple probe employed in these measurements is that no voltage sweep is required. As mentioned previously, the three probes provide measurements of the ion saturation voltage, floating voltage, and a voltage between

the floating potential and plasma potential. Because only three points are taken, a fine analysis of the electron energy distribution is sacrificed in favor of the ability to measure a less accurate electron temperature on the order of probe response time. This allows for the temporal measurements shown in the microsecond order of time. Obviously with such a method, the true distribution of electron temperature (to account for beams, high energy components, etc.) is not completely described. The theoretical model will be used to illuminate the reasoning behind phenomena observed in the process of Sn deposition as well as the measured latent energetic flux and arrival time of this flux at the intermediate.

5.2 Determination of Secondary Plasma Origins

It will be shown in the upcoming sections that there exist three different observable plasmas, each of which has a different speed of propagation. The first plasma originates from the expansion of the highest energy electrons that are ejected from the EUV plasma, the second plasma is coupled with the ejection of the high energy ions, which slow them down, while the final plasma propagating through the chamber originates from the expansion of the bulk EUV emitting plasma. These different plasmas are diagrammed in figure 5.1 to provide clarity.

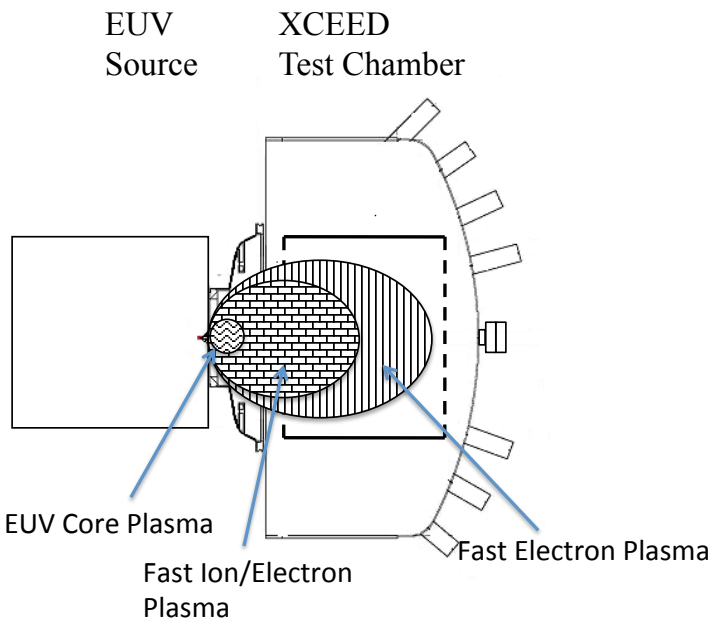

Figure 5.1: The fast electron plasma, fast ion/electron plasma, and the EUV plasma core are shown with outlines showning the bulk of the ion density. Measurements outside of the outer collector optic measure contributions from the plasma electrons that are scattered to those locations. The fast electrons, which undergo less scattering inside of the EUV emitting plasma during relaxation, are more forward peaked than the slower electron contributions from the other plasmas.

As shown in figure 5.2a-c, which shows the electron densities for each of the experimental conditions inside of the inner collector optic, the first plasma arrives nearly instantly after EUV plasma initiation (0-10 μs), the second plasma arrives shortly after (10-30 μs) the first plasma, and the last plasma traverses half of the chamber in approximately 100-200 μs after the initial plasma formation. It was originally hypothesized that the first plasma originated from the photoionization of buffer gas by EUV/VUV/DUV photons emitted from the plasma source. The second plasma was originally hypothesized to be caused by ion-impact ionization, or through photoemission of electrons from the near by walls. Lastly, it was hypothesized that the remaining plasma was the *only* plasma directly linked to the

expansion of the EUV plasma. It will presently be shown that these predictions were incorrectly made, for the contributions by each of these processes cannot account for the ion densities observed by the triple probes located 0.36 m into the EUV chamber. In order to determine the contributions of various components to electron density, comparisons will be made to the measurements found at the 0.36 m distance inside of the inner collector optic. This location has the least occluded view, and consequently will show electron density measurements with the least amount of influence by the collector shells' obscuration of the line of sight between the triple probe and the Z-pinch plasma location.

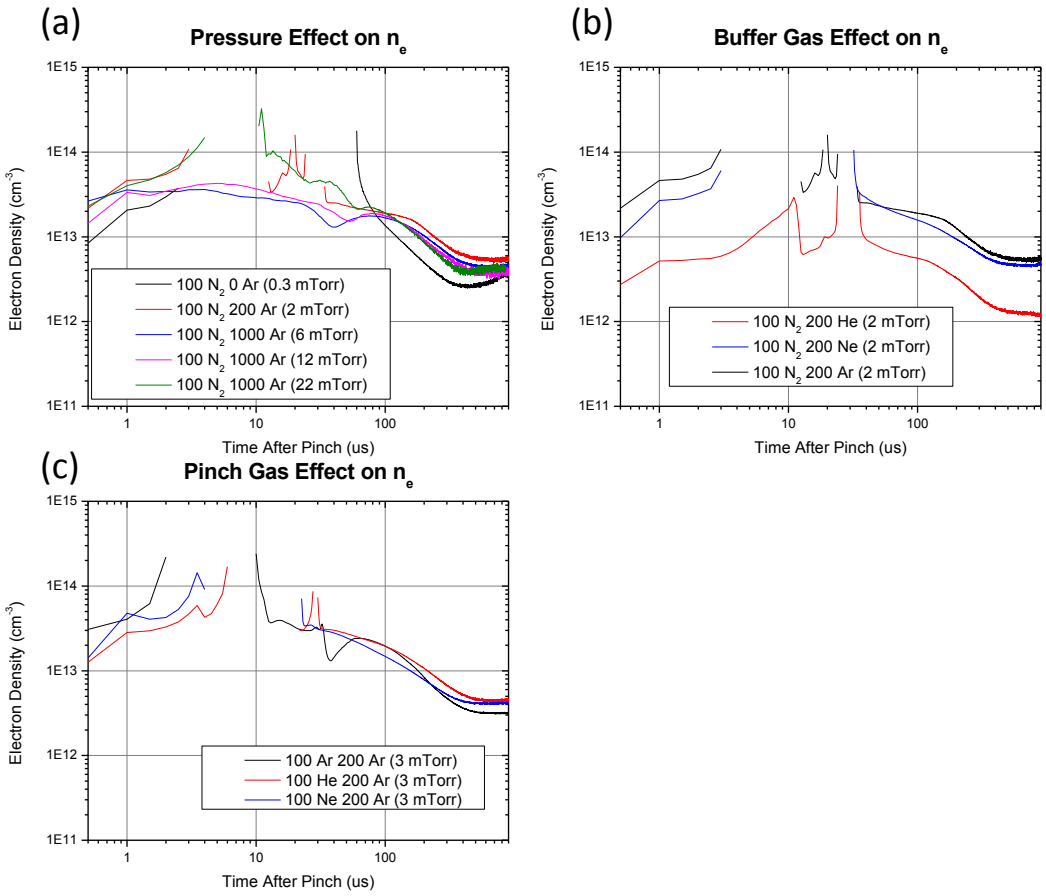

Figure 5.2: Shown are the measured electron densities at 0.36 m from the pinch at the inside of the innermost collector optic. The three plots are for the (a) pressure experiments with a N_2 pinch and Ar buffer gas, the (b) buffer gas experiments with N_2 pinch gas and varying buffer gas at 2 mTorr, and the (c) pinch gas experiments with Ar buffer gas at 3 mTorr. Error for Te~6% and n_e~12%.

5.2.1 EUV core plasma expansion

The measurements presented in this first totality of section 5.2 will be explored in more depth in the appropriate sections to follow, but the results will be presented here to explain the deduction process that led to the determination that each of the three secondary plasmas all originate from the expansion of the EUV emitting plasma. The first step in this deduction process requires a look at the last plasma to reach the triple probes. In nearly every trial, the peak electron density of

this plasma expansion fell into the 1-3x10^{13} cm^{-3}. Because the free expansion of the plasma proceeds isotropically, it is possible to back calculate from the measured plasma density to the density that would be observed during the peak compression when the electrodes are discharged to create EUV light emission. The Z-pinch plasma is known to have the cylindrical dimensions of 3mm length by 1mm radius. In order to calculate the change in density caused by expansion, assuming the ratio of pressure to electron temperature stays the same, one simply has to multiply by the ratio of the chamber volume at 0.36 m to the volume of the pinch plasma (a factor of 2x10^{7}). Since the electron densities are measured with peak values of approximately 2±0.6x10^{13}, this would suggest an EUV pinch plasma with a density on the order of $10^{20}cm^{-3}$. This is precisely within the orders of magnitude that are observed with EUV emitting plasmas (10^{19}-$10^{21}cm^{-3}$). If the calculation is extended to include the peak contributions from the first and second plasmas (~$10^{14}cm^{-3}$), we see that the entire plasma observed with the triple probes back calculates to measured plasma on the order of $10^{21}cm^{-3}$, again on the order expected for an EUV emitting plasma. This result immediately suggests that the majority of the plasma measured with the triple probes originates from the EUV plasma expansion, though calculations of photoionization, ion-impaction ionization, and photon-wall electron liberation further enhance this hypothesis.

5.2.2 Photoionization contribution

The calculation of the contribution of photoionization processes proceeds with several assumptions: 75% of all energy put into creating the EUV plasma goes

into the production of light from 5 eV (250 nm) to 50 eV (25nm), 1% goes into the production of light from 50 eV (25 nm) to 125 eV (10 nm), there is a uniform emission spectrum across each of these ranges, and the absorption of photons across the distance of the chamber is negligible [62]. The last assumption is sufficient given the estimation of <0.1% absorption per meter of travel in sub-22 mTorr pressures of Ar, He, and Ne by the NIST X-ray Transmission model [85]. Knowing that 5 J goes into each pulse, 3.75 J goes into the DUV/VUV photons, while 0.05 J goes into the generation of EUV photons. The photon flux for each of these components can be found by integrating the constant photons/pulse across the respective energy ranges. The resulting photon flux for each of the different pinch gases is given in table 5.1.

Table 5.1: The estimated photon flux contributions for each pinch gas at 0.36 m are shown.

Pinch Gas	Energy CE to Ions/Neutrals [%]	VUV Contribution (0.36 m) [photons/cm^2-pulse]	EUV Contribution (0.36 m) [photons/cm^2-pulse]
He	13.05	4.37E+12	7.06E+10
Ne	3.40	5.05E+12	7.06E+10
N_2	38.06	2.61E+12	7.06E+10
Ar	6.33	4.85E+12	7.06E+10

To determine the produced electron density, due to photoionization, the following expression is utilized: $R=I\sigma\rho$, where R [e/cm^3-pulse], I [photons/cm^2-pulse] is the photon flux just quantified, σ [cm^2] is the reaction cross section, and ρ [cm^{-3}] is the gas density of the targets being ionized. The values of σ for this reaction are plotted in figure 5.3 from [86].

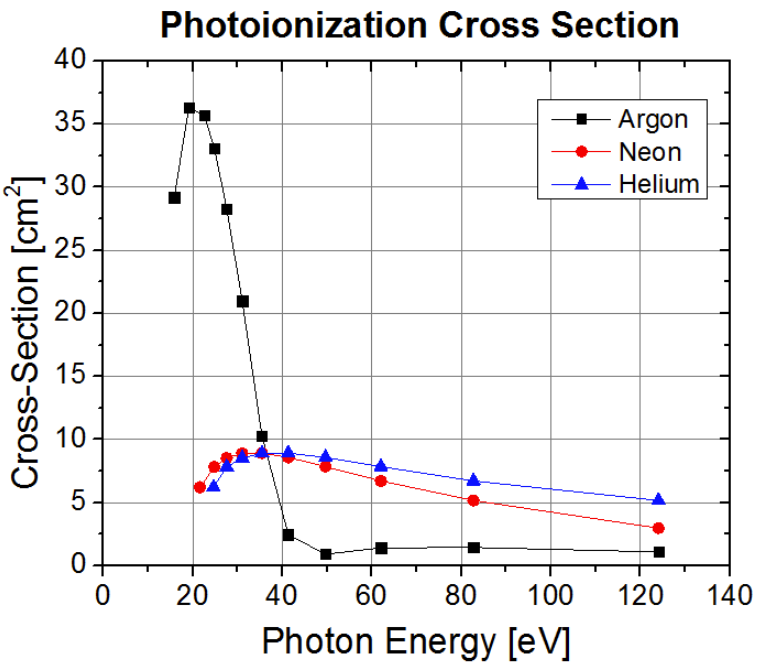

Figure 5.3: The photoionization of neutral He, Ne, and Ar gas atoms are shown as a function of photon energy in the range from threshold values to 125 eV. Data values taken from [86].

The values of photon flux, at each energy, were multiplied by the cross section and the neutral gas density, which was derived using the ideal gas law at room temperature, and then integrated to get a measure of the electron density at 0.36 m caused by photon flux. The resulting values shown in table 5.2 reveal electron densities on the order of less than $10^{11}cm^{-3}$, which is approximately two orders of magnitude less than what was observed. At 22 mTorr, using Ar buffer gas and N_2 pinch gas, the total contribution comes to an order of magnitude less than what was measured, suggesting that further increases in pressure may result in the dominance of plasma generation by photoionization. In general, however, the small contributions to electron density rule photoionization out as the major contributor to the measured electron density in the first plasma observed (the speed of light restricts these plasma contributions to only the fastest observed plasma).

Table 5.2: The contribution to electron density by photoionization is shown. These densities are several orders of magnitude less than the density observed with the triple probes, suggesting photoionization is not the predominant cause of the observed plasma.

Pressure [mTorr]	e/cm^3 @0.36 m	Buffer Gas Mass [AMU]	e/cm^3 @0.36 m	Pinch Gas Mass [AMU]	e/cm^3 @0.36 m
0.3	3.13E+10	4	1.00E+10	4	2.62E+11
2	1.04E+11	20	5.01E+10	20	3.02E+11
6	3.00E+11	40	1.04E+11	40	2.90E+11
12	6.00E+11				
22	1.15E+12				

5.2.3 Ion impact ionization contribution

The flux of ions or neutrals with sufficient energy can result in the ionization of a neutral gas atom. It was originally believed that the second observed plasma, which corresponds to the predicted arrival time of the high-energy ions and neutrals, could possibly be caused by these high-energy species impacting the stagnant neutral gas species. Using the same methodology from section 5.2.3, where reaction rate R is defined using the factors of ion flux, ion-impact ionization cross-section, and neutral gas density. The values of ion/neutral flux were taken from the measurements shown in chapter 4, with no buffer gas present in the chamber. Obviously this represents a higher number than would actually be observed inside of the inner collector optic, especially with pressures up to 22 mTorr, since gas scattering would decrease the flux reaching the middle of the chamber, nevertheless these values are presented in table 5.3 for reference.

Table 5.3: The flux measurements of ions and neutrals at 0.36 m are presented with relative error values of ±0.96%

Pinch Gas	Total Flux at 0.36 m [cm^{-2}]	Ion Flux at 0.36 m [cm^{-2}]	Neutral Flux at 0.36 m [cm^{-2}]
He	1.23E+10	9.23E+09	3.07E+09
Ne	1.38E+09	7.87E+08	5.93E+09
N_2	9.67E+09	7.95E+09	1.72E+09
Ar	8.34E+08	6.23E+08	2.11E+08

Unfortunately, there is very little experimental or theoretical data available for the impact ionization cross-sections from 0.1 to 50 keV. There was only one resource discovered, that even remotely covered the required reaction cross sections, which showed an average cross section of $3x10^{-16}$ cm^2 for an $Ar\text{-}Ar^+$ reaction from 0.1 to 100 keV [87]. It is assumed that all atom-ion interactions in this experimental regime behave the same way, and so the same cross section was used for each measurement. The resulting electron density contribution due to ion-neutral/neutral-neutral impact ionization are shown in table 5.4

Table 5.4: The contribution to electron density by ion/neutral impact ionization is shown. These densities are several orders of magnitude less than the density observed with the triple probes, suggesting photoionization is not the predominant cause of the observed plasma.

Pressure [mTorr]	e/cm^3 @0.36 m	Buffer Gas Mass [AMU]	e/cm^3 @0.36 m	Pinch Gas Mass [AMU]	e/cm^3 @0.36 m
0.3	5.72E+07	4	1.91E+08	4	3.65E+08
2	1.91E+08	20	1.91E+08	20	4.09E+07
6	5.72E+08	40	1.91E+08	40	2.47E+07
12	1.14E+09				
22	2.10E+09				

While it was originally hypothesized that the energetic ions caused ionization of the neutral gas, which resulted in the second plasma being formed, the contribution total electron density by ion/neutral-atom impact ionization is negligible. The small amount of incident ion/neutral flux, coupled with the relatively small 10^{-16} cm^2 cross-section of interaction, simply does not produce

enough electrons to develop a plasma with the density observed in the second plasma.

5.2.4 Photoelectric contribution

A third source of possible electrons comes from the photoelectric effect. In this process, a photon with sufficient energy to overcome the work function of a material surface (typically on the order of 4 eV for metals) has the possibility of exciting the electron out of the material. Given the large energies of the EUV and VUV photons, it was originally hypothesized that this process could be a significant contributor to the electron density. The first step in this calculation involved the calculation of total photons incident on the inner collector optic (again, only focusing on this location for its least perturbed path from the EUV emitting plasma). To perform this calculation, the difference in solid angle reaching the front of the inner collector optic shell and the back of the inner collector optic shell was divided by the solid angle of a sphere. This provides a measurement ratio of the total number of photons that are incident on the inner collector optic surface to the total number of photons generated. In total this accounts for only ~0.11% of total photons reaching the inner surface of the inner collector optic.

The ability for a photon to remove an electron from the surface largely depends on its energy, and its penetration depth into the surface. Photons with high depth penetration will still create electron-hole pairs deep in the surface, but the electrons will undergo many energy robbing collisions that make them unable to overcome the surface potential if they reach it. The quantitative measurement of

importance in such a reaction is the electron yield, which defines the average number of electrons ejected by at photon at a given energy. Unfortunately, once again, there is nearly no electron yield information to adequately calculate the actual contribution – carrying out the calculation, however, reveals that this is of little consequence. The average total photon generation in 4π sr for each of the pinch gases comes out to be on the order of 10^{17} photons. Out of this number, only 10^{14} reach the inner collector optic. If n electrons are created per photon, a density of $nx10^{14}/\pi x6.4^2x15$ cm^3, or $\sim nx5x10^{10}$ e/cm^3 are generated. If n were a value of 10^3, this phenomena would be a relevant contributing factor to the plasma density throughout the chamber in the first few microseconds. Unfortunately, typical values of n for different materials actually only on the order of 10^{-1} to 10^{-3} [88, 89]. Clearly, this makes the photoelectric effect the least plausible process for generating a secondary plasma.

5.2.5 EUV expansion contribution

The predominant electron-atom interactions are ionization and scattering. Recombination is minimized at these pressures, due to the requirement of a three-body collision to conserve energy and momentum. Since the previously described processes do not generate enough electrons, with enough energy, to cause multiple ionizations (generally speaking an ionization event robs the initial electron of at least the ionization potential of the neutral species, meaning that an electron under these experimental conditions is unlikely to cause more than one ionization event), it is unlikely that they contribute significantly to the observed densities. As such,

the only possible explanation for the presence of the three different plasmas is that they originate from the EUV plasma expansion. With very little removal of the electrons through ionization and scattering processes, it should be possible to back calculate the electron densities from the current measurements using the Faraday cup in the Sniffed detector.

Figure 5.4 shows a representative Faraday cup measurement at the intermediate focus. Highlighted are two different electron fluxes, the ion flux, as well as a bulk plasma measurement. If the travel speed of the electrons is assumed to remain constant from plasma to intermediate focus (in reality this isn't the case, but for the purpose of this calculation the estimate serves to just isolate the electron flux contributions of the first and second plasma expansions), then it is evident that the first electron flux measured is a result of the fast electrons and the first plasma, while the second electron flux corresponds to the energy retarded electrons that are restrained by the propagation of the energetic ions.

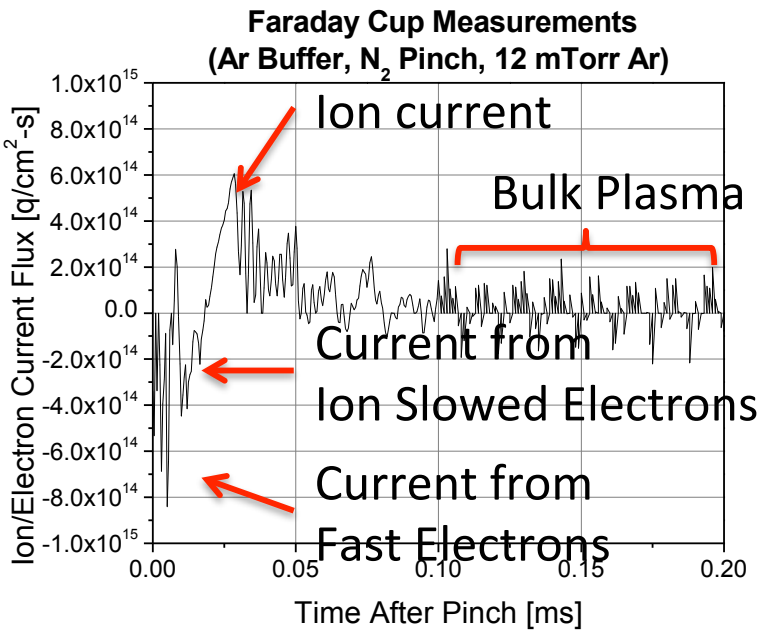

Figure 5.4: Shown is a representative Faraday cup current flux measurement at the intermediate focus. The measurement of four predominant fluxes is labeled. The initial electron current corresponds to the fast electrons leaving the EUV plasma, decoupled from the fast ions, which propagate at much slower velocities due to reduced mobility. The electrons that do not completely escape the imposed electric field of the fast ions arrive ~ 10-20 μs later. This flux is followed by the arrival of the energetic ions, which in turn is followed by the flux of the bulk plasma.

If the two individual electron currents are integrated over time, the resulting electron flux can be used to back calculate the number of electrons present inside of the inner collector optic. Because the intermediate focus is twice the distance from the pinch as the triple probe is, then the flux measured at the triple probe should arrive twice as fast. The first electron current, from figure 5.4, arrives in the time period of 1-10 μs, and the second electron current arrives roughly from 10-25 μs after the pinch initiation. Halving these times corresponds nearly exactly to the time during which the first and second plasmas arrive at the 0.36 m point. If it is assumed that the sum of the electron flux in these regions corresponds to the electrons present at the midway point in the chamber during the triple probe

measurements, it is possible to determine the electron density as caused by these measured electrons.

The resulting electron densities, taking into consideration the partial contribution of the measured flux to the total flux at the intermediate focus (remember we're only measuring through a 2 mm orifice located on the 10 cm projection of the intermediate focus due to the depth of the detectors within SNIFFED), and then multiplying by the surface are of the intermediate focus orifice, coupled with ratio of total species reaching the inner collector versus total created, are turn out to be those shown in table 5.4 and 5.5. These two tables show the back calculated electron density, due to the expansion of the plasma to the intermediate focus, as it would be observed where the inner collector is located for the first plasma and second plasma respectively.

Table 5.5: Shown are the electron densities back calculated from the flux measured using the Faraday cup located inside of the SNIFFED apparatus. These measurements represent the electron density that would be attributable to these electrons if they were located at the halfway point of the chamber. These are on the order of the measurements observed with the triple probes.

Pressure [mTorr]	e/cm^3 @0.36 m	Buffer Gas Mass [AMU]	e/cm^3 @0.36 m	Pinch Gas Mass [AMU]	e/cm^3 @0.36 m
0.3	6.42E+13	4	3.61E+13	4	6.55E+13
2	7.46E+12	20	4.39E+13	20	3.49E+13
6	1.94E+12	40	7.46E+12	40	3.54E+13
12	1.75E+13				
22	3.30E+13				

These measured values are within an order of magnitude difference (slightly lower due to the loss in electrons by scattering to the walls) from those measured with the triple probes. The significance of this, coupled with the fact that other predominant interactions do not significantly contribute to the total electron

density, is that these electrons must have originated from the EUV plasma. The decoupling of the fast electrons found in the first plasma is evident as the current flux drops to 0 between the two electron fluxes diagrammed in figure 5.4. A second drop to 0 also occurs, which will be significant in the next few sections as there are observed disappearances of plasma without sufficient chamber pressure. Ultimately, however, these analyses served to push the fact that despite initial hypotheses, the three measured plasmas originate from the three different components emanating from the relaxation of the EUV emitting plasma.

5.3 Pressure Effects

Buffer gas is commonly used as a principle player in energy dampening debris mitigation, which attempts to prevent the energetic EUV emitting plasma products from reaching collector optics. This technique is most effective when an energetic species has to undergo a large number of energy robbing collisions en route to the collector surface. The number of collisions is a function of the mean free path, which is a direct function of chamber pressure, as shown in equations 4.15-4.16 . For this first investigative analysis, a N_2 fueled EUV plasma (with the solid Sn electrode) was driven into an Ar buffer gas filled chamber at 0.3,2,6,12, and 22 mTorr at a rate of 20 Hz. For theoretical purposes, the energetic ion and neutral emission spectra was gathered (recall figure 4.4) at 0.3 mTorr to estimate the characteristics of the species traveling from the plasma to the intermediate focus. The primary components of the ejected energetic debris were found to be the electrode materials (Sn, Cu, Mo) and gaseous chamber contaminants incorporated

into the EUV plasma (O_2, C, Ar). As mentioned previously, these species are emitted from the cylindrical cathode with a cosine distribution and energies up to 50 keV.

5.3.1 Expanding EUV plasma components analysis

As mentioned previously, the EUV plasma expands into the chamber with three different plasma regions: one originating from the high energy electrons that are decoupled from the EUV plasma core, one originating from the high energy electrons that are slowed down by the presence of slower high energy ions, and lastly the plasma formed by the interaction between the expanding bulk of the EUV emitting plasma's interaction with the energized buffer gas. As shown in figures 5.5-5.8, the high energy electron plasma arrives very soon after initiation of the EUV plasma pinch. An unimpeded 30 eV electron would travel the length from the pinch to the intermediate focus in 220 ns, so it is not shocking that the arrival of the electrons occurs in less than 1 μ. There is an initial increase in density and electron temperature with the arrival of the bulk of these electrons. The plasma is observable at all locations within the chamber that have line of sight to the plasma origin. Occluded locations observed the plasma with a slight delay, due to transit time, in arrival as the plasma expands and the electrons scatter outwards to the walls. Like the high energy ions, high energy electrons will generally be forward peaked. Given the axial geometry of the discharge, and the pinch instabilities that create high inductive zones, most of the lower energy electrons have a wider emittance angle due to scattering (thus their lower energy) in the highly dense plasma as it expands.

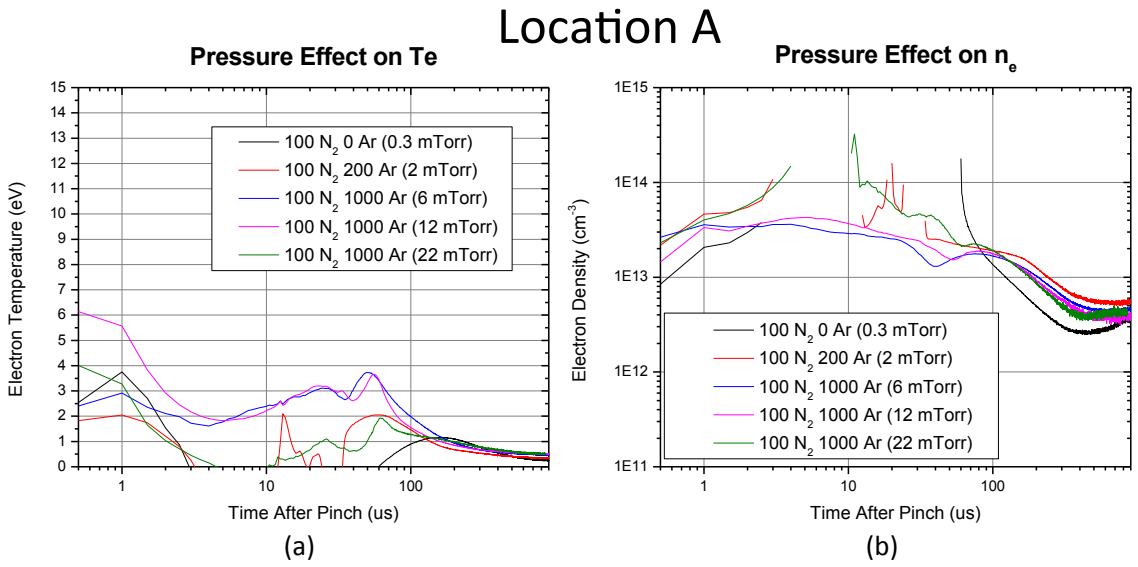

Figure 5.5: Shown are the electron temperature (a) and the electron density (b) inside of the inner most shell during the first millisecond after EUV emitting plasma formation. Three plasmas are observable: Fast electron driven (0-3μs), energetic ion and coupled electron driven (3-30μs), and bulk EUV plasma expansion (30-1000μs). Between 6 and 12 mTorr, the neutral density is optimal to sustain plasma throughout the duration between pinches. Above this pressure and neutral-electron collisions stifle plasma sustainment, while below this pressure there is not enough neutral density to sustain the plasma. The sharp peaks in electron density that occur when Te disappears are simply mathematical errors formed as a result of the use of Te in the quotient for determining electron density. Error is approximately ±12% for n_e and ±6% for Te. Location is 0.3 m into the chamber.

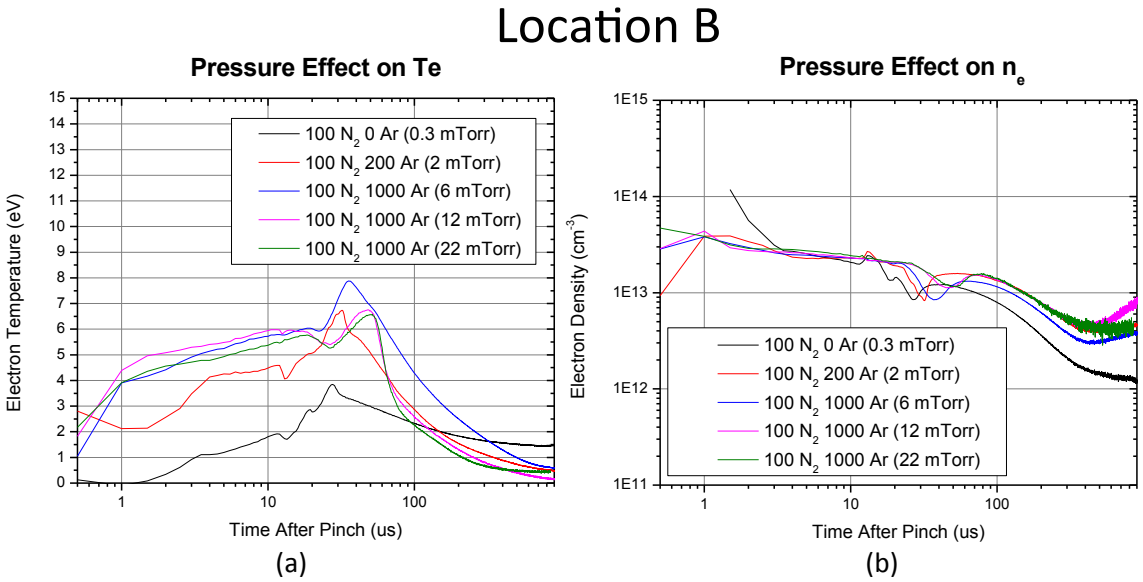

Figure 5.6: Shown are the electron temperature (a) and the electron density (b) inside of the inner most shell during the first millisecond after EUV emitting plasma formation. Three plasmas are observable: Fast electron driven (0-3μs), energetic ion and coupled electron driven (3-30μs), and

bulk EUV plasma expansion (30-1000μs). The three plasmas are sustained throughout this period due to the unobscured path from the plasma source and the increased scattering at the wider angle. This results in less of an abrupt fall off in electron density between the two plasma arrivals. Electron temperature increases with chamber pressure, but density remains the same except for the lowest pressure expansion of the bulk EUV emitting plasma. The sharp peaks in electron density that occur when Te disappears are simply mathematical errors formed as a result of the use of Te in the quotient for determining electron density. Error is approximately ±12% for n_e and ±6% for Te. Location is 0.36 m into the chamber.

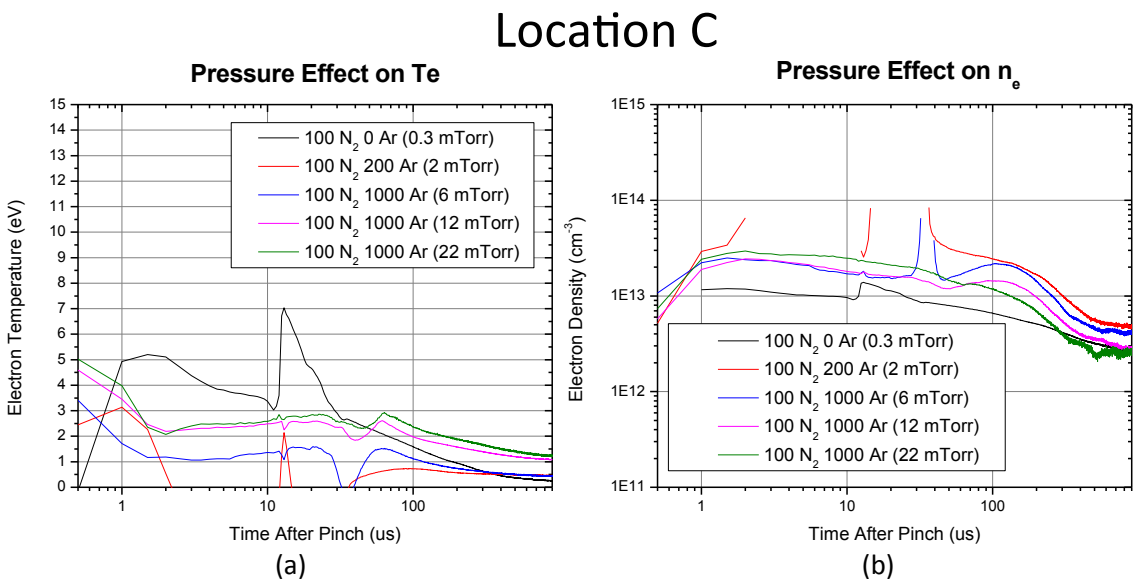

Figure 5.7: Shown are the electron temperature (a) and the electron density (b) inside of the inner most shell during the first millisecond after EUV emitting plasma formation. Three plasmas are observable: Fast electron driven (0-3μs), energetic ion and coupled electron driven (3-30μs), and bulk EUV plasma expansion (30-1000μs). Because of the obscured path between the source and the probe, at low pressures each plasma dissipates to the walls before the next plasma arrives. Above 2 mTorr, further increases in pressure increase electron temperature as well as density. The sharp peaks in electron density that occur when Te disappears are simply mathematical errors formed as a result of the use of Te in the quotient for determining electron density. Error is approximately ±12% for n_e and ±6% for Te. Location is 0.36 m into the chamber.

In general, for the high energy electron driven plasma, the electron temperature and density increase with increasing pressure above 2 mTorr at location A. The initial increase in plasma temperature is a result of the slight increase in scattering of the high energy species towards the center of the chamber (remember that any species reaching the inner collector optic has to go around the brackets as well). The electron temperatures are highest inside of the inner collector optic because the least amount of scattering is required since most of the

highest energy electrons are forward peaked. As radial distance is increased from the centerline, more collisions are required to reach that location, and consequently the electron temperature decreases at location C. A peak electron temperature is observed at location A with 12 mTorr at 6±1 eV, at location B with 2 mTorr at 3±0.5 eV, and at location C with 6 mTorr at 5±1 eV. Densities are in the range of $1\pm0.3x10^{13}$ and $3\pm1x10^{13}$ cm^{-3}, though the lowest electron densities are observed at location C (an obscured view to the pinch), where the plasma must expand from areas of irradiation to the where the probe resides. Consequently, electrons can lost to the walls before reaching the probe. The density increase with pressure is readily explained by the decrease in number of species lost to the walls because of the increased scattering collisions required to reach the walls. The electron temperature of the photon-driven plasma generally peaks at 12 mTorr. It should be noted that increasing pressure in the chamber increases the confinement efficiency (can drive more current through more ionized species) and can consequently create a denser warmer plasma In general, there is a small decrease in electron density from the center of the chamber to the outside of the chamber (position A->C) due to the increased radial distance from the plasma source and the resulting r^{-2} drop off in photon flux. The perpetual plasma presence at position B is due to the fact that this location has the largest visibility to the plasma source, and consequently more electrons (despite being forward peaked) can reach this location. Location A is largely occluded by the joining of the brackets and location C has no line of sight to the plasma origin. Because of the increased collisions in going from location A to C, scattering has a larger effect and plasma is present throughout the production of the

three separate plasmas, but the lack of ionized species near locations A and C allows the plasma to quickly diffuse to the walls until the next plasma arrives.

The second observed plasma begins to arrive nearly 3 μs after the end of EUV emitting plasma formation, when the confinement is sufficiently relaxed to eject energetic ions and electrons. As mentioned previously, this plasma is a result of the emitted high energy electrons "dragging" on some of the high energy electrons. To give an idea of energy-time relations, 3 μs corresponds to the arrival time of 1keV nitrogen ions. As with the high energy electron generated plasma, it is generally observed that the plasma density increases with pressure at locations A and C, with a general density falling between $2\pm0.6 \times 10^{13}$ and $10\pm3 \times 10^{13}$ cm^{-3}. *The spikes in the electron density are a mathematical error that arises when the electron temperature sharply declines as the electron flux dissipates (recall how the Faraday cup current fell to 0)*. Once again, for positions A and C, the plasma is only persistently observed for the 6 mTorr and 12 mTorr cases. Electron temperatures are highest at 12 mTorr with a $T_e \approx 3\pm0.5$ eV at position A, 6±1 eV at position B. A large electron temperature of 7±1 eV is observed at 0.3 mTorr at position C, though this appears to be an outlier as the other values peak once again with 12 mTorr at 2.5±0.3 eV. At position B, the electron induced plasma serves to increase the chamber plasma density, and furthermore the electron temperature is increased. At this location, there are two walls near the probe that could result in an increase in plasma temperature as the electron temperature increases to account for an increase in loss to the walls. This is not as present at location A because of the occlusion by of the pinch by the brackets.

The last observed plasma occurs as a result of the expansion of the energetic EUV emitting plasma. The bulk of the once 30 eV, 10^{20} cm^{-3} plasma expands and begins to incorporate buffer gas species. The energy of the electrons (those not ejected early on) is considerably less than 30 eV after the collisions that occur at the peak of EUV photon emission. The energetic ions and neutrals scatter off of the buffer gas providing energy to the buffer gas species. As such, the important species for determining electron density is the buffer gas species, and the important parameters for plasma propagation are the mass of the buffer gas, the chamber pressure, and the energy deposition during scattering. As a result, the increase in pressure results in the front of the plasma arriving time of 60±5 μs, 35±5 μs, 35±5 μs, 40±5 μs, and 50±5 μs for 0.3, 2, 6, 12, and 22 mTorr respectively at location A. This is counterintuitive to typical plasma expansion, where diffusion times increases linearly with pressure through ambipolar diffusion. The more traditional expansion is experienced at locations B and C, however, thus illuminating the effect of buffer gas-energetic atom interactions. The ejection of the most energetic species coming out of an EUV emitting plasma are forward peaked due to the electric fields established as well as the lack of scattering involved. This results in an increase in energy in a cone directed at the intermediate focus, and consequently there is a reduction in arrival time for the centermost part of the plasma when pressure's energy abosrbtion and collision increases are optimized (~2-6 mTorr). The densities of each condition are nearly the same in the range from 3±1 to 6±2x$10^{12}$$cm^{-3}$. This plasma is cooler than the other two and has a peak energy of

4±1 eV at 12 mTorr for location A, 8±1.5 eV at 6 mTorr for location B, and 3±0.5 eV at 22 mTorr.

5.3.2 Charged flux analysis

The consequence of the development of these secondary plasmas within the chamber is apparent in two different forms, contamination transport and charging of post-intermediate focus optics. The latter is of concern due to the fact that charging of a surface can result in sputtering or undesired current flow. This additional current flow can heat the mirror nearest the intermediate focus, causing inter-layer diffusion – not an ideal scenario for multilayer features. For these experiments, the current reaching the intermediate focus was measured using a ±100V bias capable Faraday cup. Shown in figure 5.8a-e are the positive and negative components of the flux with the noise signal removed. Both electron fluxes are visible for each of the species (see figure 5.4 for a representative diagram). At the lowest pressures, 0.3 to 6 mTorr, there is very little measured positive flux in the first 100 μs due to the fact that most of the energetic ions lose their charge to the walls, since gas scattering collisions are considerably rare at these pressures. An increase in pressure up to 12 mTorr shows a more present positive flux as gas scattering allows energetic ions to reach the intermediate focus without undergoing a wall collision. It is also possible for energetic neutrals to undergo charge exchange with the electrons liberated by the photon-initiated plasma. After 100 μs the arrival of the EUV core plasma becomes evident, and additional increases in pressure only

serve to increase the density of this plasma as more species are accumulated into the plasma.

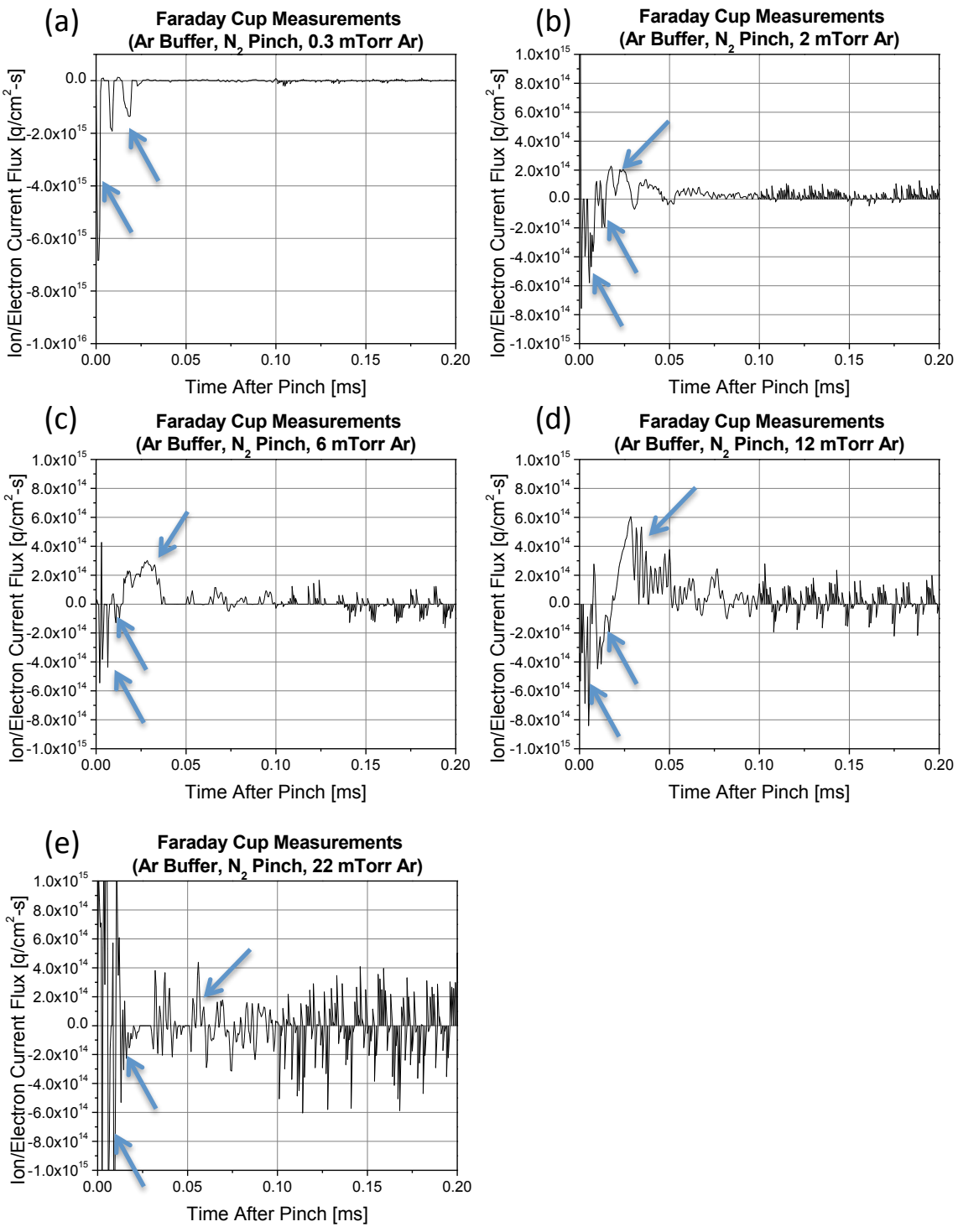

Figure 5.8: Figures a-e show the Faraday cup measurements at each of the pressures used in these experiments with a nitrogen pinch and argon buffer gas. The signals were averaged over 256 trials with a positive 100 V and negative 100 V bias applied to remove noise. The resulting signals of each of these biases were stitched together to proved the presented data. At too low of pressure, no energetic ions reach the intermediate focus. At higher pressures, however, energetic ions can

be scattered off of gas without losing charge to the optic surfaces. After 100 μs, plasma is measured at all locations, with increasing pressure leading to increased combined current. Location is at 0.72m. The locations of the fast electron, ion-coupled electron, and ion flux components are indicated from left to right. The electron presence is slightly unclear as the pinch was not very stable and resulted in multiple pinches. Error is approximately ±31%.

If one sums up the current across the entire initial 200 μs, an interesting phenomena is observed. As shown in figure 5.9, the combined positive and negative flux does not largely vary, with an average total flux of $-0.25\pm0.1\text{x}10^{11}$ e-cm^{-2} for all pressures. An increase in pressure from 0.3 to 2 mTorr increases the measured flux from $-0.5\pm0.2\text{x}10^{11}$ e-cm^{-2} to $0.1\pm0.03\text{x}10^{11}$ e-cm^{-2}. The increased gas pressure scatters the energetic ions from the pinch to the intermediate focus before they can scatter off a wall (possibly depositing or losing charge). What is interesting, however, is the fact that as pressure increases, the magnitudes of total positive and negative flux increases. This is a consequence of the increased plasma density that accompanies the increase in neutral gas pressure. It will be shown shortly that this results in net erosion of the Sn coated quartz crystal located inside of SNIFFED at the intermediate focus for pressures above 6 mTorr.

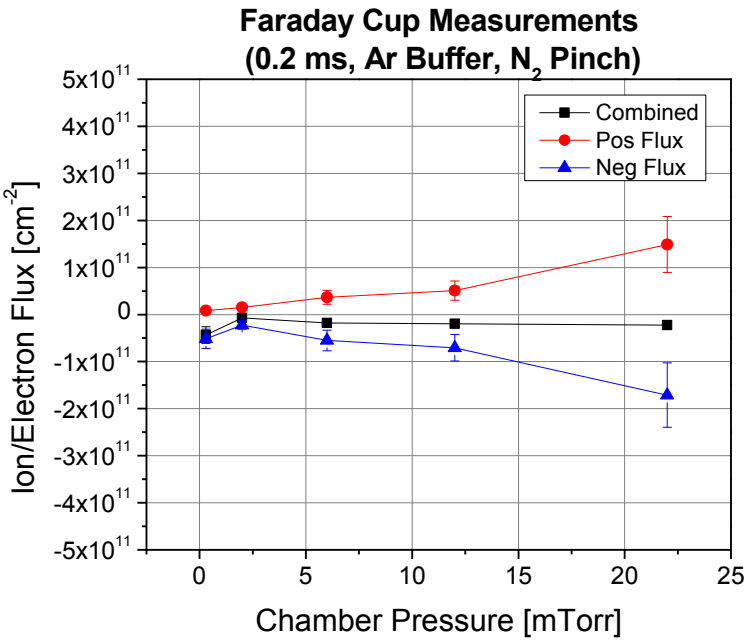

Figure 5.9: As pressure increases, outside of the decrease in negative current observed from 0.3 to 2 mTorr, the combined charged flux is relatively constant as pressure increases. There is an increase in the total amount of positive and negative charge, however. The increased flux creates an increased ion flux to the surface, leading to increased erosion. Location is at 0.72 m Error bars not visible should be assumed to be the size of the marker.

5.3.3 Deposition analysis

Using the quartz crystal microbalance located in the SNIFFED apparatus, it is possible to ascertain the effects of the charged flux reaching the surface of the intermediate focus. As shown in figure 5.10, below 12 mTorr there is an observed net deposition onto the Sn coated Au crystal. This deposition will be shown to consist primarily of C and O, with minor contribution from the electrode materials Sn, Cu, and Mo. Referring back to figure 5.9, this net positive deposition corresponds to the pressures with least plasma density. Conceptually, it would be thought that increasing pressure should increase the amount of deposition at the intermediate focus, since more C and O would be liberated from the walls and introduced into the chamber atmosphere. What occurs however is the increased

sputtering of the surface, due to more ions as well as more scattering of energetic pinch species, that overcomes the deposition rate of C and O. This, coupled with the suppression of electrode materials, increases the amount of etching at the surfaces facing the intermediate focus. After 2 mTorr, the increase in etching overcomes the increase in deposition, and as a result there is less observed deposition. There will be some discrepancy between these results and those observed with the Si witness plates because of the Sn coating used on the crystal. Carbon is well known to be an excellent gaseous component for removing C (and vice-versa) from Sn, and as such, there is a chemical reaction occurring at higher pressures, where much of the C and O film are removed and further sputtering removes deeper layers than will be observed with a Si witness plate [90]. As such, the Si witness plates will provide a clearer understanding of the effects of pressure on intermediate focus facing optical components.

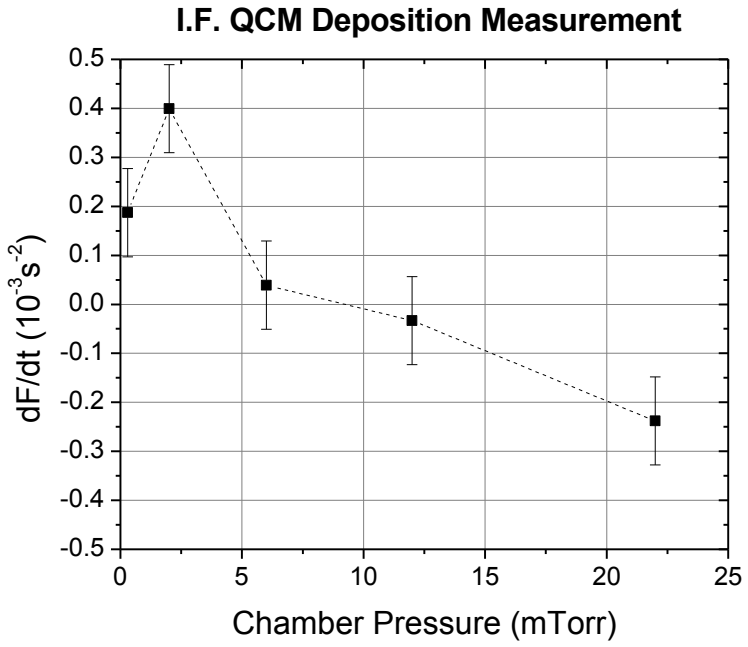

Figure 5.10: The flux reaching the intermediate focus initially causes a net deposition from 0.3-6 mTorr. Beyond this point, the plasma flux reaching the intermediate focus has more energy and a larger sheath barrier due to an increase in electron flux. This results in a net erosion of intermediate focus facing components. Location is at 0.72 m.

Having observed the effects of the plasma transport on the intermediate focus, it is prudent to know what species and how much of each species is deposited there. The sets of Si witness plates located on each collector shell, and at the intermediate focus (shown again in fig. 5.12), help to provide a quantitative analysis of the relative and total amounts of different species deposited at each location. X-ray photoelectron spectroscopy (XPS) was used to analyze every sample located at the intermediate focus, as well as a complete analysis of the 2 mTorr Ar buffer gas case. The relative composition of the films formed at the intermediate focus is plotted in figure 5.11 as a function of pressure. It is immediately apparent that carbon and oxygen contamination are a large concern (carbon and oxide films readily absorbs EUV light). As mentioned previously, the carbon originates from the

walls of the chamber, which are frequently exposed to pump oil in atmosphere. As the pressure increases, and the density of the plasma increases, the resulting increase in flux of ions to the chamber walls liberates more pump oil and adsorbed water from the walls. This composition of O and C is known to be a consequence of exposure to the EUV plasma source because of the amount observed. An unexposed sample of Si will only develop a native oxide of approximately 10 Å with negligible amounts of C deposition. These samples were cleaned two times with isopropyl alcohol and acetone, a typical cleaning method, to remove any possible excessive contamination from atmosphere as well. The fact that greater than 90% of film composition consisted of the combination of C and O (>10 nm at many locations), suggests that the measurements observed are composed of less than 10% native oxide. The remaining film composition consists of the near-pinch metals Sn, Mo, and Cu, as well as trace amounts of F (from the use of Viton gaskets). The cathode is made out of Sn, and the anode is made out of Cu. With ongoing ablation between each gaseous discharge, Mo from the collimated foil trap is released and introduced into the pinch, thus it will be observed in smaller proportions than the other two materials. As gas pressure is increased, these materials are suppressed, with near complete suppression occurring at 22 mTorr where less than 0.12% of the film was composed of the electrode materials. The cause of this is obviously due to increased buffer gas collisions that prevent the electrode material from reaching the intermediate focus.

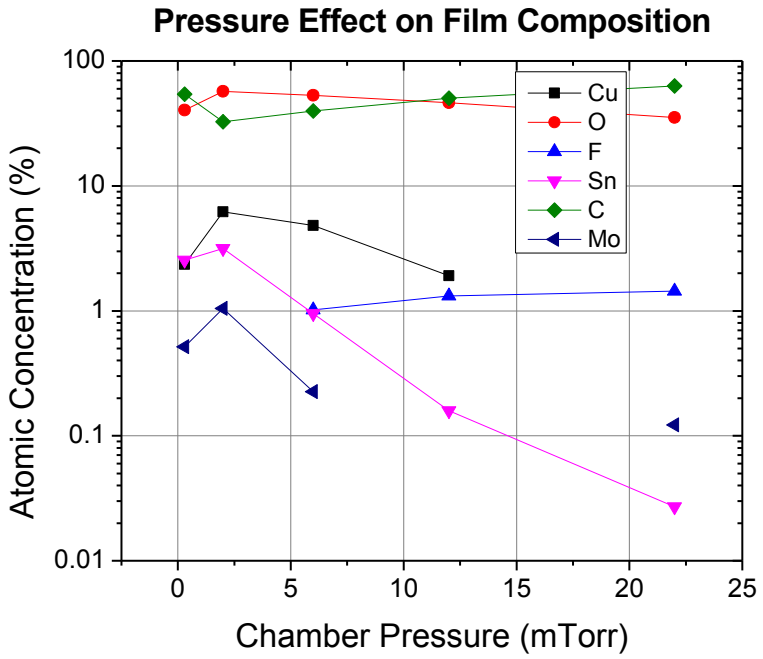

Figure 5.11: A plot of the relative concentrations of the various components in the film deposited at the intermediate focus. The predominant species are oxygen and carbon. The carbon comes as a consequence of the secondary plasmas liberating and ionizing carbon contamination from the walls. The oxide is a result of oxygen present in the chamber as well as exposure to oxygen during sample transport. The remaining material composition consisted of molybdenum, copper, and tin – each an element used in the construction of the electrodes. Sample location is at 0.72 m. Measurement error is less than 5% for any data point.

A complete atomic percent concentration analysis of the 2 mTorr Ar buffer gas condition was performed as well to give a representative contamination analysis throughout the chamber. Once again, as shown in figure 5.8, the predominant film consists of oxygen and carbon. The atomic concentration of Sn increases slightly with increasing distance along the inside of the inner collector shell, from 1.24% to 1.9%. The backside of this shell – where Sn predominately reaches after colliding off of the inside of the outer collector shell - shows a high relative concentration of Sn at 5.9%. Cu and Mo show similar concentrations along the inner collector shell. While Sn increases from 2.6% to 2.9% along the inside of the outer shell, there is an observed drop in Cu from 1.9% to 1.5%, and an observed drop in Mo from 3.1% to

1.65%. Both of these species are lighter than Sn, and of closer mass to Ar, so they are better shielded and do not reach as far into the chamber as the energetic Sn atoms. Mo is nearly completely suppressed at the intermediate focus while Sn and Cu have concentrations of 3.15% and 6.19% respectively. It will be later verified that the anode (Cu) and the cathode (Sn) are in higher quantities at the intermediate focus than can be explained by simple atom transport, and this is due to the fact that arcing occurs between the two electrode. During source operation, visible sparks exist on both electrodes, caused by the non-uniform discharge of the electrical discharge through the plasma. The arc discharges produce micron-sized particulates, which increase deposition rates above those that would be caused by normal pinch operation. Obviously these are detrimental to the lifetime of the downfield components, and exist as a very large risk to tool implementation.

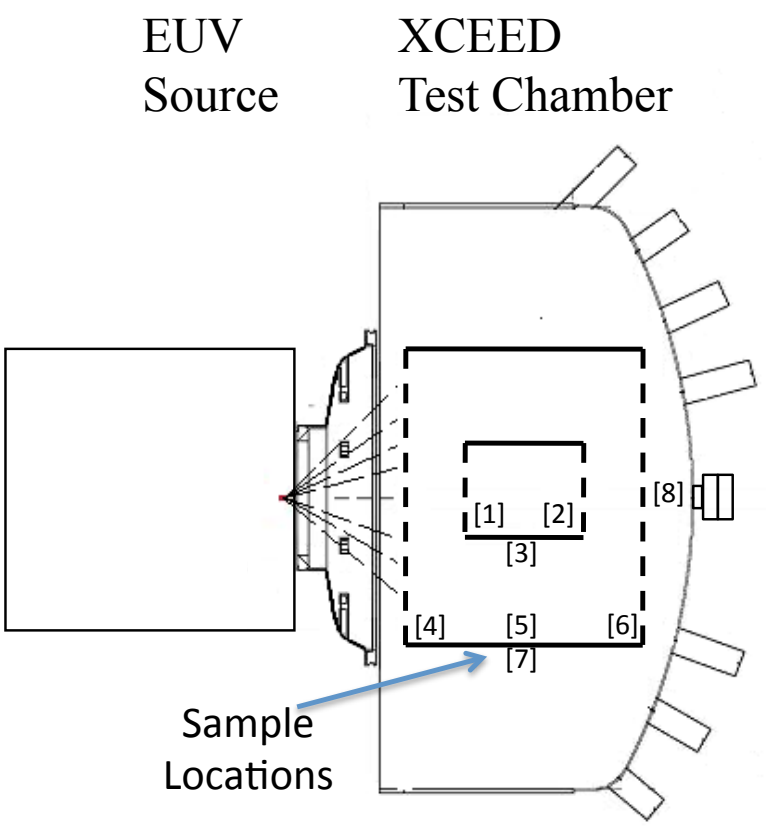

Figure 5.12: Shown are the locations of the Si witness plates within the chamber. Sample 8 corresponds to the intermediate focus at 0.72 m. Positions 1 and 2 are on the inside of the inner collector optic, positions 4,5, and 6 are on the inside of the outer collector optic. Positions 3 and 7 are on the outsides of the inner and outer collector optic respectively.

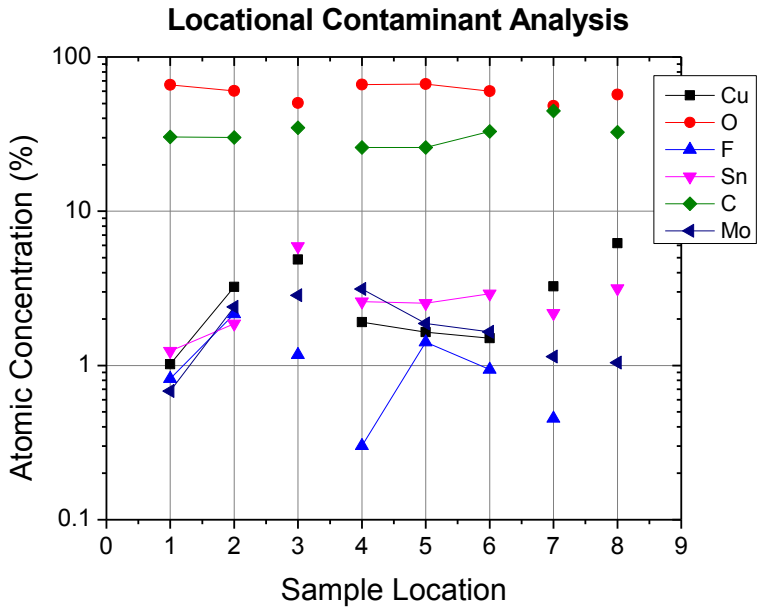

Figure 5.13: A locational film XPS composition analysis for each location inside of the EUV light source chamber is shown. Location 1 and 2 are on the inside of the inner collector, location 3 is on the outside of that shell, location 4-6 are on the inside of the outer collector, location 7 is on the outside of that collector, and lastly location 8 is at the intermediate focus location (refer to figure 5.12 for a visual diagram. There is a considerable amount of C and O contamination observed, as well as a presence of the electrode materials Sn, Cu, and Mo. Measurement error is less than 5% for any point.

It is possible to combine the relative proportions with the measured deposition amounts to calculate a more quantitative measurement of the total deposition rate of each species. As shown in figure 5.14, the amount of electrode material deposited onto the Si witness plates is actually very small. The peak net deposition occurred at 2 mTorr with a deposition rate of approximately $5\pm0.8\text{x}10^{-6}$ nm/pulse observed. The deposition rate of the electrode materials falls off exponentially with a linear increase in pressure, which is to be expected with the reduction in mean free path that accompanies an increase in pressure. Once again it is observed that the electrode materials only account for nearly one tenth of the total deposited film. As pressure is increased from 12 to 22 mTorr, the buffer gas

becomes more effective, and there is a two-order of magnitude drop off in total deposition rate from $3\pm1\text{x}10^{-5}$ nm/pulse to $2.3\pm46\text{x}10^{-7}$ nm/pulse (large error caused by surface roughness on the order of 10^{-6} nm/pulse). It is believed this is a consequence of both the suppression of energetic contaminants, as well as the etching or sputtering of the surface as measured by the quartz crystal microbalance. Because these samples were located inside of the XCEED chamber during the experiment, they are more widely exposed to the chamber's carbon contamination and consequently don't experience the net erosion observed with the quartz crystal microbalance.

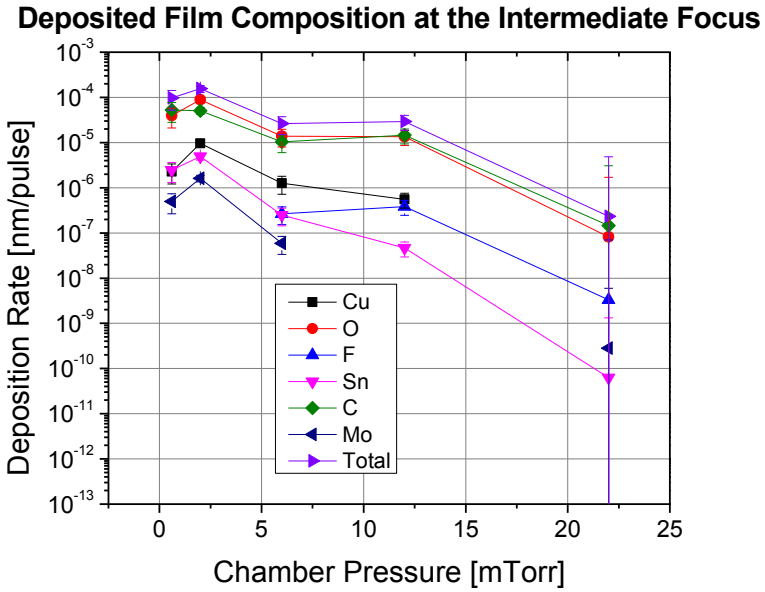

Figure 5.14: Shown are the effects of pressure on the deposition rate of the various species observed at the intermediate focus. While there is an increase in electrode material deposition from 0.3 to 2 mTorr, an exponential drop-off is observed with increasing pressure. This is due to the exponential decrease in survival time between collisions with a linear increase in pressure. With higher pressure, the energetic electrode species are more widely scattered. There is a net decrease in all deposited species at 22 mTorr due to the creation of the widely dispersed buffer gas plasma, which aids in the sputtering of surface contaminants off of the Si witness plates. Location is at 0.72 m. Error bars not observed should be assumed to be the size of the marker.

5.3.4 Theoretical versus experimental locational deposition analysis

If we isolate the Sn deposition amounts at the intermediate focus *(please note that these measurements are at the intermediate focus, as change in location would result in changes in deposition rate as a function of r^2)* for each pressure (fig. 5.15), we see that there is an initial 100% increase in deposition rate from $2.5\pm1.1\text{x}10^{-6}$ nm/pulse to $5\pm0.8\text{x}10^{-6}$ nm/pulse with an increase from 0.3 to 2 mTorr. The theoretical model estimates these values to be $3\pm2\text{x}10^{-7}$ nm/pulse and $1\pm2\text{x}10^{-6}$ nm/pulse respectively, representing an estimation error of 80% and 60% respectively. Increasing the pressure from 2 mTorr to 6 mTorr reduces the measured Sn deposition rate by 95% down to $2.5\pm1\text{x}10^{-7}$ nm/pulse, with the model predicting a deposition rate of $5.58\text{x}10^{-7}$ nm/pulse. Subsequent increases in pressure reduce the deposition rate to $4.6\pm1.5\text{x}10^{-8}$ nm/min and $6.3\pm125\text{x}10^{-11}$ nm/min (effectively no measured deposition) for 12 and 22 mTorr respectively. For a trial of 10000 test atoms, there were no observed Sn species reaching the intermediate focus. The increase in deposition rate at the intermediate focus in going from 0.6 mTorr to 2 mTorr is a result of the increased scattering that occurs at the higher pressure. At 0.6 mTorr, most of the Sn atoms readily reach the walls before undergoing gas collisions. Increasing the pressure to 2 mTorr scatters more species away from the walls, and consequently more electrode contaminants are capable of reaching the intermediate focus before being deposited onto a wall. Further increases in pressure actually suppress the transport of the Sn to the intermediate focus, causing the observed drop in deposition rate.

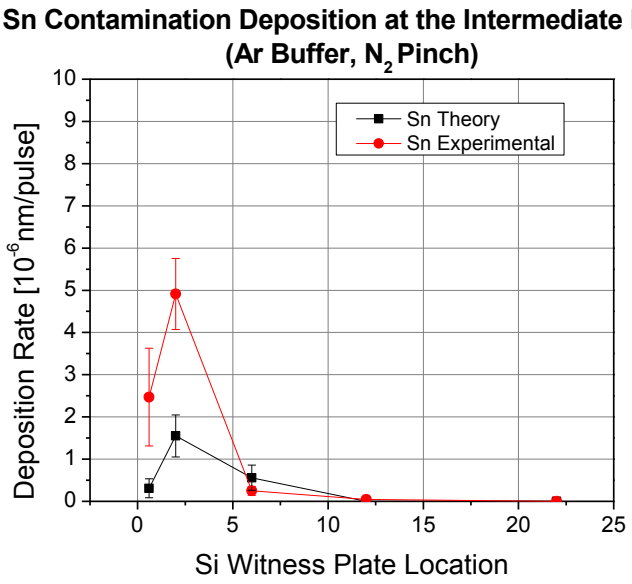

Figure 5.15: Shown is the experimental versus theoretical measurement of the deposition rate of Sn at the intermediate focus as a function of pressure. C is the calibration factor used for the measurements. Location is at 0.72 m.

The theoretical measurements are lower than the measured deposition rate by a difference of 2.1 nm/pulse and 3.35 nm/pulse for 0.3 mTorr and 2 mTorr respectively. At 6 mTorr, however, the theoretical deposition rate differs from experiment by and overestimate of only 0.31 nm/pulse. This suggests that something not modeled is occurring at the lower pressures, which doesn't occur at higher pressures. These offsets can be explained simply by considering electrode arcing, which produces micron sized particulates, and electrode sputtering, which produces sub 100 eV neutral electrode atoms that are not accounted for in the model since they are not measured by the energetic ion and neutral energy analyzers.

Electrode arcing is more prevalent at lower pressure operation conditions and higher buffer gas masses. The source operates best when there is sufficient gas

pressure to deposit the discharge current uniformly across the anode, and if the pressure is too low, current is driven more strongly at random locations around the electrode, and the ionized buffer gas serves to sputter the electrode surface. The produced micron-sized particles are not as influenced by the repelling force of atomic gas collisions at these low pressures, and consequently are able to make their way to the intermediate focus under the influence of gravity and wall reflection. This causes the deposition at the intermediate focus to be higher than anticipated using the debris transport model at these two low pressures.

To evaluate the contribution of electrode sputter, it is useful to calculate the amount of electrode erosion that would be required to produce the amount of Sn deposited around the chamber. For this calculation, the 2 mTorr experimental deposition rates are isolated. First, the total volume of Sn deposited inside of the chamber is calculated by multiplying the thickness of Sn deposition on each surface by the surface area onto which it was deposited. Assuming a density of 5.33 g/cm^3, this volume can be converted to calculate the total mass of Sn removed from the electrode and deposited on the various surfaces within the chamber ($1.41x10^{-8}$ g determined experimentally and $5.19x10^{-9}$ g determined theoretical). Since the only source of Sn is the electrode, it is possible to calculate the erosion rate of Sn from the surface of the electrode. The electrode surface has an area of 3.8 cm^2, and in order to produce a mass deposited around the chamber, a surface erosion rate of $7x10^{-3}$ nm/pulse and $2.8x10^{-3}$ nm/pulse are required. In more practical values, for all of the experiments performed, a total of $2.4x10^6$ pulses were performed, resulting in net erosion of 16.8 μm and 6.7 μm were removed.

If we account for the Sn removal caused by sputtering, which creates the low energy deposition flux not accounted for by the model, the cause for the discrepancy between theory and experiment is made clear. To determine the removal rate by sputtering, it is first required to calculate the ion flux to the surface of the electrode. If the EUV plasma is assumed to form formed 3 mm in front of the electrode, and only the contribution of oxygen ions and neutrals is considered (the most abundantly measured species from a N_2 pinch driven plasma), then a flux measurement of the total ions and neutrals hitting the electrode can be calculated. A fractional contribution of the total oxygen flux reaching the electrode is found to be 13.1%, when considering the solid angle subtended from the plasma to the electrode. That is to say that out of all of the oxygen ions/neutrals created only 13.1% reach the electrode's face from 3 mm away. The average energy of these oxygen species was found to be near 7.5 keV, and it are assumed to strike the surface at an average angle of 45^o (only considering the face, not the inner part of the electrode where most of the species would be ionized, accelerated in the pinch, and measureable by the ion energy analyzer or the neutral detector). A quick SRIM calculation, with these conditions, reveals a sputtering yield of 2.7 Sn atoms/O atom. These sputtered atoms are found to also have an average energy of only 73 eV, which nearly all but rules them out from traversing the chamber with enough energy to be measured by the energy detectors. If the total number of Sn atoms sputtered out of the electrode is calculated as a function of oxygen flux, a measured Sn removal rate from the electrode surface of $\sim 5.27 \times 10^{-2}$ nm/pulse is observed.

This would result in a total removal of ~33 μm from the electrode over the course of the $2.4x10^6$ pulses, a value on the order of that calculated in the previous paragraph. Consequently, the amount of Sn deposited at the various points around the chamber will be significantly higher, since the model does not account for this contribution, thus explaining the underestimation observed theoretically.

The total (as measured using the profilometer) deposition rates at each location along the collector optics and intermediate focus are plotted in figure 5.16. The lack of gas scattering at 0.3 mTorr is evident in the relatively large amount of deposition on the inside of the collector optics versus that seen in every other condition. An average deposition rate of $1.3\pm0.5x10^{-4}$ nm/pulse is measured inside of the inner optic (average calculated by measuring the deposition rate at the center of the Si witness plate, then taking the average of the values at locations 1 and 2), and an average deposition rate of $2.8\pm0.4x10^{-4}$ nm/pulse is measured inside of the outer optic (average calculated by measuring the deposition rate at the center of the Si witness plate, then taking the average of the values at locations 4,5, and 6). The increase in deposition rate observed at the middle of the outer optic is a function of two things: increased reflection probability at higher angles of incidence (lower deposition further away from the pinch) and an increased likelihood of forward peaked Sn ion and neutral emission from the pinch. As pressure is increased to 2 mTorr, deposition across the inner optics is reduced to an average of 1.0 ± 0.4 $x10^{-4}$ nm/pulse and 1.6 ± 0.2 $x10^{-4}$ nm/pulse for the inside of the inner and outer collector optic respectively. Gas suppression is even more evident in the fact that deposition rate decreases with distance from the pinch, suggesting fewer species reaching the

farthest point, and an increased number of Sn atoms that are scattered into the closest point with reduced energy to promote deposition over backscattering. A further increase in pressure to 6 mTorr reduces the deposition rates down to $3.5\pm2\text{x}10^{-5}$ nm/pulse and $5.2\pm1.5\text{x}10^{-5}$ nm/pulse. Increases in pressure above 6 mTorr yield little change in the deposition rates, suggesting that Sn deposition is nearly completely suppressed by the buffer gas, and carbon and oxygen deposition is all that remains. This is supported by the drop in intermediate focus deposition fraction from 3.15% at 2 mTorr down to 0.95%, 0.15%, and 0.02% for 6,12, and 22 mTorr respectively.

The general reduction in the negative slope observed along the outer collector optic, with increases in pressure, is a result of the increased scattering that occurs with higher pressures. For the low pressure cases, where gas scattering is not a predominant occurrence, the increased scattering angle with increased distance from the pinch results in more species being backscattered as opposed to depositing. This is why at 2 mTorr there is such a large gradient in measured deposition rates. At 0.3 mTorr, where gas scattering is almost not a factor at all, the closest point to the pinch on the outer collector optic would generally lead to more sputtering of the shallowly deposited low energy sputtered Sn atoms. Above 6 mTorr, there is very little decrease in deposited material with increase in pressure, suggesting that the oxygen and carbon species (which compose most of the deposition) that are incorporated into the EUV plasma are suppressed, and what is left is only the contribution liberated from the walls by the secondary plasmas.

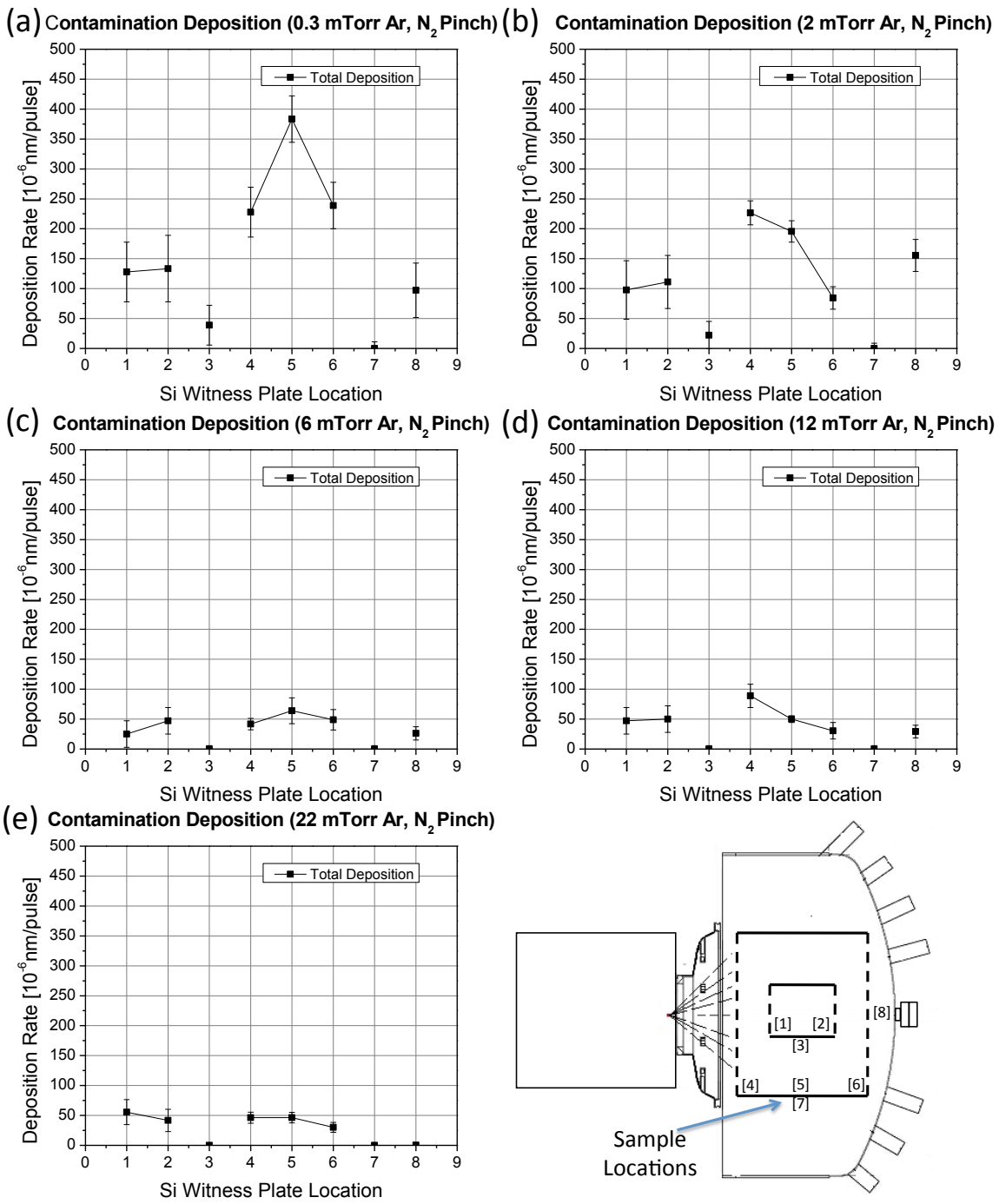

Figure 5.16: Shown are the total (C,O,Sn,Mo, and Cu combined) deposition rates at each location within the chamber for (a) 0.3 mTorr, (b) 2 mTorr, (c) 6 mTorr, (d) 12 mTorr, and (e) 22 mTorr.

If we isolate the 2 mTorr case specifically, plots of location deposition rates of Sn, Mo, and Cu can be created since the compositional analysis is available at each

location. Before returning to the actual measurements, it should once again be emphasized that the deposition rates of each location are position dependent. While a deposition rate of x nm/pulse would be observed at the intermediate focus of the described experimental setup with the intermediate focus at 0.72 m, a deposition at 2 m would have a lower deposition rate. The change in deposition rate cannot simply be converted by taking the change in surface area due to the complex nature of flux suppression. Because the energy of the pinch species changes with distance (number of collisions), there will be a point where no more deposition occurs. This would be similar to the abrupt end point observed in range calculations.

The resulting locational deposition rates and corresponding theoretical fits are shown in figure 5.17a-c. While the model predicts there to be a decrease in deposition rate in going from near to far along the inside of the inner collector optic (position 1 to 2), a slight increase in deposition is actually observed. Once again this discrepancy extends from the unaccounted for contribution from sputtering of the Sn electrode. Because the sputtered Sn atoms are very low in energy, they are unlikely to deposit deeply into the predominately carbon/oxygen coated surfaces. As such, position 1, which is closer than position 2 to the plasma source, will likely have most of the low energy Sn sputtered away by the high energy flux coming from the EUV plasma. At position 2, where the energy of the flux is reduced and sputtering is reduced, the deposition from the sputtered Sn atoms is not as sputtered away, thus resulting in the increase of deposition observed where the model predicts a decrease. Along the outer collector optics, at locations 4, 5, and 6, the experimental trend is largely followed by the theory, with the factor of

difference between model and theory reducing with increased distance from the pinch. The changing difference is caused by a decrease in flux of the sputtered Sn atoms with a r^{-2} dropoff, as well as a decrease in the number of species that hasn't yet been deposited. As such, at the furthest location, very little contribution from the sputtered Sn atoms is present and the model fits well with the experiment. Since the additional, theoreitcally unaccounted for, flux is considerably reduced at the intermediate focus, the discrepancy between theory and experiment can be mostly attributed to the large electrode material contaminants caused by arcing. This is confirmed by figure 5.17c, which is a plot of the Mo deposition at each location. Because Mo comes from the foil trap, it is not actively involved in the arcing. So while it will still have the same contribution of additional sputtered species, it will not produce the large contaminants caused by arcing. As such the model and the experimental deposition amount agree within 30%.

The general increase in deposition rates located along the outer collector optic in comparison to those along the inner collector optic is caused by the net decrease in scattering angle as well as the reduction of average Sn atom energy. Lower scattering angles mean that there is an increase in the relative probability of deposition in relation to the probability of scattering. A reduction in energy (because the highest energy ions/neutrals are forward peaked, the average energy of species at larger angles is reduced) also leads to a decrease in sputtering as well as an increase in deposition likelihood. Furthermore, the trend of reduced deposition with increased distance from the pinch along the outer optic can be

explained by the r^{-2} drop off of total Sn flux as well as the increased scattering angle that would generally lead to an increased likelihood of reflection.

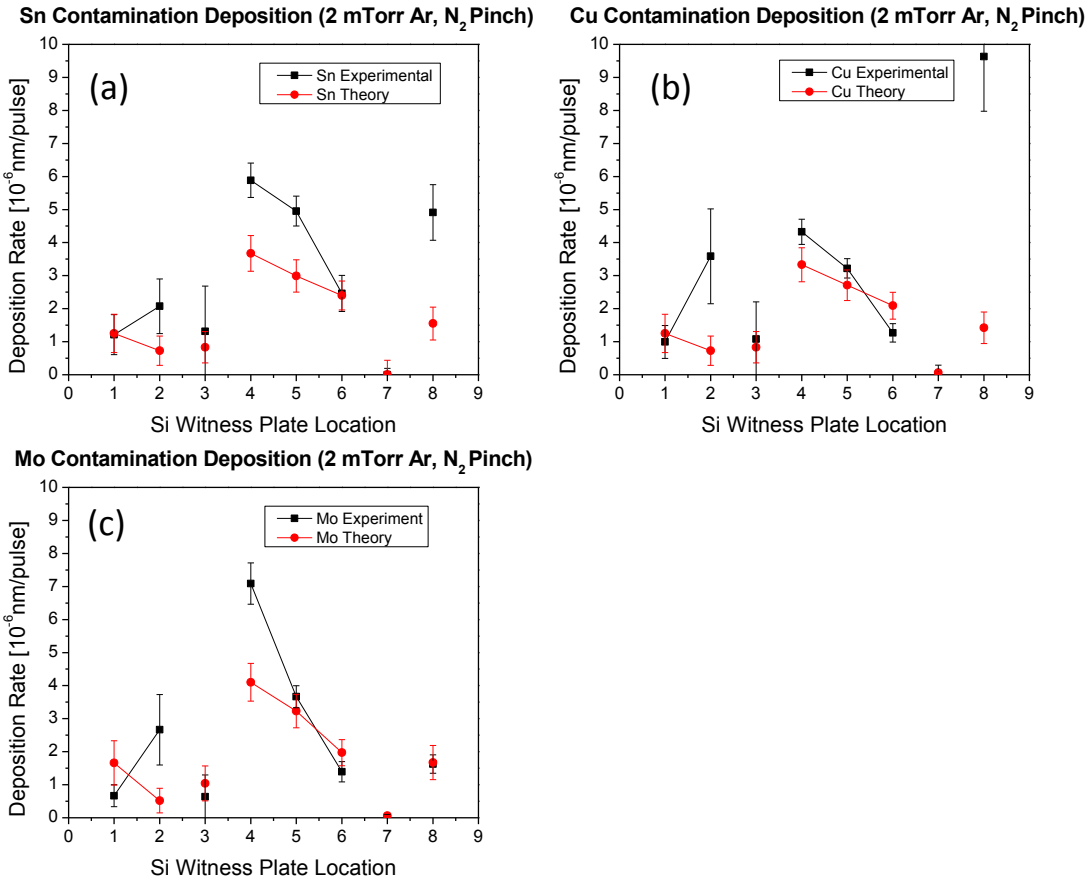

Figure 5.17: Shown are the positional deposition rates of (a) Sn, (b) Mo, and (c) Cu at 2 mTorr Ar buffer gas. Because of electrode sputtering, the model underestimates the actual deposition rate at the intermediate focus.

Looking at the actual surfaces of the Si witness plates at the intermediate focus further emphasizes the occurrence of micron-sized particle deposition at 2 mTorr. As seen in figure 5.18a-e, at 2 mTorr and 22 mTorr, there are very few observed metallic particulates. At 2 mTorr and 6 mTorr, where the debris transport model vastly underestimates the deposition rate of Sn at the intermediate focus,

there is a considerable portion of the surface covered by particulate contaminates on the order of 10-20 μm in diameter. These particulates are direct evidence to the occurrence of non-ideal electrode discharge, and help to explain why the model underestimates the flux of Sn to the surface. Obviously running at any of these conditions would be extremely detrimental to the lifetime of a collector optic source, and thus why pressures are usually maintained around 1 Torr to suppress such transport. In laser produced plasma sources, this debris would be manifested from the incomplete ionization of the Sn droplet, while with the rotating disk electrode sources this debris would because caused by the plume of Sn debris ablated off of the rotating disk.

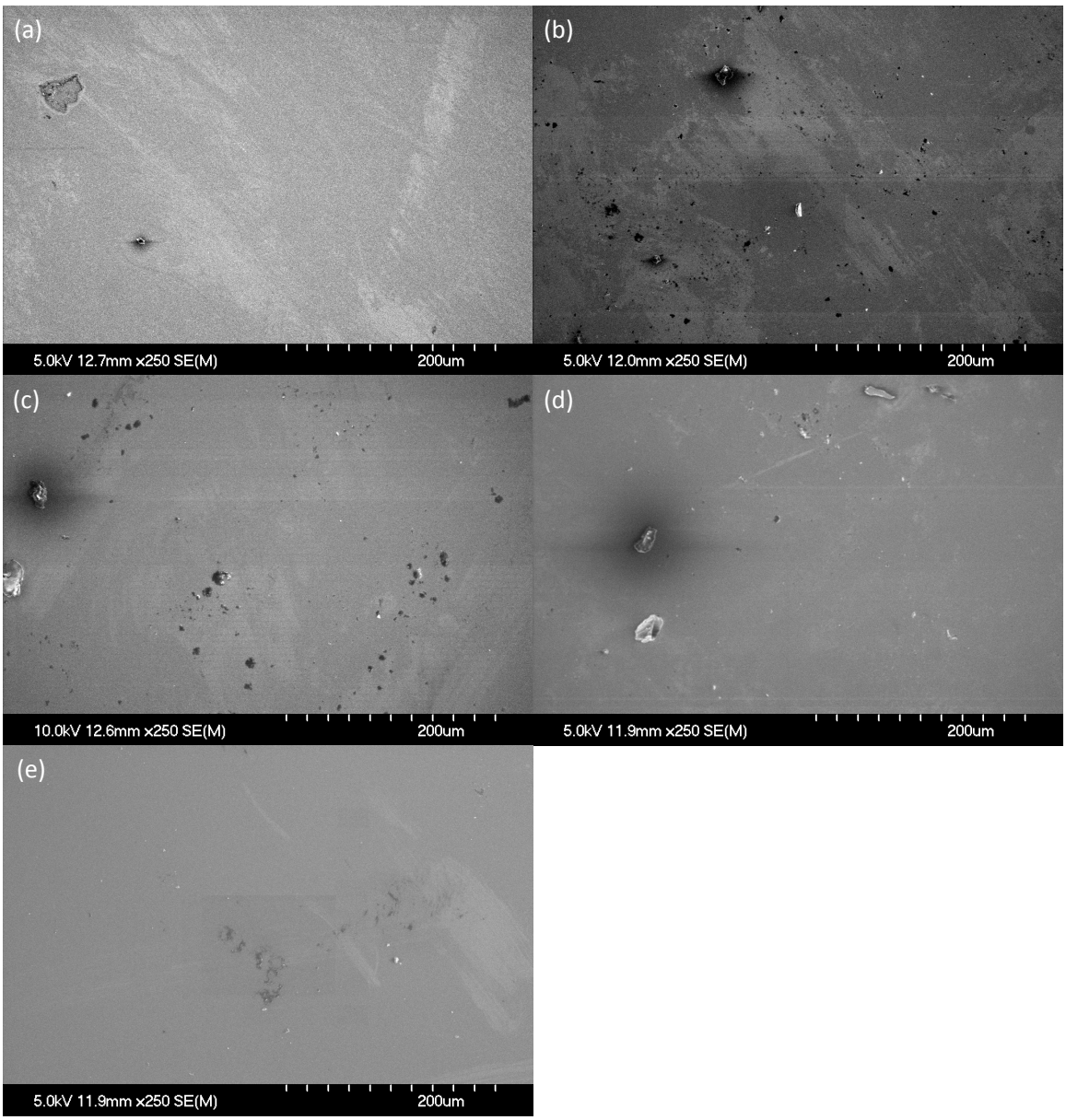

Figure 5.18: Scanning electron microscope images of the Si witness plate surfaces at 250x magnification reveal that at (a) 0.3 mTorr the surface is relatively devoid of micron-sized particle deposition. Increasing the pressure to (b) 2 mTorr, (c) 6 mTorr, and (d) 12 mTorr, however reveals the effects of electrode arcing. Large particles on the order of 10-20 μm are deposited onto an otherwise smooth carbon/oxygen film. Particles still exist, but are considerably reduce at (e) 22 mTorr, where there is sufficient gas pressure to allow ideal electrode discharge across the gas. Location is at 0.72 m.

5.3.5 Theoretical versus experimental energized buffer gas analysis

Up to this point, the focus has been on the presence and origination of, carbon contamination, oxygen contamination, as well as electrode contaminants. It is now prudent, however, to discuss an energetic predominately neutral flux observed at the intermediate focus. The source of this flux is from the excitation of buffer gas atoms due to the collisions between the energetic ions/neutrals ejected from the EUV emitting plasma and the buffer gas. As mentioned in section 4.5.2, the energetic species elastically scatter off of the buffer gas species, imparting a significant portion of their energy into the bulk of the buffer gas – especially as pressures increase. These species then go onto create more energetic species, resulting in an energetic flux that arrives at the intermediate focus well after the initiation of EUV plasma.

As mentioned in the experimental setup section, the microchannel plates have a low-end sensitivity threshold somewhere below 100 eV. Any impact with an ion or neutral with less than the threshold energy simply does not produce a large enough electron cascade to measure. Consequently it is impossible to measure the impingement of background room temperature gas, but it is possible to measure the energetic ions emanating from the EUV emitting plasma. Two measureable signals are observed using the microchannel plates. The first, occurring in the first 100 μs, is due to the arrival of the scattered high-energy pinch-origin species. The second flux, beginning around 100 μs after pinch formation, is due to the expansion of the energized buffer gas in the chamber. As shown in figure 5.19, this flux is primarily

neutral - a consequence of wall collisions and charge exchange to species reaching wall surfaces. While the front of the energetic gas expansion arrives at 100 μs, the bulk of the species arrives nearly 500 μs later and persists for just over 2 ms after its arrival.

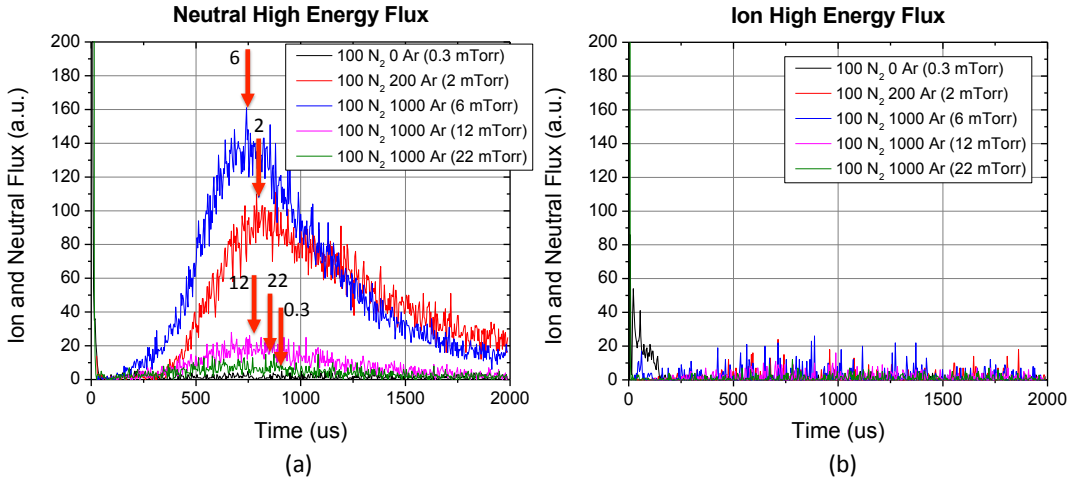

Figure 5.19: An energetic neutral flux arrives at the intermediate focus nearly 250 us after initial plasma formation. The bulk of this plasma arrives at 750 us and trails out past 2 ms. This is the resulting energetic plasma caused by gas scattering of z-pinch species after they are ejected from the plasma core. The peaks are indicated with Location is at 0.72 m. Error is approximately ±9.6%.

This arriving flux is the buffer gas species Ar. There are two reasons that suggest this to be the case: later it will be shown that changing the pinch gas while maintaining the same buffer gas results in a change in the magnitude of the flux without changing the arrival time of the flux peak, and the modeled flux and arrival time of only the buffer gas species largely follows the observed measurements. The comparison between experimental and theoretical buffer gas flux are shown in figure 5.20, where the total hit counts of the flux measurement is summed for the first 2 ms and compared with the modeled buffer gas flux. It needs to be made clear that for the microchannel plates the value of "hits" does not have a 1:1 relationship

with the number of species measured. Because there is no possible direct measurement of energy or mass with the detector (for these measurements), it is not possible to procure a true number of species arriving, and as such the theoretically measured flux had to be converted into the flux that would be expected if the arriving modeled species were being measured by the microchannel plates.

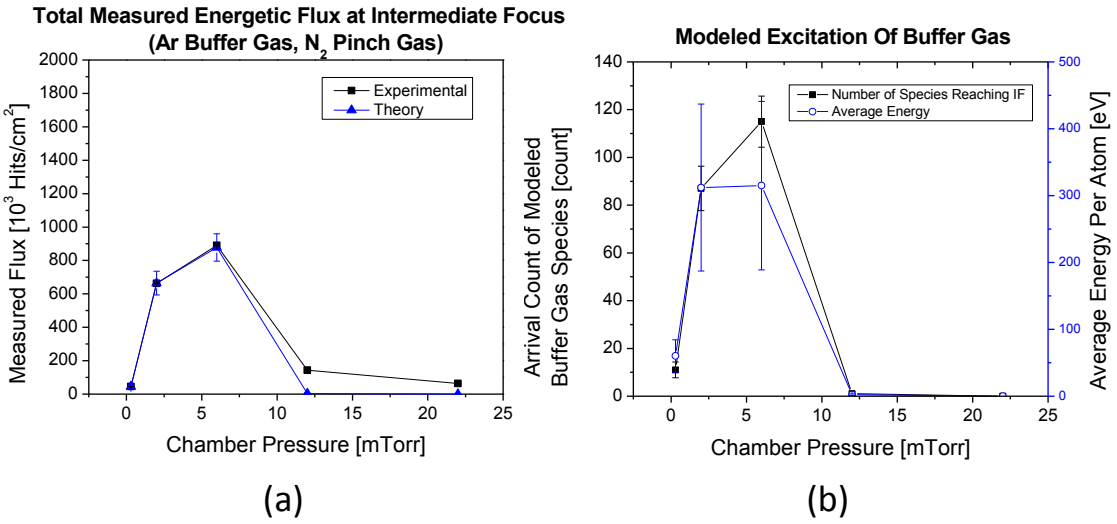

Figure 5.20: (a) The total measured energetic flux is shown as a sum from 0.25 ms to 2 ms for the Ar buffer gas and N2 pinch with a sampling period of 2 minutes. The increase in total flux is due to the deposition of the energy from energetic pinch species into the buffer gas through scattering. Because of the threshold energy measurement of the detector, only species with a minimum of ~100 eV are measureable, and consequently increases in buffer gas from 0.3 mTorr to 6 mTorr results in an increase in the total flux measured. At higher pressures, even though >99% of energy is absorbed in the buffer gas, the increased scattering reduces the ability to measure the flux arriving at the intermediate focus. C is the calibration factor used to fit the data. (b) The theoretically modeled arrival flux and average buffer gas energy are shown. Location is at 0.72 m.

In order to compare theoretical measurements of the number of buffer gas species reaching the intermediate focus to the number measured with the microchannel plates, the arriving number of atoms measured theoretically had to be back calculated to estimate the number of measured "hits" one would expect to see

with that given atomic flux. This is to say the model is converted from a measurement of actual atomic flux to the flux that would be observed using microchannel plate detection.

A flux of only 45580±4380 hits/cm^2 (0.5% model error) was measured at 0.3 mTorr, 663387±2405 hits/cm^2 (0.1% model error) at 2 mTorr, 890032±3201 hits/cm^2 (1.3% model error) at 6 mTorr, 142806±553 hits/cm^2 (200% model error) at 22 mTorr, and 63451±260 hits/cm^2 (model error not applicable due to no measured species). As has been intimated previously, at 0.3 mTorr collisions are dominated by atom-wall interactions because the cross section of gas scattering is so low. The debris transport model, as shown in figure 5.21, suggests that at 0.3 mTorr, only 7.75% of the total initial energy is deposited into the buffer gas, whereas 92.15% is deposited into the chamber walls (0.1% of the energy reaches the intermediate focus). An increase to 2 mTorr causes significantly more scattering, and the result is that 44% of the energy from the pinch species is deposited into the buffer gas. The net effect of this energy absorption, as shown in figure 5.20b, is that increasing pressure from 0.3 to 2 mTorr results in an increase in the average energy and total number of energetic buffer gas species reaching the intermediate focus. Further increasing pressure to 6 mTorr does not largely change the average energy of the species, but a further increase in total number of energetic Ar atoms is observed. Further increases in pressure has the effect of reducing the average energy of arriving species considerably, as well as limiting the number of energetic atoms reaching the intermediate focus. While more energetic Ar species are actually created throughout the chamber at these high pressures, they are generally

created nearer to the pinch and most of their energy is lost before they are able to reach the intermediate focus. At 0.3 mTorr the average modeled energy of the scattered species is 60 eV, while at 2, 6, 12, and 22 mTorr it is 312 eV, 315 eV, 2 eV, and 0 eV (no measured flux) respectively, when reaching the intermediate focus. The large error in the model-theory comparison at 12 mTorr simply arises because only one atom was found to reach the intermediate focus. If more trials were run, this number would increase and likely the error would be more in line with the values observed at other flux measurements.

Table 5.6: The computationally derive flux and conversion factors are shown for the creation of the comparison between theory and experiment. The conversion process first involves multiplying the number of hit counts by the average momentum. The calibration factor is then used to account for the relative nature of the model used.

Pressure [mTorr]	Number of BG Species at IF	Error [±]	Average Energy [eV]	Theoretical Hits [hits]	Error
0.3	11	3.3	60.2	45334	13668
2	87	9.3	312.0	664380	71229
6	115	10.7	315.0	878204	81893
12	1	1	2.4	3672	3672
22	0	0	0.0	0	0

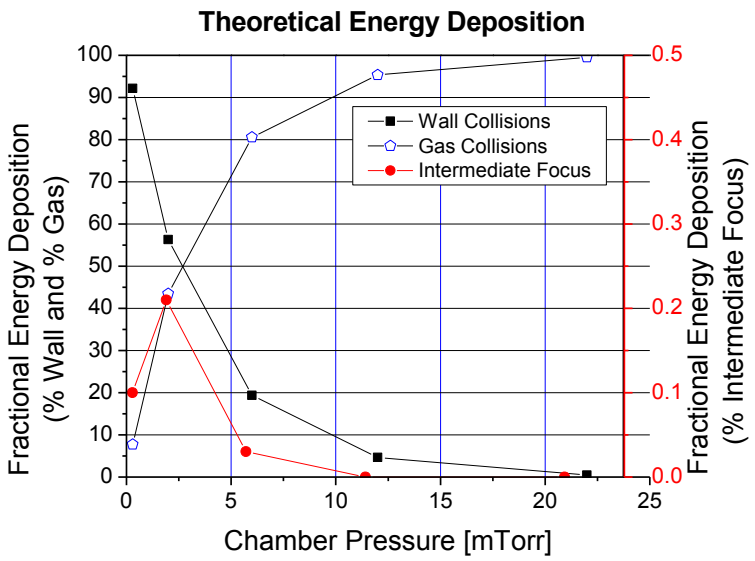

Figure 5.21: Shown is a plot detailing the theoretical fractional energy loss of the energetic pinch atoms to the walls, buffer gas, and the intermediate focus.

The arrival time of the peak buffer gas flux is plotted in figure 5.22 . There is initially a decrease in arrival time from 0.3 mTorr to 2 mTorr from 850±100 μs to 750±50 μs, which is caused by the increased absorption of energy creating a more energetic expansion. An increase to 6 mTorr results in an 8% decrease in arrival time, though further increase in pressure increase the arrival time to 700±50 μs and 830±50 μs respectively. As pressure is increased past 6 mTorr, the further increase of collision frequency overcomes the increase in buffer gas energy deposition, thus requiring more time to arrive at the intermediate focus. The theoretical measurements of arrival time are provided, though the lack of total species reaching the intermediate focus has its toll on accuracy for the 0.3 mTorr, 12 mTorr, and 22 mTorr trials. Where there is a sufficient number of species making the intermediate focus, the fit is quite good. There is no calibration factor used or needed for this comparison.

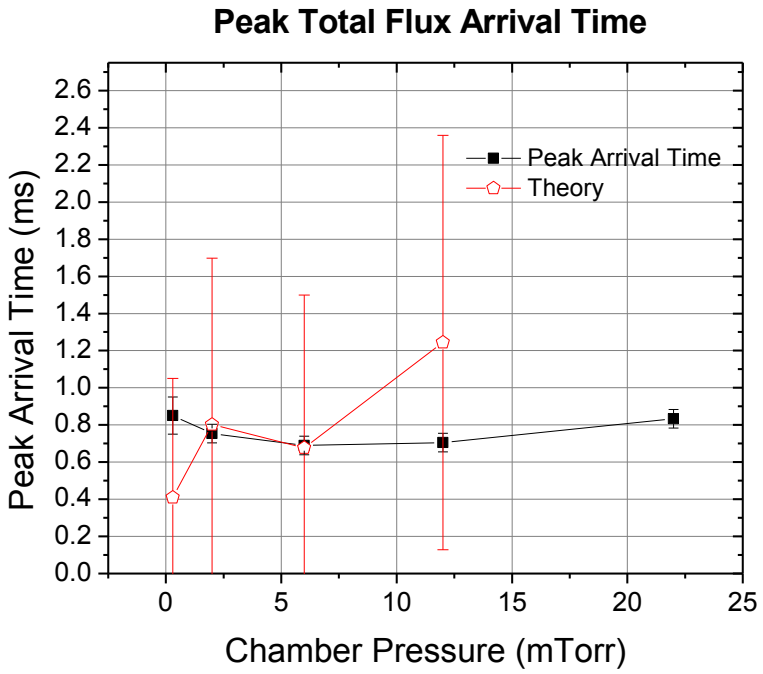

Figure 5.22: Shown are three plots diagraming the arrival times of the actual plasma front at 0.36 m, the anticipated arrival of this plasma at the intermediate focus if it retained that temperature, and the actual arrival time at the intermediate focus of the peak flux. The plasma obviously cools as it expands into the chamber and electrons undergo scattering collisions. In order for the arrival time to arrive at the actual time, the average electron temperature during transit from 0.36 m to 0.72 m must on average drop to just 8% of that measured on average transit from the EUV emitting plasma to the probes at 0.36 m.

5.3.6 Residual gas analysis

The last analysis performed investigates the transport of residual gaseous contaminants across the intermediate focus threshold. The predominant species observed are plotted in figure 5.23. The partial pressure of Ar obviously increases as gas flow is increased from 0.3-6mTorr, with a peak partial pressure of $1\pm0.15\times10^{-5}$ Torr observed. At this point, where no additional flow rate and pump throttling is introduced with a variable gate valve, the increase in partial pressure is reduced with increasing changes in pressure. It is interesting to note that after 6 mTorr, when the plasma density in the chamber increases, the partial pressure of residual

pump oil is reduced. The experiments were not performed in a direct order of pressure, so the reduction is significant. The hydrocarbon chains are cracked in the higher density secondary plasma, resulting in a reduction of the high-mass (50-100 AMU) species. Because the RGA is not in line of sight to the intermediate focus, there are no observed Sn species floating around. Previous experiments with the RGA in line of sight did not observe any Sn species as well, and this is to be expected given the low energy of the Sn species by the time the arrive at the location of measurement; low energy Sn is much more likely to deposit onto a surface than to back scatter given its high condensability.

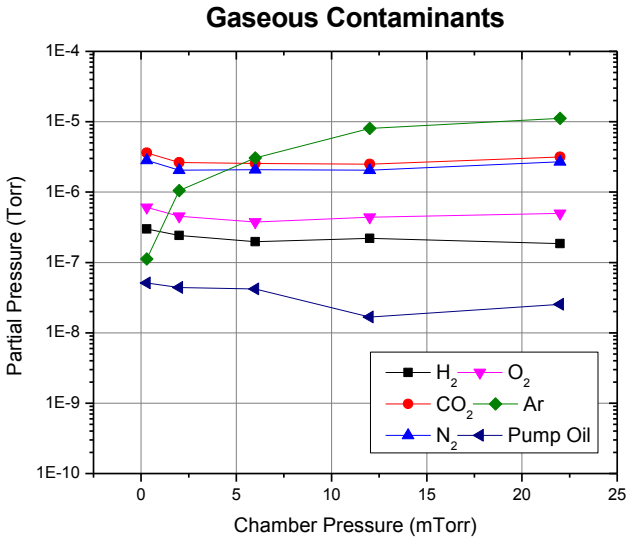

Figure 5.23: The partial pressures of the gas species at the intermediate focus are plotted as a function of chamber pressure (Ar buffer gas). As the chamber pressure is increased with reduction of pump efficiency, the partial pressure of Ar understandably increases. Of interest is the fact that the pump oil contribution drops above 6 mTorr, where the plasma density is largest inside of the XCEED chamber. Error not visible should be assumed to be the size of the marker.

Ultimately, the combined observations of plasma development, transport, and the subsequent energizing of stagnant buffer gas species reveal that while increasing buffer gas pressure may serve to reduce the detrimental sputtering

energy of the ions and neutrals leaving the EUV emitting plasma, their deleterious effect is not completely muted. Three different plasmas were observed to grow warmer and denser with increases in pressure. These three plasmas, one initiated by high energy EUV emitted electrons, one initiated by the expansion of the high-energy ions and electrons, and one supported by the expansion of the relaxing EUV core plasma, interact with the chamber walls and the optic surfaces at the intermediate focus. It was observed that their interaction with the chamber walls introduces carbon (from pump oil) and oxygen contamination (from adsorbed water to the walls) to the intermediate focus. Furthermore, there exists a largely neutral >100 eV flux that is caused by the excitation of buffer gas from the scattering collisions with the energetic ions and neutrals. These species can cause sputtering of the surface material, which was observed with the quartz crystal microbalance when deposition rates of C and O were minimized with increases in pressure forcing the introduced species back towards the wall.

5.4 Buffer Gas Effects

In the previous section, the effects of increasing Ar buffer gas pressure were explored. It was shown that increasing pressure results in an increase of relative carbon and oxygen contamination, due to increased ion flux to the walls caused by an increased plasma density. Increasing pressure also serves to suppress (at the very least their energy) the transmission of the very energetic species leaving the EUV emitting plasma. It was also proposed that the energetic species measured by the microchannel plates were a product of the energizing of the buffer gas, and as

such if the buffer gas is changed, there should be a noticeable change to the arrival time and quantity of this this energetic flux with changes in buffer gas mass. In this section the effect of changing the mass of the buffer gas from 40 AMU (Ar) to 20 AMU (Ne) and 4 AMU (He) is examined. Noble gases were utilized to discriminate against possible molecular interactions having an effect on debris transport. Each experiment was performed at 2 mTorr, with a pinch repetition rate of 20 Hz, using N_2 pinch gas, with the only variable being the buffer gas mass.

5.4.1 Expanding EUV plasma analysis

As before, the first analysis will be that of the secondary plasmas observed between each pinch. Figures 5.25-5.27 diagram the electron temperature and electron density at the three different locations inside and outside of the mock-up collector optic. It is very clear at the innermost location that increasing the buffer species from 4 to 40 AMU results in a decrease in electron temperature. This is caused by the decreased ionization potential that follows an increase from 4 AMU to 20 AMU to 40 AMU. While initially it may be questioned how a change in buffer gas could affect the temperature of the fast electrons emitted by the EUV plasma, the answer lies in the fact that buffer gas is mixed in with the pinch gas. The EUV plasma actually exists several millimeters into the chamber, and it is at this location that the mixing occurs. Because the ionization potential of outer shell electrons are easier to remove from Ar than Ne and He, the excitation and further ionization of the higher mass species results in more electrons being liberated with the same amount of energy. Each pinch deposits on the order of 10^{19} eV, from which the ejection of

several electrons/atom can occur. He only has 2 electrons to liberate; Ne has 10, while Ar has 18. This is confirmed in the measurement of electron density, as He has a density of $5\pm1.5\text{x}10^{12}$ cm^{-3}, Ne has a density of $2.5\pm0.75\text{x}10^{13}$ cm^{-3}, and Ar has a density of $4.5\pm1.3\text{x}10^{13}$ cm^{-3} at 1 μs. The ratio of these densities corresponds to the number of electrons available for removal.

No fast ion/electron induced plasma is observed with Ne, though it is observed with Ar and He. Looking at the cross sections (fig. 5.24) sheds some light on this issue. The noble gases are known to behave uniquely near 1 eV, where in general the scattering cross-section drops to zero. It is an effect called the Ramsauer-Townsend effect, and is only explainable by considering the quantum mechanical e-atom interaction from a wave principle standpoint. The incident electron at the low energy point (typically around 1 eV), effectively undergoes diffraction near the atom, resulting in a complex scattering angle [91]. He is not shown to exhibit this phenomenon, and consequently has a much higher scattering cross section from 10 eV than that observed with Ne. While argon does exhibit the Ramsauer-Townsend effect, the higher interaction cross section results in a scattering cross section that is still higher than He at all energies. The consequence of this is that the forward peaked electrons will not be scattered outward at sub 10 eV energies as readily as would be observed in Ar or He interactions. This is further reinforced by the fact that the fast electron plasma is only observed for Ar at location C, since it is the only species with a high enough electron scattering cross section to redirect the fast electrons outward.

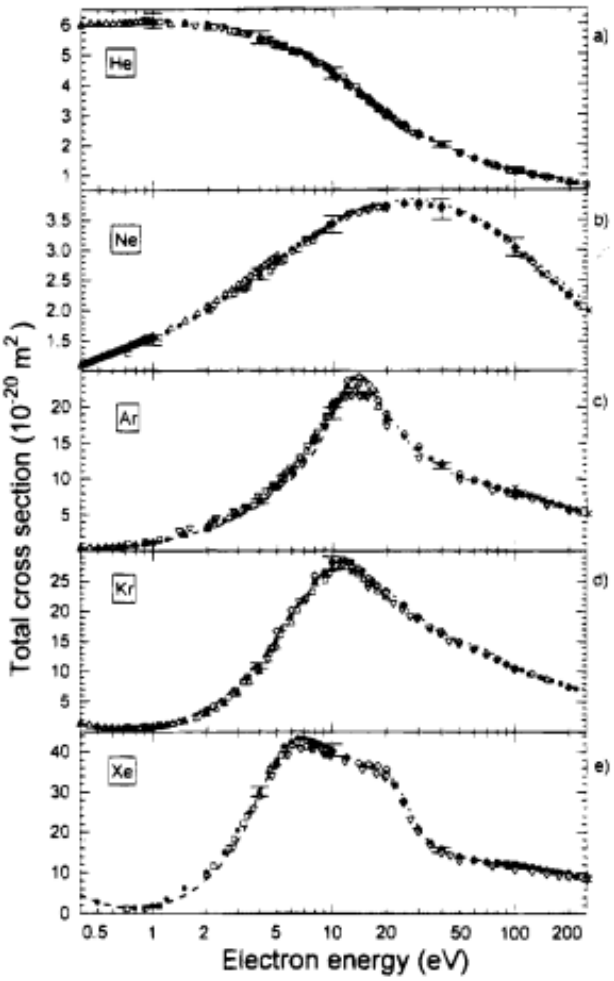

Figure 5.24: The electron scattering cross sections from 0.5 - 200 eV are plotted for the noble gases He, Ne, and Ar. At the lower range of energy, where most of the electrons from these experiments exist, the He reaction rate for scattering is much higher than that that of the Ne reaction rate. This can account for the absence of measured electrons for Ne at locations B and C, and also for He fast electron absence at location C since the scattering cross section is so much lower [91].

Unlike the first high energy electron driven plasma, the peak electron density of the final plasma is the same for Ne and Ar at a peak of $3\pm1x10^{13}$ cm^{-3}, though with He there are less electrons to eject, so there is an observed reduction in density down to $1x10^{13}$ cm^{-3}.

A lower general electron temperature and electron density is observed in between the two shells. There is no sustainment of the fast electron driven plasma

using Ne, but the He and Ar buffer gases sustain a plasma at 5.5±0.8 eV and 2±0.3 eV respectively at 1 μs. Because the distance from the EUV emitting plasma to location B is further than that to location A, and the highest energies are forward peaked in direction, the effects of buffer gas mass become more apparent as it takes longer for the energetic ion produced plasma to arrive as mass is increased. The increased scattering with higher buffer gas mass lowers the average electron energy and also serves to increase the likelihood of a wall collision before reaching the destination. The electron temperature of the second plasma increases up to 6.5±1 eV, 3.5±0.5 eV, and 6.5±1 eV respectively for He, Ne, and Ar respectively. Furthermore, the electron density increases to $1\pm0.3\text{x}10^{12}$ cm^{-3}, $3\pm1\text{x}10^{12}$ cm^{-3}, and $3\pm1\text{x}10^{12}$ cm^{-3} respectively. Once again there is very little relative difference from location A to location B and C for the expansion of the EUV core, which expands more isotropically.

At the furthest location, the generated plasmas have traveled an even further distance without line of sight to the pinch, consequently resulting the lowest temperatures and densities of the three measured locations. The only fast electron driven plasma that is visible is with the Ar buffer gas, which has a high enough electron density, at $4\pm1.3\text{x}10^{13}$ cm^{-3}, to travel that far out (it's a matter of species survival). Sub-2 eV electron temperatures are observed with the second plasma, and the life of this plasma lasts only 10 μs as the energetic ions and electrons pass. Once again though, the bulk expansion of the EUV plasma, and the resulting excitation of the buffer gas, allows the plasma to expand proficiently to the outer edges of the chamber. All electron temperature energies peak at ~1 eV and the

densities of the He, Ne, and Ar buffer gases are $6\pm2x10^{12}$ cm^{-3}, $2\pm0.6x10^{13}$ cm^{-3}, $3\pm1x10^{13}$ cm^{-3}, at peak values respectively.

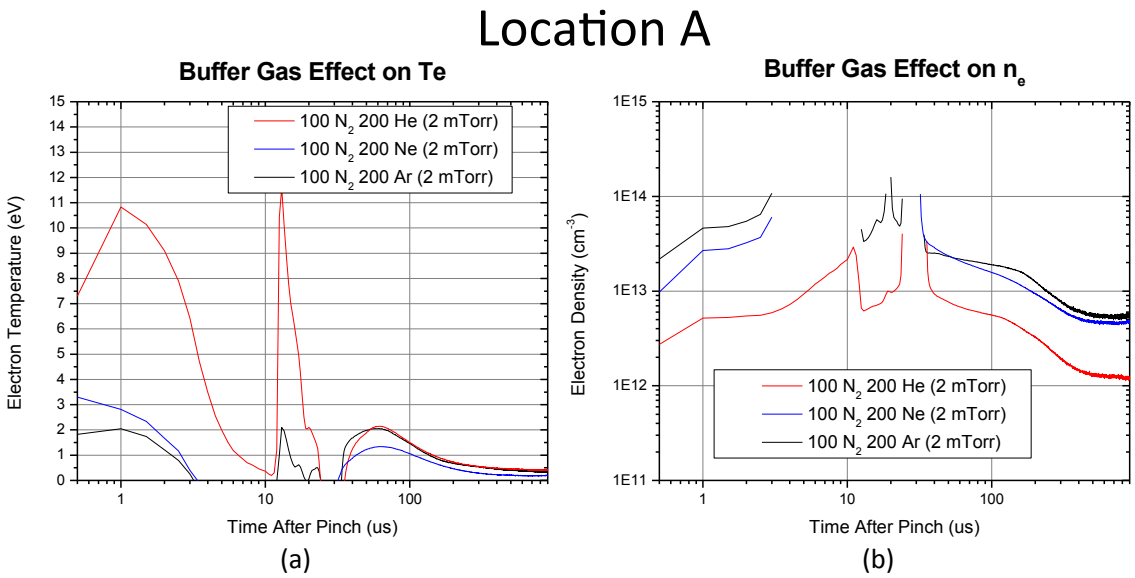

Figure 5.25: Shown are the electron temperature (a) and the electron density (b) inside the inner shell of the mock-up collector optic during the first millisecond after EUV emitting plasma formation at z=0.32 m. Three plasmas are observable: EUV photon initiated (0-10μs), energetic ion, neutral, and electron initiated (10-30μs), and bulk EUV plasma expansion (30-1000μs). Electron temperature decreases with increasing mass due to the binding energy of the outermost electrons being lower. The ionizing energy is dispersed into the ejection of more electrons with a lower energy per electron. This results in the higher observed electron density. Because of the He electrons come out with so much energy, they last longer and are able to cause more net ionization, thus the sustainment of plasma from the photon generation to the fast ion causing plasma. The sharp peaks in electron density that occur when Te disappears are simply mathematical errors formed as a result of the use of Te in the quotient for determining electron density. Location is at 0.36 m. Error is approximately ±32% for n_e and ±15% for Te.

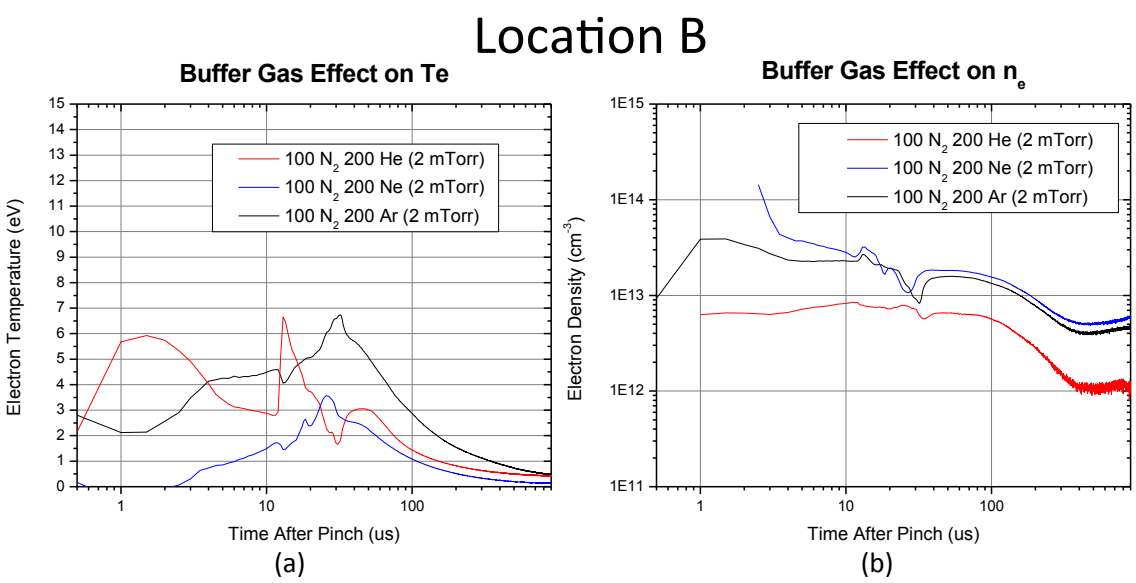

Figure 5.26: Shown are the electron temperature (a) and the electron density (b) between the inner and outer shells of the mock-up collector optic during the first millisecond after EUV emitting plasma formation at z= 0.32 m. Three plasmas are observable: Fast electron driven (0-3μs), energetic ion and coupled electron driven (3-30μs), and bulk EUV plasma expansion (30-1000μs). The fast electron driven plasma has the highest electron temperature with He, and a lower temperature plasma is generated with Ar, though a plasma is not sustained with Ne. The larger gap between the shells allows the plasma to last longer before diffusing to the walls. The sharp peaks in electron density that occur when Te disappears are simply mathematical errors formed as a result of the use of Te in the quotient for determining electron density. Location is at 0.36m. Error is approximately approximately ±32% for n_e and ±15% for Te.

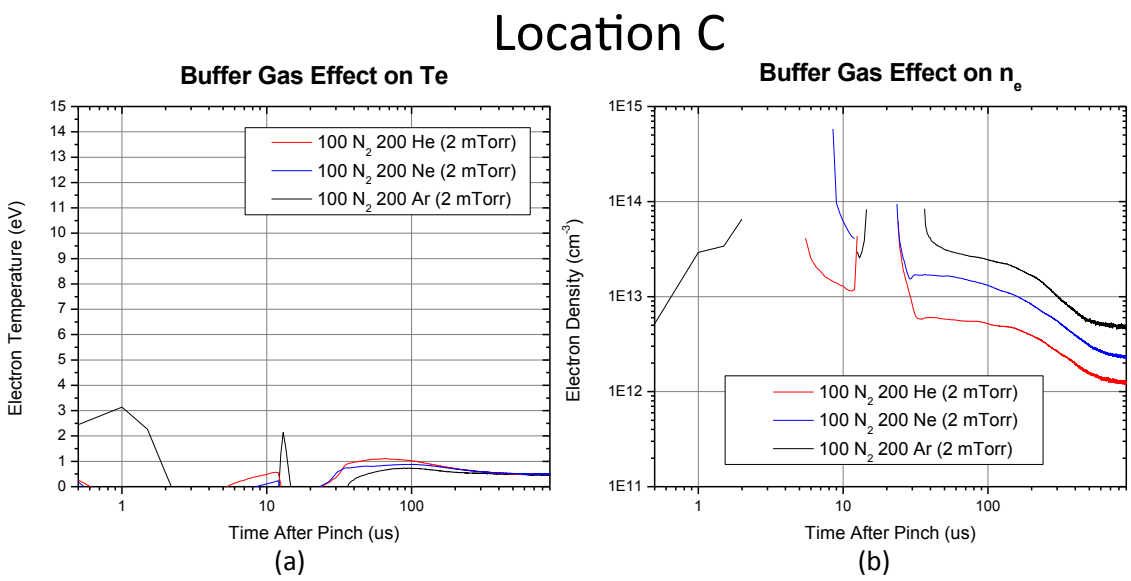

Figure 5.27: Shown are the electron temperature (a) and the electron density (b) outside of the mock-up collector optic during the first millisecond after EUV emitting plasma formation at z=0.32 m. Without direct line of sight to the EUV emitting plasma, the Ne and He buffer gasses are subject to the fast electron plasma at this location, and there is not enough near by ionization to create a measureable plasma. The second energetic ion/slowed electron driven plasma is observed to a small degree for each species, with Ne having the highest observed density. Each buffer gas species sustains the plasma created by the EUV emitting plasma expansion, with once again the higher mass exhibiting the highest density. The sharp peaks in electron density that occur when Te disappears are simply mathematical errors formed as a result of the use of Te in the quotient for determining electron density. Location is at 0.36 m. Error is approximately ±32% for n_e and ±15% for Te.

5.4.2 Charged flux analysis

The expansion of these plasma components introduces several concerns to the post-intermediate focus surfaces. As mentioned previously, because the plasma reaches all surfaces inside of the chamber, carbon and water (oxygen) contamination are sputtered off of the walls and introduced to the intermediate focus. Furthermore, charging of each surface can occur, developing a thermal load and or sputtering of the surface with the development a sheath at the surface closest to the intermediate focus. Shown in figures 5.28a-c are the charged fluxes observed at the intermediate focus for the first 200 μs. Once again the first two electron

fluxes can be made out with the Ne and Ar buffer gas cases. The distinction is not as visible with He, as the higher mobility of the ions results in the arrival of the fast ions with the electrons they are somewhat slowing down. While each buffer gas case has the general transmittance of the energetic ions during the first 50 μs, followed by a largely negative flux, the buffer gas plasma arrives at increasing times with increasing mass. The plamas arrives at ~60 μs, ~75 μs, and 100 μs as buffer gas mass is increased from 4 AMU, to 20 AMU, to 40 AMU.

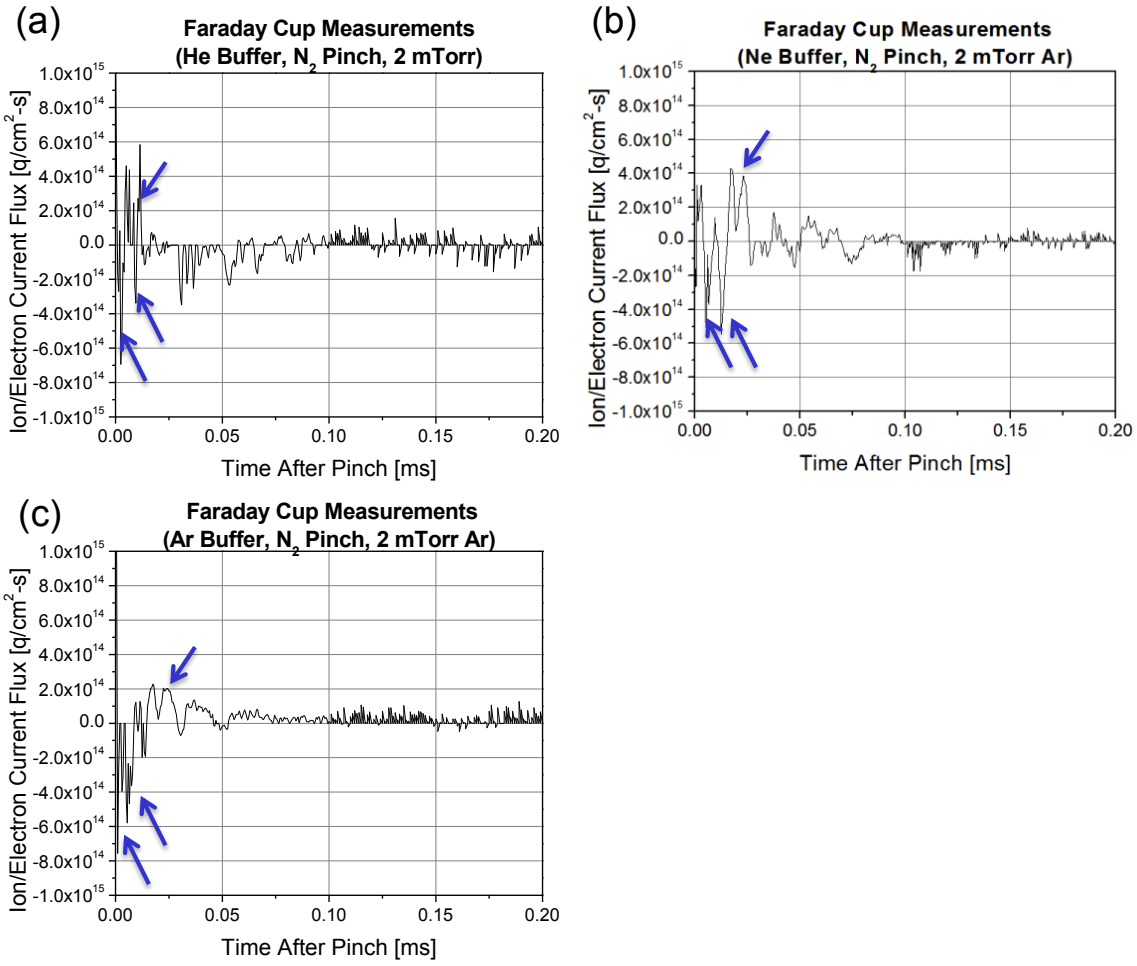

Figure 5.28: Figures a-c show the Faraday cup measurements at the intermediate focus for each buffer gas utilized. The signals were averaged over 256 trials with a positive 100 V and negative 100 V bias applied to remove noise. The resulting signals of each of these biases were stitched

together to proved the presented data. With each of these conditions, the initial arrival of the most energetic ions is observed in the first 50 μs, followed by the buffer gas plasma with increasing time as buffer gas mas is increased. The locations of the fast electron, ion-coupled electron, and ion flux components are indicated from left to right. The electron presence is slightly unclear as the pinch was not very stable and resulted in multiple pinches. Location is at 0.72 m. Error is approximately ±31%

Tallying the total charge reaching the intermediate focus for the first 200 μs reveals the total charge buildup that needs to be managed to protect the nearest surfaces. As observed in figure 5.29, the net charge reaching the surface is actually negligible. As buffer gas mass is increased from 4 AMU to 20 AMU, there is no change in total positive current flux ($3.5\pm1.5x10^{10}$ e-cm^{-2}), though there is a decrease in negative current flux from $-4\pm1.5x10^{10}$ e-cm^{-2} to $-3\pm1.5x10^{10}$ e-cm^{-2}. While more electrons are created (increased electron density) with higher buffer gas mass, the number of ions created increases as well. The increased scattering caused by Ar helps to diminish these ions and electrons by increasing wall collisions. A further increase to 40 AMU causes the positive current flux to drop to 1.8 ± 0.7 $x10^{10}$ e-cm^{-2}, and the negative current flux to drop to $-2.2\pm0.9x10^{10}$ e-cm^{-2}.

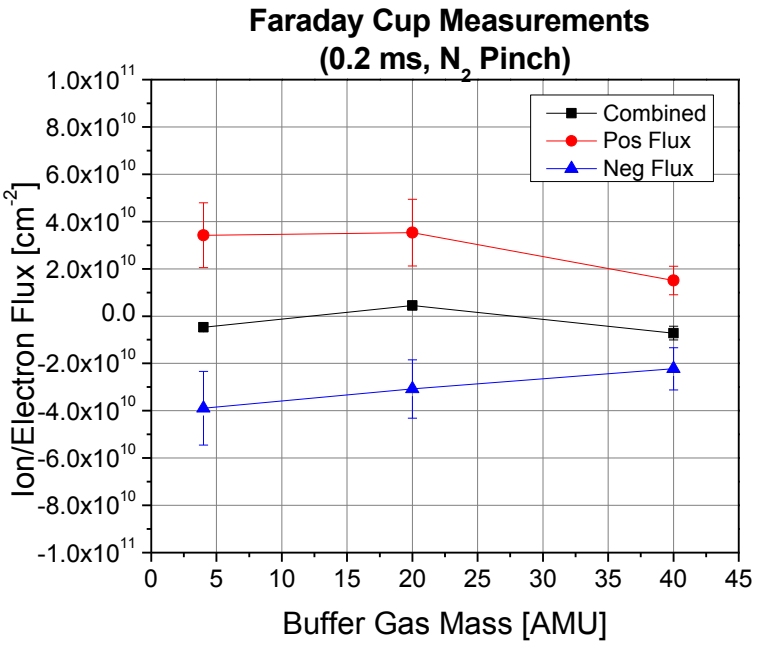

Figure 5.29: As buffer gas mass increases, there is a net drop in the total positive and total negative charge measured. There is a negligible amount of total net current observed. The feature of importance, however is the fact that the difference between the magnitudes of the positive and negative flux decreases as mass is increased. Location is at 0.72 m.

5.4.3 Deposition analysis

As observed with the changes to pressure, a decrease in the gap between positive and negative current flux results in less erosion of the Sn coated quartz crystal microbalance. As shown in figure 5.10, there is a nearly linear increase in deposition rate with increasing buffer gas mass. This is obviously a concern for the down-field optics, which require a surface roughness on the order of angstroms to optimally reflect EUV light. He and Ne buffer gases, which do no sputter as much carbon and oxygen off the walls as Ar does, have net erosion rates observed. This suggests that their lack of effective energy reduction of the pinch gas species causes sputtering at a rate faster than the deposition of electrode materials and the carbon and oxygen contaminants on the Sn coated surface.

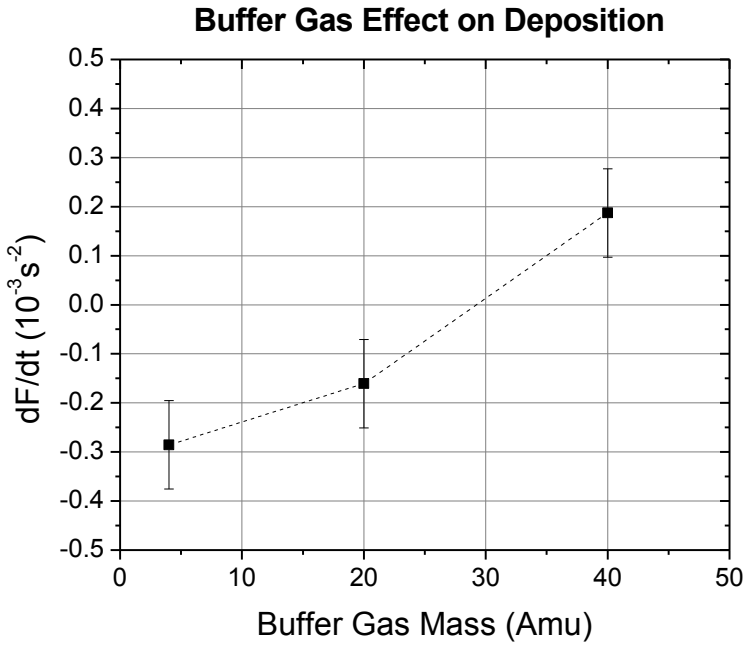

Figure 5.30: Increasing buffer gas mass increases the deposition rate. For 4 AMU and 20 AMU, a net erosion of the Sn coated surface is observed, while at 40 AMU, a positive deposition rate is observed. Location is at 0.72 m.

Because the gas pressure is held constant at 2 mTorr, previous measurements suggested that transportation of the energetic electrode species to the intermediate focus should happen. This is observed in figure 5.31, which is a plot of the atomic concentrations of the predominant species deposited at the intermediate focus for the three different buffer gasses. There is very little difference in relative concentrations of deposited electrode species, with Sn accounting for 6±0.3%, 4.3±0.2%, and 3±0.1%, Cu accounting for 6.9±0.4%, 5.6±0.3%, 6.2±0.3%, and Mo accounting for 3.8±0.2%, 4.4±0.1%, and 1.04±.05% of the total film using He, Ne, and Ar buffer gases respectively. While the concentrations of Sn and Mo drop with increasing buffer mass, the relative

concentration of Cu remains the same, suggest that perhaps the sputtering of the Cu gasket used to simulate the intermediate focus might play a roll in its presence.

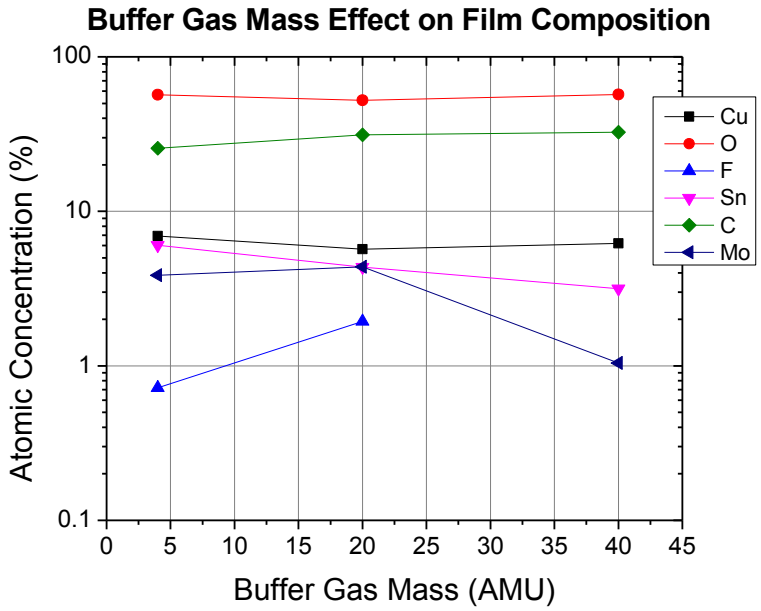

Figure 5.31: A plot of the deposited species' concentrations at the intermediate focus reveals very little change in the relative concentration of electrode species reaching the intermediate focus. The percentage of the film that is carbon based increases slightly with increased buffer gas mass, likely due to increased sputtering of the walls. Location is at 0.72 m. Measurement error is less than 5%.

Coupling the film concentrations with total measured deposition rates provides the fractional deposition rates of each species at the intermediate focus, as shown in figure 5.32. There is a net increase in deposition amount observed with an increase in buffer gas species. The only explanation for this observation is that by increasing the buffer gas mass, the resulting reduction in average energy of the species reaching the intermediate focus allows causes less sputtering and improved transport to the intermediate focus. The larger mass buffer gas species have a larger cross section (more scattering), and a higher energy transfer capability for the large mass electrode materials. This is further confirmed in the increase in Sn, Mo, and Cu

deposition rates with an increase in buffer gas mass. There is of course the increase in C and O deposition rates as well, since the larger buffer gas mass interacts more effectively with the contamination deposited onto the walls of the chamber.

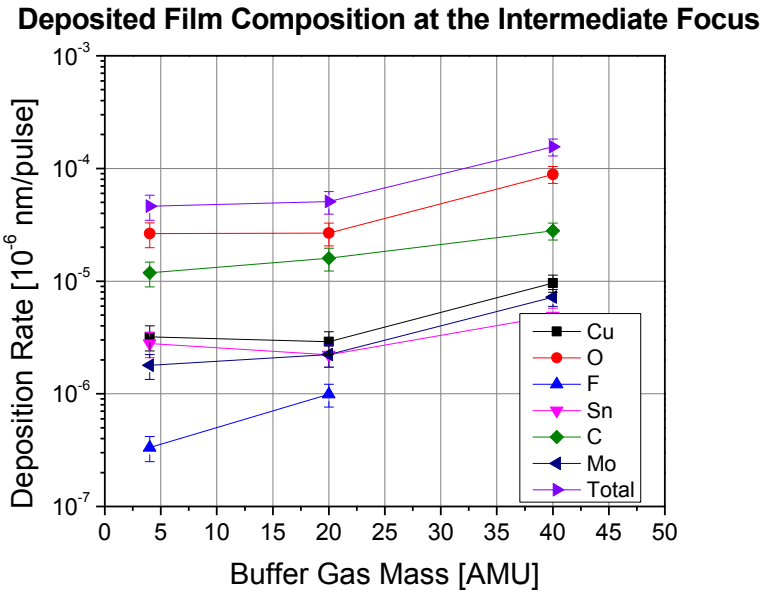

Figure 5.32: Shown are the deposition rates of the various deposited species at the intermediate focus at three different buffer gas masses. There is a general increase in deposition rate as buffer gas mass is increased, suggesting that the decreasing in energy (larger scattering cross section, higher energy transfer) associated with the increased mass permits species to deposit instead of simply sputter the surface. Location is at 0.72 m. Error not visible should be assumed to be the size of the marker.

5.4.4 Theoretical versus experimental deposition analysis

If the deposition of Sn alone is isolated, it is possible to better understand the reasoning behind what it observed (fig. 5.33). As mentioned previously, using argon buffer gas at 2 mTorr produces a considerable amount of micron-sized particulates, as well as low energy sputtered electrode atoms, which inflate the deposition rates of the electrode materials. This is once again observed by the fact that the model predicts 71% less deposition at the intermediate focus with an Ar buffer gas at 2

mTorr. With He and Ne as the buffer gas, however, there is less on-going sputtering of the electrodes (less mass typically equates to a lower sputtering yield) and furthermore less arcing occurs at the electrode source. This is visibly evident in the scanning electron microscope images of figure 5.35, but also visible in the fact that the model more accurately predicts the deposition rates of He and Ne buffer gas. From a buffer gas mass of 4 to 20 AMU, there is a measured reduction of deposition rate from $2.8\pm0.7\text{x}10^{-6}$ nm/pulse (23% model error) to $2.2\pm0.5\text{x}10^{-6}$ nm/pulse (43% model error). Increasing to 40 AMU increases the measured deposition rate to $4.9\pm0.8\text{x}10^{-6}$ nm/pulse (149% model error). The model does, however, predict the increase in deposition rate with an increase from 20 AMU to 40 AMU. It should be reiterated for clarity that the calibration factor used in these theoretical comparisons is the same as that used in the comparisons made in section 5.3. The same reasoning laid out in section 4.7 holds, and the underestimate causing the offset between theory and experiment is largely caused by the lack of calculated low energy Sn sputtering of the electrode.

Deposition is a function of angle of incidence, energy, and of course incident species. The increase in scattering cross section with increasing buffer mass from 4 to 20 AMU is not particularly important given the similar atomic radii of these smaller atoms. The largest factor is the increase in energy transfer, thus causing more deposition along the inner and outer collectors with higher buffer gas mass. More species reflect off of the collectors to the intermediate focus with He than with Ne. With Ar, however, there is an increase in total scattering, as well as an increase in energy transfer. Consequently there will be an increase in the number of species

reaching the intermediate focus with Ar buffer gas when compared to Ne buffer gas. There is also, according to the model, an increase in deposition nearest to the pinch side of the outer collector optic, and a further reduction further away due to the better suppression of species with scattering. Furthermore, increasing buffer gas mass, which is also complicit in electrode sputtering, increase the sputtering yield from 0.26 (7.5 keV at 50°) for He to 4.5 and 7.3 for Ne and Ar respectively.

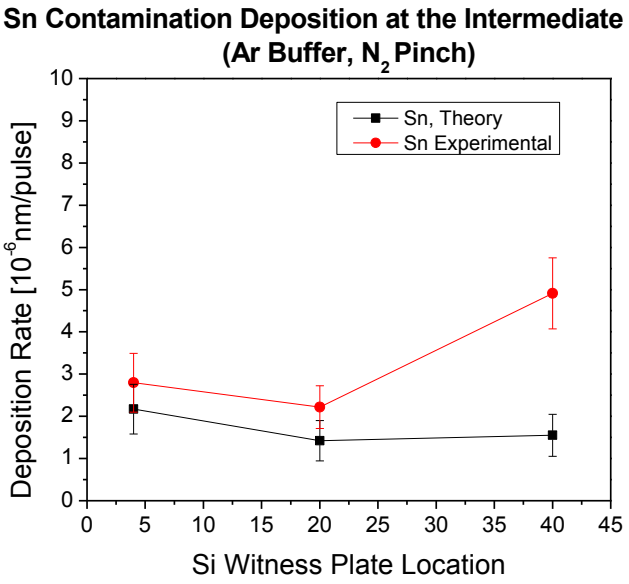

Figure 5.33: While the predicted deposition rate at the intermediate focus predicts a decreasing deposition rate with increasing buffer gas mass, an increase is observed at 40 AMU. This is due to the particulate Sn contaminants that are ejected from the electrodes because of arcing. Location is at 0.72 m.

This deposition trend is also observed on a total deposition scale as shown in figure 5.34a-c. An average decrease across all location from $6\pm2\text{x}10^{-5}$ nm/pulse to $4.5\pm1.5\text{x}10^{-5}$ nm/pulse is measured with an increase in mass from 4 to 20 AMU. Increasing the buffer gas mass to 40 AMU results in the average increase up to $14.5\pm4\text{x}10^{-5}$ nm/pulse. It is observed that along the inner collector optic that as buffer mass increased, the relative rates between the furthest point from the pinch

to the nearest point to the pinch increases. This is due to an increase in scattering. In general for He and Ne buffer gasses there is an increase in deposition rate with increased distance from the pinch for the outer collector optic. The opposite is observed with Ar, and suggests that the better suppression/scattering capabilities of Ar reflect more species to the intermediate focus than would originally deposit at the furthest point of the outer collector optic.

The pronounced gradient along the outer collector optic using Ar buffer gas, as opposed to the relatively flat trend observed with the other species, is due to the increased scattering efficiency of the larger atom. A total increase in the deposition rates is likely due to the increase in sputtering of contaminants which in turn increases the amount of carbon and oxygen incorporated into the pinch.

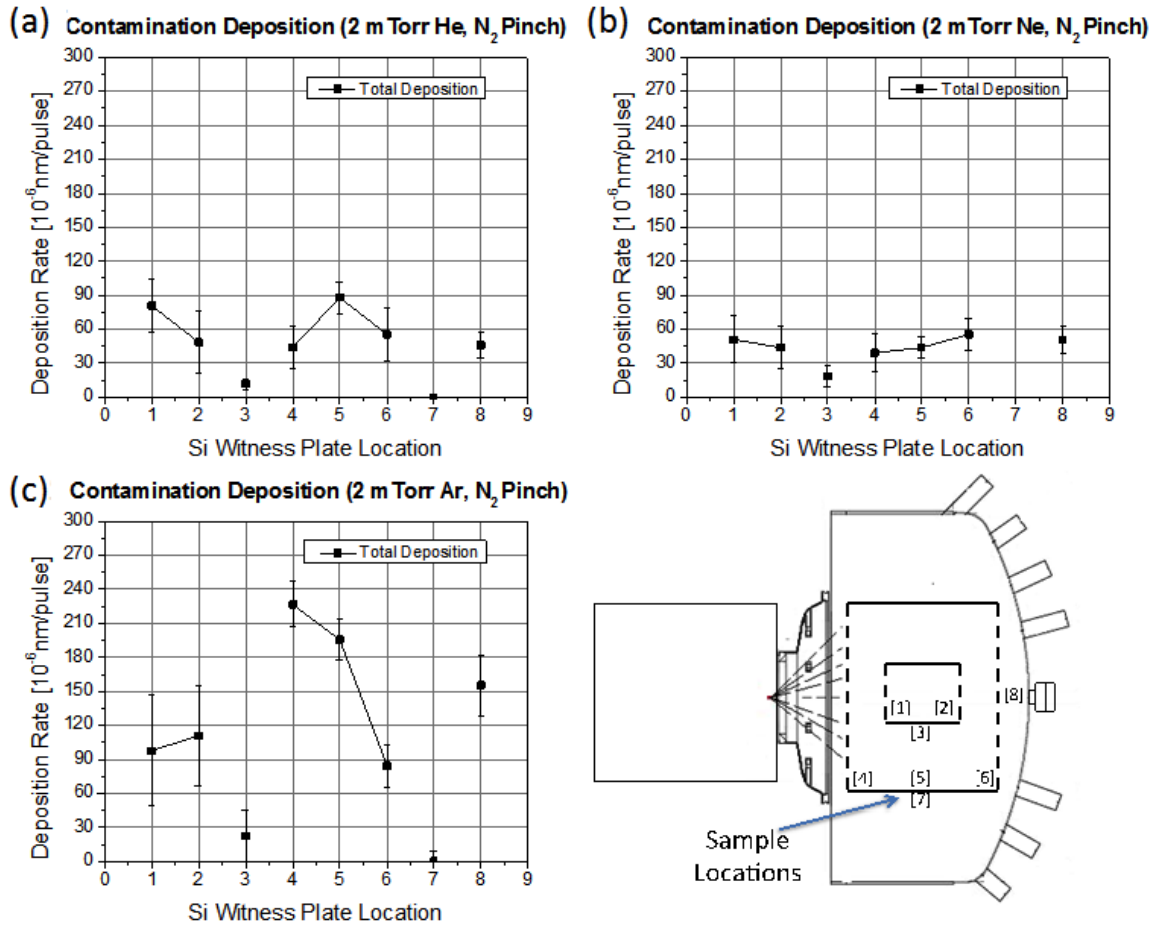

Figure 5.34: The highest deposition rate throughout the chamber is typically located on the inside of the outer collector optic. While there is the predicted decrease from He buffer gas to Ne buffer gas with increased suppression from the electrodes, an increase is observed using Ar. Once again this is due to the arcing at the electrode and is quite visible with SEM analysis.

Looking at the scanning electron microscope images of the surface of each intermediate focus deposition, figure 5.35, reveals the increased deposition of particulates with He and Ar. It is not exactly clear why He has more particulates than Ne, though this was observed at many places around the sample surface. The large number of particulates using Ar buffer gas has previously been discussed, but should be reiterated because of its importance to debris transport to the intermediate focus. In general, the deposition with He and Ne is much smoother

than that observed with Ar buffer gas because of the decreased amount of electrode particulates.

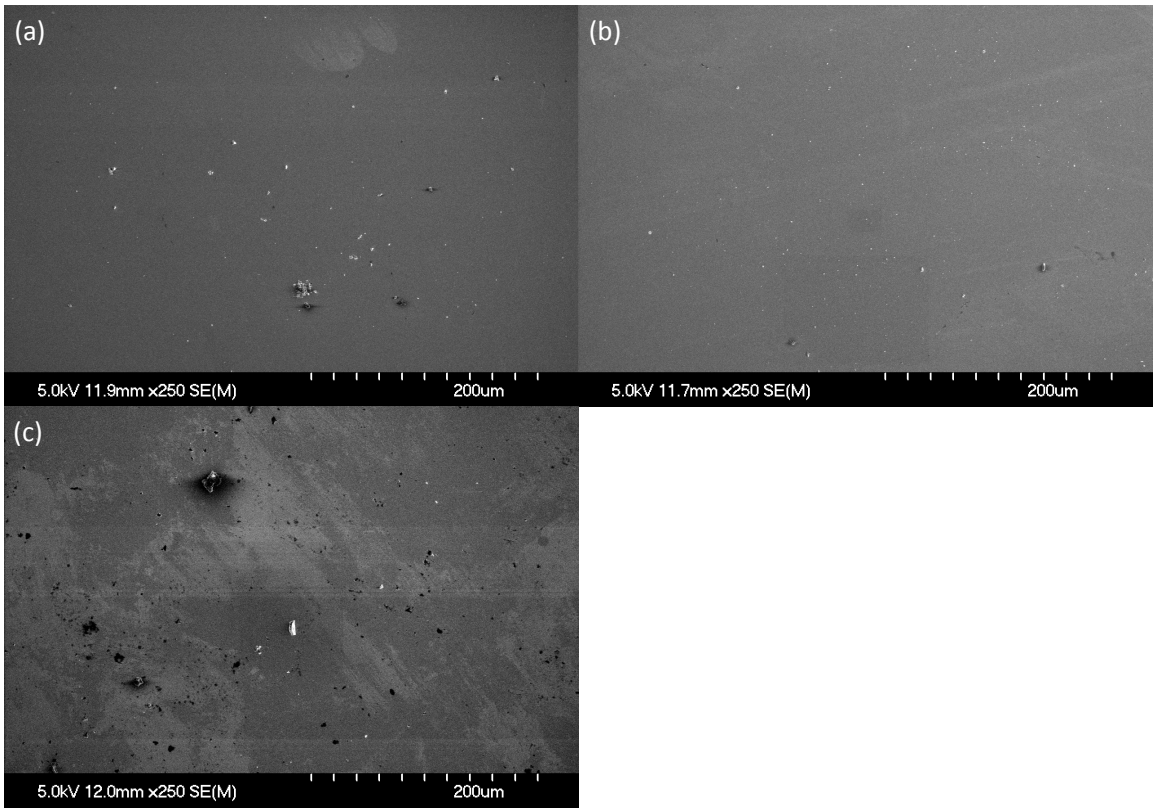

Figure 5.35: Shown are the scanning electron microscope images of the intermediate focus Si witness plates after exposure to a 2 mTorr N_2 driven pinch with (a) 432000 pulses using He buffer gas, (b) 432000 pulses using Ne buffer gas, and (c) 225000 pulses using Ar buffer gas. Particulate buildup is clear in all cases, and originates from arcing between the cathode and anode. Location is at 0.72 m.

5.4.5 Theoretical versus experimental energized buffer gas analysis

The increased energy transfer from the energetic pinch species to the buffer gas species is most noticeable when observing the energetic flux as it arrives at the intermediate focus. It is to be mentioned once again that the flux measured using the microchannel plates is significantly above room temperature, given the threshold sensitivity of the plates at this energy. Figure 5.36 shows that there is a

larger flux using Ar buffer gas than that observed with Ne or He. In elastic scattering, two masses of similar object have the largest amount of energy transfer in a given collision. Since He and Ne have relatively low masses compared with Sn, Cu, or Mo, the energy transfer is inefficient and the incident species retain quite a bit of their energy. With the post 400 μs flux being due to the energized scattered buffer gas species, it only makes sense that the Ar buffer gas would have the largest signal (it absorbs the energy of the energetic ions and neutrals more effectively). This is exactly what is observed in figure 5.36. Furthermore, due to the higher mobility of the lower mass species, the peak of He arrives at ~450 μs, while the peaks of the Ne and Ar buffer gas flux arrive at ~720 μs and ~800 μs respectively. The flux arrives faster for lower buffer gas masses due to the increased mobility of the lower mass species. The arrival of the Ar buffer gas arrives very close to the time Ne arrives due to the initial increase in electron temperature observed in figure 5.26a. Once again, however, it is noticed that very few of these species are ions, a result of charge exchange and plasma cooling with expansion, as well as the large proportion of species from the pinch being neutral. There is a large ion signal for each of these species very near after the EUV emitting plasma formation, and this is correlated to the arrival of the scattered energetic ions leaving the EUV plasma during the relaxation of the compressive fields.

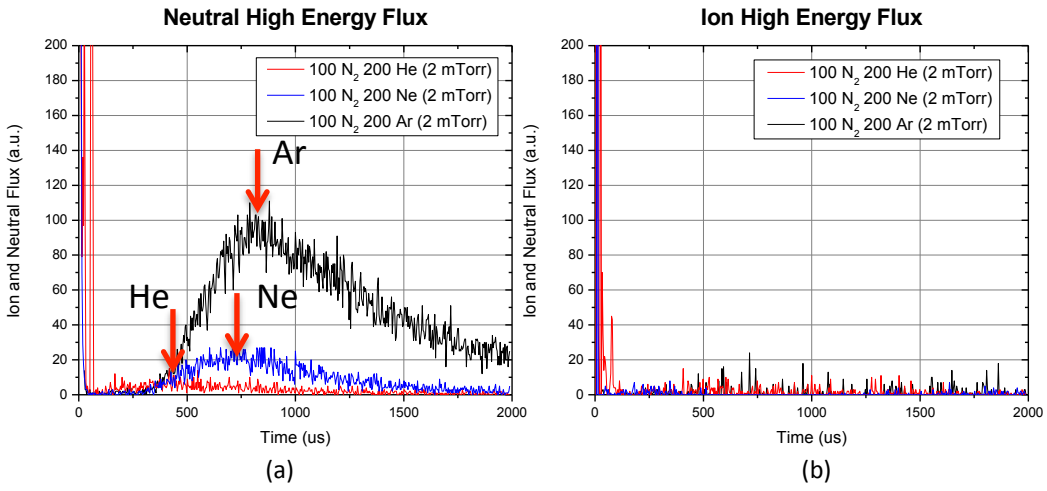

Figure 5.36: The energetic (>100 eV) flux reaching the intermediate focus for the given He, Ne, and Ar buffer gasses (with an N_2 Pinch) is largely neutral. The energetic ion and neutral flux originating from the EUV plasma is visible in the first 50 μs, and the expanding energized neutral buffer gas begins to arrive nearly 400 μs after the initial plasma formation. The largest flux corresponds to the largest mass due to its efficiency at absorbing the energy of the energetic ions and neutrals as they are scattered on their way to the intermediate focus. The peaks are diagrammed and labeled. Location is at 0.72 m. Error is approximately ±9.6%.

The sum of the fluxes are plotted in figure 5.37 with corresponding theoretical predictions plotted alongside. The model suggests that the average energy of the buffer gas species increases from 24eV to 60 eV to 315 eV with increases from 4 to 20 to 40 AMU. The increased energy is caused by the better mass transfer and increased collision likelihood with the larger buffer gas species. The number of species arriving is computed with roughly the same number for He and Ne, and nearly 150% increase with an increase to 40 AMU. With changes in pressure, it was observed that there was an optimal condition at 6 mTorr where the increase in number of species was maximized with the amount of energy deposited into the buffer gas. With variations in buffer gas mass at a constant pressure, there is simply an increase in measured hit counts with increasing buffer gas mass – at least at these conditions. Again, this is due to the increased power deposition of the

more efficient power absorption of like-mass collisions. Furthermore, microchannel plates are mass and energy sensitive detectors, and as such a higher mass species will create a larger signal at the same energy as a lower detector. When the measured theoretical buffer gas flux is adjusted to account for relative masses and total energy deposition into the buffer gas species, the flux measurements align quite well with those observed experimentally. A total of 46290±4443 (58% model error), 148483±14254 (11% model error), and 663387±63685 (5% model error) hits were measured for He, Ne, and Ar buffer gas respectively. The larger error assosciated with He is likely due to the fact that many carbon and oxygen contaminants are present in the buffer gas, which would absorb more energy and increase the measured flux above that observed theoretically. This effect is muted with Ne and Ar buffer gases since these species have higher cross sections and energy transfer than the gas contaminants. A plot of the estimated flux of species arriving is plotted in figure 5.37b along with the average buffer gas energy of species making the intermediate focus. In this particular set of experiments, it becomes evident that the choice of Ar over Ne or He is actually detrimental to the intermediate focus at 2 mTorr. A larger flux of heavier species, without a drastic reduction in energy will result in more damage, without the evident benefit of energetic pinch species suppression (if the model is followed in opposition of the additional deposition observed with Ar due to electrode ablation).

Table 5.7: Shown are the theoretically measured number of buffer gas atoms reacing the intermediate focus. The number of hits is compared to the measured flux by multiplying by the average momentum of the buffer gas species, and then multiplying by the conversion factor.

Buffer Gas Mass [AMU]	Number of BG Species at IF	Error [±]	Average Energy [eV]	Theoretical Hits [hits]	Error
4	69.0	8.3	24.0	283870	1626
20	64.0	8.0	60.0	409935	1395
40	92.0	9.6	315.0	1253520	4832

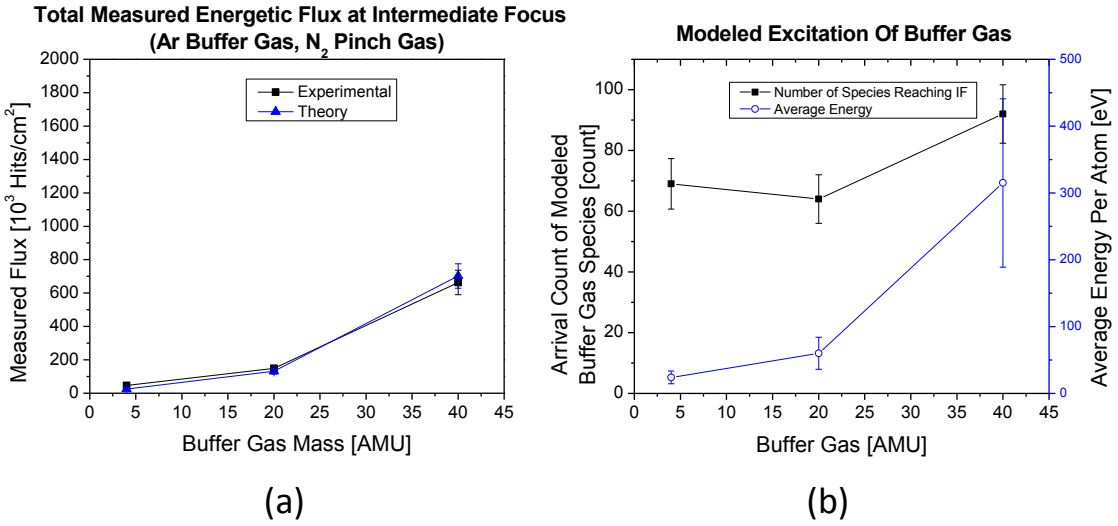

Figure 5.37: The measured flux of the high-energy atoms at the intermediate focus increases with increasing mass. The microchannel plates are momentum sensitive devices, and as such although there are less species reaching the intermediate focus at higher buffer gas masses, because they are more energetic and higher in mass, a larger signal is detected. (b) The theoretically modeled arrival flux and average buffer gas energy are shown. Location is at 0.72 m. Error not visible should be assumed to be the size of the marker.

The arrival of the peak buffer gas flux, plotted in figure 5.38, increases by 75% from 400±50 μs to 720±50 μs in going from 4 AMU to 20 AMU. A sequential increase to 40 AMU only increases the arrival time by 8% to 750±50 μs. The average measurement of modeled species reaching the intermediate focus predicts this time period quite well (the error bars are ±1σ and falls right around the range observed in the total flux, though this is plotted in reference to the peak flux whose error bars simply correspond to the error in peak time measurement). The increase

in arrival time has to do with an increase in energy transfer, as well as the number of species being created and where they are created. Although the He buffer gas will in general have less energy, since the pinch atoms retain much of their energy in a collision, they will travel faster with their reduced mass, and undergo fewer collisions. Increased buffer gas provides more energy to the buffer gas species, but increased collisions and slower mobility delay the arrival of the bulk buffer gas.

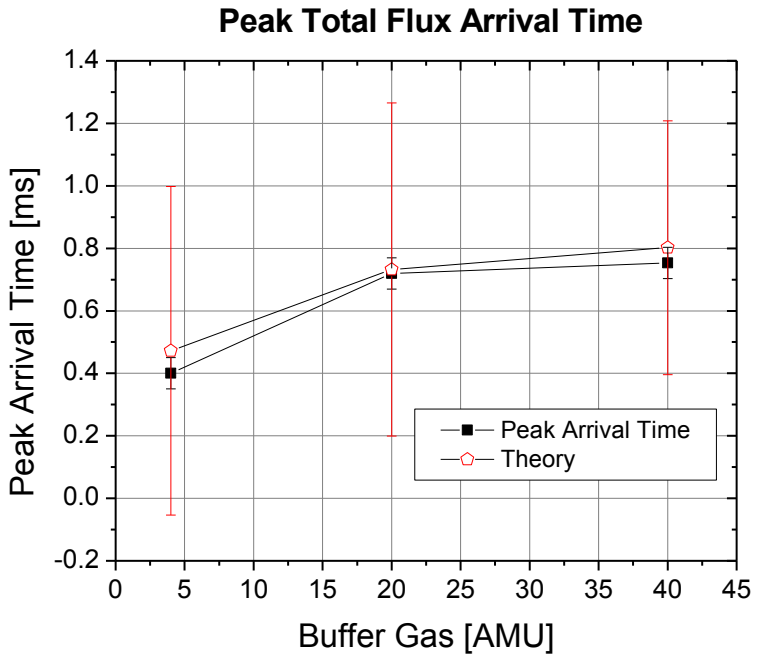

Figure 5.38: The arrival time of the energetic buffer gas species increases with increasing buffer gas mass due to increased collisions at the higher cross section.

Increasing buffer gas mass, and the cross section of elastic scattering, results in many more buffer gas species being energized, as well as a larger portion of the total energy deposition being absorbed. As shown in figure 5.39, there is an increased absorption of energy from ~30% to nearly 45% of the total energy deposited into the chamber via the EUV emitting plasma by going from 4 AMU to 40

AMU (this only accounts for ions/neutrals, not photon or electron heating). The increased mass in going from He to Ne allows for greater energy transfer, but due to the small amount of increase in the scattering cross section, there is a negligible change in total number of scattered species from 69 with He to 64 with Ne. Changing to Ar increases this total count up to 92 species reaching the intermediate focus with an introduction of 10000 test atoms.. The increased scattering of the newly energized species with higher buffer gas mass causes a net increase in total species observed in addition to an increase in the average energy of species arriving at the intermediate focus.

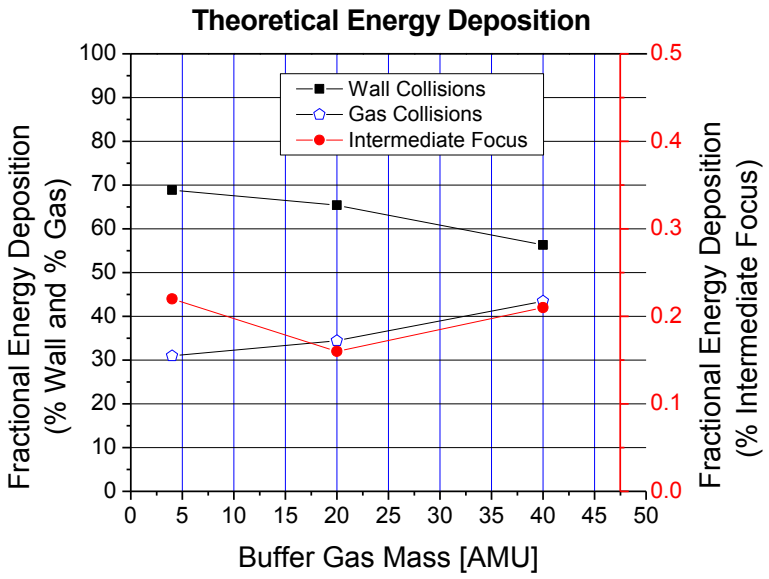

Figure 5.39: Energy deposition into the walls of the chamber is decreased with increasing buffer gas mass. This is because of more effective coupling between the Sn, Cu, and Mo electrode materials and the higher mass. As such, with each buffer gas collision, more energy is deposited into the buffer gas species.

5.4.6 Residual gas analysis

Analyzing the gas contaminants at the intermediate focus reveals that the primary effect of changing buffer gas is only to increase the partial pressure of the buffer gas species. This would provide concern in the use of reactive species inside of the EUV light emitting chamber, such as the use of carbon chained molecules for infrared light absorption, or using species from the halogens for Sn cleaning of collector optics. The slight increase in partial pressures using Ne is a consequence of the increased average energy of the buffer gas as mentioned previously. The increase in average temperature causes an increase in observed pressure, resulting in higher measurements of all species. A similar drop is observed with Ar buffer gas (lowest average buffer gas energy).

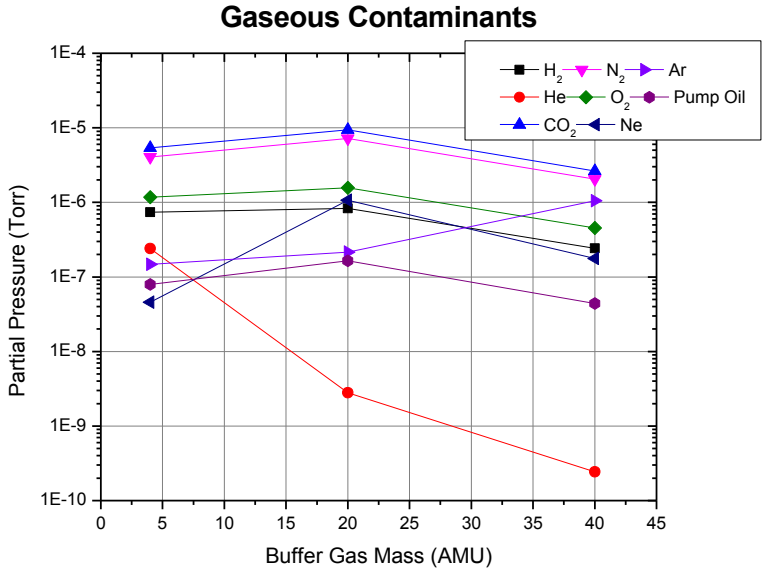

Figure 5.40: The typical pump oil and air contaminants dominate the partial pressure of the gas observed at the intermediate focus. Increasing buffer gas mass obviously contributes to increases in observed pressures of these species as well. Error not visible should be assumed to be the size of the marker.

5.5 Pinch Gas Effects

It will be shown in this section that changing pinch gas mass has greatest consequence to the energizing of buffer gas species. The energy transfer between two different scattering atoms increases as the difference between their masses decreases, and consequently, with the use of Ar buffer gas, an increase in energy transfer will be noticed as pinch gas mass is increased to 40 AMU. Unfortunately, deposition comparisons will not be available for this set of experiments due to the fact that all deposition experiments (not the ones made with the SNIFFED apparatus) required the removal of the collimated foil trap to achieve measureable depositions in a reasonable period of time. With the foil trap in place, the pressure near the pinch is increased due to the decrease in pumping rate through the small wholes. With the non-N_2 pinch gases, this was evidently necessary for functional operation of the source to occur. With the foil trap not in place, the resulting inadequacy of the pinch process resulted in direct discharge between the cathode and anode. So as not to destroy the tool, Si witness plate deposition analysis was not performed for these experiments.

5.5.1 Expanding EUV plasma components analysis

There is largely no effect observed on the electron temperature and electron density outside of the fact that it appears an increase in pinch gas mass results in an increase in density for the primary fast electron driven plasma, as shown in figures 5.41-5.44. This is likely due to the inevitable intermixing of gas species at the onset of gas flow. The peak photon generated electron temperatures fall in the range of

roughly 2.2±0.8 eV to 3.5±0.5 eV at location A, is only observed with Ar at 1±0.4eV at position B, and is not observed with any species at position C. In general the electron density is higher at position B than A due to a wider solid angle of photon acceptance, though most densities fall near $4\pm1.2x10^{13}$ cm^{-3}. The fast ion/electron generated plasma is measured with a peak temperature of 2.3±0.8 eV for Ar at position A (no observed plasma with He or Ne), 6±1 eV, 5±1 eV, 3±0.5 eV for Ar, Ne, and He respectively at position B, and 5±1 eV, 2±0.5 eV, 1.5±0.5 eV for Ne, Ar and He respectively at position C. It is generally observed that electron density is roughly the same at each condition for the second and third plasma expansions, which is to be expected since these two plasmas are generally formed with and supported by buffer gas. The second plasma is only observable at position A with Ar pinch gas, suggesting that energy transfer is an important part of the ionization of the buffer gas during this time period. The arrival of the second and third plasmas also increases at all other locations with increasing buffer gas mass due to the energy loss, and resulting slower arrival time, of the pinch gas species and slower electrons.

Position A

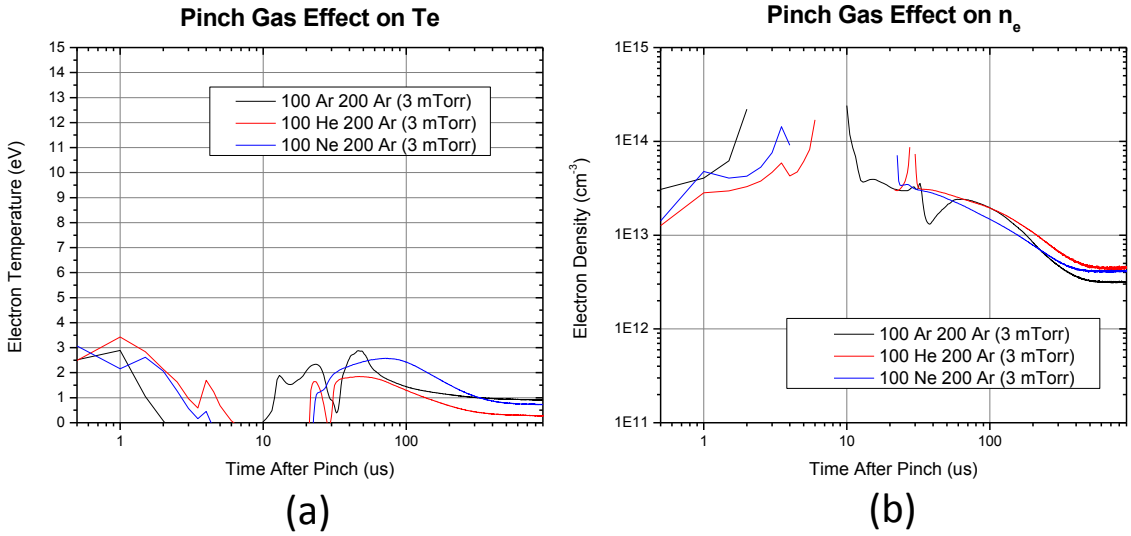

Figure 5.41: Shown are the electron temperature (a) and the electron density (b) inside the inner shell of the mock-up collector optic during the first millisecond after EUV emitting plasma formation at z=0.32 m. Three plasmas are observable: Fast electron driven (0-10μs), energetic ion/retarded electron initiated (10-30μs), and bulk EUV plasma expansion (30-1000μs). Electron temperature and density are largely not affected by the change in pinch gas pressure except for a change in the arrival time of the second and third plasmas. The sharp peaks in electron density that occur when Te disappears are simply mathematical errors formed as a result of the use of Te in the quotient for determining electron density. Location is at 0.36 m. Error is approximately ±12% for n_e and ±6% for Te.

Position B

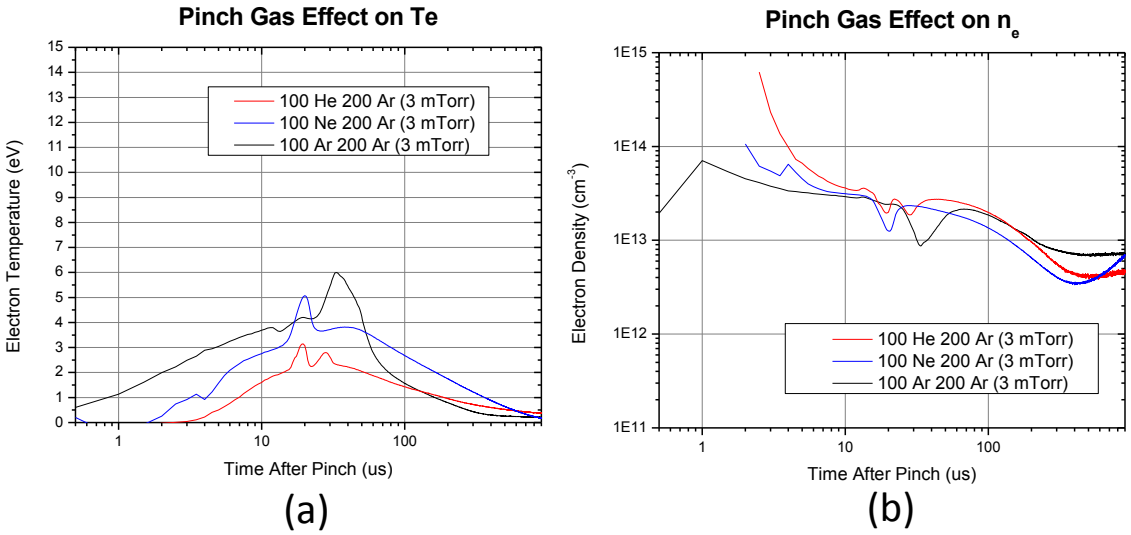

Figure 5.42: Shown are the electron temperature (a) and the electron density (b) between the inner and outer shells of the mock-up collector optic during the first millisecond after EUV emitting plasma formation at z= 0.32 m. Three plasmas are observable: Fast electron driven (0-10μs), energetic ion/retarded electron initiated (10-30μs), and bulk EUV plasma expansion (30-1000μs). The fast electron plasma appears delayed, though it's a function of lack of scattering of the high energy electrons. The arrival of the second and third plasmas is delayed with increasing pinch gas mass. The sharp peaks in electron density that occur when Te disappears are simply mathematical errors formed as a result of the use of Te in the quotient for determining electron density. Location is at 0.36 m. Error is approximately ±12% for n_e and ±6% for Te.

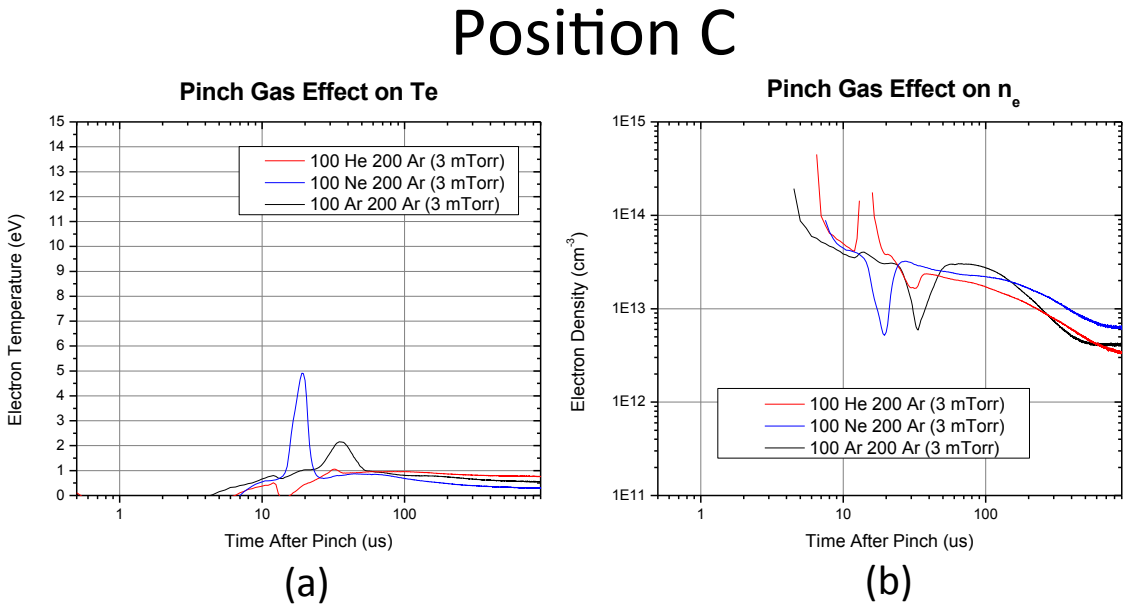

Figure 5.43: Shown are the electron temperature (a) and the electron density (b) outside of the mock-up collector optic during the first millisecond after EUV emitting plasma formation at z=0.32 m. Without direct line of sight to the EUV emitting plasma, none of the species exhibit ionization by photons. The second fast-ion generated plasma is observed to a small degree for each species, with Ne having the highest observed electron temperature. The arrival of this plasma is delayed according to pinch species, with Ar the latest due to its increased collision frequency with other argon buffer gas atoms. The sharp peaks in electron density that occur when Te disappears are simply mathematical errors formed as a result of the use of Te in the quotient for determining electron density. Location is at 0.36 m. Error is approximately ±12% for n_e and ±6% for Te.

5.5.2 Charged flux analysis

The evidence of these three different plasmas is once again observed using the Faraday cup for charge analysis (fig 5.44a-c). The initial negative peak at the start of the measurement correlates to the arrival of the fast electrons and slightly slowed electrons from the first and second plasmas. After this, and right around 50 μs are the energetic ions. The small amount of ion flux, coming from the reflected high-energy ions ejected from the EUV emitting plasma, is visible starting at ~100μs. It should be noted that operating the pinch with these conditions fell into a very non-optimal pinch with the foil trap in place. This is a possible explanation of the

strange oscillation observed in figure 5.44c. If multiple arcs occur within a rapid period of time, the photon/electron signal will be staggered as it is shown, or this could simply be the results of offset noise signals between the positive and negatively biased measurements.

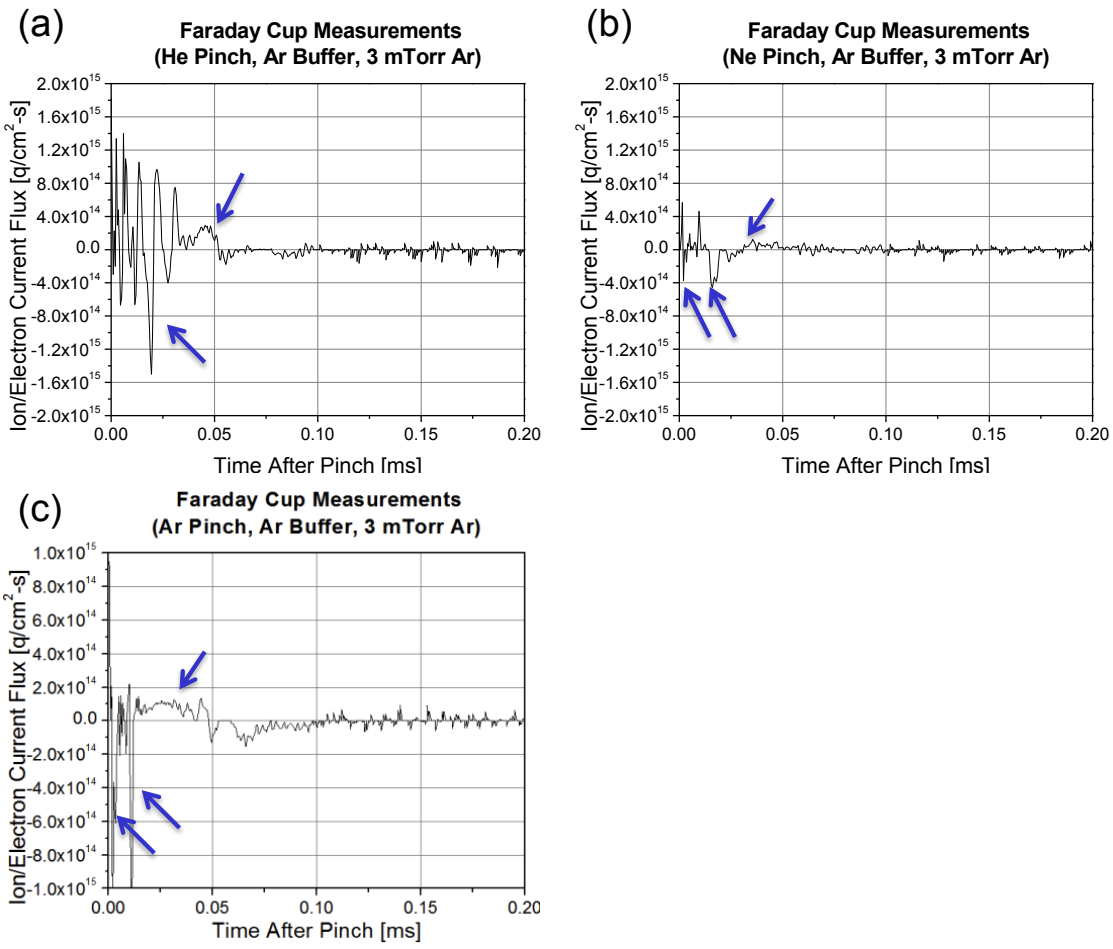

Figure 5.44: Figures a-c show the Faraday cup measurements at the intermediate focus for each pinch gas utilized. The signals were averaged over 256 trials with a positive 100 V and negative 100 V bias applied to remove noise. The resulting signals of each of these biases were stitched together to proved the presented data. With each of these conditions, the initial arrival of the most energetic ions is observed in the first 50 μs, followed by the buffer gas plasma with increasing time as pinch gas mas is increased. The locations of the fast electron, ion-coupled electron, and ion flux components are indicated from left to right. The electron presence is slightly unclear as the pinch was not very stable and resulted in multiple pinches. The EUV plasma core expansion begins to arrive at 0.10 ms Location is at 0.72 m. Error is approximately ±31%.

Once again very little net flux is observed, though using Ne creates a positive net flux of ~2±0.8x10^{10} ions-cm^{-2} while the other two gasses shown net currents of ~2±0.8x10^{10} e-cm^{-2}, as shown in figure 5.45. From figure 5.44, it is noticeable that the most pinch originating ions were observed with the He pinch. Given the low energy transfer of He atoms to the Ar buffer gas, as well as the reduction in elastic scattering cross-section due to He's small size, the likelihood of reaching the intermediate focus while retaining positive charge is increased. The arrival time of the fast ions increases with increasing pinch gas mass, as is to be expected given the slower transit times of heavier species of similar energies. The third plasma begins to arrive nearly 100 μs after EUV emitting plasma generation as is verified by the microchannel plate analysis. In general the amount of positive flux is reduced with increasing buffer gas mass due to more ions either undergoing charge exchange or being deflected into a wall because of the additional scattering collisions caused by the more massive element. It is unclear whether the oscillating signal in figure 5.44c is caused by rapid discharge, or if the ions and electrons (they are real signals, not just noise) actually are produced in this fashion by the z-pinch. If it is a rapid signal change caused by sequential pinching, it is probably the reason that the total positive signal isn't higher than that of Ne, though this is just pure speculation.

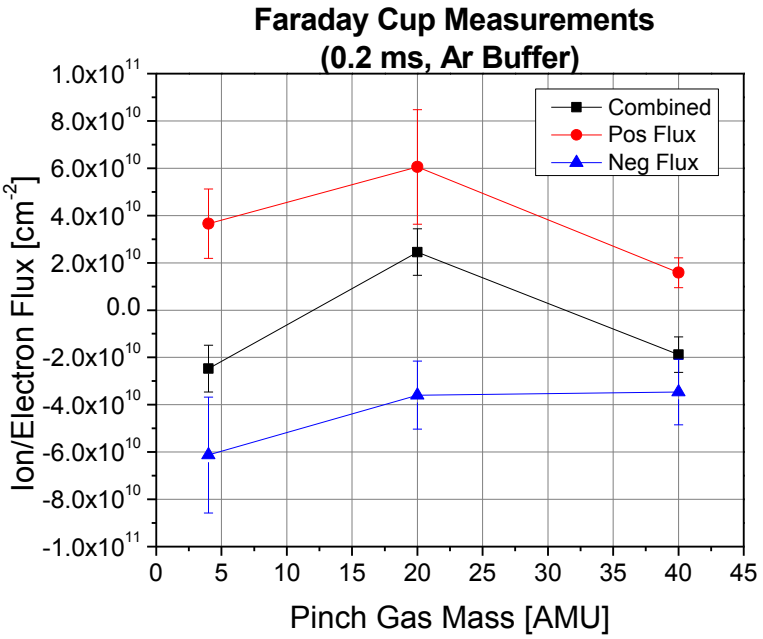

Figure 5.45: There is a net positive charge flux observed using Ne as a pinch gas, while He and Ar show a net negative charge flux. In general the total negative flux increases with increasing pinch gas mass, while a general net positive flux is reduction is observed. Location is at 0.72 m.

At 3 mTorr, with no change to the buffer gas mass, there is negligible total erosion/deposition of the Sn coated quartz crystal at each of the pinch gas conditions. This result, in light of the fact that more than 95% of the total deposition exists as carbon or oxygen, suggests that deposition and erosion are largely controlled by the mass and pressure of the buffer gas plasma. As shown in figure 5.46, it is also theoretically observed that there is less than 10% change in fractional energy deposited into the buffer gas with an increase in pinch mass from 4 to 40 AMU. Because there is more or less the same amount of ion/neutral energy being created by the pinch, the result is that there is no real effect on the bulk of the buffer gas species. Although there is a reduction in energy caused by the mass change of the pinch gases, more of the energy transfer originates from the much more massive electrode materials that are accelerated through the buffer gas. With the buffer gas

having relative the same amount of average energy (the peak energy is different as shown by the microchannel plate measurements), and similar densities as shown in figures 5.40-5.43, there should be little change in the carbon/oxygen removal from the walls. Consequently the interaction with the walls produces similar amounts of contaminant removal and there is negligible change in deposition/erosion rates with changing pinch gas mass.

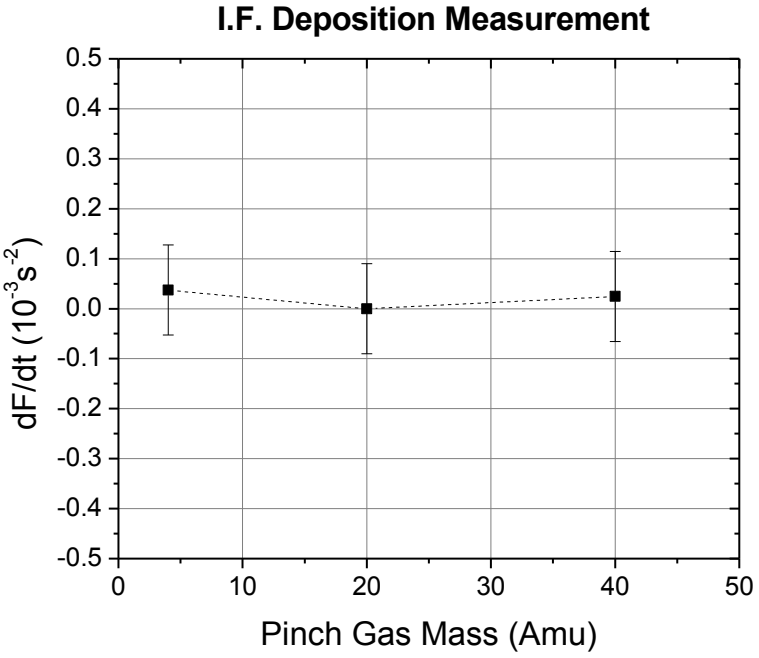

Figure 5.46: There is no evident effect of pinch gas mass on the deposition or erosion of Sn off of the quartz crystal, suggesting that buffer gas is the primary contributor to this effect. Location is at 0.72 m.

5.5.3 Theoretical versus experimental energized buffer gas analysis

Recalling the theory that the energetic flux measured at the intermediate focus after 100 μs originates from the energizing of buffer gas through energetic ion/neutral scattering, it is visible in figure 5.47 that with the same buffer gas mass, the arrival times of the flux more or less does not change. This is to be expected

since the mobility of the buffer gas is largely unchanged, with only minor differences in the total average energy of the buffer gas species. A theoretical comparison of the total measured flux suggests that there is an increase in detrimental flux reaching the intermediate focus at lower pinch gas mass, although there is actually a decrease in the total amount of species reaching the intermediate focus (136±12,123±11,93±10 counts for He, Ne, and Ar respectively shown in figure 5.48b). When energy and mass considerations are once again taken into consideration, the profile observed in figure 5.47 is measured. The less massive He pinch species have poor energy transfer to the buffer gas, and consequently have more average scattering collisions before thermalization occurs. With increasing pinch gas mass, there is an increase in energy transfer, but fewer scattered buffer gas species present. The ultimate result is that using He has an average arrival buffer gas energy of 20 eV, while using the more massive Ar species in the model results in an average arrival energy of 615 eV. The increased energy and mass of the Ar atoms results in a larger observed signal. There is an average of 60 eV per Ne scattering atom reaching the intermediate focus, though the additional mass creates a signal that is slightly larger than that observed with He pinch gas. (Once again the same calibration factor used in sections 5.3.5 and 5.4.5 was used here. Refer to section 4.7 for a more detailed analysis of the model's calibration.) There is a pronounced amount of charged flux at these pressures, suggesting that total charge exchange neutralization is not adequate below 6 mTorr when compared to the results witnessed in section 5.2.

It is interesting to observe that varying the pinch gas causes a change in the relative (model to theory) error. With He, Ne, and Ar respectively, a total measured flux of 283870±27251 hits/cm^2 (50% model error), 409935±39353 hits/cm^2 (20% model error), and 1253516±120337 hits/cm^2 (15% model error) were observed. The effect of overestimated flux using the calibration factors is decreased with increasing pinch gas species. If one considers, once again, that the true buffer gas environment has a significant proportion of low mass O and C contaminants, then the He and Ne pinch gases would be more largely effected by these species since they are very close in mass. As such, the measurement of the flux with He pinch gas in comparison to the model should suggest a larger overestimate in measured flux because less energy is lost by the modeled pinch species in buffer gas collisions. This produces more species as scattering is increased, without an incredibly significant change to the energy transfer. This supports the suggestion that not modeling O and C in the buffer gas is a source of error in the model.

Another possible source of this error is due to the changes in pinch conditions. The calibration used for these fits was based off of the N_2 pinch and the number of nitrogen ions/neutrals generated. The calibration factor was said to account for the underestimation of this total pinch gas flux, and consequently with a change in pinch gas species it is possible that there is a change in the total flux of pinch gas ions/neutrals. This factor is very difficult to measure experimentally due to the fact that no knowledge of the composition of the >28 keV flux is available.

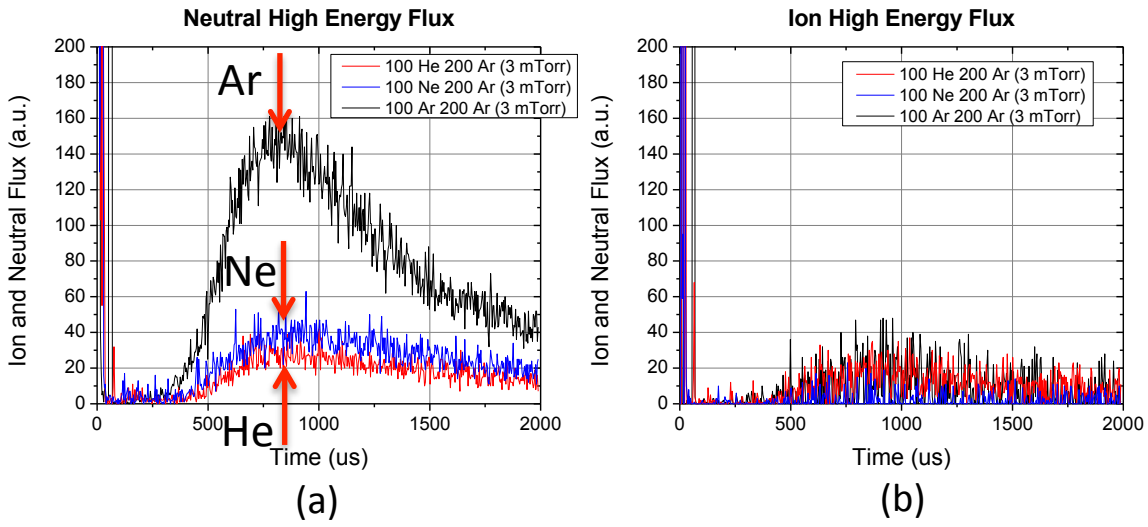

Figure 5.47: Increasing buffer gas mass serves only to increase the amount of energy deposited into the stagnant buffer gas species. This results in an increased average energy of the buffer gas flux at the intermediate focus. The arrival time, however, is the same for each pinch gas species, once again suggesting that buffer gas mass is the key contributor to this observed flux arrival time. Location is at 0.72 m. Error is approximately 10%.

Table 5.8: Shown are the theoretically measured numbers of buffer gas atoms reaching the intermediate focus as a function of pinch gas mass. The number of hits is compared to the measured flux by multiplying by the average momentum of the buffer gas species, and then multiplying by the conversion factor.

Pinch Gas Mass [AMU]	Number of BG Species at IF	Error [±]	Average Energy [eV]	Theoretical Hits [hits]	Error
4	136	11	20.8	492365	42220
20	123	11	60.0	506922	45707
40	93	10	615	1090100	113038

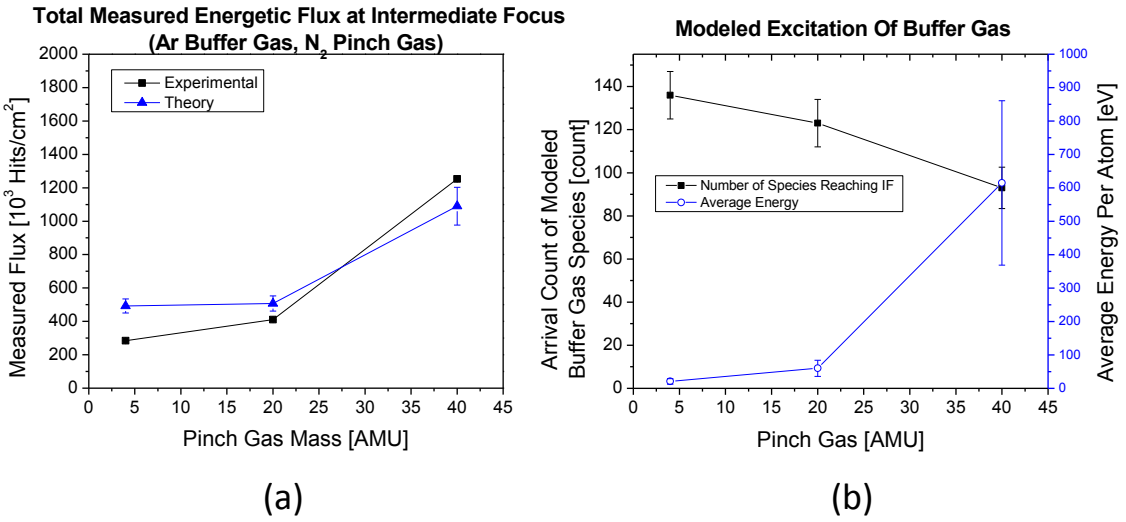

Figure 5.48: (a) Increasing buffer gas mass serves only to increase the amount of energy deposited into the stagnant buffer gas species. This results in an increased average energy of the buffer gas flux at the intermediate focus. (b) The theoretically modeled arrival flux and average buffer gas energy are shown. Location is at 0.72 m.

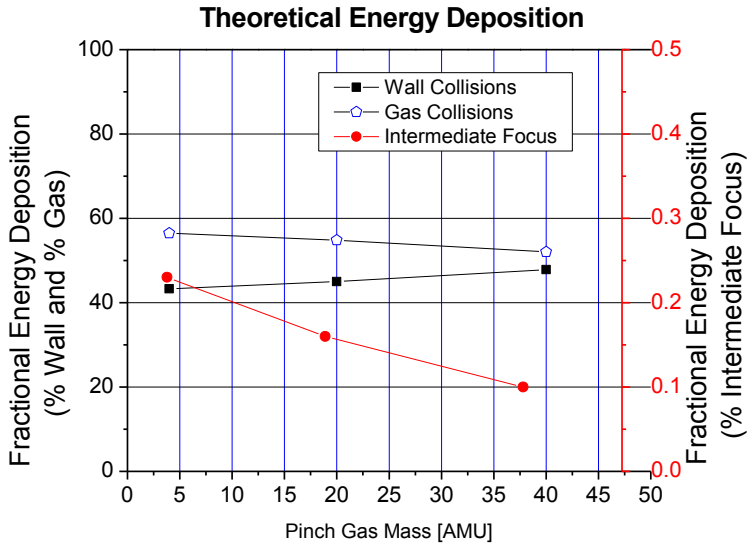

Figure 5.49: There is only a slight increase in fractional energy absorbed within the buffer gas. In general, as the pinch gas is increased, the resulting energy deposition into the buffer gas causes a reduction in average energy reaching the intermediate focus.

The peak flux arrival time is a strong indicator that buffer gas is the sole contributor of the second flux measured with the microchannel plates. There is

negligible change in the arrival time of the measured peak flux, which comes to the intermediate focus on average 800±25 μs after EUV emitting plasma formation. The model predicts that with He arrives with an average arrival time of 580±477 μs, with Ne the time increases to 547±475 μs, and with Ar the time falls around 524±518 μs. The error bars are the standard deviations of the arrival times for the conditions. These values are somewhat misleading as the representative data calculations come from a relatively small amount of measured species reaching the intermediate focus. With 10000 test atoms, nearly 380000 first generation buffer gas species were created for the Ar pinch gas trial. Out of this number of species, only 93 reached the intermediate focus! This coupled with the fact that only the first generation of scattered species was monitored, does not provide the highest level of accuracy in comparison to the experimental measurements. They do, however, help to provide a first order quality prediction of arrival time.

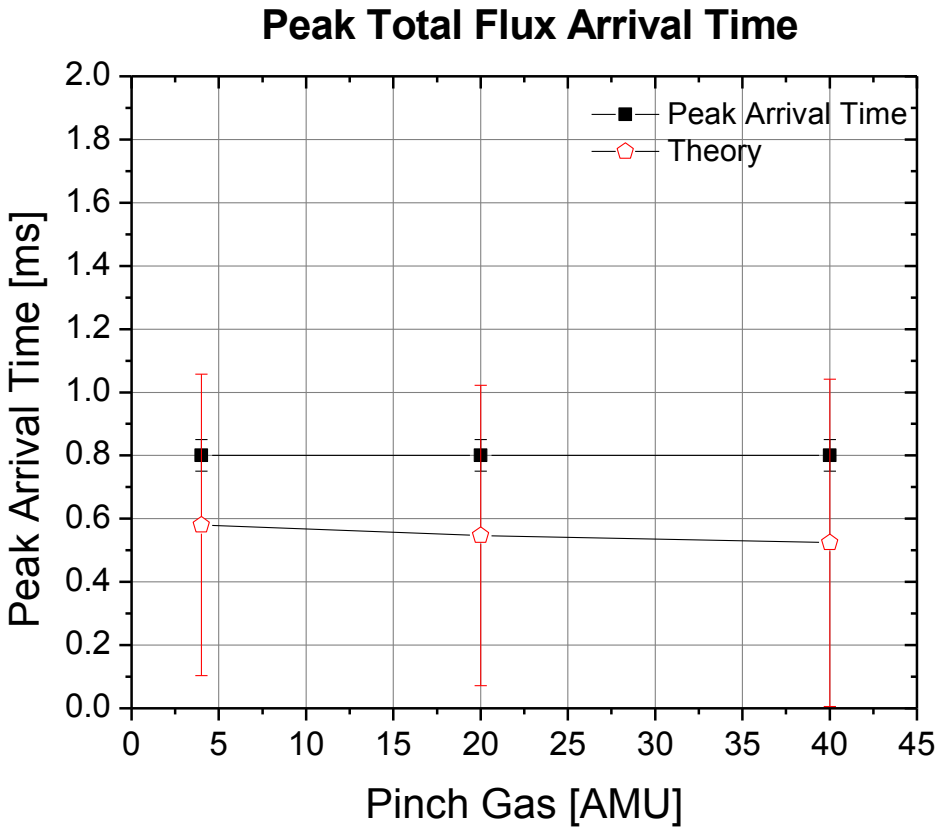

Figure 5.50:The arrival time of the peak flux remains relatively the same at each pinch gas condition, suggesting that the arrival time of at the intermediate focus of the buffer gas flux is more dependent on the mobility and ongoing collisions than it is the energy of the colliding species.

5.5.4 Residual gas analysis

Once again, an examination of the partial pressures of gas contaminants at the intermediate focus revealed the presence of the carbon contamination as well the oxygen contamination from water molecules cracked off the surface of the chamber. It should be noted that while there are small increases in the total partial pressure of each of the utilized pinch gases, the difference is considerably less than that observed when using different buffer gas species. The injection of gas through the cathode is only at 100 sccm, while buffer gas is injected at 200 sccm for these

trials. Ultimately, there is very little noticeable difference between different conditions other than the changes in pinch gas partial pressures.

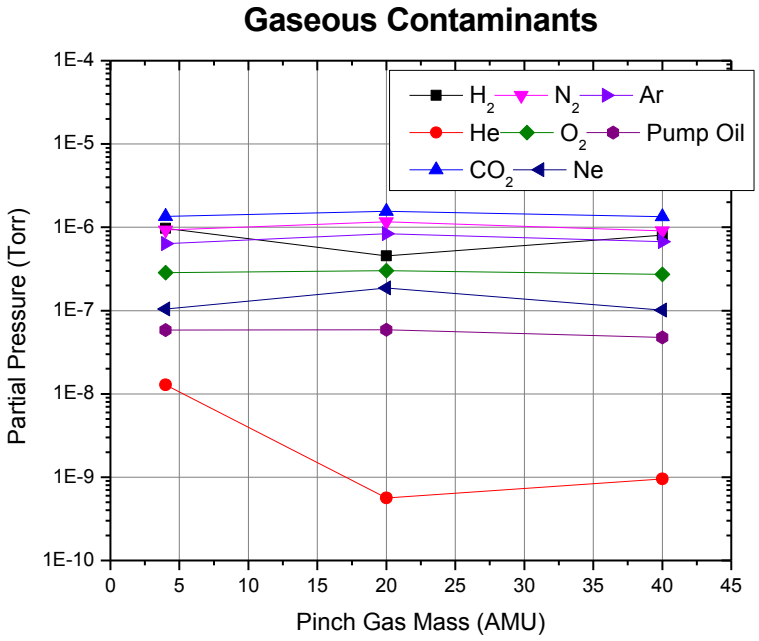

Figure 5.51: The gaseous contaminant analysis shows no extraneous results, with the similar proportions between pump oil, air contaminants, and introduced pinch gas species being similar to those observed with the pressure and buffer gas trials. Error not visible should be assumed to be the size of the marker.

5.6 Error Analysis

There is a certain degree of uncertainty associated with any theoretical or experimental measurement. Understanding the amount of error associated with any given data point lends credence to the results trying to be conveyed. For these sets of experiments, representative error calculations for the Faraday cup measurements, triple probe measurements, residual gas analysis, microchannel plate measurements, as well as the computational uncertainty are presented in the following subsections. Error measurements for these experiments are based off of

the uncertainty of certain components. The error propagation rules used for any of the given uncertainty calculations are as follows, where σ is the measured uncertainty of a value x, y, or the calculated value u:

$$u = x \pm y : \sigma_u = \sqrt{\sigma_x^{\,2} + \sigma_y^{\,2}} \tag{5.1}$$

$$u = xy : \left(\frac{\sigma_u}{u}\right) = \sqrt{\left(\frac{\sigma_x}{x}\right)^2 + \left(\frac{\sigma_y}{y}\right)^2} \tag{5.2}$$

$$u = X^{\pm y} : \frac{\sigma_u}{u} \approx y\frac{\sigma_x}{x} \tag{5.3}$$

For the purpose of these experiments, this uncertainty serves as a measurement of error to give the range over which the calculation is believed to exist in light of the errors introduced by the measurement process.

5.6.1 Faraday cup error

The sources of error in the Faraday cup current flux measurements stem from the measurement of the potentials across the resistor, the measurement of the limiting orifice area, the measurement of the resistance. The two potential measurements (for determining the voltage drop across a resistor thus measuring the current to the Faraday cup) had measurement uncertainty of ±0.10 mV. This results in potential difference uncertainty of ±0.14 mV. The area of the radius of the limiting orifice had a measurement error of 0.5 mm using a micrometer, resulting in a measured area of 0.031±0.013 cm^2. A 15±1.2 Ω resistor was used in the current measurement (error provided by the manufacturer). For a representative calculation, a 1.5±0.14 mV potential difference, between the two voltage probes,

results in a current flux measurement of 0.0032±0.0010 A-cm^{-2}, or ~ 31% error. Obviously the amount of incoming signal readily influences this error calculation, and as such higher potential difference have less error, and lower potential difference have more error. In general, however, 31% serves as a high end error measurement for the areas of interest in the results presented.

5.6.2 Triple probe error

The error of the triple probe measurements can be broken down into two components: electron temperature and electron density. The electron temperature error is easily calculated because of the fact that Te~1.44 V_{d2}, where V_{d2} is simply the potential difference between the first and second probes as shown in section 3.5.3. The measured noise in these experiments was higher than that of the faraday cups, despite using the same probes, due to the fact that the triple probes themselves are less shielded from the electrostatic noise created by the discharging pinch. The signal, however, was larger and the resulting error less severe. The measured error of the potential difference V_{d2} was ±80 mV. With a representative measurement of 1.38±0.08 V, an electron temperature of 2.0±0.11 eV (5.8% error) is measured. For a 5 eV measurement, only 2.3% error is observed, and at 0.5 eV 23% error is observed.

This error propagates into the measurement of electron density based on the dependence of n_e of the factor $Te^{-1/2}$ as shown in equation 5.4. Further error is introduced with the measurement of the probe's surface area, the impedance of the resistor, and the measurement of the potential difference across the resistor.

$$n_e(t) = \frac{i_{sat}(t)}{0.61 e A_x} \sqrt{\frac{M}{T_e(t)}} \tag{5.4}$$

The probe area (A_x) was found to be 4.30±0.5x10^{-6} m^2, immediately introducing an 12% error. The resistance was calculated at 119±3 Ω (manufacturer provided), with a typical voltage drop of ~2±0.08 V. This results in a current (i_{sat}) of 0.017±0.00079 A through the resistor. The resulting current flux is then calculated at 3900±490 A-m^{-2}. The inverse square root of Te, found using equation 5.3, is 0.71±0.014 eV$^{-1/2}$. Multiplying these terms results in a value of 2800±350 A-m^{-2} eV$^{-1/2}$. From there, the remaining terms are multiplied out with M=M_{Ar}=6.6x10^{-26} kg, e=1.602x10^{-19} Coul, to achieve a final value of 1.8±0.23x10^{13} e-cm^{-3}, or roughly 12% error.

5.6.3 Residual gas analyzer error

The error involved in the residual gas analyzer measurements comes from the company as a being sensitive down to 10^{-11} Torr, and consequently the error introduced by measurement is relatively inconsequential. Over time, however, with variations in the condition of the materials used in the ionization process, degradation of the total calibration of the detector occurs. In order to compensate for this, the integrated total pressure of the measurements was calibrated to the measured pressure using an pirani ion gauge. The accuracy of this gauge is assumed to be ±15% to err on the safe side of measurement.

5.6.4 Microchannel plate error

Error in the microchannel plate flux measurements is a consequence of the calibration process by which the number of hits measured by the microchannel plates are converted to number of ions/neutrals observed for a given energy. The calibration formula is shown in equation 5.5, where $X_{(1400eV)}$ (10865±104 hits) is the total number of microchannel plate hits measured with 1400 eV and 1+ charge isolation using an ion gun set at 1400 eV output voltage. I_{FC} ($0.22\pm0.05\times10^{-9}$ A) is the total current measured using the faraday cup in a time period t (60±2 s), and %ΔE is the fraction of this total current that is attributable to the flux at 1400 eV (0.071±0.011). $DE_{(1400\ eV)}$ (0.18±0.02) is the detector efficiency at 1400 eV. Using these values, the calibration factor is determined to be 96000±27000 atoms/hit, which is a 28% error without including the error taken into account by taking the square root of the hits and detection efficiency at an actual measurement. This calibration value is for the microchannel plates of the energetic energy analyzer, which was a set of plates over 5 years old. The corresponding calibration factor for the neutral energy analyzer and the plates used in the SNIFFED apparatus had error values of 9% and 10% respectively.

$$N = C\frac{X_{(E)}}{DE_{(E)}} = \frac{DE_{(1400eV)}I_{FC}t\%\Delta E}{X_{(1400eV)}e}\cdot\frac{X_{(E)}}{DE_{(E)}} \tag{5.4}$$

5.6.5 Silicon witness plate measurements

The last experimental measurement that requires error analysis is the deposition analysis of the Si witness plates. Si was chosen as a substrate layer due

to its highly crystalline nature that results in very planar surfaces. Measurements of deposition step height was made by dragging the profilometer needle from an area unexposed (plain Si) to an area of deposition. This provides a very planar region from which to measure the deposition amount with a decent amount of accuracy. A typical profilometer measurement is shown in figure 5.52. The error measurement then proceeds using the average roughness of a measurement for both sides. In this representative case, the Si side (which was used to level the profilometer measurement) had an average height of ~0.05±1.1 nm and the deposited side had a height of 14.5±3.4 nm. The propagation of error in this measurement results in a step height of 14.5±3.6 nm. This measurement was made using 432000 pulses, so the deposition rate is calculated to be $3.4\pm3.6\times10^{-5}$ nm/pulse, or roughly 25% measurement error.

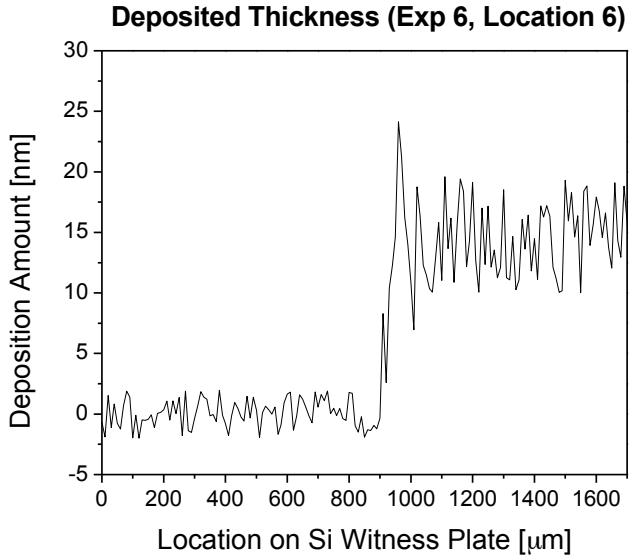

Figure 5.52: Shown is the profilometer measurement of the step height from bare Si to the film deposited by the EUV emitting plasma for experiment 6 (22 mTorr Ar buffer gas, N_2 pinch gas, 432000 pulses). The Si side had an average height of 0.05±1.1 nm while the deposited side had a height of 14.5±3.4 nm resulting in an step height of 14.5±3.6 nm

5.6.6 Model error

The two computational results presented in this dissertation consisted of a comparison to the flux measurements made with the microchannel plates, and a comparison to the deposition amount observed at various locations. The predominant method of error calculation involved taking the square root of the experimentally derived counts for each given measurement. The inclusion of the microchannel plate calibration factor in the calculation of hit flux from modeled atom flux also introduced error in the theoretical measurement. For example, the theoretical calculation of the hit flux at 2 mTorr Ar buffer gas using the N_2 pinch was calculated to have an error of 22% due to the contribution of error from the detector efficiency (0.03±.005), the base calibration (203±20), and the square root of the total its (90±9.6).

5.7 Applications to Industry

The work in this paper has largely been funded by industry with the express intent of better understanding the cause and effect relationship between debris mitigation techniques and debris transport. When this work was originally postulated, it was not completely understood that plasma was so prevalent in the light source chamber, and that it could cause such concern. The net reaction by industry, in an effort to maximize the lifetime of collector optics, has been to increase the chamber pressure up to 1 Torr, and use either Ar or H_2 buffer gases. Hydrogen buffer gas is largely used for its Sn cleaning capabilities, as well as very high EUV light throughput. For the current consideration, however, the effects of

using 1 Torr of Ar buffer gas will be considered under the pinch conditions described using the N_2 pinch gas.

When run through the debris transport model, it becomes immediately clear that energetic ions and neutrals, as well as scattered buffer gas species, are of much less consequence at 1 Torr of Ar buffer gas (fig. 5.53). Nearly 99.2% of all energy from the EUV plasma is deposited into the gas, with the remaining 0.8% deposited into the plasma-side wall. While this sounds optimal, considering sputtering is much less of an issue without high-energy ions and neutrals, further problems exist.

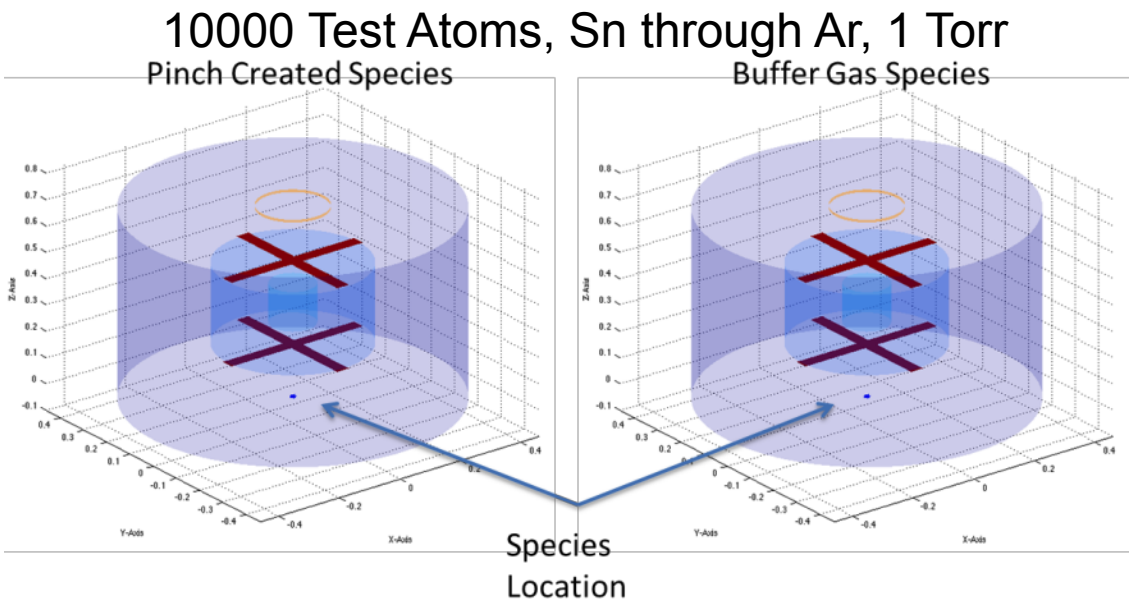

Figure 5.53: Shown are the propagation paths of the pinch species and the scattered buffer gas species for an N_2 pinch and 1 Torr of Ar buffer gas. The pressure sufficiently absorbs all of the species' energy within the first few millimeters, revealing that energetic ions and neutrals are largely dealt with by the 1 Torr.

As mentioned in section 5.2.2, at these pressures, the process of photoionization becomes much more critical. If the same photon flux is utilized, approximately $7x10^{15}$ total photons are created in a single pinch. If the absorption

profile diagrammed in figure 5.54 is accounted for, then in a given pulse, only $3x10^{14}$ photons will reach the intermediate focus (assuming 100% collection of EUV photons). In reality another 25% is lost on reflectivity off of the mirrors, 50% is lost to the back wall (for grazing incidence collectors), and 70% is lost in lack of collection efficiency [62]. In total this suggests that $1.5x10^{13}$ EUV photons will reach the intermediate focus for each pulse. If this is scaled to 100 kHz, as is likely to be used in industry, a total flux of $1.5x10^{18}$ EUV photons/s will be collected. This corresponds to an intermediate focus power of a mere 0.25 W (they need over 125 W for initial integration points).

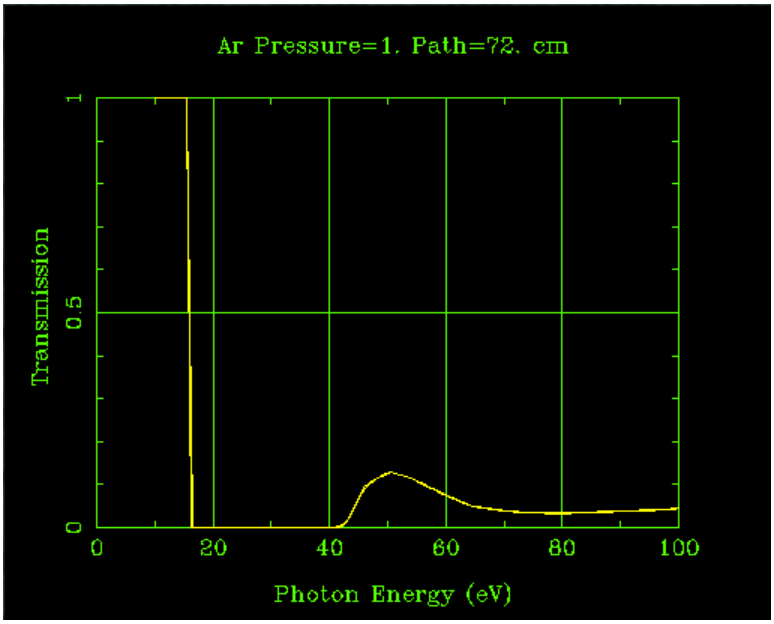

Figure 5.54: The absorbtion of EUV light is quite significant in a 1 Torr Ar environment. For the distance of 0.72 m, only 5% of all EUV light is transmitted. This value increases to 91% with the use of H_2, which is one of the reasons its use is more popular with the lower plasma ejecta energy laser produced plasmas [85].

If we assume that all of these photons are focused onto a 1 mm diameter orifice, at 1 Torr pressure (neglecting out of band radiation with the assumption that mirrors don't optimally reflect wavelengths in the VUV range), a plasma will be

generated with a rate of $\sim 10^{16}$ e/cm^2-s. Given how much of an issue sputtering and wall contaminants were at the three orders of magnitude lower plasma densities observed in this dissertation, this plasma clearly has the potential to cause damage to down field components if a post-intermediate focus mitigator is not utilized. Indeed industry has found the need to create such devices, where created very high pressure in a very short gap, thus extinguishing the plasma before it can propagate to the next chamber.

The EUV photons also have the unfortunate side effect of cracking carbon molecules that are located on the chamber walls. While the debris transport does not consider the slow diffusion of species across the chamber, this process does occur and actually allows the transport of thermalized Sn atoms to the collector optics and the intermediate focus. Ultimately, the only true solution to solving this problem is to limit the mass of the Sn target being utilized, and develop in-situ cleaning systems that allow for rapid return to high reflectivity values without considerable tool downtime. Work is currently ongoing in the Center for Plasma-Material interactions to address just this issue with the use of a hydrogen plasma generated using the collector optic as an antenna.

CHAPTER 6

FUTURE WORK

While the work presented within this thesis provides a solid understanding of the contributions to, and the propagation of debris from the EUV light emitting plasma to the Intermediate focus, there is still more work to be done. The results of this work highlight the need for a better understanding of wall contamination removal. Further depth is required to be able to quantify the contribution of EUV photon cracking of carbon molecules, as well as surface sputtering by the propagation of the EUV plasma through the chamber. A further investigation into the axial dependence on electron temperature (as opposed to the radial dependence highlighted in this section) as a function of distance from the EUV plasma would help to completely quantify the cooling of the EUV plasma as it propagates through the chamber. In regards to the model provided, further improvements could be made on the handling of wall surfaces. While sputtering calculations were largely not considered necessary to describe the measured results, a better understanding of contaminant transport could be had if the wall could be modeled with changing material parameters. This incorporated with an inclusion of the carbon and oxygen contamination deposition rates would allow for a very in depth analysis of how carbon and oxygen contaminants are reaching the intermediate focus. Lastly, it is evident that - especially with industry utilized 1 Torr pressures - a complete spectrum analysis of the emitted photon flux through the EUV and VUV ranges would allow for a better understanding of the coupling between EUV photons and

the production of a secondary plasma. While these are just a few of the many possible next courses of action, any one of these would help to better understand methods by which the lifetime of a lithography tool could be extended.

CHAPTER 7

CONCLUSION

The goal of this research was to better understand the mechanisms by which debris is transported to the intermediate focus of an EUV light source from the plasma used to create 13.5 nm photons. Tool manufacturers have largely relied on the use of high pressures of buffer gas to prevent extremely energetic plasma generated ions and neutrals from reaching and damaging the collector optics. Damage results in the form of sputtering, as well as deposition, and while this problem has largely been remedied with pressures approaching 1 Torr in use, the story is not told to completion. The last chapter in debris mitigation involves an understanding of how the debris, that no longer hits the collector optics, is distributed through the vacuum chamber.

At lower pressures, even though the energetic ion spectrum is considerably reduced, there is still a considerable amount of non-EUV photon debris reaching the intermediate focus. Anything that is not an EUV photon has the potential to damage down-field optical components, which increases the cost of ownership of the tool, and ultimately could make EUV lithography a non-viable option for next generation lithography. This dissertation seeks to provide an understanding of where this debris comes from, how it is transported to the intermediate focus, and what are the possible consequences of its existence. Three different parameters, chamber pressure, buffer gas mass, and pinch gas mass, were altered to understand how the ejected debris from the EUV emitting plasma interacts with the buffer gas to affect

deposition rates, intermediate focus facing component charging, as well the generation of a damaging energetic flux observed nearly 100 μs after. Experimental results were coupled with a Monte-Carlo atom path determining program, which utilized gas scattering as well as wall interactions to analyze the ongoing interactions in an energetic plasma emitted atom's lifetime.

It was shown experimentally that the EUV emitting plasma goes on to make three separate secondary plasmas within the vacuum of the light source chamber. The first generated plasma is caused by the ejection of energetic 30 eV electrons from the bulk of the EUV emitting plasma. These electrons are not coupled to the plasma, so they do not experience the coulombic pull of the EUV plasma, which is still significantly electronegative. Peak values of 6±1 eV were observed at 12 mTorr in the center of the chamber, with an electron density of ~5±1.8x10^{13} cm^{-3}. In general, it was observed that increases in pressure up to 12 mTorr from 0.3 mTorr increased the plasma temperature and density for this first plasma. It was further shown that decreasing buffer gas mass greatly increased the electron temperature, with a peak of 11±2 eV observed using He buffer gas at 2 mTorr. The opposite trend was observed, with the less tightly bound electrons of Ar generating nearly an order of magnitude larger density around 5±1.8x10^{13} cm^{-3}. Increased collisions were found to reduce the electron temperature above 12 mTorr. Increases in pinch gas served only to increase the arrival time of the second and third plasmas, and very little change was observed in the fast electron driven plasma. The second plasma was generated by the interaction between the ejected energetic (up to 50 keV) ions and and the slightly less energetic electrons that did not escape the pull of

the energetic ions. Electron temperature and density were found to increase with increasing pressure as more buffer gas species were incorporated into the EUV plasma to create more liberated electrons of high energy. For the most part, higher electron temperatures in the range of 4-7 eV were measured in between the two collector optics with less energy observed inside of the inner collector (less energy transfer with the forward peaked high energy ions) and outside of the outer shell (less ions present in general). The plasma densities of this second plasma fell into the range of 10^{13}-10^{14} cm^{-3} for nearly all experiments, with increasing pressure and increasing buffer gas mass leading to increases in density. For the second and third plasmas, buffer gas was the primary influence on electron temperature and density, and consequently very little changes were observed in either plasma as a function of pinch gas mass. Lastly, the third plasma was found to originate in the expansion of the EUV emitting plasma as it cooled from its 30 eV, 10^{20} $cm^{-3}$and incorporated buffer gas. Consequently, the density of this plasma increased with increasing pressure, and increased with increasing buffer gas mass. Electron temperatures of this plasma were lower than the other two more energetic plasmas, falling in the range of 1-3 eV and densities on the range of 10^{12}-10^{14} cm^{-3}.

It was observed that these plasmas interacted with the chamber surface to cause sputtering of carbon and oxygen off of the walls. The carbon originates from the exposure of the walls to pump oil during the years of venting the chamber to atmosphere. Adsorbed water was also the origin of the oxygen contamination. At the lowest pressures, where wall collisions dominate the transport of energetic ions and neutrals from the source to the intermediate focus and wall sputtering products

can easily intermix with the chambers environment, deposition is found to be highest. The largest contributors to deposition were the oxygen and carbon contaminants, which accounted for more than 90% of all deposited species. Increasing pressure decreased the transport of these species, increased the sputtering of the IF facing surfaces, and furthermore suppressed the transport of Sn, Mo, and Cu (the metal contaminants from the electrode and collimated foil trap), to result in lower net deposition. A peak of 2 mTorr was observed to contribute the most deposition, as the increase in plasma density liberated more contaminant species, and more electrode materials were scattered into the intermediate focus before depositing onto a wall surface. The highest total (all species) deposition rate was found to be $1.5\pm0.3x10^{-4}$ nm/pulse at 2 mTorr Ar buffer gas and N_2 pinch gas, with a corresponding Sn deposition rate of $\sim6\pm1.5\pm x10^{-4}$ nm/pulse. The effect of buffer gas at 2 mTorr was found to have the highest Sn deposition rate using He, while increasing buffer gas mass should have theoretically reduced the deposition rate. What was experimentally measured, however, was that pinch operation using Ar led to high levels of particulate contamination leaving the electrode surfaces through sputtering and arcing. These particulates resulted in a much larger deposition rate than would be expected by atomic deposition alone. Unfortunately the EUV light source was not operable with He, Ne, or Ar as the pinch gasses due to severe arcing between the electrodes, which was not observed using N_2 pinch gas.

The interaction between the energetic plasma expansion and the buffer gas was found to create an energetic, mostly neutralized, flux at the intermediate focus as a result of high energy ion/electron energy transfer through scattering. The peak

of this flux was observed at 6 mTorr, where gas pressure was high enough to gain a lot of energy from the pinch gas species, but not too high as to suppress its arrival energy with collisions. It was found experimentally and theoretically that increasing buffer mass u to 6 mTorr would increase the measurement of this flux with microchannel plates, though in reality the number of species reaching the intermediate focus would actually reduce-albeit with an increased average energy-with increases in buffer gas mass. Pinch gas mass was also an important contributor due to the increased scattering cross section and energy transfer between the higher massed species and the Ar buffer gas.

Ultimately, the importance of this work revolves around the issues that are important for tool manufacturers to create cost effective EUV light emitting plasma sources. Wall contamination, gas contamination, as well as electrode materials play an important and crucial roll in the development and transport of debris to the intermediate focus. Without proper gas pressure considerations, as well as buffer gas and pinch gas choices, the effect of buffer gas mitigation schemes could actually increase the total amount of deposition. Furthermore, while increases in buffer gas pressure sequentially improve upon the deposition of contaminants, the higher neutral density serves to sustain the energetic secondary plasmas created by high energy electrons, slower electrons coupled with the ejected fast ions, and the expansion of the EUV emitting plasma core itself. The value of this work, however stands in the development of a model, based on gas scattering and wall collisions, that aptly predicts and explains how buffer gas collisions lead to the distribution of

deposition products throughout the chamber as well as generate a damaging flux at the intermediate focus.

REFERENCES

1. Moore, G., *Cramming more components onto integrated circuits.* Proceedings of the IEEE, 1998. **86**(1): p. 82-85.
2. *60 Years of the Transistor: 1947-2007*. [cited 2010 February 22]; Available from: http://www.intel.com/technology/timeline.pdf.
3. Hawryluk, A.M. and L.G. Seppala, *Soft x-ray projection lithography using an x-ray reduction camera.* Journal of Vacuum Science & Technology B: Microelectronics and Nanometer Structures, 1988. **6**(6): p. 2162-2166.
4. Teramoto, Y., et al. *Development of Sn-fueled high-power DPP EUV source for enabling HVM*. in *Emerging Lithographic Technologies XI, 27 Feb. 2007*. 2007. USA: SPIE - The International Society for Optical Engineering.
5. Wu, B. and A. Kumar, *Extreme ultraviolet lithography: A review.* Journal of Vacuum Science & Technology B: Microelectronics and Nanometer Structures, 2007. **25**(6): p. 1743-1761.
6. Levenson, M.D., *Wavefront Engineering for Photolithography.* Physics Today, 1993. **46**(7): p. 28.
7. Nazmov, V., J. Mohr, and E. Reznikova, *Visualization of the development process in deep X-ray lithography.* Nuclear Instruments and Methods in Physics Research Section A: Accelerators, Spectrometers, Detectors and Associated Equipment, 2009. **603**(1-2): p. 153-156.
8. Wakana, K., et al. *Optical performance of laser light source for ArF immersion double patterning lithography tool*. 2009. San Jose, CA, USA: SPIE.
9. Owen, G., et al. *1/8 mu m optical lithography*. 1992. Orlando, Florida (USA): AVS.
10. Jain, K., *Excimer Laser Lithography*. 1990, Bellingham: SPIE Optical Engineering Press.
11. Levinson, H.J., *Principles of Lithography*. 2001, Bellingham: SPIE-The International Society for Optical Engineering.
12. Liebmann, L.W. *Resolution enhancement techniques in optical lithography: It's not just a mask problem*. 2001. Kanagawa, Japan: SPIE.
13. Lin, B.J., *The ending of optical lithography and the prospects of its successors.* Microelectronic Engineering, 2006. **83**(4-9): p. 604-613.
14. Torres, J.A., O. Otto, and F.G. Pikus. *Challenges for the 28nm half node: Is the optical shrink dead?* 2009. Monterey, CA, USA: SPIE.
15. Pfeiffer, H.C., *Advanced E-Beam Systems for Manufacturing*, in *Electron-Beam, X-Ray, and Ion-Beam Submicrometer Lithographies for Manufacturing II*1992, SPIE. p. 100-110.
16. Hohn, F.J., *Electron Beam Lithography, Directions in Direct Write and Mask Making*, in *SPIE Electron-Beam, X-Ray, and Ion-Beam Technology: Submicrometer Lithographies IX*1990, SPIE. p. 152-163.
17. Austin, M.D., et al., *Fabrication of 5nm linewidth and 14nm pitch features by nanoimprint lithography.* Applied Physics Leters, 2004. **84**: p. 5299-5301.
18. Chou, S.Y., P.R. Krauss, and P.J. Renstrom, *Imprint Lithography with 25-Nanometer Resolution.* Science, 1996. **272**(5258): p. 85-87.

19. Dunsky, C., *High-speed microvia formation with UV solid-state lasers.* Proceedings of the IEEE, 2002. **90**(10): p. 1670-1680.
20. Allen, P.C., *Laser scanning for semiconductor mask pattern generation.* Proceedings of the IEEE, 2002. **90**(10): p. 1653-1669.
21. Klosner, M. and K. Jain, *Massively parallel, large-area maskless lithography.* Applied Physics Leters, 2004. **84**(15).
22. Basting, D., K. Pippert, and U. Stamm. *History and future prospects of excimer laser technology*. in *Focused on 2nd International Symposium on Laser Precision Microfabrication*. 2002.
23. Ronse, K., et al., *Lithography Options for the 32 nm Half Pitch Node and Beyond.* Circuits and Systems I: Regular Papers, IEEE Transactions on, 2009. **56**(8): p. 1884-1891.
24. Hazelton, A.J., et al., *Double-patterning requirements for optical lithography and prospects for optical extension without double patterning.* Journal of Micro/Nanolithography, MEMS and MOEMS, 2009. **8**(1): p. 011003-11.
25. Dusa, M., et al. *Pitch doubling through dual-patterning lithography challenges in integration and litho budgets*. 2007. San Jose, CA, USA: SPIE.
26. Levenson, M.D., et al., *The phase-shifting mask II: Imaging simulations and submicrometer resist exposures.* Electron Devices, IEEE Transactions on, 1984. **31**(6): p. 753-763.
27. Noguchi, M., et al. *Subhalf-micron lithography system with phase-shifting effect*. 1992. San Jose, CA, USA: SPIE.
28. Brunner, T.A. *Rim phase-shift mask combined with off-axis illumination: a path to .5 Lambda/NA geometries*. 1993. San Jose, CA, USA: SPIE.
29. Matthew, I., et al. *Design restrictions for patterning with off-axis illumination*. 2004. San Jose, CA, USA: SPIE.
30. Rigolli, P., et al. *High-order distortion effects induced by extreme off-axis illuminations at hyper NA lithography*. 2009. San Jose, CA, USA: SPIE.
31. ITRS, *International Technology Roadmap for Semiconductors*, in *Lithography*2009.
32. Attwood, D.T., in *Soft X-rays and Extreme Ultraviolet Radiation*. 1999, Cambridge University Press: Cambridge. p. 1-21.
33. Borisov, V.M., *EUV sources using Xe and Sn discharge plasmas.* Journal of physics. D, Applied physics, 2004. **37**(23): p. 3254-65.
34. Nastoyashchii, A.F. *Optimal physical conditions for extreme UV generation*. 2004. Taos, NM, USA: SPIE.
35. Masnavi, M., et al., *Estimation of optimum density and temperature for maximu efficiency of tin ions in Z discharge extreme ultraviolet sources.* Journal of Applied Physics, 2007. **101**(033306).
36. Hassanein, A., et al. *Effects of plasma spatial profile on conversion efficiency of laser produced plasma sources for EUV lithography*. 2009. San Jose, CA, USA: SPIE.
37. Mohanty, S.R., et al., *Influence of electrode separation and gas curtain on extreme ultraviolet emission of a gas jet z-pinch source.* Applied Physics Letters, 2006. **89**(4): p. 041502-3.

38. Zhang, C.H., et al. *Gas flow rate effects from a Z-pinch discharge plasma on extreme ultraviolet emission*. in *Electrical and Computer Engineering, 2009. CCECE '09. Canadian Conference on*. 2009.
39. Stamm, U., *Extreme ultraviolet light sources for use in semiconductor lithography-state of the art and future development.* Journal of Physics D: Applied Physics, 2004. **37**: p. 9.
40. Banine, V. and R. Moors, *Plasma Sources for EUV Lithography Exposure Tools.* Journal of Physics D: Applied Physics, 2004. **37**(23).
41. Masnavi, M., et al., *Potential of discharge-based lithium plasma as an extreme ultraviolet source.* Applied Physics Letters, 2006. **89**(3): p. 031503-3.
42. Neumann, M.J., et al., *Plasma cleaning of lithium off of collector optics material for use in extreme ultraviolet lithography applications.* Journal of Micro/Nanolithography, MEMS and MOEMS, 2007. **6**(2): p. 023005-6.
43. Nagano, A., *Extreme ultraviolet source using laser-produced Li plasma.* IEEJ Trans. on Elec. Inform. and Sys., 2009. **129**(2): p. 249-52.
44. Ter-Avetisyan, S., et al., *Efficient extreme ultraviolet emission from xenon-cluster jet targets at high repetition rate laser illumination.* Journal of Applied Physics, 2003. **94**(9): p. 5489-5496.
45. Komori, H., *EUV radiation characteristics of a CO2 laser produced Xe plasma.* Applied physics. B, Lasers and optics, 2006. **83**(2): p. 213-218.
46. Bianucci, G., et al. *Thermal management design and verification of collector optics into high-power EUV source systems*. 2007. San Jose, CA, USA: SPIE.
47. Cummings, A., et al., *Conversion efficiency of a laser-produced Sn plasma at 13.5 nm, simulated with a one-dimensional hydrodynamic model and treated as a multi-component blackbody.* Journal of physics. D, Applied physics, 2005. **38**(4): p. 604-16.
48. Shimada, Y., et al., *Characterization of extreme ultraviolet emission from laser-produced spherical tin plasma generated with multiple laser beams.* Applied Physics Letters, 2005. **86**(5): p. 051501-3.
49. Krucken, T., *Fundamentals and limits for the EUV emission of pinch plasma sources for EUV lithography.* Journal of physics. D, Applied physics, 2004. **37**(23): p. 3213-24.
50. Shin, H., R. Raju, and D.N. Ruzic. *Remote plasma cleaning of Sn from an EUV collector mirror*. 2009. San Jose, CA, USA: SPIE.
51. Farrar, N.R., et al., *EUV laser produced plasma source development.* Microelectronic Engineering. **86**(4-6): p. 509-512.
52. Feigl, T., et al. *Enhanced reflectivity and stability of high-temperature LPP collector mirrors*. 2008. San Diego, CA, USA: SPIE.
53. Tao, Y., *Mass-limited Sn target irradiated by dual laser pulses for an extreme ultraviolet lithography source.* Optics Letters, 2007. **32**(10): p. 1338-40.
54. Borisov, V.M., et al., *Xenon and Tin Pinch Discharge Sources*, in *EUV Sources for Lithography*, V. Bakshi, Editor. 2006, SPIE - The international Society for Optical Engineering: Bellingham.
55. Bianucci, G., et al. *Design and fabrication considerations of EUVL collectors for HVM*. 2009. San Jose, CA, USA: SPIE.

56. Maury, H., et al., *Non-destructive X-ray study of the interphases in Mo/Si and Mo/B4C/Si/B4C multilayers.* Thin Solid Films, 2006. **514**(1-2): p. 278-286.
57. Hecquet, C., et al. *Design, conception, and metrology of EUV mirrors for aggressive environments*. 2007. Prague, Czech Republic: SPIE.
58. Bajt, S., *Oxidation resistance of ru-capped EUV multilayers.* Proceedings of SPIE--the international society for optical engineering, 2005. **5751**(1): p. 137-46.
59. Bajt, S., et al., *Improved reflectance and stability of Mo-Si multilayers.* Optical Engineering, 2002. **41**(8): p. 1797-1804.
60. Qiu, H., *Time exposure performance of Mo-Au Gibbsian segregating alloys for extreme ultraviolet collector optics.* Applied optics, 2008. **47**(13): p. 2443-51.
61. Braic, V., M. Balaceanu, and M. Braic. *Grazing incidence mirrors for EUV lithography*. in *Semiconductor Conference, 2008. CAS 2008. International*. 2008.
62. *EUV Sources for Lithography*. Vivek Bakshi. 2005, Bellingham: SPIE-The International Society for Optical Engineering.
63. Andruczyk, D., Sporre, J., Elg, D., Cho, T.S., Ruzic, D.N., *Energetic ion and neutral energy analyzer for extreme-ultraviolet light sources.* Proc. SPIE, 2012. **8322**.
64. Gielissen, K., *The nature and characteristics of particles produced by EUV sources*, 2009, Eindhoven Technical University.
65. Ruzic, D.N., *The Effects of Elastic Scattering in Neutral Atom Transport.* Physics of Fluids B, 1993. **5**: p. 3140-3147.
66. Sporre, J., Raju, R., Ruzic, D.N., Surla, V., Goodwin, F., *Measurement of particle flux at the intermediate focus of a DPP source*. Vol. 7271. 2009.
67. Shin, H., Sporre, J.R.; Raju, R.; Ruzic, D.N., *Reflectivity degradation of grazing-incident EUV mirrors by EUV exposure and carbon contamination.* Microelectronic Engineering, 2009. **86**(1): p. 99-105.
68. Stamm, U., et al. *Development status of EUV sources for use in beta-tools and high-volume chip manufacturing tools*. 2006. SPIE.
69. Thompson, K.C., et al., *Experimental test chamber design for optics exposure testing and debris characterization of a xenon discharge produced plasma source for extreme ultraviolet lithography.* Microelectronic Engineering, 2006. **83**(3): p. 476-484.
70. Sporre, J., Ruzic, D.N., *Extreme Ultraviolet Light Lithography for Producing Nanofeatures in Next-Generation Semiconductor Processing*, in *Plasma Processing of Nanomaterials*, R.M. Sankaran, Editor. 2012, Taylor & Francis Group, LLC.: Boca Raton. p. 35-55.
71. Thompson, K., *Characterization and Mitigation of Ion Debris Ejected from a Z-Pinch Plasma EUV Light Source*, in *Electrical and Computer Engineering*2007, University of Illinois at Urbana-Champaign: Urbana.
72. Antonsen, E.L., et al., *Ion Debris Characterization from a Z-Pinch Extreme Ultraviolet Light Source.* Journal of Applied Physics, 2006. **99**(063301).
73. Sporre, J., et al., *Ionic Debris Measurement of Three Extreme Ultraviolet Sources.* Journal of Applied Physics, 2009. **106**(043304).
74. Wiza, J.L., *Microchannel Plate Detectors.* Nuclear Instruments and Methods, 1979. **162**: p. 587-601.

75. Ziegler, J.F., Biersack, J.P., Ziegler, M.D., *SRIM - The Stopping and Range of Ions in Matter*. Vol. 7. 2008, Chester: SRIM Company.
76. Greenwood, J., *The correct and incorrect generation of a cosine distribution of scattered particles for Monte-Carlo modelling of vacuum systems.* Vacuum, 2002. **67**(2): p. 217-222.
77. Ruzic, D.N., *The effects of elastic scattering in neutral atom transport.* Phys. Fluids B, 1993. **5**(93): p. 3140-3147.
78. Myers, A.M., Ruzic, D.N., Doyle, J.R., *Monte Carlo Simulations of Sputter Atom Transport in Low-Pressure Sputtering; The effects of Interaction Potential, Sputter Distribution and System Geometry.* J. Appl. Phys, 1992. **72**: p. 3064-3071.
79. Abrahamson, A.A., *Born-Mayer-Type Interatomic Potential for Neutral Ground-State Atoms with Z=2 to Z=105*.* Physical Review, 1969. **178**(1): p. 76-79.
80. Van Sciver, S.W., *Helium Cryogenics*. 2nd ed. 2012, New York: Springer.
81. Mehdipour, N., Moosavi, F., *A perturbed hard-sphere equation of state for liquid metals.* J. Phys. Chem. Liq., 2001. **49**(3): p. 347-354.
82. Leuty, G.M., Abu-Nada, A., Tsige, M., *Multilayer Adsorption of Methane and Chloromethane on the Molybdenum (100) Surface.* J. Phys. Chem. C, 2012. **116**: p. 14514-14525.
83. Hwang, H.J.K., O.; Kang, J.W., *Copper nanocluster diffusion in carbon nanotube.* Solid State Communications, 2004. **129**(11): p. 687-690.
84. Child, M.S., *Molecular Collision Theory*. 1974, New York: Academic Press.
85. LBL. [cited 2013 May 1]; Available from: http://henke.lbl.gov/optical_constants/gastrn2.html.
86. Marr, G.V., *Absolute Photoionization Cross-Section Tables for Helium, Neon, and Krypton in the VUV spectral Regions.* Atom. Data and Nucl. Data Tables, 1976. **18**: p. 497-508.
87. Phelps, A.V., *Cross Sections and Swarm Coefficients for Nitrogen Ions and Neutrals in N2 and Argon Ions and Neutrals in Ar for Energies from 0.1 eV to 10 keV.* J. Phys. Chem. Ref. Data., 1990. **20**(3): p. 557-573.
88. Davies, L.P., *The Photo-Electric Properties of some Metals in the Soft X-Ray Region.* Proc. Royal Soc. of London, Series A, 1928. **119**(783): p. 543-552.
89. Rustgi, O.P., Weissler, G.L., *Optical and Photoelectric Properties of Thin Metallic Films in the Vacuum Ultraviolet.* J. Opt. Soc. Amer., 1964. **49**(5): p. 471-474.
90. Moore, J.W., Stanitski, C.L., Jurs, P.C., *Principles of Chemistry, The Molecular Science*. 2010, Belmont: Brooks/Cole.
91. Szmytkowski, C., Maciag, K., *Absolute Electron-Scattering Total Cross Section Measurements for Noble Gas Atoms and Diatomic Molecules.* Physica Scripta, 1996. **54**: p. 271-280.

APPENDIX A

DEBRIS TRANSPORT CODE

The debris transport model is operated by calling the function main(), with inputs of number of test atoms, number of generations, batch run option, save file option, as well as preallocation number. Typically the value of the preallocation number is set to 10 times the vaue of the number of test atoms, though this is heavily dependent on the number of generations used. It is recommended that a value of $A*10^{(n-1)}$ species are preallocated, where n is the number of generations and A is the number of test atoms. This speeds up the modeling process, since it avoids Matlab having to expand the size of the matrix on the fly. The output of the main() code is the set of data describing the histories of each test atom, as well as the structural geometry that was used in the

A.1 main()

```
function
[savedAtomData,shellSize]=main(numTestAtoms,generations,saveNosave,batc
hRun,preAllocNum)
clear atomdata;
format long;

%   Variable assignments
%   Preallocation of data
%   Main Code
%       calculate free path distance location
%       see if an atom collision occured recalc direction and location
%       see if a wall collision occurred recalc direction and location
%           could also be an end game that is tested for\
%           also if deposition occurs
%       see if atom is less than minimum energy

%test atoms are definied by a normalized direction vector, velocity,
and
%energy and mass.
```

```
%all values are in amu, kg, eV, m, m/s units
%saveNOsave = 1 then we save, =0 then we don't save

%These values turn on and off consideration of either sputtering or gas
%scattering
gasAddersONOFF=1;%1=on 0=off
sputterAddersONOFF=1;

%Add this for running batch files


%INITIAL CONDITIONS and BATCH CONDITIONS
testConditions(1).testAtoms = numTestAtoms;
testConditions(1).generations = generations;
testConditions(1).saveNosave = saveNosave;
testConditions(1).plotNoplot = 1;
testConditions(1).pinchGas = 'N';
testConditions(1).pinchSpecies = 'Sn';
testConditions(1).pinchMass = 118;
testConditions(1).bufferSpecies = 'Ar';
testConditions(1).bufferMass = 40;
testConditions(1).mirrorSurface = 'SN_SS';
testConditions(1).pressure = 2e-3;%Torr
testConditions(1).timeStep = 10e-6;%S
testConditions(1).maxNumSteps = 10000;
testConditions(1).minEnergy = 5;
testConditions(1).maxTimePerAtom = 1;%S
testConditions(1).temperature = 300; %K
i=2;
%%%
%pressure variations
% testConditions(2) = testConditions(1);
% testConditions(2).pressure = 0.3e-3;
% testConditions(3) = testConditions(1);
% testConditions(3).pressure = 6e-3;
% testConditions(4) = testConditions(1);
% testConditions(4).pressure = 12e-3;
% testConditions(5) = testConditions(1);
% testConditions(5).pressure = 22e-3;

%species variations Using N as a pinch Gas
% testConditions(6) = testConditions(1);
% testConditions(6).pressure = 2e-3;
% testConditions(6).pinchSpecies = 'Mo';
% testConditions(7) = testConditions(1);
% testConditions(7).pressure = 2e-3;
% testConditions(7).pinchSpecies = 'Cu';
% testConditions(8) = testConditions(1);
% testConditions(8).pressure = 2e-3;
% testConditions(8).pinchSpecies = 'N';

%buffer gas variations
testConditions(i) = testConditions(1);
testConditions(i).pressure = 2e-3;
testConditions(i).bufferSpecies = 'He';
i=i+1;
testConditions(i) = testConditions(1);
```

```
testConditions(i).pressure = 2e-3;
testConditions(i).bufferSpecies = 'Ne';
i=i+1;

%pinch gas variations   diff pinch species through Ar buffer Gas
testConditions(i) = testConditions(1);
testConditions(i).pressure = 3e-3;
testConditions(i).pinchGas = 'Ar';
testConditions(i).pinchSpecies ='Sn';
i=i+1;

testConditions(i) = testConditions(1);
testConditions(i).pressure = 3e-3;
testConditions(i).pinchGas = 'He';
testConditions(i).pinchSpecies ='Sn';
i=i+1;

testConditions(i) = testConditions(1);
testConditions(i).pressure = 3e-3;
testConditions(i).pinchGas = 'Ne';
testConditions(i).pinchSpecies = 'Sn';
i=i+1;



%%%
```

```
        pressure = testConditions(batchIX).pressure;%Torr
        timeStep = testConditions(batchIX).timeStep;%S
        maxNumSteps = testConditions(batchIX).maxNumSteps;
        minEnergy = testConditions(batchIX).minEnergy;
        maxTimePerAtom = testConditions(batchIX).maxTimePerAtom;%S
        temperature = testConditions(batchIX).temperature; %K
    end



    totalTime = 0;

    %%% LOCATION PATHS

    reflectionsPath = '/Users/jrs/Documents/Work/Files/PhD/Theory/IF
Flux Code/Reflection Data/';
    energyDataPath = '/Users/jrs/Documents/Work/Files/PhD/Theory/IF
Flux Code/Energy Data/';
    scatteringPath =
'/Users/jrs/Documents/Work/Files/PhD/Theory/Scattering Tables/';
    xSectionPath =
'/Users/jrs/Documents/Work/Files/PhD/Theory/Scattering Tables/';
    bMaxPath = '/Users/jrs/Documents/Work/Files/PhD/Theory/Scattering
Tables/';
    savePath =
strcat('/Users/jrs/Documents/Work/Files/PhD/Theory/Results/');
    saveFileName =
strcat(pinchSpecies,'_off_',mirrorSurface,'_thru_',bufferSpecies,'_',nu
m2str(pressure*1000),'mTorr','_',num2str(numTestAtoms));
    %%% CALCULATED VARIABLES



    k = 1.38*10^-23; %j/K
    n = (pressure*133.3)/(k*temperature); %133 is conv factor to pascal
    %sigma = 3.1416 * (bufferGasDiam)^2;
    %meanFreePath = 1/(n*sigma); %meters
    %bMax = 7;

    %%% COLLECTOR/CHAMBER GEOMETRY VALUES
        %1: inner shell
        %2: outer shell
        %3: outer chamber shell
        %4: intermediate focus
    shellSize(1,1)=.064; %inner shell radius
    shellSize(1,2)=.15; %inner shell length
    shellSize(1,3)=.285; %inner shell dist from pinch to coll
optic .435 .585

    shellSize(2,1)=.216; %outer shell radius
    shellSize(2,2)=.305; %outer shell length
    shellSize(2,3)=.2075; %outer shell dist from pinch to coll
optic .2075 .5125

    shellSize(3,1)=.46; %Outside shell radius   (chamber)
    shellSize(3,2)=.72; %Outside shell length
    shellSize(3,3)=0; %Outside shell dist from pinch to coll optic
```

```
    shellSize(4,1)=.1; %IF radius
    shellSize(4,2)=0; %shell length/0 because it's at the end
    shellSize(4,3)=shellSize(3,2); %distance from pinch to IF

    shellSize(5,1)=shellSize(2,1); %radius of the brackets blocking
trajectory holding collector shape
    shellSize(5,2)=shellSize(2,2)+2*.006; %distance from first set of
brackets to second in z direction
    shellSize(5,3)=shellSize(2,3)-.006; %location of the z-pinch
proximal set of brackets
    shellSize(5,4)=.019; %half-width of the brackets




    %%% CALCULATE THE energyHitsMatrix WHICH CONTAINS THE TOTAL FLUX
[x]
    %%% MEASUREMENTS FOR THE APPROPRIATE SPECIES.
    %energyHitsMatrix = xlsread(strcat(energyDataPath,pinchSpecies,'
flux.xls'));

    totalAtomList =
[cellstr('He'),cellstr('N'),cellstr('Ne'),cellstr('Ar'),cellstr('Cu'),c
ellstr('Mo'),cellstr('Sn')];
    totalAtomMassList = [4,14,20,40,63.5,96,118];
    bufferAtomList = [cellstr('He'),cellstr('Ne'),cellstr('Ar')];
    bufferAtomMassList = [4,20,40];
    counter = 1;
    for i = 1:length(totalAtomList)
        for j = 1:length(bufferAtomList)
            interactionList(1,counter)=totalAtomList(i);
            interactionList(2,counter)=bufferAtomList(j);
            counter = counter+1;
        end
    end

    %Input the Reflection Data for the Appropriate Species
    counter = 1;
    for i = 1:length(totalAtomList(:))%makes a quick access list to
send on an individual basis.
        tempSpecies = totalAtomList(i);
        reflectMatrix(i).species = totalAtomList(i);
        reflectMatrix(i).sputSpecies = cellstr('Sn');
        reflectMatrix(i).sputSpeciesMass = 118;
        reflectMatrix(i).deposFract =
xlsread(strcat(reflectionsPath,char(tempSpecies),'_on_',mirrorSurface,'
.xls'),'Depos Fract');
        reflectMatrix(i).sputFract =
xlsread(strcat(reflectionsPath,char(tempSpecies),'_on_',mirrorSurface,'
.xls'),'Sput Fract');
        reflectMatrix(i).scatFract =
xlsread(strcat(reflectionsPath,char(tempSpecies),'_on_',mirrorSurface,'
.xls'),'Back Scat Fract');
        reflectMatrix(i).ionPerIonSput =
xlsread(strcat(reflectionsPath,char(tempSpecies),'_on_',mirrorSurface,'
.xls'),'Sputt Ion per sput causing ion');
```

```
        reflectMatrix(i).totSputYield =
xlsread(strcat(reflectionsPath,char(tempSpecies),'_on_',mirrorSurface,'
.xls'),'Tot Sput Yield');
        reflectMatrix(i).avgEnergy =
xlsread(strcat(reflectionsPath,char(tempSpecies),'_on_',mirrorSurface,'
.xls'),'Avg Energy');%avg backscatter energy
        reflectMatrix(i).uThetaScat =
xlsread(strcat(reflectionsPath,char(tempSpecies),'_on_',mirrorSurface,'
.xls'),'uTheta-BS');
        reflectMatrix(i).sThetaScat =
xlsread(strcat(reflectionsPath,char(tempSpecies),'_on_',mirrorSurface,'
.xls'),'sTheta-BS');
        reflectMatrix(i).uPhiScat =
xlsread(strcat(reflectionsPath,char(tempSpecies),'_on_',mirrorSurface,'
.xls'),'uPhi-BS');
        reflectMatrix(i).sPhiScat =
xlsread(strcat(reflectionsPath,char(tempSpecies),'_on_',mirrorSurface,'
.xls'),'sPhi-BS');

        reflectMatrix(i).uThetaSput =
xlsread(strcat(reflectionsPath,char(tempSpecies),'_on_',mirrorSurface,'
.xls'),'uTheta-SP');
        reflectMatrix(i).sThetaSput =
xlsread(strcat(reflectionsPath,char(tempSpecies),'_on_',mirrorSurface,'
.xls'),'sTheta-SP');
        %reflectMatrix(i).uPhiSput =
xlsread(strcat(reflectionsPath,char(tempSpecies),'_on_',mirrorSurface,'
.xls'),'uPhi-SP'); %not really going to be used, it's uniform around
phi
        %reflectMatrix(i).sPhiSput =
xlsread(strcat(reflectionsPath,char(tempSpecies),'_on_',mirrorSurface,'
.xls'),'sPhi-SP'); %not really going to be used, it's uniform around
phi
        reflectMatrix(i).avgSputEnergy =
xlsread(strcat(reflectionsPath,char(tempSpecies),'_on_',mirrorSurface,'
.xls'),'Avg Sput Energy'); %average sputtered atom energy
    end

    for i = 1:length(interactionList(1,:)) %makes a quick access list
to send on an individual basis.
        tempPinchSpecies = char(interactionList(1,i));
        tempBufferSpecies = char(interactionList(2,i));

        %%% LOAD IN THE SCATTERING DATA
        scatterMatrix(i).incidentSpecies = interactionList(1,i);
        scatterMatrix(i).bufferSpecies = interactionList(2,i);

scatterMatrix(i).data=csvread(strcat(scatteringPath,tempPinchSpecies,'-
',bufferSpecies,'.csv'));

        %%% LOAD IN THE CROSS SECTION DATA FOR GIVEN SPECIES
        xSectionMatrix(i).incidentSpecies = interactionList(1,i);
        xSectionMatrix(i).bufferSpecies = interactionList(2,i);
        xSectionMatrix(i).data =
csvread(strcat(xSectionPath,tempPinchSpecies,'-
',bufferSpecies,'_xSec.csv'));
```

```
        %%% LOAD IN THE MAX IMPACT FACTOR DATA FOR A GIVEN SPECIES
        bMaxMatrix(i).incidentSpecies = interactionList(1,i);
        bMaxMatrix(i).bufferSpecies = interactionList(2,i);
        bMaxMatrix(i).data =
csvread(strcat(bMaxPath,tempPinchSpecies,'-
',bufferSpecies,'_maxB.csv'));
    end


%%% LOAD IN THE ENERGY DATA
    energyData = csvread(strcat(energyDataPath,pinchGas,'.csv'));
    clear atomdata
%%% SET UP THE INITIAL CONDITIONS AND PREALLOCATE FOR SPEED [x]
    sprintf('PREALLOCATING')

    if preAllocNum < numTestAtoms
        preAllocNum = numTestAtoms;
    end

for i = 1:preAllocNum
    atomdata(i).parentAtom=0;%it's an original, the rest will become
this.
    atomdata(i).energy = randEnergy(energyData); % testing purposes
randEnergy(energyHitsMatrix);
    atomdata(i).direction =
randDirection();%normVector([0,.064,.36]);%%1:x,2:y,3:z
    atomdata(i).mass = pinchMass;
    atomdata(i).species = cellstr(pinchSpecies);
    atomdata(i).velocity =
EtoVconv(atomdata(i).energy,atomdata(i).mass);
    atomdata(i).location(1:3)=0;%1:x,2:y,3:z
    atomdata(i).birthType=1; %1=pinch species, 2=sputtered species,
3=scattered species
    atomdata(i).generation=1;
    atomdata(i).histEnergy(1)=atomdata(i).energy;
    atomdata(i).histVelocity(1)=atomdata(i).velocity;
    atomdata(i).histLoc(1,1:3)=0;%1:x,2:y,3:z

atomdata(i).histDir(1,1:3)=atomdata(i).direction(1:3);%1:xHat,2:yHat,3:
zHat
    atomdata(i).histTime(1)=0;
    atomdata(i).histInsideOut(1)=cellstr('neither');

atomdata(i).histProjLoc(1,1:3)=atomdata(i).location+atomdata(i).directi
on*atomdata(i).velocity*timeStep;
    atomdata(i).histVNorm(1,1:3)=0;
    atomdata(i).histDistTrav(1)=0;
    atomdata(i).histInAngle = 0;
    atomdata(i).histOutAngle = 0;
    atomdata(i).histIncid(1)=0; %incident history,
                                % 0 = nothing, normal flight
                                % 1 = atom-buffer collision
                                % 2 = atom-wall collision
                                % 3 = deposited
                                % 7 = made IF
                                % 8 = max time taken
                                % 9 = max steps
```

```
                                % 10 = thermalized
                                % 11 = glitched, left chamber

end
    %

%%% MAIN CODE
    sprintf('RUNNING')
    exitcommand = 0;
    j=1;
    maxJThisGen = numTestAtoms;
    endOfAtomData = numTestAtoms;
    genAtomCount= 1;
    codeStartTime = tic;
    prevGenTime = 0;
    newGenNum = atomdata(1).generation;
    prevGenNum = atomdata(1).generation;
    while exitcommand == 0
        j;


        %clear tempData
        %now determine the reflectData, xSectionData,bMaxData, and
        %scatterMatrix for the individualized atomdata species

        %scatterMatrixData
        for k = 1:length(scatterMatrix(:))
            if
isequal(scatterMatrix(k).incidentSpecies,atomdata(j).species) &&
isequal(scatterMatrix(k).bufferSpecies,cellstr(bufferSpecies))
                bufferSpecies = scatterMatrix(k).bufferSpecies;
                scatterMatrixData = scatterMatrix(k).data;
                %sprintf('scatterMatrix Determined: %s
and %s',char(scatterMatrix(k).incidentSpecies),char(scatterMatrix(k).bu
fferSpecies))
            end
        end
        %xSectionMatrixData
        for k = 1:length(xSectionMatrix(:))
            if
isequal(xSectionMatrix(k).incidentSpecies,atomdata(j).species) &&
isequal(xSectionMatrix(k).bufferSpecies,cellstr(bufferSpecies))
                xSectionMatrixData = xSectionMatrix(k).data;
                %sprintf('xSectionMatrix Determined: %s
and %s',char(xSectionMatrix(k).incidentSpecies),char(xSectionMatrix(k).
bufferSpecies))
            end
        end
        %bMaxMatrixData
        for k = 1:length(bMaxMatrix(:))
            if
isequal(bMaxMatrix(k).incidentSpecies,atomdata(j).species) &&
isequal(bMaxMatrix(k).bufferSpecies,cellstr(bufferSpecies))
                bMaxMatrixData = bMaxMatrix(k).data;
                %sprintf('bMaxMatrix Determined: %s
and %s',char(bMaxMatrix(k).incidentSpecies),char(bMaxMatrix(k).bufferSp
ecies))
```

```
            end
        end
        for k = 1:length(reflectMatrix(:))
            if isequal(reflectMatrix(k).species,atomdata(j).species)
                reflectMatrixData = reflectMatrix(k);
                %sprintf('reflectMatrix Determined: %s
on %s',char(reflectMatrix(k).species),mirrorSurface)
            end
        end




        if atomdata(j).generation == generations %if our current
species is at the max generation already, we don't create anymore
species.
            createSecSpecies = 0;
            gasAddersONOFF=0;
            sputterAddersONOFF;
        end



[atomdata(j),newAtoms]=IFTheory(atomdata(j),minEnergy,maxNumSteps,maxTi
mePerAtom,shellSize,timeStep,reflectMatrixData,xSectionMatrixData,n,bMa
xMatrixData,bufferMass,scatterMatrixData,bufferSpecies,j,gasAddersONOFF
,sputterAddersONOFF);



        if ~isequal(newAtoms,0)
            start = endOfAtomData+1;
            stop = start+length(newAtoms)-1;
            atomdata(start:stop) = newAtoms(:);
            endOfAtomData = endOfAtomData+length(newAtoms);
            clear newAtoms
        end



        if j<endOfAtomData %still more to go through
            sprintf('Finished atom #%i/%i in this
generation',j,maxJThisGen)
            j=j+1;
        else %we have no more species to consider
            exitcommand = 1;
        end




        if exitcommand == 1 || ((j-1) == maxJThisGen) %use j-1 here
because i increment it before this code
            curTotalTime = toc(codeStartTime);
            genTotalTime = curTotalTime-prevGenTime;
            prevGenTime = prevGenTime+ curTotalTime;
```

```
            avgGenAtomTime = genTotalTime/genAtomCount;
            sprintf('Batch # %i\nFinished Generation %i: %i Test
Atoms,%i Atoms in Next Gen, Avg.
Time: %0.4f\n',batchIX,atomdata(j).generation,maxJThisGen,endOfAtomData
-maxJThisGen,avgGenAtomTime)
            genAtomCount = 0;
            maxJThisGen = endOfAtomData;
        end

        if exitcommand == 1 %now if we exit we need to know how to
minimize our overly preallocated data
            savedAtomData(1:endOfAtomData) = atomdata(1:endOfAtomData);
        end

        prevGenNum = newGenNum;
        genAtomCount = genAtomCount + 1;
    end


[depColl,madeIF,maxTime,maxSteps,thermal,screwUp]=stats(savedAtomData);
    sprintf('Deposited: %i,Avg Time:%0.1fus\nMade IF: %i,Avg
Time:%0.1fus\nMax Time: %i\nMax Steps: %i\nThermalized: %i,Avg
Time:%0.2fus\nGlitched: %i',depColl.count,depColl.timeAvg*10^6,madeIF.c
ount,madeIF.timeAvg*10^6,maxTime.count,maxSteps.count,thermal.count,the
rmal.timeAvg*10^6,screwUp.count)

    if saveNosave == 1
    %SAVE DATA TO THE FOLDER
    sprintf('Saving Data...\n')
    fileSaver(savedAtomData,savePath,saveFileName);%auto saves as
a .mat file
    end


end
```

A.2 ifTheory()

```
function
[atomdata,newAtoms]=IFTheory(atomdata,minEnergy,maxNumSteps,maxTimePerA
tom,shellSize,timeStep,reflectData,xSectionData,n,bMaxData,bufferMass,s
catterMatrix,bufferSpecies,parent,gasAddersONOFF,sputterAddersONOFF)

format long;
clear newAtoms
%%% MAIN CODE

exitCommand = 0;
newAtomsIndex = 0;
j = 1;

while exitCommand == 0
    if exitCommand ~= 1
        j=j+1;
```

```
    %%%  PERFORM ENDPOINT CHECKS [x]

        radCheck =
sqrt(dot([atomdata.location(1),atomdata.location(2),0],[atomdata.locati
on(1),atomdata.location(2),0]));
        if (atomdata.energy < minEnergy) %THERMALIZED
            atomdata.histIncid(j-1)=10;
            atomdata.histEnergy(j-1)=0;
            exitCommand = 1;
        elseif j > maxNumSteps %TOO MANY STEPS
            atomdata.histIncid(j)=9;
            atomdata.histEnergy(j-1)=0;
            exitCommand = 1;
        elseif atomdata.histTime>maxTimePerAtom  %TOOK TOO LONG
            atomdata.histIncid(j-1)=8;
            atomdata.histEnergy(j-1)=0;
            exitCommand = 1;
        elseif (radCheck > shellSize (3,1)) ||
(atomdata.location(3)<shellSize(3,3)) ||
((atomdata.location(3)>shellSize(3,2)) && (radCheck > shellSize
(4,1))) %SOME GLITCH OCCURRED AND NOW WE'RE OUTSIDE CHAMBER
            atomdata.histIncid(j)=11;
            exitCommand = 1;
        else %no endpoints hit, so we continue on

    %%%  SET DEFAULT VALUES FOR ATOM [x]

            oldLoc=atomdata.location;

projLoc=oldLoc+atomdata.direction*atomdata.velocity*timeStep;
            projDist = sqrt(dot(projLoc-oldLoc,projLoc-oldLoc));

            atomdata.histIncid(j)=0;
            atomdata.histInsideOut(j)=cellstr('neither');


    %%%  TEST FOR ATOM-WALL COLLISIONS [x]

[wallCollOccurred,surfSide,tempLocWall,tempDirWall,tempEWall,tempInAngl
eWall,tempOutAngleWall,tempNormalWall,tempNewWallScatAtom,sputOccurred]
=wallCollision(oldLoc,projLoc,atomdata.energy,reflectData,shellSize,ato
mdata.velocity,timeStep,atomdata.generation,sputterAddersONOFF,parent);
            tempVWall = EtoVconv(tempEWall,atomdata.mass);
            if wallCollOccurred >0
                tempWallDist = sqrt(dot(tempLocWall-oldLoc,tempLocWall-
oldLoc));
            else
                tempWallDist = projDist;
            end
    %%%  TEST FOR ATOM-GAS COLLISIONS (pending atom-wall collision test
results)[]
            sigma = twoPointEstimate(xSectionData,atomdata.energy);
            meanFreePath = 1/(n*sigma);
            bMax = twoPointEstimate(bMaxData,atomdata.energy);

[gasCollOccurred,tempLocGas,tempDirGas,tempEGas,tempNewGasScatAtom]=gas
AtomCollision(meanFreePath,bMax,min(projDist,tempWallDist),oldLoc,atomd
```

```
ata.direction,atomdata.energy,atomdata.velocity,atomdata.mass,bufferMas
s,scatterMatrix,timeStep,bufferSpecies,atomdata.generation,gasAddersONO
FF,parent);
            tempVGas = EtoVconv(tempEGas,atomdata.mass);

    %%%  CARRY OUT DIRECTION UPDATE
            if gasCollOccurred == 1
                atomdata.location = tempLocGas;
                atomdata.direction = tempDirGas;
                atomdata.energy = tempEGas;
                atomdata.velocity = tempVGas;
                atomdata.histIncid(j)=1;
                if gasAddersONOFF==1 %only do it if we're going to
track them
                    newAtomsIndex = newAtomsIndex+1;
                    newAtoms(newAtomsIndex)=tempNewGasScatAtom;
                end

                clear tempNewGasScatAtom

            elseif wallCollOccurred > 0
                %now we need to add the sputtered species, so long as
we didn't
                %reach the IF.
                if sputterAddersONOFF == 1 %only car to add them if we
need them
                    if sputOccurred == 1
                        for newAtomStep = 1:length(tempNewWallScatAtom)
                            newAtomsIndex = newAtomsIndex+1;

newAtoms(newAtomsIndex)=tempNewWallScatAtom(newAtomStep);
                        end
                    end
                end

                switch wallCollOccurred
                    case 1  %simple wall collision
                        atomdata.location = tempLocWall;
                        atomdata.direction = tempDirWall;
                        atomdata.energy = tempEWall;
                        atomdata.velocity = tempVWall;
                        atomdata.histIncid(j)=2;
                        atomdata.histInAngle(j)=tempInAngleWall;
                        atomdata.histOutAngle(j)=tempOutAngleWall;
                        atomdata.histVNorm(j,:)=tempNormalWall;
                        atomdata.histInsideOut(j)=cellstr(surfSide);
                    case 2  %reached intermediate focus
                        atomdata.location = tempLocWall;
                        atomdata.histIncid(j)=7;
                        atomdata.histInAngle(j)=tempInAngleWall;
                        atomdata.histOutAngle(j)=tempOutAngleWall;
                        atomdata.histVNorm(j,:)=tempNormalWall;
                        atomdata.histInsideOut(j)=cellstr(surfSide);
                        exitCommand = 1;
                    case 3  %deposited on the surface
                        atomdata.location = tempLocWall;
                        atomdata.energy = tempEWall;
```

```
                        atomdata.velocity = tempVWall;
                        atomdata.histIncid(j)=3;
                        atomdata.histVNorm(j,:)=tempNormalWall;
                        atomdata.histInsideOut(j)=cellstr(surfSide);
                        exitCommand = 1;
                    otherwise
                        sprintf('wall scatter error')
                end
            else
                atomdata.location = projLoc;
                atomdata.histIncid(j)=0;
            end


    %%%  SAVE HISTORIES FOR GIVEN INCREMENT []
            atomdata.histEnergy(j)=atomdata.energy;
            atomdata.histVelocity(j)=atomdata.velocity;
            atomdata.histLoc(j,:)=atomdata.location;
            atomdata.histDir(j,:)=atomdata.direction;
            atomdata.histTime(j) = sqrt(dot((atomdata.location-
atomdata.histLoc(j-1)),(atomdata.location-atomdata.histLoc(j-
1))))/atomdata.histVelocity(j-1)+atomdata.histTime(j-1);
            atomdata.histDistTrav(j)=atomdata.histDistTrav(j-
1)+sqrt(dot(atomdata.histLoc(j)-atomdata.histLoc(j-
1),atomdata.histLoc(j)-atomdata.histLoc(j-1)));
            atomdata.histProjLoc(j,:)=projLoc;
        end
    end
end

if newAtomsIndex == 0
    newAtoms = 0;
end
```

A.3 wallCollision()

```
function
[collOccurred,inOrOut,newLoc,vScatRefl,newE,inAngle,thetaScat,vNorm,tem
pNewWallScatAtom,sputOccurred] =
wallCollision(curLoc,projLoc,energy,bsData,shellSize,velocity,timeStep,
generation,createSecSpecies,parent)
%sprintf('W.C. START\nOld Loc: [%0.3f,%0.3f,%0.3f], Proj Loc:
[%0.3f,%0.3f,%0.3f], Old E: %0.2f,Vinc:
[%0.3f,%0.3f,%0.3f]',curLoc,projLoc,energy,normVector(projLoc-curLoc))

%till things are added
%collOccurred = 0-didn't, 1-simple collision, 2-madeIF, 3-deposited

%to be added to final wallCollision post-testing
%inputs %,iHat,jHat,kHat,energy,velocity,mass,scatFracMat,avgEngMat,avg
```

```
AngMat,sVertCoefMat,sHorizCoefMat
%outputs %,iNew,jNew,kNew,energyNew,velNew

%this program takes in a previous location and a projected location.
it
%then tests if these were different.  if they are, then we need to
%calculate the location of intersection, and consequent new direction
from
%there.  this is what is returned.  the main program will alter the
time
%period so that the new starting point is at the appropriate time and
%subsequent collisions can be dealt with on a turn by turn basis and
not in
%this program function.
%collOccurred return: 0 no collision, 1: simple collision, 2:Made IF,
3:deposited
%this is returned with an inOrOut of "none", "in", or "out", for
deciding
%where it was deposited, if it caused sputtering, inOrOut is the number
of
%created atoms.*to be added if necessary

% x0,y0,z0 = initial atom position
% xP,yP,zP = projected, unaltered path, new location
% iHat,jHat,kHat




%shell 1=inner, 2=outer, 3=chamber *must always be chamber



%%% DEFAULT RETURN VALUES
newLoc = projLoc;
newE=energy;
vScatRefl=normVector(projLoc-curLoc);
collOccured = 0;
inOrOut = 'neither';
inAngle=1000;
thetaScat=1000;
phiScat=1000;
vInc = normVector(projLoc-curLoc);
vNorm = [0,0,0];
sputOccurred = 0;

if createSecSpecies==1
    tempNewWallScatAtom(1).parentAtom = parent;
    tempNewWallScatAtom(1).energy = 0.01;
    tempNewWallScatAtom(1).direction =
normVector([0,0,1]);%normVector([0,.064,.36]);%%1:x,2:y,3:z
    tempNewWallScatAtom(1).mass = bsData.sputSpeciesMass;
    tempNewWallScatAtom(1).species = bsData.sputSpecies;
    tempNewWallScatAtom(1).velocity =
EtoVconv(tempNewWallScatAtom(1).energy,tempNewWallScatAtom(1).mass);
    tempNewWallScatAtom(1).location=newLoc;%1:x,2:y,3:z
```

```
    tempNewWallScatAtom(1).birthType=2; %1=pinch species, 2=sputtered
species, 3=scattered species
    tempNewWallScatAtom(1).generation = generation+1;
    tempNewWallScatAtom(1).histEnergy(1)=tempNewWallScatAtom(1).energy;

tempNewWallScatAtom(1).histVelocity(1)=tempNewWallScatAtom(1).velocity;

tempNewWallScatAtom(1).histLoc(1,1:3)=tempNewWallScatAtom(1).location;%
1:x,2:y,3:z

tempNewWallScatAtom(1).histDir(1,1:3)=tempNewWallScatAtom(1).direction(
1:3);%1:xHat,2:yHat,3:zHat
    tempNewWallScatAtom(1).histTime(1)=0;
    tempNewWallScatAtom(1).histInsideOut(1)=cellstr(inOrOut);

tempNewWallScatAtom(1).histProjLoc(1,1:3)=tempNewWallScatAtom(1).locati
on+tempNewWallScatAtom(1).direction*tempNewWallScatAtom(1).velocity*tim
eStep;
    tempNewWallScatAtom(1).histVNorm(1,1:3)=0;
    tempNewWallScatAtom(1).histDistTrav(1)=0;
    tempNewWallScatAtom(1).histInAngle = 0;
    tempNewWallScatAtom(1).histOutAngle = 0;
    tempNewWallScatAtom(1).histIncid(1)=0;
else
    tempNewWallScatAtom = 0;
end




%basically we derive the parametric line between the init and proj
%locations as a function of t.  We then use the radii of the shells and
set
%that as R and determine t such that R is met.  for the shells, Z is
then
%calculated to see if it lies with in the length range of the shell,
and
%thus a collision occurred.  The two possible intersection values are
%determined by the quadratic solution.  Only + values are taken
%(progressing in direction of movement).  If there are 2 + values (goes
%through the same shell twice near and far) then the smallest t value
%(first part of shell to be impacted) is taken.  t values are
calculated
%for all shells in this manner.  The front and rear walls are
calculated by
%first solving the z coordinate of the parametric equation for t.  Then
the
%x and y values are solved for and consequently R is determined at the
%point of intersection.  this is used to determine if the intersection
is
%actually a collision or out of bounds.  All t values are saved, and
the
%lowest one is used.  all t values are between 0 and 1 for viable
%collisions, non-viable collisions (false t=0 at the start point,
%intersection occurs outside of shell bounds)

%j: 1=inner shell, 2=outer shell, 3=outer chamber wall cylinder
```

```
%   4=pinch side wall, 5=IF side wall


%break down to more logical units
x0=curLoc(1);
y0=curLoc(2);
z0=curLoc(3);

xp=projLoc(1);
yp=projLoc(2);
zp=projLoc(3);


%TEST SHELL COLLISIONS
    %calculate values needed for quadradic solution
    %i: 1=inner shell, 2=outer shell, 3=outer chamber wall cylinder
j = 1;
for i = 1:3%
    a = ((yp-y0)^2+(xp-x0)^2);
    b = (2*x0*(xp-x0)+2*y0*(yp-y0));
    c = x0^2+y0^2-shellSize(i,1)^2;
    if a~=0 %it will penetrate a shell because there is radial
translation
        %now we go ahead and determine the two possible t values that
our
        %projection line crosses through the the radius in question
        t = [(-b+sqrt(b^2-4*a*c))/(2*a),(-b-sqrt(b^2-4*a*c))/(2*a)];
        x = x0+t.*(xp-x0);
        y = y0+t.*(yp-y0);
        z = z0+t.*(zp-z0);
        r = sqrt(x.^2+y.^2);

        for k = 1:2 %goes through two values of t calculated
            if (z(k)>=shellSize(i,3)) &&
(z(k)<=(shellSize(i,3)+shellSize(i,2))) && (t(k)>0.00001) && (t(k)<=1)
&& isreal(t(k))
                rangeTest(k)=t(k);
            else
                rangeTest(k)=2;
            end
        end
        tChart(j)=min(rangeTest(:));
    else %we have a simply z direction path
        tChart(j)=2;%t doesn't exist so make it 2
    end
    j = j + 1;
end

%TEST FRONT BACK WALL COLLISIONS
    %t(1) = pinch side wall, t(2) = IF side wall
if (zp-z0)~=0 %there is translation in the z direciton
    t = [(shellSize(3,3)-z0)/(zp-z0),(shellSize(3,2)-z0)/(zp-z0)];
    x = x0+t.*(xp-x0);
    y = y0+t.*(yp-y0);
    z = z0+t.*(zp-z0);
    r = sqrt(x.^2+y.^2);
```

```
    for k = 1:2
        if (r(k)>=0) && (r(k)<=shellSize(3,1)) && (t(k)>0.00001) &&
(t(k)<=1) && isreal(t(k))
            tChart(j)=t(k);
        else
            tChart(j)=2;
        end
        j=j+1;
    end
else
    tChart(j)=2;
    j=j+1;
    tChart(j)=2;
    j=j+1;
end

%TEST FRONT BRACKET COLLISIONS

%these are set up as a vertical and horizontal cross

if (zp-z0)~=0 %needs to b z translation for this wall collision
    t = [(shellSize(5,3)-z0)/(zp-z0),((shellSize(5,2)+shellSize(5,3))-
z0)/(zp-z0)]; %the ts to get to the front and back of the outer
collector where the brackets are located

    x = x0+t.*(xp-x0);
    y = y0+t.*(yp-y0);
    z = z0+t.*(zp-z0);
    r = sqrt(x.^2+y.^2);

    for k=1:2
        if (r(k)<=shellSize(5,1)) &&
(abs(x(k))<=shellSize(5,4)||abs(y(k))<=shellSize(5,4)) &&
(t(k)>0.00001) && (t(k)<=1) && isreal(t(k))
            tChart(j)=t(k);
        else
            tChart(j)=2;
        end
        j=j+1;
    end
end

for tTest = 1:length(tChart)
    if tChart(tTest) == 0
        tChart(tTest)=2; %this assures that we're not using the origin
off of a shell as our collision point
    end
end
[tToUse,cellColl] = min(tChart); %determined the correct t value


%CALCULATE NEW LOCATION FOR POINT OF COLLISION
if tToUse == 2 %never actually crossed a surface
    collOccurred = 0;
    newLoc = [0,0,0];%could be set to anything.
elseif tToUse>0 %we crossed a shell, find location of intersection
    newLoc = [x0+tToUse*(xp-x0),y0+tToUse*(yp-y0),z0+tToUse*(zp-z0)];
```

```
    collOccurred = 1;
else
    collOccurred = 0;
    newLoc = [0,0,0];
end

timeStart = sqrt(dot(newLoc-curLoc,newLoc-
curLoc))/velocity;%conditional calculation of the time of collision.

%TEST FOR IF ARRIVAL
if (sqrt(newLoc(1)^2+newLoc(2)^2))<=shellSize(4,1) && (newLoc(3) ==
shellSize(4,3))
    %reached IF!!
    collOccurred = 2;

end

%CORRECT NEW LOCATION FOR ROUNDING ERRORS AT EDGES
if collOccurred == 1

    if sqrt(newLoc(1)^2+newLoc(2)^2)>shellSize(3,1)
        sprintf('used radius correction\n');
        divFactor = sqrt(newLoc(1)^2+newLoc(2)^2)/shellSize(3,1);
        newLoc(1)=newLoc(1)/divFactor;
        newLoc(2)=newLoc(2)/divFactor;
    end
    if newLoc(3)~=maxMinRange(newLoc(3),0,shellSize(3,2))
        sprintf('used axial correction\n');
        newLoc(3)=maxMinRange(newLoc(3),0,shellSize(3,2));
    end
end



%NEW DIRECTION CALCULATION
if collOccurred==1 %so long as it crosses something
    %calculate incident unit vector
    vInc = normVector([(xp-x0),(yp-y0),(zp-z0)]);
    curAngle = atan2(newLoc(2),newLoc(1));

    r = sqrt(curLoc(1)^2+curLoc(2)^2); %radius at start of all this
    %calculate normal unit vector (all vectors point away from surface
towards atom start point)
    switch cellColl
        case 1 %inner collector shell
            if r>shellSize(1,1) %from outside to inside
                vNorm = normVector([cos(curAngle),sin(curAngle),0]);
                inOrOut = 'out';
            else %from inside to outside
                vNorm = normVector([-cos(curAngle),-sin(curAngle),0]);
                inOrOut = 'in';
            end
        case 2 %outer collector shell
            if r>shellSize(2,1) %from outside to inside
                vNorm = normVector([cos(curAngle),sin(curAngle),0]);
                inOrOut = 'out';
```

```
            else %from inside to outside
                vNorm = normVector([-cos(curAngle),-sin(curAngle),0]);
                inOrOut = 'in';
            end
        case 3 %outer chamber shell
            if r>shellSize(3,1) %from outside to inside not an option
really.
                vNorm = normVector([cos(curAngle),sin(curAngle),0]);
                inOrOut = 'out';
            else%from inside to outside
                vNorm = normVector([-cos(curAngle),-sin(curAngle),0]);
                inOrOut = 'in';
            end
        case 4 %pinch wall
            vNorm = normVector([0,0,1]);
            inOrOut = 'in';
        case 5 %IF wall
            vNorm = normVector([0,0,-1]);
            inOrOut = 'in';
        case 6 %pinch-side brackets norm vector face outwards on both
sides
            if z0>shellSize(5,3)
                vNorm = normVector([0,0,1]);
                inOrOut = 'in';
            else
                vNorm = normVector([0,0,-1]);
                inOrOut = 'out';
            end
        case 7 %IF-side brackets norm vector faces outwards on both
sides
            if z0<shellSize(5,3)+shellSize(5,2)
                vNorm = normVector([0,0,-1]);
                inOrOut = 'in';
            else
                vNorm = normVector([0,0,1]);
                inOrOut = 'out';
            end
    end

    %calculate angle between incident vector and normal vector
    inAngle=acos(dot(vNorm,-vInc)); %make vInc neg to align tails for
angle measurement

    %sprintf('incident angle: %0.2f rad, %0.2f
degrees',inAngle,inAngle/(2*pi)*360)

    %If the originating location was on the same shell as the one we're
    %hitting, then we need to correct the incident angle by subtracitng
    %pi/2 from it. can't switch them though if they're the hard outer
    %boundaries.


    %the next code also accounts for the fact that you can start
outside of
    %a shell in regards to radius, but then end up on the inside of the
    %shell
    if abs(inAngle)>(pi/2) %&& cellColl~=4 && cellColl~=5
```

```
        vNorm = -vNorm;
        inAngle=acos(dot(vNorm,-vInc));
        if isequal(inOrOut,'in')
            inOrOut = 'out';
        end
        if isequal(inOrOut,'out')
            inOrOut = 'in';
        end
    end

    %calculate orthogonal unit vector
    vOrth = normVector(cross(vInc,vNorm));
    vOrthRot = normVector(cross(-vInc,vNorm)); %this gets us with the
orth in the positive direction for later rotation

    thetaScat =
maxMinRange(cosineScatter(maxMinRange(fourPointEstimate(bsData.uThetaSc
at,energy/1000,inAngle/(2*pi)*360),0,pi),maxMinRange(fourPointEstimate(
bsData.sThetaScat,energy/1000,inAngle/(2*pi)*360),0,pi/2)),0,pi);
    phiScat =
maxMinRange(cosineScatter(maxMinRange(fourPointEstimate(bsData.uPhiScat
,energy/1000,abs(inAngle)/(2*pi)*360),-
pi,pi),maxMinRange(fourPointEstimate(bsData.sPhiScat,energy/1000,inAngl
e/(2*pi)*360),0,pi)),-pi,pi);

    %tests for specular reflections
    %thetaScat = inAngle;
    %phiScat = 0;

    %first rotate the normal (which will become our new direction
vector) about the orthogonal vector
    %i make vOrth negative to get the vector facing the right way
    vFirstScatRot = rotVector(vNorm,vOrthRot,thetaScat);
    %now we rotate it around the normal vector to get it faced in the
right
    %dirction by an angle of phi
    vScatRefl = rotVector(vFirstScatRot,vNorm,phiScat);

    %rotate reflected vector around orthogonal matrix by scatAngle &
    %stragAngle
    %vRefl =
normVector(rotVector(rotVector(vNorm,vOrth,thetaScat),vNorm,phiScat));
end



%NEW ENERGY CALCULATION
if collOccurred == 1 %we don't want to change energy if we made the IF
o

newE=fourPointEstimate(bsData.avgEnergy,energy/1000,inAngle/(2*pi)*360)
; %divide by 1000 to correspond with the keV units of the reflection
data.
elseif collOccurred == 2
    newE=energy; %want to maintain entrance energy to IF
end
```

```
%TEST FOR DEPOSITION
deposProb =
maxMinRange(fourPointEstimate(bsData.deposFract,energy/1000,inAngle/(2*
pi)*360),0,1);
fpEDP=fourPointEstimate(bsData.deposFract,energy/1000,inAngle/(2*pi)*36
0);
randProb = rand();

%if collOccurred>0
%sprintf('dep prob: %0.2f, rand prob: %0.2f, energy: %0.2f,
angle: %0.2f, FPE: %0.2f',deposProb,randProb,
energy,inAngle/(2*pi)*360,fourPointEstimate(bsData.deposFract,energy/10
00,inAngle/(2*pi)*360))
%end

if (randProb<=deposProb && (collOccurred == 1)) || newE<0
    %then we have deposited onto the surface or into it anyways
    sprintf('deposition occurred');
    vScatRefl = [0,0,0];
    newE = 0;
    collOccurred = 3;
end

%TEST FOR SPUTTERING
if createSecSpecies == 1 %no need to worry about sputtering if we're
not going to make anything anyways

    sputProb =
maxMinRange(fourPointEstimate(bsData.sputFract,energy/1000,inAngle/(2*p
i)*360),0,1);
    randProb = rand();

    %if collOccurred>0
    %sprintf('sput prob: %0.2f, rand prob: %0.2f, energy: %0.2f,
angle: %0.2f,
FPE: %0.2f',sputProb,randProb,energy,inAngle/(2*pi)*360,fourPointEstima
te(bsData.sputFract,energy/1000,inAngle/(2*pi)*360))
    %end


    if randProb<=sputProb
        if collOccurred == 1 || collOccurred == 3 %only allow non-IF
Reaching collisions to contribute
            if
round(fourPointEstimate(bsData.ionPerIonSput,energy/1000,inAngle/(2*pi)
*360))>=1
                sprintf('sputtering occurred');

                sputOccurred=1;
                sputAtomsPerAtom =
round(fourPointEstimate(bsData.ionPerIonSput,energy/1000,inAngle/(2*pi)
*360));
                avgSputEnergy =
fourPointEstimate(bsData.avgSputEnergy,energy/1000,inAngle/(2*pi)*360);
                %this is the number of atoms expected to be created on
```

```
average for a
                %sputter inducing ion that reaches the surface.

                %now we need to go about making each species, giving
them a direction
                %energy, etc.
                for i = 1:sputAtomsPerAtom
                    thetaSput =
maxMinRange(cosineScatter(maxMinRange(fourPointEstimate(bsData.uThetaSp
ut,energy/1000,inAngle/(2*pi)*360),0,pi),maxMinRange(fourPointEstimate(
bsData.sThetaSput,energy/1000,inAngle/(2*pi)*360),0,pi/2)),0,pi);
                    phiSput = rand()*2*pi-pi; %make this random because
it's observed to be pretty uniform for
sputtering  %cosineScatter(fourPointEstimate(bsData.uPhiSput,energy/100
0,inAngle/(2*pi)*360),fourPointEstimate(bsData.sPhiSput,energy/1000,abs
(inAngle)/(2*pi)*360));

                    sprintf('New Sputtered Atom Created: theta: %f
phi:%f',thetaSput,phiSput);
                    vFirstSputRot =
rotVector(vNorm,vOrthRot,thetaSput);
                    %now we rotate it around the normal vector to get
it faced in the right
                    %dirction by an angle of phi
                    vScatRefl =
rotVector(vFirstSputRot,vNorm,phiSput);%this is the direction of the
sputtered species

                    tempNewWallScatAtom(i).parentAtom = parent;
                    tempNewWallScatAtom(i).energy = avgSputEnergy;
                    tempNewWallScatAtom(i).direction =
normVector(vScatRefl);%normVector([0,.064,.36]);%%1:x,2:y,3:z
                    tempNewWallScatAtom(i).mass =
bsData.sputSpeciesMass;
                    tempNewWallScatAtom(i).species =
bsData.sputSpecies;
                    tempNewWallScatAtom(i).velocity =
EtoVconv(tempNewWallScatAtom(i).energy,tempNewWallScatAtom(i).mass);
                    tempNewWallScatAtom(i).location=newLoc;%1:x,2:y,3:z
                    tempNewWallScatAtom(i).birthType=2; %1=pinch
species, 2=sputtered species, 3=scattered species
                    tempNewWallScatAtom(i).generation = generation+1;

tempNewWallScatAtom(i).histEnergy(1)=tempNewWallScatAtom(i).energy;

tempNewWallScatAtom(i).histVelocity(1)=tempNewWallScatAtom(i).velocity;

tempNewWallScatAtom(i).histLoc(1,1:3)=tempNewWallScatAtom(i).location;%
1:x,2:y,3:z

tempNewWallScatAtom(i).histDir(1,1:3)=tempNewWallScatAtom(i).direction(
1:3);%1:xHat,2:yHat,3:zHat
                    tempNewWallScatAtom(i).histTime(1)=timeStart;

tempNewWallScatAtom(i).histInsideOut(1)=cellstr(inOrOut);

tempNewWallScatAtom(i).histProjLoc(1,1:3)=tempNewWallScatAtom(i).locati
on+tempNewWallScatAtom(i).direction*tempNewWallScatAtom(i).velocity*tim
```

```
eStep;
                    tempNewWallScatAtom(i).histVNorm(1,1:3)=0;
                    tempNewWallScatAtom(i).histDistTrav(1)=0;
                    tempNewWallScatAtom(i).histInAngle = 0;
                    tempNewWallScatAtom(i).histOutAngle = 0;
                    tempNewWallScatAtom(i).histIncid(1)=0;
                end
            end
        end
    end
end
%sprintf('W.C. START\nOld Loc: [%0.3f,%0.3f,%0.3f], Proj Loc:
[%0.3f,%0.3f,%0.3f], Old E: %0.2f,Vinc: [%0.3f,%0.3f,%0.3f]\nW.C.
EXIT\nColl Type: %i, Surface: %i\nOld Loc: [%0.3f,%0.3f,%0.3f], New
Loc: [%0.3f,%0.3f,%0.3f], Old E: %0.2f,New E: %0.2f\nInc. Angle: %0.2f,
Out Angle: %0.2f, Straggle Angle: %0.2f, Rand. Prob: %0.2f, Dep.
Prob: %0.2f\nIncident Vector: [%0.3f,%0.3f,%0.3f], Norm Vector:
[%0.3f,%0.3f,%0.3f], Exit Vector:
[%0.3f,%0.3f,%0.3f]\n',curLoc,projLoc,energy,normVector(projLoc-
curLoc),collOccurred, cellColl, curLoc,newLoc, energy, newE,
inAngle/(2*pi)*360,scatAngle/(2*pi)*360,stragAngle/(2*pi)*360,
randProb,deposProb,vInc,vNorm,vRefl)




if collOccurred==1
    if abs(inAngle)>(pi/2)
        sprintf('incident angle issue');
    end
end
```

A.4 gasAtomCollision()

```
function
[gasCollOccurred,newLoc,newDir,newE,tempNewGasScatAtom]=gasAtomCollisio
n(meanFreePath,bMax,pathDist,curLoc,curDir,energy,incVelocity,incMass,b
ufferMass,scatterMatrix,timeStep,bufferSpecies,generation,createSecSpec
ies,parent)

%this function deals with gas atom scattering collisions.  This
utilizes
%the rainbow scattering method.  If this function is called, it has
already
%been determined that a collision has occurred in the length of
pathDist.
%Step one is to determine where in that path the collision occurs.  we
%assume a exponential probability with the beginning point being 0
probability
%and the end point being 1 probability and a term constant of mean free
%path.

%DEFAULT VALUES
gasCollOccurred = 0;
newLoc = curLoc;
```

```
newDir = curDir;
newE = energy;
%bMax = 7;%manually determinable at this point

randProb=rand();%probability a collision doesn't occur
sprintf('rand prob: %0.2f, gas scat prob: %0.2f, MFP: %0.2f, path
dist: %0.2f',randProb,exp(-
pathDist/meanFreePath),meanFreePath,pathDist);

%ANALYZE IF THERE IS A COLLISION WITHIN THE DISTANCE PROJECTED
if randProb>exp(-pathDist/meanFreePath);  %if random chosen probability
is greater than the probability of a collision not occurring, we have a
collision
    gasCollOccurred = 1;

    %DETERMINE ACTUAL DISTANCE TRAVELED TO COLLISION
    %calculate max percentage value of CDF for path dist
    maxProb = 1-exp(-pathDist/meanFreePath);
    randProbNew = rand()*maxProb;                          %set equal
to the actual probability at the distance travelled.Headache inducing
line here...
    distTrav = -meanFreePath*log(1-randProbNew);
    if distTrav > pathDist
        sprintf('Glitch, atom tunneled through a wall again...cant take
them anywhere')
        sprintf('rand prob: %0.2f, gas scat prob: %0.2f, dist
trav: %0.2f, MFP: %0.2f, path dist: %0.2f',randProb,exp(-
pathDist/meanFreePath),distTrav,meanFreePath,pathDist)

    end



    newLoc = distTrav*curDir+curLoc;
    timeStart = sqrt(dot(newLoc-curLoc,newLoc-
curLoc))/incVelocity;%conditional calculation of the time of collision.


    %DETERMINE COM VALUES ASSUMING STATIONARY BUFFER GAS PARTICLE AND
THE
    %RESULTING ENERGY OF THE SCATTERED INCIDENT ATOM
    bIP=sqrt(rand())*bMax; %random selection of impact parameter
    KEinc=1/2*(incMass*1.66*10^-27)*incVelocity^2;


thetaCOM=maxMinRange(fourPointEstimate(scatterMatrix,bIP,KEinc*(6.2415e
18)),0,pi); %extract thetaCOM data

    phiLF=atan2(sin(thetaCOM),(incMass/bufferMass+cos(thetaCOM)));%this
is for the incident species
    thetaLF=-atan2(sin(thetaCOM),1-cos(thetaCOM));

    newE=
((incMass^2+2*incMass*bufferMass*cos(thetaCOM)+bufferMass^2)/(incMass+b
ufferMass)^2)*energy;
    scatteredE = ((2*incMass*bufferMass*(1-
```

```
cos(thetaCOM)))/(incMass+bufferMass)^2)*energy;


    tempProjDir=normVector([cos(phiLF),sin(phiLF),0]); %in the lab
reference frame, but in the same reference frame of an x direction
collision.
    tempProjDirScattered = normVector([cos(thetaLF),sin(thetaLF),0]);

    %ROTATE THE PROJECTED DIRECTION AROUND THE X-AXIS A RANDOM THETA TO
    %RANDOMIZE THE LOCATION OF THE COLLISION WITH THE OTHER ATOM.
    randAngle = rand()*2*pi;
    Rx=[1,0,0;0,cos(randAngle),-
sin(randAngle);0,sin(randAngle),cos(randAngle)];
    RxScat = Rx;

    projDir = normVector((Rx*tempProjDir')');
    projDirScattered= normVector((RxScat*tempProjDirScattered')');


    %NOW ROTATE TO ORIGINAL DIRECTION FROM THE [1,0,0] REFERENCE WE'VE
BEEN
    %USING FOR THE CALCULATIONS

    %first find the angle between the intended direction and the
[1,0,0]
    %vector

    rotAngle = -acos(dot(normVector(curDir),[1,0,0])); %it's negative
because we're going back the way we "came"

    if (rotAngle ~= 0) && (rotAngle ~= pi) %just making sure that
they're not equal or opposite
        %create orthogonal vector to rotate around
        orthVect = normVector(cross(normVector(curDir),[1,0,0]));
        %now lets rotate the vector we made around that orthogonal
vector
        %at an angle of rotAngle to get our results!
        newDir=rotVector(projDir,orthVect,rotAngle);
        newDirScat=rotVector(projDirScattered,orthVect,rotAngle);
    else %So we are either in the same direction, in which case we
don't
        %change anything, or we are in the opposite direction and we
change it all negative
        if rotAngle == 0
            newDir=projDir;
            newDirScat=projDirScattered;
        else
            newDir=-projDir;
            newDirScat=-projDirScattered;
        end
    end

    %NOW CREATE THE ATOMDATA EQUIVALENT VARIABLE FOR THE NEW SPECIES
THAT
    %GOT SCATTERED.
    if createSecSpecies == 1
```

```
        tempNewGasScatAtom.parentAtom = parent;
        tempNewGasScatAtom.energy = scatteredE; % testing purposes
randEnergy(energyHitsMatrix);
        tempNewGasScatAtom.direction =
newDirScat;%normVector([0,.064,.36]);%%1:x,2:y,3:z
        tempNewGasScatAtom.mass = bufferMass;
        tempNewGasScatAtom.species = bufferSpecies;
        tempNewGasScatAtom.velocity =
EtoVconv(tempNewGasScatAtom.energy,tempNewGasScatAtom.mass);
        tempNewGasScatAtom.location=newLoc;%1:x,2:y,3:z
        tempNewGasScatAtom.birthType=3; %1=pinch species, 2=sputtered
species, 3=scattered species
        tempNewGasScatAtom.generation = generation+1;
        tempNewGasScatAtom.histEnergy(1)=tempNewGasScatAtom.energy;
        tempNewGasScatAtom.histVelocity(1)=tempNewGasScatAtom.velocity;

tempNewGasScatAtom.histLoc(1,1:3)=tempNewGasScatAtom.location;%1:x,2:y,
3:z

tempNewGasScatAtom.histDir(1,1:3)=tempNewGasScatAtom.direction(1:3);%1:
xHat,2:yHat,3:zHat
        tempNewGasScatAtom.histTime(1)=timeStart;
        tempNewGasScatAtom.histInsideOut(1)=cellstr('neither');

tempNewGasScatAtom.histProjLoc(1,1:3)=tempNewGasScatAtom.location+tempN
ewGasScatAtom.direction*tempNewGasScatAtom.velocity*timeStep;
        tempNewGasScatAtom.histVNorm(1,1:3)=0;
        tempNewGasScatAtom.histDistTrav(1)=0;
        tempNewGasScatAtom.histInAngle = 0;
        tempNewGasScatAtom.histOutAngle = 0;
        tempNewGasScatAtom.histIncid(1)=0;
    else
        tempNewGasScatAtom=0;
    end

    if newE<0
        newE=0;
    end

else
    gasCollOccurred = 0;
    tempNewGasScatAtom = 0;
end
```

A.5 twoPointsEstimate()

```
function [estVal]=twoPointEstimate(rawMat,vertValue)

%this code takes a raw matrix such as:
% 0 1
% 1 1.5
% 2 1.23
% 3 2
% and provides a linear estimate at the value of vertValue, where
vertValue
```

```
% is the value that corresponds to the numbers in the first column.


%first create a difference matrix between vertValue and the rawMat
values

for i = 1:length(rawMat(:,1))
    diffMat(i,1)=rawMat(i,1);
    diffMat(i,2)=(rawMat(i,1)-vertValue)^2; %square it to factor out
effects of negative numbers
end

[sortMat,ix] = sort(diffMat(:,2));

x1 = rawMat(ix(2),1);
x2 = rawMat(ix(1),1);

y1 = rawMat(ix(2),2);
y2 = rawMat(ix(1),2);


%y=mx+b
m = (y2-y1)/(x2-x1);
b = y2-m*x2;

estVal = m*vertValue+b;
```

A.6 stats()

```
function [depColl,madeIF,maxTime,maxSteps,thermal,screwUp]=stats(data)
%[bob,dimin]=IFTheory(10);IFPlotter(bob(:),dimin);[depColl,madeIF,maxTi
me.maxSteps,thermal,screwUp]=test(bob);sprintf('Deposited: %i,Avg
Time:%0.1fus\nMade IF: %i,Avg Time:%0.1fus\nMax Time: %i\nMax
Steps: %i\nThermalized: %i,Avg
Time:%0.1fus',depColl.count,depColl.timeAvg*10^6,madeIF.count,madeIF.ti
meAvg*10^6,maxTime.count,maxSteps.count,thermal.count,thermal.timeAvg*1
0^6)


inc1=0;
inc2=0;
inc3=0;
inc7=0;
inc8=0;
inc9=0;
inc10=0;
inc11=0;


bgColl.atom=0;
bgColl.time=0;
bgColl.count=0;
bgCollTimeTotal=0;
bgColl.timeAvg=0;
```

```
wallColl.atom=0;
wallColl.time=0;
wallColl.count=0;
wallCollTimeTotal=0;
wallColl.timeAvg=0;

depColl.atom=0;
depColl.time=0;
depColl.count=0;
depCollTimeTotal=0;
depColl.timeAvg=0;

madeIF.atom=0;
madeIF.time=0;
madeIF.count=0;
madeIFTimeTotal=0;
madeIF.timeAvg=0;

maxTime.atom=0;
maxTime.count=0;

maxSteps.atom=0;
maxSteps.time=0;
maxSteps.count=0;

thermal.atom=0;
thermal.time=0;
thermal.count=0;
thermalTimeTotal=0;
thermal.timeAvg=0;

screwUp.atom=0;
screwUp.count=0;


for i = 1:length(data(:))
    result = data(i).histIncid(length(data(i).histIncid(:)));

    distTrav = 0;
    for k = 2:length(data(i).histLoc(:,1))
        vectA=data(i).histLoc(k,:)-data(i).histLoc(k-1,:);
        distTrav = distTrav+sqrt(dot(vectA,vectA));
    end

    switch result
        case 1
            inc1 = inc1+1;
            bgColl.atom(inc1)=i;

bgColl.time(inc1)=data(i).histTime(length(data(i).histTime(:)));
            bgColl.count = inc1;
            bgCollTimeTotal = bgCollTimeTotal+bgColl.time(inc1);
            bgColl.timeAvg=bgCollTimeTotal/inc1;
            bgColl.distTrav(inc1) = distTrav;
```

```
        case 2
            inc2 = inc2+1;
            wallColl.atom(inc2)=i;

wallColl.time(inc2)=data(i).histTime(length(data(i).histTime(:)));
            wallColl.count = inc2;
            wallCollTimeTotal=wallCollTimeTotal+wallColl.time(inc1);
            wallColl.timeAvg=wallCollTimeTotal/inc2;
            wallColl.distTrav(inc2) = distTrav;
        case 3
            inc3 = inc3+1;
            depColl.atom(inc3)=i;

depColl.time(inc3)=data(i).histTime(length(data(i).histTime(:)));
            depColl.count = inc3;
            depCollTimeTotal = depCollTimeTotal+depColl.time(inc3);
            depColl.timeAvg = depCollTimeTotal/inc3;
            depColl.distTrav(inc3) = distTrav;
        case 7 %made IF
            inc7 = inc7+1;
            madeIF.atom(inc7)=i;

madeIF.time(inc7)=data(i).histTime(length(data(i).histTime(:)));
            madeIF.count = inc7;
            madeIFTimeTotal=madeIFTimeTotal+madeIF.time(inc7);
            madeIF.timeAvg = madeIFTimeTotal/inc7;
            madeIF.distTrav(inc7) = distTrav;
        case 8
            inc8 = inc8+1;
            maxTime.atom(inc8)=i;

maxTime.time(inc8)=data(i).histTime(length(data(i).histTime(:)));
            maxTime.count = inc8;
            maxTime.distTrav(inc8) = distTrav;
        case 9
            inc9 = inc9+1;
            maxSteps.atom(inc9)=i;

maxSteps.time(inc9)=data(i).histTime(length(data(i).histTime(:)));
            maxSteps.count = inc9;
            maxSteps.distTrav(inc9) = distTrav;
        case 10
            inc10 = inc10+1;
            thermal.atom(inc10)=i;

thermal.time(inc10)=data(i).histTime(length(data(i).histTime(:)));
            thermal.count = inc10;
            thermalTimeTotal = thermalTimeTotal+thermal.time(inc10);
            thermal.timeAvg = thermalTimeTotal/inc10;
            thermal.distTrav(inc10) = distTrav;
        otherwise
            inc11 = inc11+1;
            screwUp.atom(inc11)=i;
            screwUp.count = inc11;
            screwUp.distTrav(inc11) = distTrav;
    end
end
```

A.7 rotVector()

```
function [vNew] = rotVector(vOld,u,angle)

%u = vector of axis of rotation
%vOld = vector to be rotated
%vNew = rotated vector
u = normVector(u);

tensorProd=[u(1)^2,u(1)*u(2),u(1)*u(3);u(1)*u(2),u(2)^2,u(2)*u(3);u(1)*
u(3),u(2)*u(3),u(3)^2];
crossProdU=[0,-u(3),u(2);u(3),0,-u(1);-u(2),u(1),0];
I=eye(3,3);

R = I*cos(angle)+sin(angle)*crossProdU+(1-cos(angle))*tensorProd;

vNew = R*vOld';
vNew = vNew';
```

A.8 randEnergy()

```
function [retIndVar] = randEnergy(PDF)
%this function has an input of a two column matrix
%(indendentVariable,dependentVariable).  IT then goes through and
%determines an appropriate random value based off of the data provided.
%the data needs to be provided in proper order with lowest starting
%independent variable at position 1;
%i.e.:
%Energy     Hits
%  0          0
%  5eV       500
%  10eV       0
% dataMatrix(1=row [indVar],2=colum[depVar])

%normalize the data by taking the area under the curve and dividing all
%points by that value

%DATA SHOULD BE PROVIDED IN ASCENDING ORDER

%created the CDF
CDF(1,1)=PDF(1,1);
CDF(1,2)=PDF(1,2);
cumValue = CDF(1,2);
for i = 2:length(PDF(:,1))
    cumValue = cumValue + PDF(i,2);
    CDF(i,1)=PDF(i,1);
    CDF(i,2)=cumValue;
end
maxIX = i;

randVal = rand()*CDF(maxIX,2); %rand val between 0 and CDF Max Value
%Now search through the CDF to find that value
difMat = (CDF(:,2)-randVal).^2;
[sortMat,IX]=sort(difMat);
```

```
%find the linear fit between the two points
x0=CDF(IX(2),1);
y0=CDF(IX(2),2);
x1=CDF(IX(1),1);
y1=CDF(IX(1),2);
m = (y1-y0)/(x1-x0);
b = y1-m*x1;
%now use the randomly determined value to determine the energy value
if m~= 0
    retIndVar = (randVal-b)/m;
else
    retIndVar = (x1+x0)/2;
end
```

A.9 randDirection()

```
function [newDirection] = randDirection()


    %use these outputs for the test function [iHat,jHat,kHat,phi,theta]
    %this function determines a random angle based on a three
dimensionals
    %cosine distribution.
    %calcuate the first rand angle
    s = pi/2; %plus or minus pi/2
    u = 0; %this angle is restricted from 0-pi
    exiter = 0;
    while exiter ==0
        randvar1 = rand()*pi/2;
        if rand()<=(2/(2*s)*(1+cos((randvar1-u)/s*pi)))
            phi = abs(randvar1);
            exiter = 1;
        end
    end


    %because we assume azimuthal symmetry, the theta coordinate has the
    %likely hood of being any direction betwee 0-2pi
    %the while loop makes it so that 0 and 2pi are not combined
    theta = 2*pi;
    while theta == 2*pi
        theta = rand()*2*pi;
    end



    %in this spherical coord system  phi extends from +z axis
    %theta extends from +x-axis
    iVal = sin(phi)*cos(theta); %init x vector
    jVal = sin(phi)*sin(theta); %init y vector
    kVal = cos(phi); %init z vector

    iHat = iVal;%/sqrt(iVal^2+jVal^2+kVal^2);
```

```
    jHat = jVal;%/sqrt(iVal^2+jVal^2+kVal^2);
    kHat = kVal;%/sqrt(iVal^2+jVal^2+kVal^2);

    newDirection=[iHat,jHat,kHat];
```

A.10 randCosDist()

```
function[randnumber] = randCosDist()
clear;
s = pi/2;
u = 0;

exiter = 0;
while exiter ==0
    randvar1 = rand()*2*pi;
    randvar2 = rand();
    probability = 1/(2*s)*(1+cos((randvar1-u)/s*pi));

    if randvar2<=probability
        randnumber = randvar1;
        exiter = 1;
    end
end
```

A.11 normVector()

```
function [unitVector] = normVector(vector)

magnitude = sqrt(vector(1)^2+vector(2)^2+vector(3)^2);

if magnitude > 0
    unitVector = vector/magnitude;
else
    unitVector = [0,0,0];
end
```

A.12 maxMinRange()

```
function [value]=maxMinRange(input,minVal,maxVal)

value=input;

if input<minVal
    value = minVal;
elseif input>maxVal
    value = maxVal;
end
```

A.13 ifAnalyzer()

```
function []=IFAnalyzer(atomdata)


totSpec = length(atomdata);



ifStep = 1;
for i = 1:totSpec

    histIncidLength = length(atomdata(i).histIncid(:));
    if atomdata(i).histIncid(histIncidLength) == 7
        madeIF(ifStep).energy=atomdata(i).energy;
        madeIF(ifStep).cell=i;
        madeIF(ifStep).generation=atomdata(i).generation;
        madeIF(ifStep).species=atomdata(i).species;

        maxTimeCell = length(atomdata(i).histTime(:));
        madeIF(ifStep).time=atomdata(i).histTime(maxTimeCell);
        ifStep=ifStep+1;
    end


end

for i = 1:length(madeIF)
    bob(i)=madeIF(i).time;
end


%plot the if arrival data
firstGen = 1;
secondGen = 1;
for i = 1:length(madeIF(:))
    if madeIF(i).generation==1
        firstGenIF(firstGen).time = madeIF(i).time;
        firstGenIF(firstGen).energy = madeIF(i).energy;
        firstGen = firstGen+1;
    else
        secondGenIF(secondGen).time = madeIF(i).time;
        secondGenIF(secondGen).energy = madeIF(i).energy;
        secondGen = secondGen+1;
    end
end

sprintf('Total made IF: %i, First Gen: %i, Second
Gen: %i',length(madeIF(:)),length(firstGenIF(:)),length(secondGenIF(:))
)

xEnergy = 0:100:2000;
xTime = 200e-6:100e-6:10e-3;
```

```
clear bob
for i = 1:length(madeIF)
    bob(i)=madeIF(i).time;
end
axis([0,10e-3,0,100]);
[n,xOut]=hist(bob,xTime);
plot(xOut,n)
averageT = mean(bob);
sprintf('Average Arrival Time: %0.2f',averageT*10^6)

clear bob
for i = 1:length(madeIF)
    bob(i)=madeIF(i).energy;
end
averageE = mean(bob);
sprintf('Average Energy: %0.2f',averageE)
```

A.14 fourPointEstimate()

```
function [retVal]=fourPointEstimate(rawMat,vertValue,horzValue)
%most likely vert=energy, horz=angle
%This function comes up with a linear approximation of a value at an
%arbitray location on a matrix map.  It uses 3 different points in the
map,
%the 3 nearest to the location of interest.  This liest of 3 is done by
the
%sort function.  A vector is drawn betwee the nearest point and third
%nearest as well as between the nearest point and the second nearest.
The
%cross product of these two vectors is taken to give the normal vector
of
%the plane that encompases all three points.  From there the vector
from
%the nearest point to the point of interest is to be calculated.
Because
%this vector is normal to the normal of the plane, the dot product is =
0,
%so we are able to calculate the unknown variable, which is the z
component
%of the vector form th enearest point to the unknown point.  The last
step
%is to calculate the addition of the vector from (0,0,0) to point 1
(the
%point nearest to the point of interest) and then add this to the
vector
%form point 1 to the point of interest and return the third component
of
%this vector, which is the estimated value at the point of interest.

%BREAK INTO COMPONENTS
maxVertCell=length(rawMat(:,1));
maxHorzCell=length(rawMat(1,:));

[vertAxisVals(:,1)]=rawMat(2:maxVertCell,1);
[horzAxisVals(:,1)]=rawMat(1,2:maxHorzCell);
for i = 2:maxVertCell
    for j = 2:maxHorzCell
```

```
        dataVal(i-1,j-1)=rawMat(i,j);
    end
end

%CREATE DIFFERENCE VALUES IN SORTED ORDER
[vertDiff(:,1),vertDiff(:,2)]=sort(abs(vertAxisVals-vertValue));
[horzDiff(:,1),horzDiff(:,2)]=sort(abs(horzAxisVals-horzValue));

%CREATE THREE NEAREST POINTS
point1=[horzAxisVals(horzDiff(1,2)),vertAxisVals(vertDiff(1,2)),dataVal
(vertDiff(1,2),horzDiff(1,2))];
point2=[horzAxisVals(horzDiff(2,2)),vertAxisVals(vertDiff(1,2)),dataVal
(vertDiff(1,2),horzDiff(2,2))];
point3=[horzAxisVals(horzDiff(1,2)),vertAxisVals(vertDiff(2,2)),dataVal
(vertDiff(2,2),horzDiff(1,2))];

%CREATE FIND NORMAL VECTOR
vectN=normVector(cross(point3-point1,point2-point1));

%CALCULATE EXPECTATION UNIT VECTOR VALUE BASED ON MATH
dataValCmpt=(vectN(1)*(horzValue-point1(1))+vectN(2)*(vertValue-
point1(2)))/-vectN(3) ;

vect1E=[horzValue-point1(1),vertValue-point1(2),dataValCmpt];
vect1=point1;
vectE=vect1+vect1E;
retVal = vectE(3);
```

A.15 fileSaver()

```
function []=fileSaver(atomdata,filePath,fileName)

mkdir(filePath);
fileSaveName = strcat(filePath,fileName,'.mat');%auto saves as a .mat
file
save(fileSaveName,'atomdata')
```

A.16 EtoVconv()

```
function [velocity] = EtoVconv(energy,mass)
%mass in amu
%energy in eV
%velocity in m/s
velocity=sqrt(2*(energy*1.602e-19)/(mass*1.66e-27));
```

A.17 energyAsAFunction()

```
function
[timeArrayValues,timeArrayAvgEnergy,timeArrayCount,timeArrayZCoord]=ene
rgyAsAFunction(atomdata)
```

```
maxTime=2e-3;
timeDivisions=100;

timeBounds = [0:maxTime/timeDivisions:maxTime];
timeArrayValues =
[maxTime/timeDivisions/2:maxTime/timeDivisions:maxTime-
maxTime/timeDivisions/2];

for timeIX = 1:(length(timeBounds(:))-1)

    maxZ=0.72;
    ZDivisions=100;

    ZBounds = [0:maxZ/ZDivisions:maxZ];
    ZArrayValues = [maxZ/ZDivisions/2:maxZ/ZDivisions:maxZ-
maxZ/ZDivisions/2];
    clear ZArrayEnergy
    ZArrayEnergy(1:length(ZArrayValues),1)=ZArrayValues;%Z
    ZArrayEnergy(1:length(ZArrayValues),2)=0;%hits
    ZArrayEnergy(1:length(ZArrayValues),3)=0;%energy
    doubleCountZ(1:length(ZArrayValues))=0;

    for iX=1:length(atomdata(:))
        iX
        for jX=1:length(atomdata(iX).histLoc(:,3))
            for j = 1:length(ZBounds)-1
                if atomdata(iX).histLoc(jX,3)>=ZBounds(j) &&
atomdata(iX).histLoc(jX,3)<ZBounds(j+1) %saying we're in the division
range
                    if doubleCountZ(j)~=1 %don't want to count the same
atom's energy twice
                        if atomdata(iX).histIncid(jX)<3 %only consider
live species
                            if atomdata(iX).birthType==3
                                if
atomdata(iX).histTime(jX)>=timeBounds(timeIX) &&
atomdata(iX).histTime(jX)<timeBounds(timeIX+1)

ZArrayEnergy(j,2)=ZArrayEnergy(j,2)+1;

ZArrayEnergy(j,3)=ZArrayEnergy(j,3)+atomdata(iX).histEnergy(jX);
                                    doubleCountZ(j)=1;
                                end
                            end
                        end
                    end
                end
            end
        end
        doubleCountZ(1:length(ZArrayValues))=0;
    end
    lengthArray=length(ZArrayEnergy(:,1));
    ZArrayEnergy(1:lengthArray,4)=ZArrayEnergy(:,3)./ZArrayEnergy(:,2);
    %semilogy(ZArrayEnergy(:,1),ZArrayEnergy(:,4),ZArrayEnergy(:,1),ZAr
rayEnergy(:,2))
```

```
timeArrayAvgEnergy(1:length(ZArrayEnergy(:,1)),timeIX)=ZArrayEnergy(1:l
engthArray,4);

timeArrayCount(1:length(ZArrayEnergy(:,1)),timeIX)=ZArrayEnergy(1:lengt
hArray,2);

timeArrayZCoord(1:length(ZArrayEnergy(:,1)))=ZArrayEnergy(1:lengthArray
,1);

end

% subplotNum=length(timeArrayValues)
% for i = 1:length(timeArrayValues)
%     hold on
%     subplot(subplotNum,1,i)
%     semilogy(timeArrayZCoord(:)',timeArrayAvgEnergy(:,i));
% end

%semilogy(ZArrayEnergy(:,1),ZArrayEnergy(:,4),ZArrayEnergy(:,1),ZArrayE
nergy(:,2))
```

A.18 depositionMonitor()

```
function [positionPlot]=depositionMonitor(atomdata,shellSize)




%only concerned about the pinch species here, so Sn
depInc = 1;
sputInc = 1;
sprintf('preallocate...');

adDepPA(length(atomdata(:)))=atomdata(1);
adSputPA(length(atomdata(:)))=atomdata(1);
runningParentSput = 0;
runningParentDep = 0;
sprintf('starting...')
incidentSpecies=atomdata(1).species;
for i = 1:length(atomdata(:))
    i
    maxLength=length(atomdata(i).histIncid);
    if isequal(atomdata(i).species,incidentSpecies)

        if atomdata(i).birthType == 1 || atomdata(i).birthType == 2
            if atomdata(i).histIncid(maxLength)==3 ||
atomdata(i).histIncid(maxLength)==7 %it stays on a wall
                if atomdata(i).birthType == 1
                    adDepPA(depInc)=atomdata(i);
                    adDepIX(depInc)=i;
                    depInc=depInc+1;
%                 else
%                     if atomdata(i).parentAtom ~= runningParentDep
%                         adDepPA(depInc)=atomdata(i);
```

```
%                           adDepIX(depInc)=i;
%                           depInc=depInc+1;
%                           runningParentDep=atomdata(i).parentAtom;
%
%                       end
                    end
                    i
                end
            end


            if atomdata(i).birthType == 2
                if atomdata(i).histIncid(maxLength)==3 ||
atomdata(i).histIncid(maxLength)==7
                    if atomdata(i).parentAtom ~= runningParentSput
                        adSputPA(sputInc)=atomdata(i);
                        adSputIX(sputInc)=i;

                        sputInc = sputInc+1;
                        runningParentSput = atomdata(i).parentAtom;
                    end
                end
            end
        end
    end

adDep=adDepPA(1:depInc-1);
adSput=adSputPA(1:sputInc-1);




insideShellINDep=0;
insideShellOUTDep=0;
outerShellINDep=0;
outerShellOUTDep=0;
chamberShellDep=0;
pinchWallDep=0;
IFWallDep=0;
insideShellINsput=0;
insideShellOUTsput=0;
outerShellINsput=0;
outerShellOUTsput=0;
chamberShellsput=0;
pinchWallsput=0;
IFWallsput=0;

sprintf('calculating deposition locations...')
if depInc>1

[insideShellINDep,insideShellOUTDep,outerShellINDep,outerShellOUTDep,ch
amberShellDep,pinchWallDep,IFWallDep]=depositionLocator(adDep,0);
end
```

```
sprintf('calculating origination of deposition locations...')
if sputInc>1

[insideShellINsput,insideShellOUTsput,outerShellINsput,outerShellOUTspu
t,chamberShellsput,pinchWallsput,IFWallsput]=depositionLocator(adSput,1
);
end




%now learn where the deposition locations are and plot it as we want.

inColZmin=.285;
inColZmax =.285+.15;
inColZdiv=15;%turns out to be a ribbon width of 1.0cm
inColEqualizer=2*pi*.064/.01;
inColStep=(inColZmax-inColZmin)/inColZdiv;
inColZ=[inColZmin:inColStep:inColZmax];
inColinCount(1:length(inColZ))=0;
inColoutCount=inColinCount;

outColZmin=.2075;
outColZmax=.2075+.305;
outColZdiv=30;%turns out to be a ribbon width of 1.01cm
outColEqualizer = 2*pi*.216/.01;
outColStep=(outColZmax-outColZmin)/outColZdiv;
outColZ=[outColZmin:outColStep:outColZmax];
outColinCount(1:length(outColZ))=0;
outColoutCount=outColinCount;

chamShellZmin=0;
chamShellZmax=.72;
chamShellZdiv=72;%turns out to be a ribbon width of 1.01cm
chamShellEqualizer = 2*pi*.46/.01;
chamShellStep=(chamShellZmax-chamShellZmin)/chamShellZdiv;
chamShellZ=[chamShellZmin:chamShellStep:chamShellZmax];
chamShellcount(1:length(chamShellZ))=0;

ifWallRmin=0;
ifWallRmax=0.46;
ifWallRdiv=10;
ifWallStep=(ifWallRmax-ifWallRmin)/ifWallRdiv;
ifWallR=[ifWallRmin:ifWallStep:ifWallRmax];
ifWallcount(1:length(ifWallR))=0;
ifEqualizer = (.046)^2/.0056^2; %makes this come out to 1cm^2 like all
other points.

zPWall=ifWallRmin;
zPWallRmax=ifWallRmax;
zPWallRdiv=ifWallRdiv;
zPWallR=ifWallR;
zPWallStep=ifWallStep;
zPWallcount(1:length(zPWallR))=0;
```

```
depMatrix((1:length(inColZ)),1)=0;
depMatrix((1:length(inColZ)),2)=0;
depMatrix((1:length(outColZ)),3)=0;
depMatrix((1:length(outColZ)),4)=0;
depMatrix((1:length(chamShellZ)),5)=0;
depMatrix((1:length(ifWallR)),6)=0;
depMatrix((1:length(zPWallR)),7)=0;

depMatrix((1:length(inColZ)),1)=0;
depMatrix((1:length(inColZ)),2)=0;
depMatrix((1:length(outColZ)),3)=0;
depMatrix((1:length(outColZ)),4)=0;
depMatrix((1:length(chamShellZ)),5)=0;
depMatrix((1:length(ifWallR)),6)=0;
depMatrix((1:length(zPWallR)),7)=0;

cellMatrix(1)=length(inColZ);
cellMatrix(2)=length(inColZ);
cellMatrix(3)=length(outColZ);
cellMatrix(4)=length(outColZ);
cellMatrix(5)=length(chamShellZ);
cellMatrix(6)=length(ifWallR);
cellMatrix(7)=length(zPWallR);
```

```
tempMatrix=0;
for i=1:7
    clear tempMatrix

    if i == 1
        tempMatrix=insideShellINDep(:,1);
        step=inColStep;
        start=.285;
    elseif i == 2
        tempMatrix=insideShellOUTDep(:,1);
        step=inColStep;
        start=.285;
    elseif i == 3
        tempMatrix=outerShellINDep(:,1);
        step=outColStep;
        start=.2075;
    elseif i == 4
        tempMatrix=outerShellOUTDep(:,1);
        step=outColStep;
        start=.2075;
    elseif i == 5
        tempMatrix=chamberShellDep(:,1);
        step=chamShellStep;
        start=0;
    elseif i == 6
        tempMatrix=pinchWallDep(:,1);
```

```
        step=zPWallStep;
        start=0;
    elseif i == 7
        tempMatrix=IFWallDep(:,1);
        step=zPWallStep;
        start=0;
    end

    for j = 1:length(tempMatrix)
        if tempMatrix(j)>0
            depMatrix(round((tempMatrix(j)-
start)/step)+1,i)=depMatrix(round((tempMatrix(j)-start)/step)+1,i)+1;
        end
    end
end

tempMatrix=0;
for i=1:7
    clear tempMatrix

    if i == 1
        tempMatrix=insideShellINsput(:,1);
        step=inColStep;
        start=.285;
    elseif i == 2
        tempMatrix=insideShellOUTsput(:,1);
        step=inColStep;
        start=.285;
    elseif i == 3
        tempMatrix=outerShellINsput(:,1);
        step=outColStep;
        start=.2075;
    elseif i == 4
        tempMatrix=outerShellOUTsput(:,1);
        step=outColStep;
        start=.2075;
    elseif i == 5
        tempMatrix=chamberShellsput(:,1);
        step=chamShellStep;
        start=0;
    elseif i == 6
        tempMatrix=pinchWallsput(:,1);
        step=zPWallStep;
        start=0;
    elseif i == 7
        tempMatrix=IFWallDep(:,1);
        step=zPWallStep;
        start=0;
    end

    for j = 1:length(tempMatrix)
        if tempMatrix(j)>0
            depMatrix(round((tempMatrix(j)-
start)/step)+1,i)=depMatrix(round((tempMatrix(j)-start)/step)+1,i);
        end
    end
end
```

```
subplot(3,2,1)
plot(inColZ,depMatrix(1:length(inColZ),1));
subplot(3,2,2)
plot(inColZ,depMatrix(1:length(inColZ),2));
subplot(3,2,3)
plot(outColZ,depMatrix(1:length(outColZ),3));
subplot(3,2,4)
plot(outColZ,depMatrix(1:length(outColZ),4));
subplot(3,2,5)
plot(ifWallR,depMatrix(1:length(ifWallR),7));


positionPlot(1)= depMatrix(round(cellMatrix(2)*1/3),1)/inColEqualizer;
positionPlot(2)= depMatrix(round(cellMatrix(2)*2/3),1)/inColEqualizer;
positionPlot(3)= depMatrix(round(cellMatrix(2)*1/2),2)/inColEqualizer;
positionPlot(4)= depMatrix(round(cellMatrix(3)/4),3)/outColEqualizer;
positionPlot(5)= depMatrix(round(cellMatrix(3)/2),3)/outColEqualizer;
positionPlot(6)= depMatrix(round(cellMatrix(3)*3/4),3)/outColEqualizer;
positionPlot(7)= depMatrix(round(cellMatrix(4)/2),4)/outColEqualizer;
positionPlot(8)= sum(depMatrix(1:2,7))/ifEqualizer;


errorVals(1) =
sqrt(depMatrix(round(cellMatrix(1)/3),1))/inColEqualizer;
errorVals(2) =
sqrt(depMatrix(round(cellMatrix(1)*2/3),1))/inColEqualizer;
errorVals(3) =
sqrt(depMatrix(round(cellMatrix(2)/2),2))/inColEqualizer;
errorVals(4) =
sqrt(depMatrix(round(cellMatrix(3)/4),3))/outColEqualizer;
errorVals(5) =
sqrt(depMatrix(round(cellMatrix(3)/2),3))/outColEqualizer;
errorVals(6) =
sqrt(depMatrix(round(cellMatrix(3)*3/4),3))/outColEqualizer;
errorVals(7) =
sqrt(depMatrix(round(cellMatrix(4)/2),4))/outColEqualizer;
errorVals(8) = sqrt(sum(depMatrix(1:2,7)))/ifEqualizer;

subplot(3,2,6)
errorbar(1:8,positionPlot(:),errorVals(:))
%plot(1:8,positionPlot(:));

%     shellSize(1,1)=.064; %inner shell radius
%     shellSize(1,2)=.15; %inner shell length
%     shellSize(1,3)=.285; %inner shell dist from pinch to coll
optic .435 .585
%
%     shellSize(2,1)=.216; %outer shell radius
%     shellSize(2,2)=.305; %outer shell length
%     shellSize(2,3)=.2075; %outer shell dist from pinch to coll
optic .2075 .5125
%
%     shellSize(3,1)=.46; %Outside shell radius   (chamber)
%     shellSize(3,2)=.72; %Outside shell length
%     shellSize(3,3)=0; %Outside shell dist from pinch to coll optic
%
```

```
%     shellSize(4,1)=.1; %IF radius
%     shellSize(4,2)=0; %shell length/0 because it's at the end
%     shellSize(4,3)=shellSize(3,2); %distance from pinch to IF
%
%     shellSize(5,1)=shellSize(2,1); %radius of the brackets blocking
trajectory holding collector shape
%     shellSize(5,2)=shellSize(2,2)+2*.006; %distance from first set of
brackets to second in z direction
%     shellSize(5,3)=shellSize(2,3)-.006; %location of the z-pinch
proximal set of brackets
%     shellSize(5,4)=.019; %half-width of the brackets
```

APPENDIX B

ANALYSIS PROGRAMS

B.1 locationPlotter()

```
function []=locationPlotter(data)
ISIinc=1;
ISOinc=1;
OSIinc=1;
OSOinc=1;
CSinc=1;
PWinc=1;
IFWinc=1;

insideShellIN(1,1:2)=0;
insideShellOUT(1,1:2)=0;
outerShellIN(1,1:2)=0;
outerShellOUT(1,1:2)=0;
chamberShell(1,1:2)=0;
pinchWall(1,1:2)=0;
IFWall(1,1:2)=0;

for i = 1:length(data(:))
   lastPt = length(data(i).histIncid(:));
   if data(i).histIncid(lastPt)==3
      x = data(i).histLoc(lastPt,1);
      y = data(i).histLoc(lastPt,2);
      z = data(i).histLoc(lastPt,3);
      r = sqrt(x^2+y^2);
      E = data(i).histEnergy(lastPt-1);
      if z>0 && z<.72
         if abs(r-.064)<=.01%inner collector
            if z>=.285 && z<=.285+.15
               if isequal(data(i).histInsideOut(lastPt),cellstr('in'))
                  insideShellIN(ISIinc,1)=z;
                  insideShellIN(ISIinc,2)=E;
                  ISIinc=ISIinc+1;
               else
                  insideShellOUT(ISOinc,1)=z;
                  insideShellOUT(ISOinc,2)=E;
                  ISOinc=ISOinc+1;
               end
            end
         end
```

```
        if abs(r-.216)<=.01%outer collector
          if z>=.2075 && z<=.2075+.305
            if isequal(data(i).histInsideOut(lastPt),cellstr('in'))
              outerShellIN(OSIinc,1)=z;
              outerShellIN(OSIinc,2)=E;
              OSIinc=OSIinc+1;
            else
              outerShellOUT(OSOinc,1)=z;
              outerShellOUT(OSOinc,2)=E;
              OSOinc=OSOinc+1;
            end
          end
        end
        if abs(r-.46)<=.01%chamber shell
          if z>0 && z<.72
            chamberShell(CSinc,1)=z;
            chamberShell(CSinc,2)=E;
            CSinc=CSinc+1;
          end
        end
      else
        if abs(z)<.01
          pinchWall(PWinc,1)=r;
          pinchWall(PWinc,2)=E;
          PWinc=PWinc+1;
        elseif abs(z-.72)<.01
          IFWall(IFWinc,1)=r;
          IFWall(IFWinc,2)=E;
          IFWinc=IFWinc+1;
        end
      end

    end
end

maxPt=max([hist(insideShellIN(:,1),50),hist(IFWall(:,1),50),hist(pinchWall(:,1),50),hist(outerShellOUT(:,1),5
0),hist(chamberShell(:,1),50),hist(insideShellOUT(:,1),50),hist(outerShellIN(:,1),50)]);
hold off
subplot(4,3,1)
hist(insideShellIN(:,1),50);
axis([0,.72,0,maxPt]);
title('Inner Collector: In. Distrib.');
hold on

subplot(4,3,2)
hist(insideShellOUT(:,1),50);
axis([0,.72,0,maxPt]);
title('Inner Collector: Out. Distrib.');


subplot(4,3,3)
clear a b;
```

```
[a,b]=hist(insideShellIN(:,2),50);
hist(insideShellIN(:,2),50);
axis([0,max(b),0,max(a)]);
title('Inner Collector: Inc. Energy');


subplot(4,3,4)
hist(outerShellIN(:,1),50);
axis([0,.72,0,maxPt]);
title('Outer Collector: In. Distrib.');

subplot(4,3,5)
hist(outerShellOUT(:,1),50);
axis([0,.72,0,maxPt]);
title('Outer Collector: Out. Distrib.');

subplot(4,3,6)
clear a b;
[a,b]=hist(outerShellIN(:,2),50);
hist(outerShellIN(:,2),50);
axis([0,max(b),0,max(a)]);
title('Outer Collector: Inc. Energy');

subplot(4,3,7)
hist(chamberShell(:,1),50);
axis([0,.72,0,maxPt]);
title('Chamber Cylinder: In. Distrib.');

subplot(4,3,9)
clear a b;
[a,b]=hist(chamberShell(:,2),50);
hist(chamberShell(:,2),50);
axis([0,max(b),0,max(a)]);
title('Chamber Cylinder: Inc. Energy');

subplot(4,3,10)
hist(pinchWall(:,1),50);
axis([0,.46,0,maxPt]);
title('Pinch-Side Wall: Distrib.');

subplot(4,3,11)
hist(IFWall(:,1),50);
axis([0,.46,0,maxPt]);
title('IF-Side Wall: Distrib.');

subplot(4,3,12)
clear a b;
[a,b]=hist(IFWall(:,2),50);
hist(IFWall(:,2),50);
axis([0,max(b),0,max(a)]);
title('IF-Side Wall: Inc. Energy');
```

```
hold off;
```

B.2 IFCountsAndAvgE()

```
function [results]=IFCountsAndAvgE(atomdata)


counter=0;
step=(10e-3-10e-6)/1000

timeSpec=[10e-6:step:10e-3];
timeCount(1:length(timeSpec))=0;
timeETot(1:length(timeSpec))=0;
timeEAvg(1:length(timeSpec))=0;


IX(length(atomdata))=0;

for i=1:length(atomdata(:))
   if (atomdata(i).birthType == 3)
      lastPt=length(atomdata(i).histIncid(:));
      if atomdata(i).histIncid(lastPt)==7

         time=atomdata(i).histTime(lastPt)
         if time<10e-3
            energy=atomdata(i).histEnergy(lastPt);

            timeCount(round(time/step)+1)=timeCount(round(time/step)+1)+1;
            timeETot(round(time/step)+1)=timeETot(round(time/step)+1)+energy;
         end

      end
   end
end

for i = 1:length(timeCount(:))
   timeEAvg(i)=timeETot(i)/timeCount(i);
end

subplot(2,1,1)
semilogx(timeSpec,timeCount)
subplot(2,1,2)
loglog(timeSpec,timeEAvg)
```

B.3 IFPlotter()

```
function []=IFPlotter(testAtom,shellSize,generations,globeSelect)
%Globe select determines the type of globe to plot if any
%1:Plot at end point, 2: plot at bounce point, 3: plot at both locations


%TEST VARIABLES
%testAtom(1).histLoc=[0,0,0;0,.46,.36;0,0,.72];
%testAtom(1).histInsideOut=[cellstr('neither'),cellstr('out'),cellstr('in')];
%testAtom(2).histLoc=[0,0,0;0,.064,.36;0,0,.72];
%testAtom(2).histInsideOut=[cellstr('in'),cellstr('out'),cellstr('neither')];
%testAtom(3).histLoc=[0,0,0;0,.216,.36;0,0,.72];
%testAtom(3).histInsideOut=[cellstr('neither'),cellstr('out'),cellstr('in')];



%PLOT CYLINDERS
hold off
for i = 1:1
   subplot(1,1,i)
plotWalls(shellSize)

if generations == 0 %we plot all of the generations
   plotAtom = testAtom;
else
   incremental = 1;
   max = length(testAtom);
   exiter = 0;
   while exiter == 0;

      if testAtom(incremental).generation <= generations
         incremental = incremental+1;
      else
         exiter = 1;
      end

      if incremental > max
         exiter = 1;
      end
   end
   plotAtom=testAtom(1:incremental-1);
end



%PLOT LINES
plotLines = 1;
if plotLines == 1
   for i = 1:length(plotAtom(:))
```

```
      plot3(plotAtom(i).histLoc(:,1),plotAtom(i).histLoc(:,2),plotAtom(i).histLoc(:,3))
   end
end

%PLOT REFLECTION GLOBE INDICATORS
incremental=1;
a=.005;
for i = 1:length(plotAtom(:))

   switch globeSelect
      case {1} %plot end point
         j=length(plotAtom(i).histIncid(:));
         if plotAtom(i).histIncid(j)==3
            [x,y,z]=sphere;

globe(incremental)=surf(x*a+plotAtom(i).histLoc(j,1),y*a+plotAtom(i).histLoc(j,2),z*a+plotAtom(i).histLoc
(j,3));
            incremental=incremental+1;
         end
      case {2} %plot bounce point
         if plotAtom(i).histIncid(length(plotAtom(i).histIncid(:)))==7
            for j = 1:length(plotAtom(i).histLoc(:,1:3))
               [x,y,z]=sphere;

globe(incremental)=surf(x*a+plotAtom(i).histLoc(j,1),y*a+plotAtom(i).histLoc(j,2),z*a+plotAtom(i).histLoc
(j,3));
               incremental=incremental+1;
            end
         end
   end
end



%PLOT PARAMETERS
shading flat

xlabel('X-Axis');ylabel('Y-Axis');zlabel('Z-Axis');
axis([-shellSize(3,1),shellSize(3,1),-shellSize(3,1),shellSize(3,1),-.1,shellSize(4,3)+.1]);



end
```

B.4 depositionLocator()

```
function
[insideShellIN,insideShellOUT,outerShellIN,outerShellOUT,chamberShell,pinchWall,IFWall]=depositionLoc
ator(atomdata,startOrEnd)
%takes in all atomdata species and returns the z location (for shells) and r
%locations (for walls) as well as the indices corresponding to the species
%startOrEnd = 0 means we're searching for the endpoint
```

```
%startOrEnd = 1 means we're searching for the start point

%this function returns arrays with the appropriate location of deposition
%and the index of the atomdata array corresponding to the atom that is
%resting there

%first column is the location, second column is the species

ISIinc=1;
ISOinc=1;
OSIinc=1;
OSOinc=1;
CSinc=1;
PWinc=1;
IFWinc=1;

insideShellIN(1,1:2)=0;
insideShellOUT(1,1:2)=0;
outerShellIN(1,1:2)=0;
outerShellOUT(1,1:2)=0;
chamberShell(1,1:2)=0;
pinchWall(1,1:2)=0;
IFWall(1,1:2)=0;
length(atomdata(:))
for i = 1:length(atomdata(:))
   lastPt = length(atomdata(i).histIncid(:));
   if atomdata(i).histIncid(lastPt) == 3 ||atomdata(i).histIncid(lastPt) == 7
        if startOrEnd == 0 %we're looking for the final point
           x = atomdata(i).histLoc(lastPt,1);
           y = atomdata(i).histLoc(lastPt,2);
           z = atomdata(i).histLoc(lastPt,3);
           r = sqrt(x^2+y^2);
        else
           x = atomdata(i).histLoc(1,1);
           y = atomdata(i).histLoc(1,2);
           z = atomdata(i).histLoc(1,3);
           r = sqrt(x^2+y^2);
        end

        if z>0 && z<.72
           if abs(r-.064)<=.01%inner collector
              if z>=.285 && z<=.285+.15
                 if isequal(atomdata(i).histInsideOut(lastPt),cellstr('in'))
                    insideShellIN(ISIinc,1)=z;
                    insideShellIN(ISIinc,2)=i;
                    ISIinc=ISIinc+1;
                 else
                    insideShellOUT(ISOinc,1)=z;
                    insideShellOUT(ISOinc,2)=i;
                    ISOinc=ISOinc+1;
                 end
              end
```

```
            end
            if abs(r-.216)<=.01%outer collector
               if z>=.2075 && z<=.2075+.305
                  if isequal(atomdata(i).histInsideOut(lastPt),cellstr('in'))
                     outerShellIN(OSIinc,1)=z;
                     outerShellIN(OSIinc,2)=i;
                     OSIinc=OSIinc+1;
                  else
                     outerShellOUT(OSOinc,1)=z;
                     outerShellOUT(OSOinc,2)=i;
                     OSOinc=OSOinc+1;
                  end
               end
            end
            if abs(r-.46)<=.01%chamber shell
               if z>0 && z<.72
                  chamberShell(CSinc,1)=z;
                  chamberShell(CSinc,2)=i;
                  CSinc=CSinc+1;
               end
            end
         else
            if abs(z)<.01
               pinchWall(PWinc,1)=r;
               pinchWall(PWinc,2)=i;
               PWinc=PWinc+1;
            elseif abs(z-.72)<.01
               IFWall(IFWinc,1)=r;
               IFWall(IFWinc,2)=i;
               IFWinc=IFWinc+1;
            end
         end

      end
end
```

B.5 avgBGEatIF()

```
function []=avgBGEatIF(atomdata)

totE=0;
counter=0;
counter2=0;
timeVals=0;
totTime=0;
for i = 10001:length(atomdata)
   lastPt = length(atomdata(i).histIncid(:));
   if atomdata(i).histIncid(lastPt)==7
      if atomdata(i).birthType == 3
```

```
      if atomdata(i).parentAtom<10001
        if atomdata(i).histEnergy(lastPt)>10
        %if atomdata(i).histTime(lastPt)>50e-6 && atomdata(i).histTime(lastPt)<2000e-6
          totE=totE+atomdata(i).histEnergy(lastPt);

          totTime=totTime+atomdata(i).histTime(lastPt);
          counter = counter+1;
          timeVals(counter)=atomdata(i).histTime(lastPt);
        end
        %end
      end
      end
    end
end
sprintf('avg energy: %0.2f, avg time: %0.2f|+/-|%0.2fus, species: %i\n',totE/counter,
totTime/counter*10^6,std(timeVals)*10^6, counter)
```

APPENDIX C

WALL SCATTERING DATA CREATOR

C.1 main()

```
function main()


%initial
conditions%%%
```

```
ionAngleStart = 0;
ionAngleFinish = 89.0;
ionAngleInc = (ionAngleFinish - ionAngleStart)/angleDiv;

%init settings
ionEnergy = ionEnergyStart;
ionAngle = ionAngleStart;
loopKill = 0;
avgTime = 0;
totalTime = 0;

%mean and
potatoes%%%
```

```
    %second
    if ionAngle >= ionAngleFinish
       ionAngle = ionAngleStart;
       ionEnergy = ionEnergy+ionEnergyInc;
    else
       ionAngle = ionAngle+ionAngleInc;
    end

    if ionEnergy >= ionEnergyFinish+ionEnergyInc
       loopKill = 1;
    end

    %calculate the average time per trial
          %show progress chart
    curAngLeft = (ionAngleFinish-ionAngle)/ionAngleInc+1;%currently left in energy group
    curEnLeft = (ionEnergyFinish-ionEnergy)/ionEnergyInc+1;
    totalLeft = (angleDiv+1)*(curEnLeft-1)+curAngLeft;
    %show progress chart
    tElapsed = toc(tStart);
    totalTime = totalTime + tElapsed;
    avgTime = totalTime/incremental;
    projTime = avgTime*totalLeft;
    hoursRem = floor(projTime/(3600));
    minsRem = floor((projTime-hoursRem*3600)/60);
    secRem = floor((projTime-hoursRem*3600-minsRem*60));
    sprintf('%i Trials and %i:%i:%i remain.\n Completed Set: Ei=%G Theta=%G Time=%0.2fs\n',
totalLeft,hoursRem,minsRem,secRem,currEnergy,currAngle,tElapsed)

    if loopKill ~= 1
      incremental = incremental + 1;
    end

end
%%%
```

```
if iMaterialTarget == 1 %stainless steel
   A = textread('C:\Users\JRS\Desktop\PHD Modeling\SRIM DATA ACQUISITION\TRIM
Inputs\TRIM_ARnSS_setup.txt','%s','delimiter','\n');
else if iMaterialTarget == 2 %sn
   A = textread('C:\Users\JRS\Desktop\PHD Modeling\SRIM DATA ACQUISITION\TRIM
Inputs\TRIM_ARnSN_setup.txt','%s','delimiter','\n');
   end
end


A(3) = cellstr(strcat([num2str(iIonZ),char(' '), num2str(iIonMass),char(' '), num2str(iIonEnergy),char(' '),
num2str(iIonAngle),char(' '),num2str(iTestNumb),char(' '),char('1'),char(' '),char('10000')]));

fid = fopen('C:\Users\JRS\Desktop\SRIM Install\TRIM.IN','w');
for i = 1:length(A(:))
      fprintf(fid, '%s\r\n', strcat(char(A(i))));
end
fclose(fid);
```

C.3 toggleTrimAuto()

```
function toggleTrimAuto(iValue)

fid = fopen('C:\Users\JRS\Desktop\SRIM Install\TRIMAUTO','w');

fprintf(fid, '%s\r\n', strcat(num2str(iValue)));


fclose(fid);
```

C.4 runTrim()

```
function runTrim()
oldfolder = cd('C:\Users\JRS\Desktop\SRIM Install\');
system('TRIM.exe');
cd(oldfolder);
```

C.5 relocateData()

```
function relocateData(dataTagName)
```

```
A = textread('C:\Users\JRS\Desktop\SRIM Install\SRIM Outputs\BACKSCAT.txt','%s','delimiter','\n');
tempNameA = strcat(char('C:\Users\JRS\Desktop\PHD Modeling\SRIM DATA ACQUISITION\Data
Files\BACKSCAT\'),char(dataTagName), '_BACKSCAT.txt');
fidA = fopen(tempNameA,'w');
for i = 1:length(A(:))
    fprintf(fidA, '%s\r\n', strcat(char(A(i))));
end
fclose(fidA);

B = textread('C:\Users\JRS\Desktop\SRIM Install\SRIM Outputs\RANGE_3D.txt','%s','delimiter','\n');
tempNameB = strcat(char('C:\Users\JRS\Desktop\PHD Modeling\SRIM DATA ACQUISITION\Data
Files\RANGE_3D\'),char(dataTagName), '_RANGE_3D.txt');
fidB = fopen(tempNameB,'w');
for i = 1:length(B(:))
    fprintf(fidB, '%s\r\n', strcat(char(B(i))));
end
fclose(fidB);

C = textread('C:\Users\JRS\Desktop\SRIM Install\SRIM Outputs\SPUTTER.txt','%s','delimiter','\n');
tempNameC = strcat(char('C:\Users\JRS\Desktop\PHD Modeling\SRIM DATA ACQUISITION\Data
Files\SPUTTER\'),char(dataTagName), '_SPUTTER.txt');
fidC = fopen(tempNameC,'w');
for i = 1:length(C(:))
    fprintf(fidC, '%s\r\n', strcat(char(C(i))));
end
fclose(fidC);

D = textread('C:\Users\JRS\Desktop\SRIM Install\SRIM Outputs\TRANSMIT.txt','%s','delimiter','\n');
tempNameD = strcat(char('C:\Users\JRS\Desktop\PHD Modeling\SRIM DATA ACQUISITION\Data
Files\TRANSMIT\'),char(dataTagName), '_TRANSMIT.txt');
fidD = fopen(tempNameD,'w');
for i = 1:length(D(:))
    fprintf(fidD, '%s\r\n', strcat(char(D(i))));
end
fclose(fidD);

E = textread('C:\Users\JRS\Desktop\SRIM Install\SRIM Outputs\TRIMOUT.txt','%s','delimiter','\n');
tempNameE = strcat(char('C:\Users\JRS\Desktop\PHD Modeling\SRIM DATA ACQUISITION\Data
Files\TRIMOUT\'),char(dataTagName), '_TRIMOUT.txt');
fidE = fopen(tempNameE,'w');
for i = 1:length(E(:))
    fprintf(fidE, '%s\r\n', strcat(char(E(i))));
end
fclose(fidE);
```

C.6 main() [for the analyzer]

```
function main()
clear;
```

```
%for data analysis change the following settings and change the folder name
%then click run and it should spit out the analysis file in the
%trim-outfolder



%initial
conditions%%%
```

```
    case 6
      saveName = 'He_on_SS';
      material = 1;
      ionZ= 2;
      ionMass= 4.003; %amu
      trialCount= 10000; %# of test atoms
    case 7
      saveName = 'Mo_on_SS';
      material = 1;
      ionZ= 42;
      ionMass= 97.905; %amu
      trialCount= 1000; %# of test atoms
    case 8
      saveName = 'N_on_Sn_SS';
      material = 1;
      ionZ= 7;
      ionMass= 14.003; %amu
      trialCount= 1000; %# of test atoms
    case 9
      saveName = 'N_on_SS';
      material = 1;
      ionZ= 7;
      ionMass= 14.007; %amu
      trialCount= 10000; %# of test atoms
    case 10
      saveName = 'Ne_on_Sn_SS';
      material = 1;
      ionZ= 10;
      ionMass= 19.992; %amu
      trialCount= 1000; %# of test atoms
    case 11
      saveName = 'Ne_on_SS';
      material = 1;
      ionZ= 10;
      ionMass= 20.18; %amu
      trialCount= 10000; %# of test atoms
    case 12
      saveName = 'Sn_on_SS';
      material = 1;
      ionZ= 50;
      ionMass= 118.71; %amu
      trialCount= 10000; %# of test atoms

    otherwise
      sprintf('Fool!')
  end
  mainFolder = 'C:\Users\JRS\Desktop\SRIM DATA ACQUISITION\';
  subFolder = strcat(char(saveName),'\TRIMOUT\');
  folderName = strcat(char(mainFolder),char(subFolder));
  saveFolder = strcat(char(mainFolder));
  %%%%
```

```
   %program manipulation for
messups.%%%
```

```
indexAngle+1,8),analyzed(indexEnergy+1,indexAngle+1,9),analyzed(indexEnergy+1,indexAngle+1,10),anal
yzed(indexEnergy+1,indexAngle+1,11),analyzed(indexEnergy+1,indexAngle+1,12),analyzed(indexEnergy+1
,indexAngle+1,13),analyzed(indexEnergy+1,indexAngle+1,14),analyzed(indexEnergy+1,indexAngle+1,15)]=
analyzeData(folderName,fileName,trialCount);
        %this is the return
[sputtYield,scattFract,normCosX,normCosY,normCosZ,avgEnergy,avgExitAngle,sVert,sHoriz]
        indexAngle = indexAngle+1;
      end
      indexEnergy = indexEnergy+1;
   end
   xlswrite(strcat(saveFolder,saveName,'.xls'),analyzed(:,:,1),'Depos Fract');%out of all incident, how many
don't leave surface again
   xlswrite(strcat(saveFolder,saveName,'.xls'),analyzed(:,:,2),'Sput Fract');%out of all incident ions how
many cause any number of sputtering events?
   xlswrite(strcat(saveFolder,saveName,'.xls'),analyzed(:,:,3),'Back Scat Fract');%out of all incident, how
many back scatter
   xlswrite(strcat(saveFolder,saveName,'.xls'),analyzed(:,:,4),'Sputt Ion per sput causing ion');%if an ion
causes sputtering, on average how many ions sputtered not including itself
   xlswrite(strcat(saveFolder,saveName,'.xls'),analyzed(:,:,5),'Tot Sput Yield');%given an incident ion,
average number of atoms that will be sputtered
   xlswrite(strcat(saveFolder,saveName,'.xls'),analyzed(:,:,6),'Avg Energy');%for backscattered atoms
   xlswrite(strcat(saveFolder,saveName,'.xls'),analyzed(:,:,7),'uTheta-BS');%average angle of scatter
   xlswrite(strcat(saveFolder,saveName,'.xls'),analyzed(:,:,8),'sTheta-BS');%cosine distribution deviance
   xlswrite(strcat(saveFolder,saveName,'.xls'),analyzed(:,:,9),'uPhi-BS');%average angle of straggle
   xlswrite(strcat(saveFolder,saveName,'.xls'),analyzed(:,:,10),'sPhi-BS');%cosine distribution deviance
   xlswrite(strcat(saveFolder,saveName,'.xls'),analyzed(:,:,11),'uTheta-SP');%cosine distribution deviance
   xlswrite(strcat(saveFolder,saveName,'.xls'),analyzed(:,:,12),'sTheta-SP');%cosine distribution deviance
   xlswrite(strcat(saveFolder,saveName,'.xls'),analyzed(:,:,13),'uPhi-SP');%cosine distribution deviance
   xlswrite(strcat(saveFolder,saveName,'.xls'),analyzed(:,:,14),'sPhi-SP');%cosine distribution deviance
   xlswrite(strcat(saveFolder,saveName,'.xls'),analyzed(:,:,15),'Avg Sput Energy');%cosine distribution
deviance

end

%%%
```

```
totalCosZ = 0;
totalBSEnergy = 0;
totalSputEnergy = 0;
sputIon = zeros(1,trialCount); %this matrix will be set to 1 for each trial that resulted in a sputtering
process, and 0 for each one that only resulted in back scattering
ionsThatSputtered = 0;
for i = 1:length(stringPull(:))

   [process ionNum energy depth cosX cosY cosZ] = strread(char(stringPull(i)),
'%c%u%*f%f%*c%f%*f%*f%f%f%f');

   %bring into typical xyz axis where incident ion comes in from -x to x
   %in the -z direction along the zx plane.  This produces
   %sputtered/backscattered atoms that have a positive z component and
   %variable x and y components
   convVect = [cosY,cosZ,-cosX];

   if process=='S'
      sputteredCount = sputteredCount+1; %progressive count of the total number of sputtered species
      totalSputEnergy = totalSputEnergy + energy;
      if sputIon(ionNum)~=1 %this test is to make sure that we're not duplicating our addition principles
         sputIon(ionNum)=1; %this sets the value of the ion number such that it knows no to duplicate the
addition of this atom
         ionsThatSputtered = ionsThatSputtered+1;
      end
      %need to get the angles of the species that are being sputtered
      %out.
      XMatrixSput(sputteredCount) = convVect(1);
      YMatrixSput(sputteredCount) = convVect(2);
      ZMatrixSput(sputteredCount) = convVect(3);
   end

   if process=='B'
      scatteredCount = scatteredCount+1; %adds one if ion is backscattered
      totalBSEnergy = totalBSEnergy + energy;
      XMatrixScat(scatteredCount) = convVect(1);
      YMatrixScat(scatteredCount) = convVect(2);
      ZMatrixScat(scatteredCount) = convVect(3);
   end



end

scattFract = scatteredCount/trialCount;
deposFract = 1-scattFract;
sputtFract = ionsThatSputtered/trialCount;
sputtYield = sputteredCount/trialCount;
sputPerIon = sputteredCount/ionsThatSputtered;
avgBSEnergy = totalBSEnergy/scatteredCount; %eV
avgSputEnergy = totalSputEnergy/sputteredCount;
```

```
%recall that x is into(+) and out(-) of surface
% y (+to the right) is the horizontal direction
% z is the in and out of the screen direction (+ is out of the screen)

if scatteredCount>0
   for i = 1:scatteredCount
      thetaScat(i) = acos(ZMatrixScat(i)/1);
      phiScat(i)=atan2(YMatrixScat(i),XMatrixScat(i));
   end
end

if sputteredCount>0
   for i = 1:sputteredCount
      thetaSput(i) = acos(ZMatrixSput(i)/1);
      phiSput(i)=atan2(YMatrixSput(i),XMatrixSput(i));
   end
end



if scatteredCount ~= 0
   [uThetaScat,sThetaScat] = cosineFit(thetaScat(:),0,pi/2,0); %0 degrees is normal incidence, the vector
we're measureing from, can only go from +/-pi/2 due to -x component on all backscattered
   [uPhiScat,sPhiScat] = cosineFit(phiScat(:),-pi,pi,0);
else
   uThetaScat=0;sThetaScat=0;uPhiScat=0;sPhiScat=0;
end

if sputteredCount ~= 0
   [uThetaSput,sThetaSput] = cosineFit(thetaSput(:),0,pi/2,0); %0 degrees is normal incidence, the vector
we're measureing from, can only go from +/-pi/2 due to -x component on all backscattered
   [uPhiSput,sPhiSput] = cosineFit(phiSput(:),-pi,pi,0);
else
   uThetaSput=0;sThetaSput=0;uPhiSput=0;sPhiSput=0;
end

randTestVar=1;
if randTestVar == 1
   [f1,x1]=hist(thetaScat,30);
   [f2,x2]=hist(phiScat,30);
   [f3,x3]=hist(thetaSput,30);
   [f4,x4]=hist(phiSput,30);

   subplot(2,2,1)%ThetaScat
   bar(x1,f1/trapz(x1,f1));
   x=uThetaScat-sThetaScat:.01:uThetaScat+sThetaScat;
   hold on
   plot(x(:),1/(2*sThetaScat)*(1+cos((x(:)-uThetaScat)*pi/sThetaScat)));

   subplot(2,2,3)%PhiScat
```

```
    bar(x2,f2/trapz(x2,f2));
    x=uPhiScat-sPhiScat:.01:uPhiScat+sPhiScat;
    hold on
    plot(x(:),1/(2*sPhiScat)*(1+cos((x(:)-uPhiScat)*pi/sPhiScat)));

    subplot(2,2,2)%ThetaSput
    bar(x3,f3/trapz(x3,f3));
    x=uThetaSput-sThetaSput:.01:uThetaSput+sThetaSput;
    hold on
    plot(x(:),1/(2*sThetaSput)*(1+cos((x(:)-uThetaSput)*pi/sThetaSput)));

    subplot(2,2,4)%PhiScat
    bar(x4,f4/trapz(x4,f4));
    %x=uPhiSput-sPhiSput:.01:uPhiSput+sPhiSput;
    %hold on
    %plot(x(:),1/(2*sPhiSput)*(1+cos((x(:)-uPhiSput)*pi/sPhiSput)));


    hold off
end
```

C.8 cosineFit()

```
function [u,s] = cosineFit(angleVals,leftMax,rightMax,plotQ)

%first need to make a histogram from -180o to 180o
% -180 (includes less than) - 85, 85-80 ...80-85, 85-90 (includes greater than)
binInc = 20;
uInc = 100;
sInc = 100;

%2 column is the histogram hit counts, 1 column is the bin values
[hits bins] = hist(angleVals,[leftMax:((rightMax-leftMax)/binInc):rightMax]);
normHits = hits/trapz(bins,hits);
%now we need to go through each of the u and s values to find the best fit.
%

sMin=(rightMax-leftMax)/sInc; %that way we don't have div by 0 errors
incremental=1;
for u = leftMax+sMin:(((rightMax-sMin)-(leftMax+sMin))/uInc):rightMax-sMin

    if u<((rightMax-leftMax)/2+leftMax)
        sMax = u-leftMax;
    elseif u>((rightMax-leftMax)/2+leftMax)
        sMax = rightMax-u;
    else
        sMax = (rightMax-leftMax)/2;
    end
    for s = sMin:sMin:sMax
```

```
      rSqrVal = 0;

      for j = 1:length(bins)
         if bins(j)>=(u-s)
            if bins(j)<=(u+s)
               cosFitValues(j) = 1/(2*s)*(1+cos((bins(j)-u)*pi/s));
            else
               cosFitValues(j) = 0;%this just makes sure that at u+/-s, the prob = 0;
            end
         else
            cosFitValues(j) = 0; %this just makes sure that at u+/-s, the prob = 0;
         end
         rSqrVal = rSqrVal+(cosFitValues(j)-normHits(j))^2;
      end

      comError(incremental,1) = u;
      comError(incremental,2) = s;
      comError(incremental,3) = rSqrVal;
      incremental = incremental + 1;
   end
end


%now find the minimum error
min = 10000000;%unlikely possible min val

for i = 1:length(comError(:,3))
   if comError(i,3) < min
      min = comError(i,3);
      u = comError(i,1);
      s = comError(i,2);
   end
end

%plot tests begin here:
if plotQ==1
   i=1;
   for j = leftMax:(rightMax-leftMax)/100:rightMax
      if j>=(u-s)
         if j<=(u+s)
            cosFitValues(i,2) = 1/(2*s)*(1+cos((j-u)*pi/s));
         else
            cosFitValues(i,2) = 0;%this just makes sure that at u+/-s, the prob = 0;
         end
      else
         cosFitValues(i,2) = 0; %this just makes sure that at u+/-s, the prob = 0;
      end
      cosFitValues(i,1)=j;
      i = i+1;

   end
```

```
    subplot(2,1,1)
    plot(cosFitValues(:,1),cosFitValues(:,2)/trapz(cosFitValues(:,1),cosFitValues(:,2)))
    subplot(2,1,2)
    hist(angleVals)
    %plot(bins,normHits)
    hold off
    sprintf('%0.3f, %0.3f, %0.3f',u-s,u,u+s)
end
```

C.9 analyzeData()

```
function
[deposFract,sputtFract,scattFract,sputPerIon,sputtYield,avgBSEnergy,uThetaScat,sThetaScat,uPhiScat,sPhi
Scat,uThetaSput,sThetaSput,uPhiSput,sPhiSput,avgSputEnergy] =
analyzeData(dataFolderName,dataTagName,trialCount)



%%%
```

```
   [process ionNum energy depth cosX cosY cosZ] = strread(char(stringPull(i)),
'%c%u%*f%f%*c%f%*f%*f%f%f%f');

   %bring into typical xyz axis where incident ion comes in from -x to x
   %in the -z direction along the zx plane.  This produces
   %sputtered/backscattered atoms that have a positive z component and
   %variable x and y components
   convVect = [cosY,cosZ,-cosX];

   if process=='S'
      sputteredCount = sputteredCount+1; %progressive count of the total number of sputtered species
      totalSputEnergy = totalSputEnergy + energy;
      if sputIon(ionNum)~=1 %this test is to make sure that we're not duplicating our addition principles
         sputIon(ionNum)=1; %this sets the value of the ion number such that it knows no to duplicate the
addition of this atom
         ionsThatSputtered = ionsThatSputtered+1;
      end
      %need to get the angles of the species that are being sputtered
      %out.
      XMatrixSput(sputteredCount) = convVect(1);
      YMatrixSput(sputteredCount) = convVect(2);
      ZMatrixSput(sputteredCount) = convVect(3);
   end

   if process=='B'
      scatteredCount = scatteredCount+1; %adds one if ion is backscattered
      totalBSEnergy = totalBSEnergy + energy;
      XMatrixScat(scatteredCount) = convVect(1);
      YMatrixScat(scatteredCount) = convVect(2);
      ZMatrixScat(scatteredCount) = convVect(3);
   end



end

scattFract = scatteredCount/trialCount;
deposFract = 1-scattFract;
sputtFract = ionsThatSputtered/trialCount;
sputtYield = sputteredCount/trialCount;
sputPerIon = sputteredCount/ionsThatSputtered;
avgBSEnergy = totalBSEnergy/scatteredCount; %eV
avgSputEnergy = totalSputEnergy/sputteredCount;


%recall that x is into(+) and out(-) of surface
% y (+to the right) is the horizontal direction
% z is the in and out of the screen direction (+ is out of the screen)
```

```
if scatteredCount>0
   for i = 1:scatteredCount
      thetaScat(i) = acos(ZMatrixScat(i)/1);
      phiScat(i)=atan2(YMatrixScat(i),XMatrixScat(i));
   end
end

if sputteredCount>0
   for i = 1:sputteredCount
      thetaSput(i) = acos(ZMatrixSput(i)/1);
      phiSput(i)=atan2(YMatrixSput(i),XMatrixSput(i));
   end
end



if scatteredCount ~= 0
   [uThetaScat,sThetaScat] = cosineFit(thetaScat(:),0,pi/2,0); %0 degrees is normal incidence, the vector
we're measureing from, can only go from +/-pi/2 due to -x component on all backscattered
   [uPhiScat,sPhiScat] = cosineFit(phiScat(:),-pi,pi,0);
else
   uThetaScat=0;sThetaScat=0;uPhiScat=0;sPhiScat=0;
end

if sputteredCount ~= 0
   [uThetaSput,sThetaSput] = cosineFit(thetaSput(:),0,pi/2,0); %0 degrees is normal incidence, the vector
we're measureing from, can only go from +/-pi/2 due to -x component on all backscattered
   [uPhiSput,sPhiSput] = cosineFit(phiSput(:),-pi,pi,0);
else
   uThetaSput=0;sThetaSput=0;uPhiSput=0;sPhiSput=0;
end

%%%
```

APPENDIX D

GAS SCATTERING COLLISION DATA CREATOR

```
function [MaxB,crossSection]=crossSectionGenerator(fileName)


thetaValues = csvread(strcat('/Users/jrs/Documents/Work/Files/PhD/Theory/Scattering
Tables/',fileName,'.csv'));

impactParam = thetaValues(2:length(thetaValues(:,1)),1);
energyParam = thetaValues(1,2:length(thetaValues(1,:)));

minAngle = 1/360*2*3.1415; %setting the max b at 1degree or less of scattering

for i = 1:length(energyParam)
   tempMaxB = 0; %set as a minimum point
   for j = 1:length(impactParam)%calculate the max impact factor for a given energy value
      if impactParam(j)<=7 %for some reason after 7A there is an error in the forumals that takes the
scattering angle back negative.
         if thetaValues(j+1,i+1)>minAngle %use the +1 term to correlate to the offsets provided in the file
            if impactParam(j)>tempMaxB
               tempMaxB = impactParam(j);
            end
         end
      end
   end
   MaxB(i,1) = energyParam(i);
   MaxB(i,2) = tempMaxB;%in Angstrom
   crossSection(i,1) = energyParam(i);
   crossSection(i,2) = 3.14159*(tempMaxB*10^-10)^2;
end

%plot(MaxB(:,1),MaxB(:,2));
%plot(crossSection(:,1),crossSection(:,2));

csvwrite(strcat('/Users/jrs/Documents/Work/Files/PhD/Theory/Scattering
Tables/',fileName,'_xSec.csv'),crossSection); %this is in m^2
csvwrite(strcat('/Users/jrs/Documents/Work/Files/PhD/Theory/Scattering
Tables/',fileName,'_maxB.csv'),MaxB);%this is in angstrom
```

D.1 scatGenMass()

```
function []=scatGenMass()

Values = csvread('/Users/jrs/Documents/Work/Files/PhD/Theory/Scattering Tables/Potential
Parameters.csv',1,0);
Titles = [cellstr('N-He');cellstr('N-Ne');cellstr('N-Ar');cellstr('Sn-He');cellstr('Sn-Ne');cellstr('Sn-
Ar');cellstr('Mo-He');cellstr('Mo-Ne');cellstr('Mo-Ar');cellstr('Cu-He');cellstr('Cu-Ne');cellstr('Cu-
Ar');cellstr('Ar-He');cellstr('Ar-Ne');cellstr('Ar-Ar');cellstr('He-He');cellstr('He-Ne');cellstr('Ne-Ne')];

for i = 16:length(Titles(:))

scatterTableGenerator(Values(1,i),Values(2,i),Values(3,i),Values(4,i),Values(5,i),char(strcat(Titles(i),'.csv')))
;
end

for i = 16:length(Titles(:))
      crossSectionGenerator(char(Titles(i)));
end
```

D.2 scatterTableGenerator()

```
function []=scatterTableGenerator(eps,sigma,A,B,D,fileName)

%%Input Parameters%%%%%%%%%%%%%
%N-Ar
%eps=.00924133; %eV
%sigma=3.513; %Ang
%A=3449.99; %eV
%B=3.71148; %Ang^-1
%D=6.2;

EcomMax=50000; %eV
EcomStep=1; %eV
EcomMin=1; %eV

inc7=1;
EcomTemp = EcomMin;
while EcomTemp <= 50000
   EcomMatrix(inc7)=EcomTemp;

   if EcomTemp < 10
      EcomStep = 1;
   elseif EcomTemp<100
      EcomStep = 10;
   elseif EcomTemp<1000
      EcomStep = 100;
```

```
    elseif EcomTemp<10000
        EcomStep = 1000;
    elseif EcomTemp<50000
        EcomStep = 10000;
    end
    EcomTemp = EcomTemp+EcomStep;
    inc7=inc7+1;
end

ImpactParamMin=0;%angstrom
ImpactParamMax=10;
ImpactParamStep=.1;
totSteps = (ImpactParamMax-ImpactParamMin)/ImpactParamStep;

eps2=10^-4;%
L=10;

%%%%%%%%%%%%%%%%%%%%%%%%%%%%%%%%%%%%

%Calculated R0 values

inc1 = 1;
for iPVal = ImpactParamMin:ImpactParamStep:ImpactParamMax %impact parameter from .001A to 15
    inc2 = 1;
    iPVal
    for j=1:length(EcomMatrix(:))
        Ecom=EcomMatrix(j);
        E(inc2)=Ecom;
        b0(inc1,1) = iPVal;

        Rg=7; %initial guess for solution to newton's parameter
        Rn=0;
        inc3 = 1;

        while abs(Rg-Rn)>.00001
            if inc3>1
                Rg=Rn;
            end
            R=Rg;



            U = A*exp(-B*R)+4*eps*sigma^12*R^(-12)-4*eps*sigma^D*R^(-D);
            Up = -B*A*exp(-B*R)+-48*eps*sigma^12*R^(-13)+D*4*eps*sigma^D*R^(-D-1);

            RHS=-b0(inc1,1)^2+R^2*(1-U/Ecom);
            RHSP=2*R*(1-U/Ecom)+R^2*(1-Up/Ecom);
            Rn=Rg-RHS/RHSP;

            inc3=inc3+1;
        end
```

```
      r0(inc1,inc2)=Rn;

      %start calculating angles
      R=r0(inc1,inc2)+eps2/2;
      U = A*exp(-B*R)+4*eps*sigma^12*R^(-12)-4*eps*sigma^D*R^(-D);
      deltaPhi(inc1,inc2)=(eps2*b0(inc1,1))/((r0(inc1,inc2)+eps2/2)^2*(1-U/Ecom-
b0(inc1,1)^2/(r0(inc1,inc2)+eps2/2)^2)^.5);

      %now calculate the integral term using riemann sums
      inc4=1;
      %preallocate
      divisions=10000;
      toIntegr(divisions,2)=0;
      toIntegr(divisions,1)=0;
      for diffX=(r0(inc1,inc2)+eps2):(L-(r0(inc1,inc2)+eps2))/divisions:L
         R = diffX;
         U = A*exp(-B*R)+4*eps*sigma^12*R^(-12)-4*eps*sigma^D*R^(-D);
         toInteg(inc4,2)=(diffX^(-2)*(1-U/Ecom-b0(inc1,1)^2/diffX^2)^(-.5));
         toInteg(inc4,1)=diffX;
         inc4=inc4+1;
      end

      %now integrate it
      sumInt=0;
      for i=2:length(toInteg(:,1))
         sumInt = sumInt + (toInteg(i,2)+toInteg(i-1,2))/2*(abs(toInteg(i,1)-toInteg(i-1,1)));
      end

      -2*b0(inc1,1)*sumInt;
      -2*asin(b0(inc1,1)/L);
      -2*deltaPhi(inc1,inc2);

      thetaCOM(inc1,inc2)=pi-2*(deltaPhi(inc1,inc2)+b0(inc1,1)*sumInt+asin(b0(inc1,1)/L));

      inc2=inc2+1;
   end
   inc1 = inc1+1;
   floor(inc1/totSteps*100);
end

%now write to a file

%combine matrices
for k=1:length(b0(:,1))
   combinedThetaMatrix(k+1,1)=b0(k,1);
end

for k=1:length(EcomMatrix(:))
   combinedThetaMatrix(1,k+1)=EcomMatrix(k);
end
```

```
for l=1:length(b0(:,1))
   for m=1:length(EcomMatrix(:))
      combinedThetaMatrix(l+1,m+1)=thetaCOM(l,m);
   end
end
csvwrite(strcat('/Users/jrs/Documents/Work/Files/PhD/Theory/Scattering
Tables/',fileName),combinedThetaMatrix);
```

APPENDIX E

RAW XPS DATA IMAGES

E.1 Experiment 2

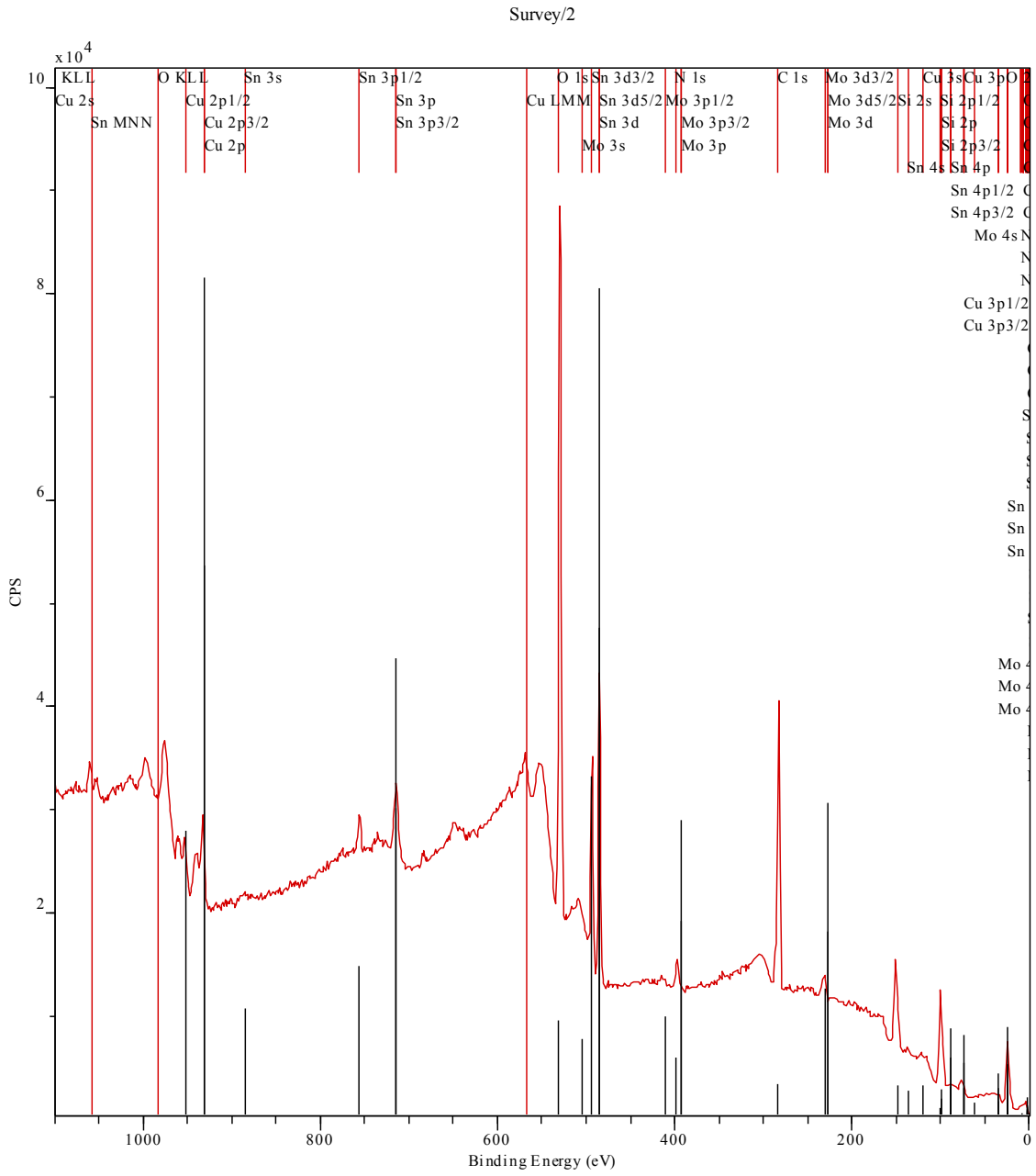

Figure E.1: Experiment 2, Position 8

E.2 Experiment 3

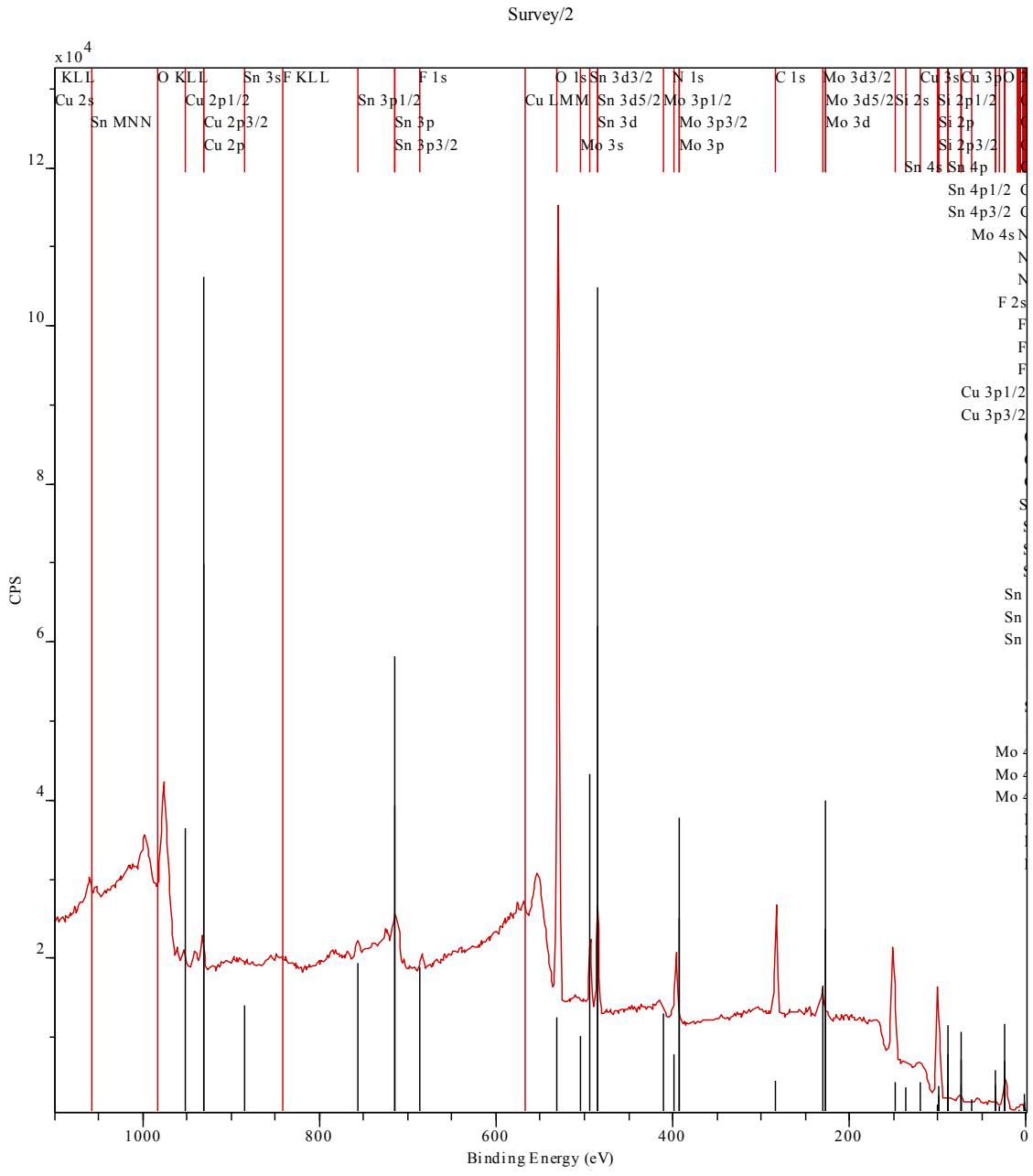

Figure E.2: Experiment 3, Position 1

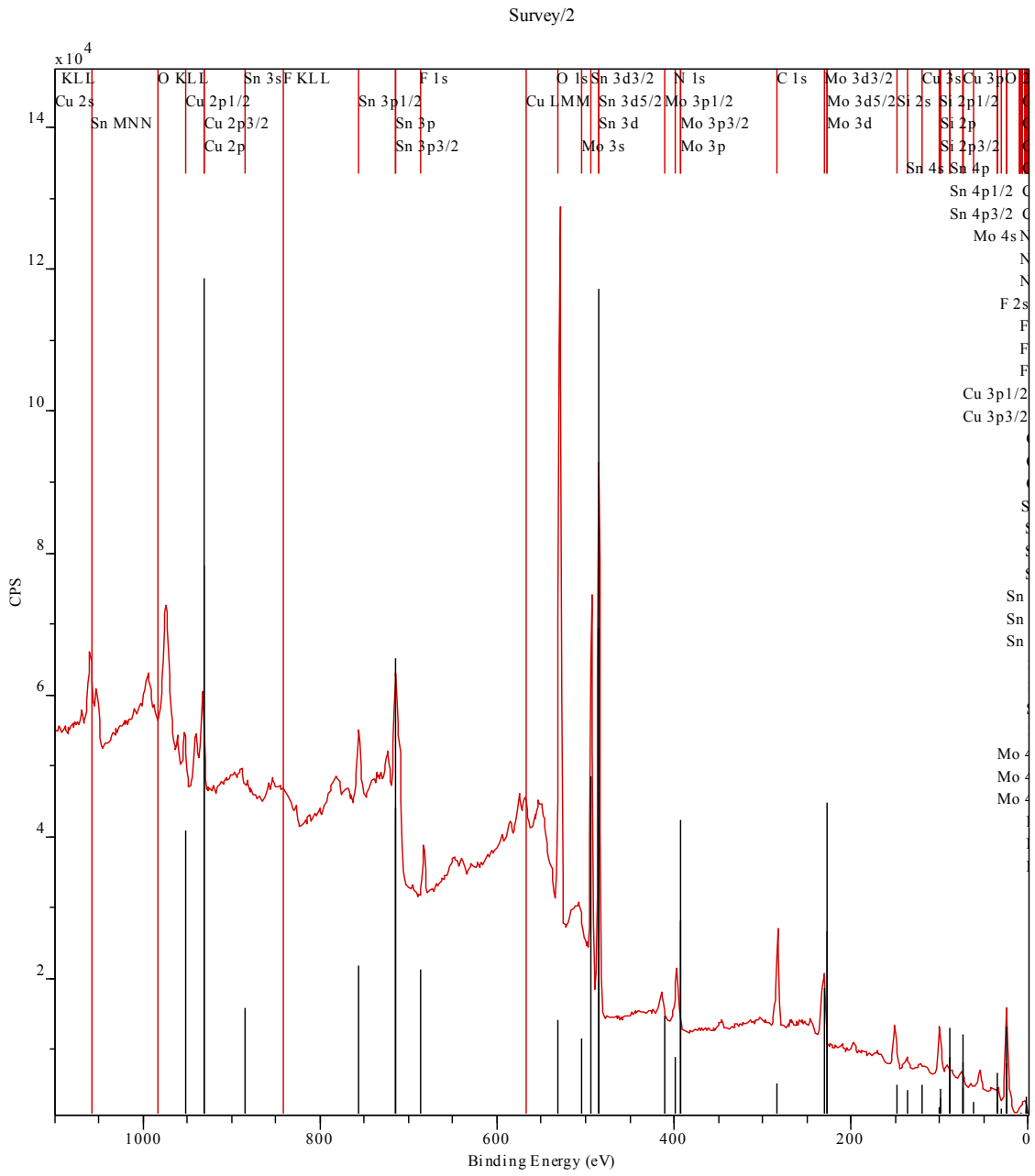

Figure E.3: Experiment 3, Position 2

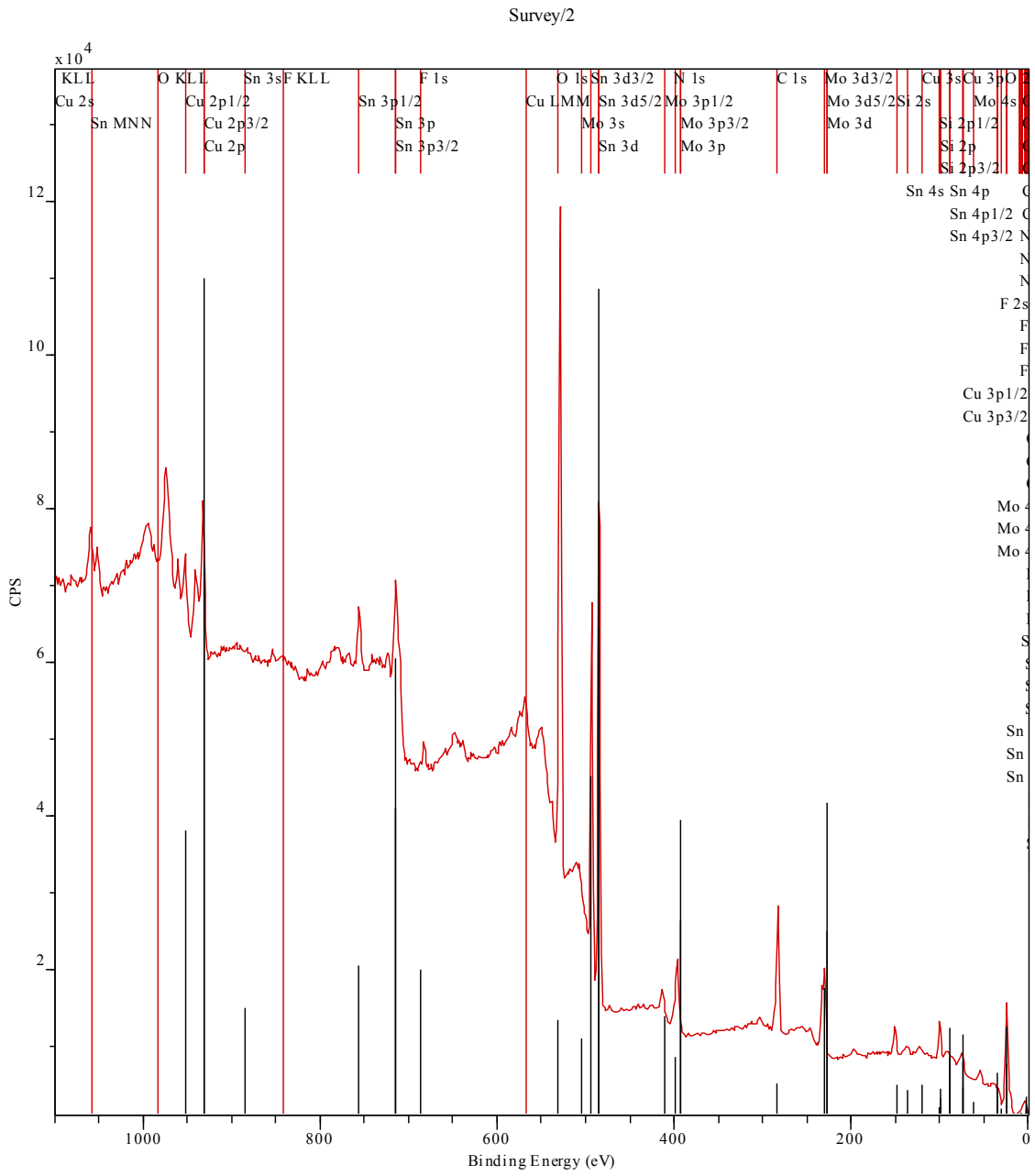

Figure E.4: Experiment 3, Position 3

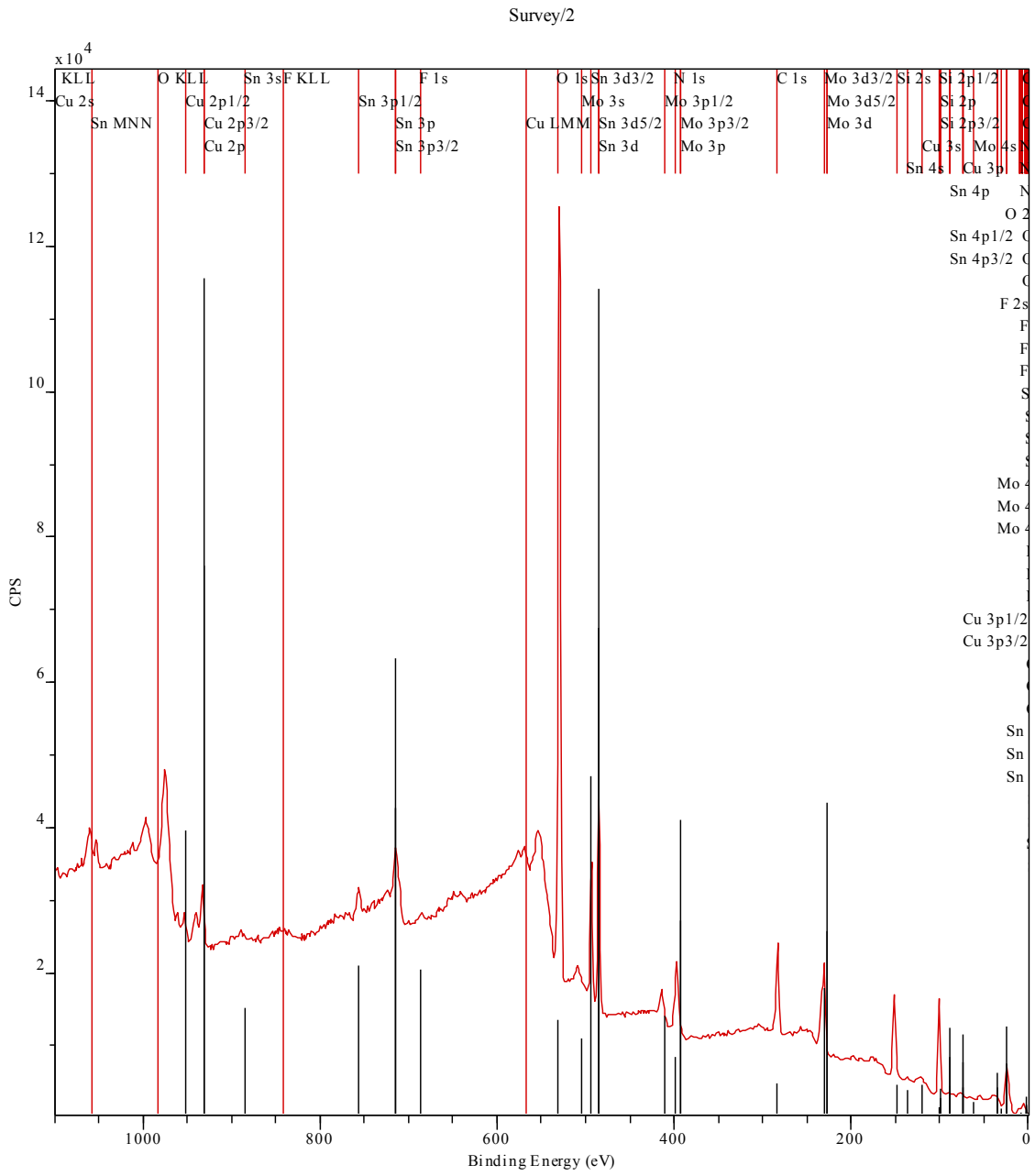

Figure E.5: Experiment 3, Position 4

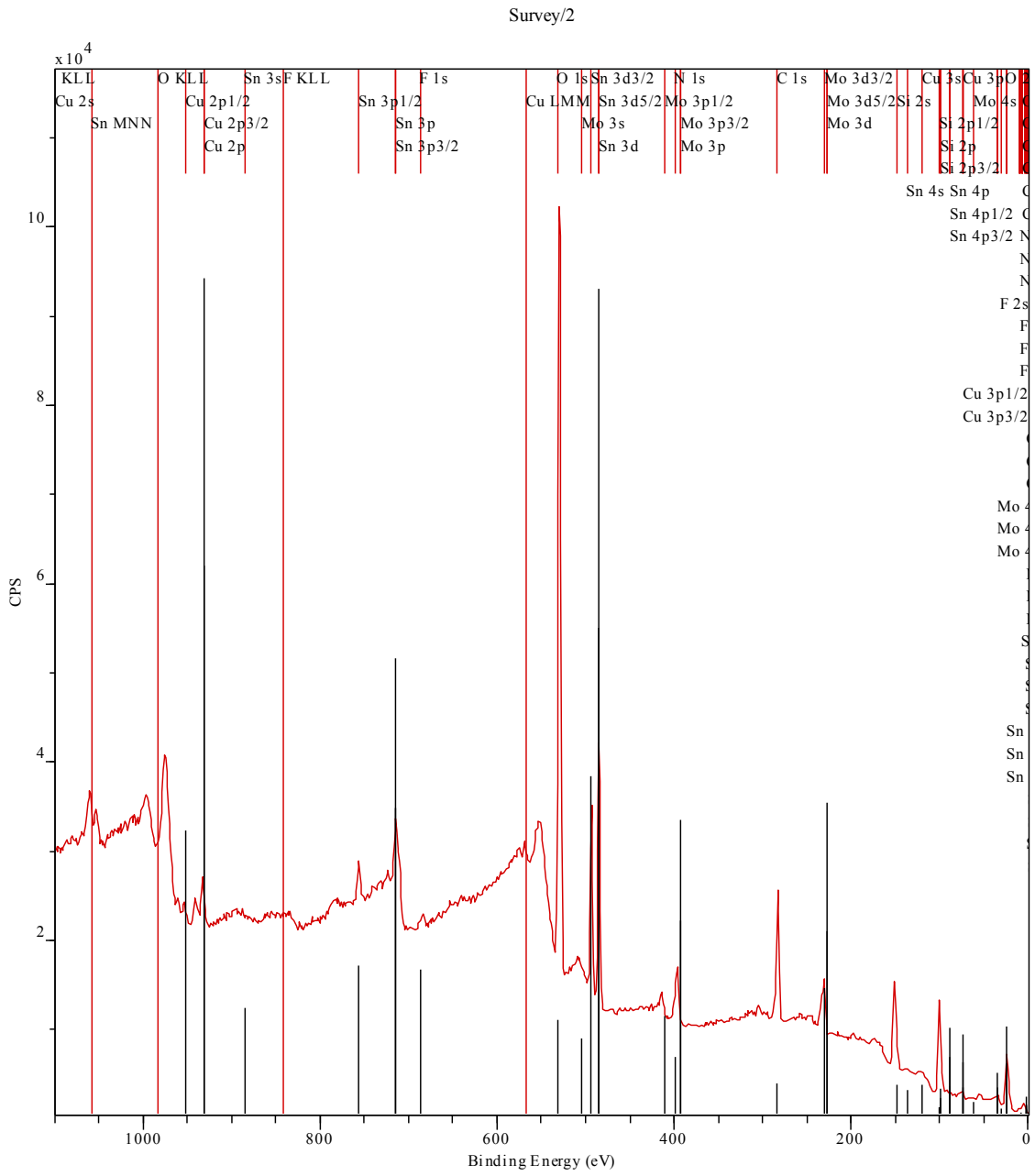

Figure E.6: Experiment 3, Position 6

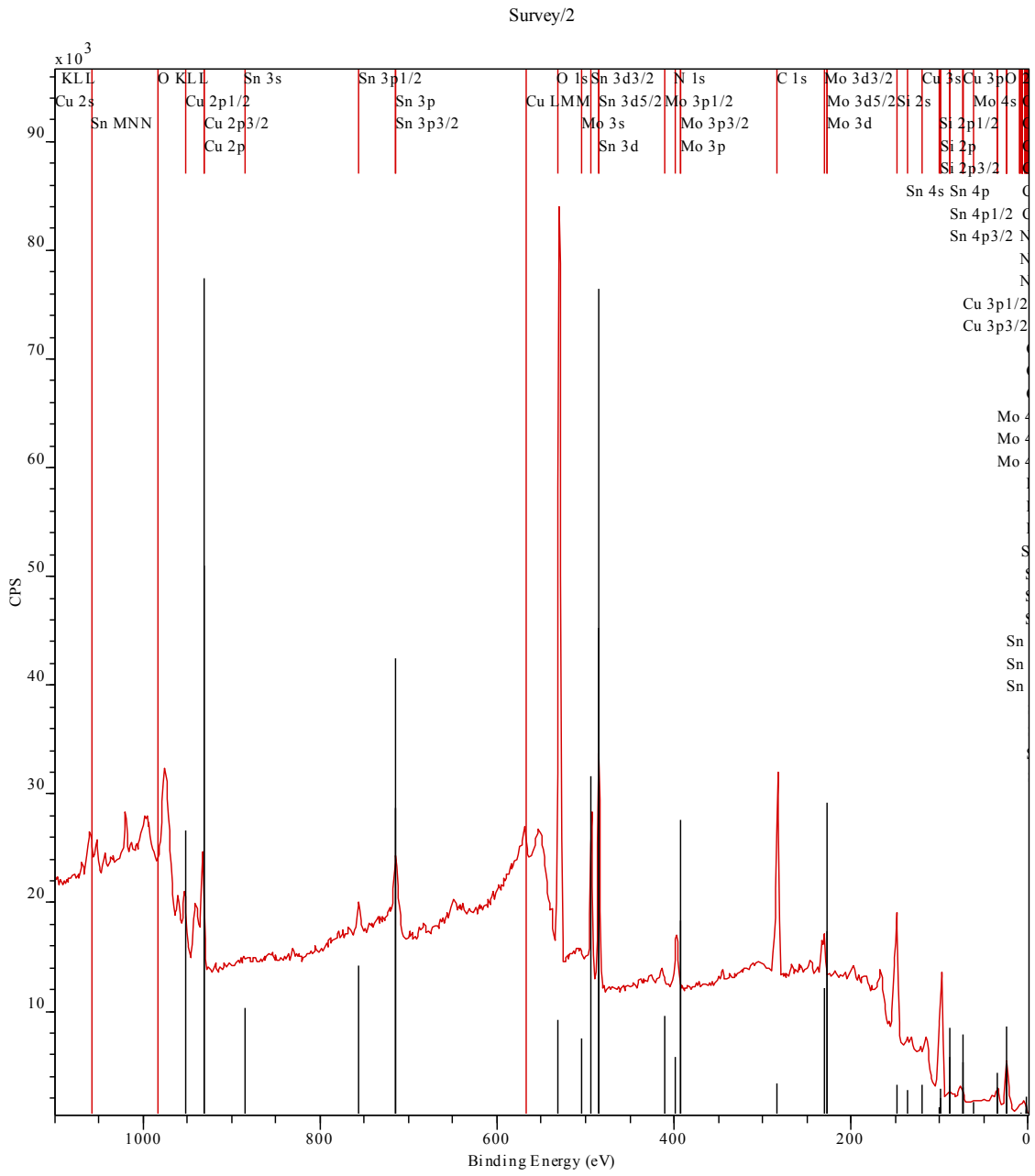

Figure E.7: Experiment 3, Position 7

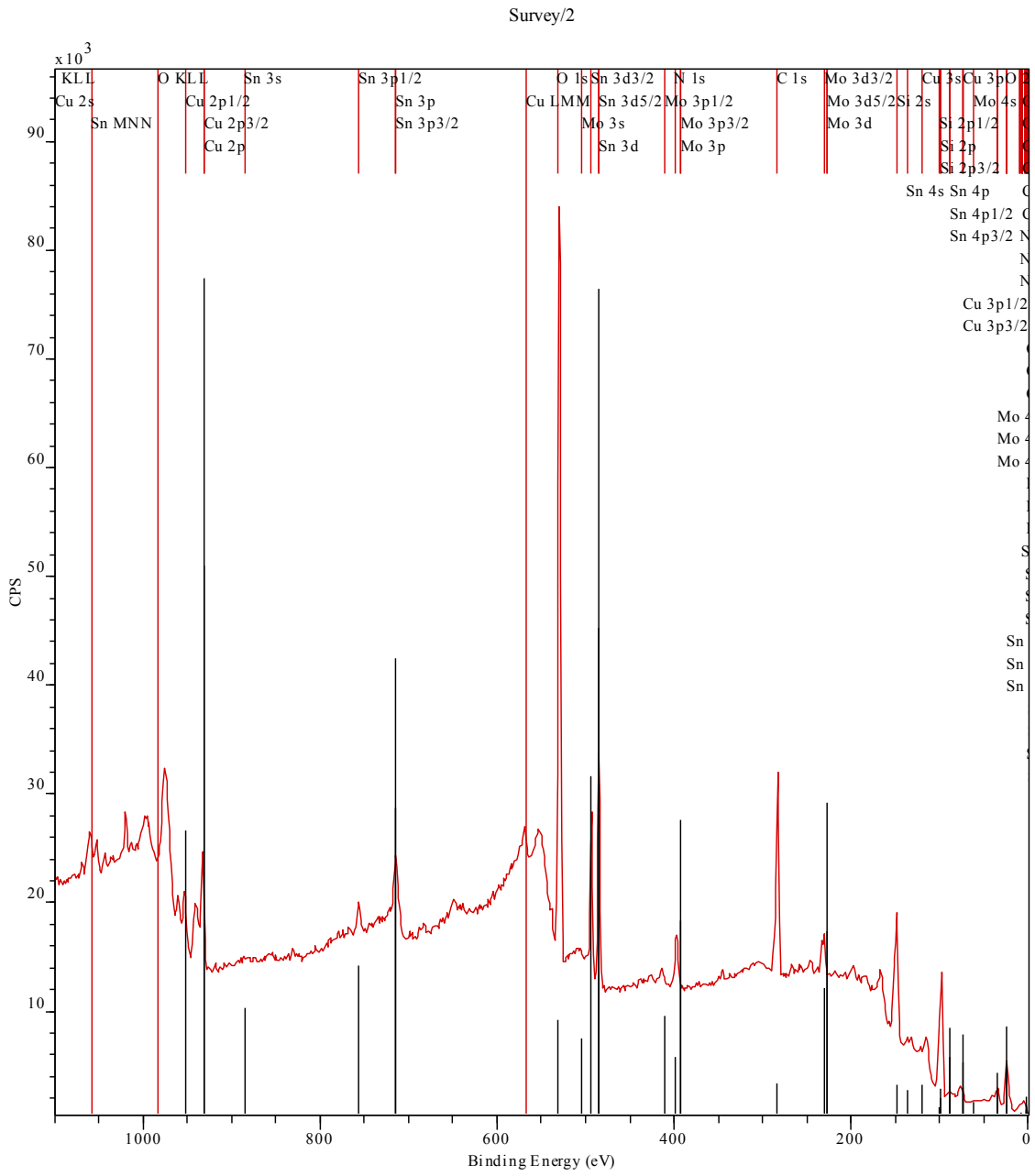

Figure E.8: Experiment 3, Position 8

E.3 Experiment 4

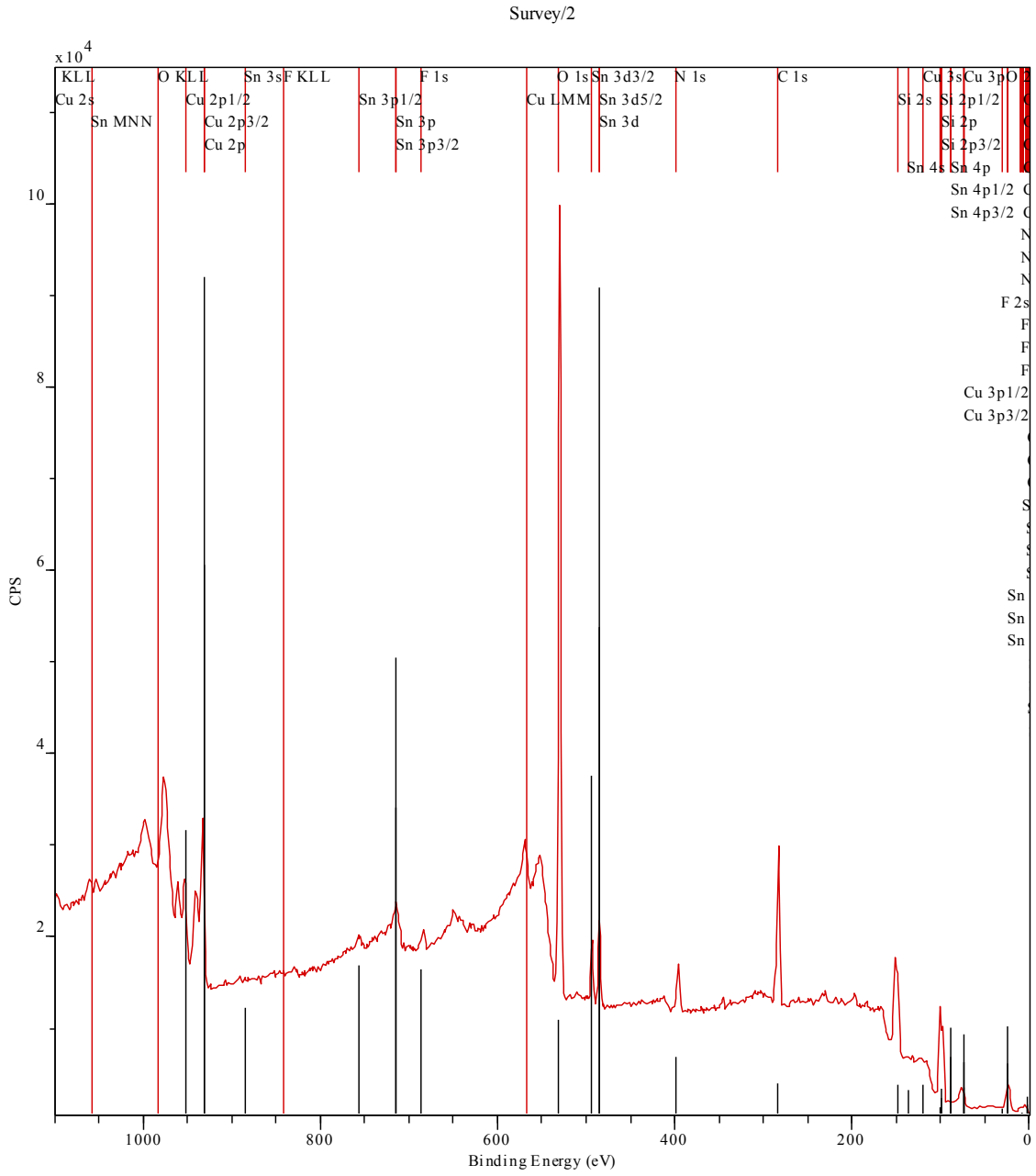

Figure E.9: Experiment 4, Position 8

E.4 Experiment 5

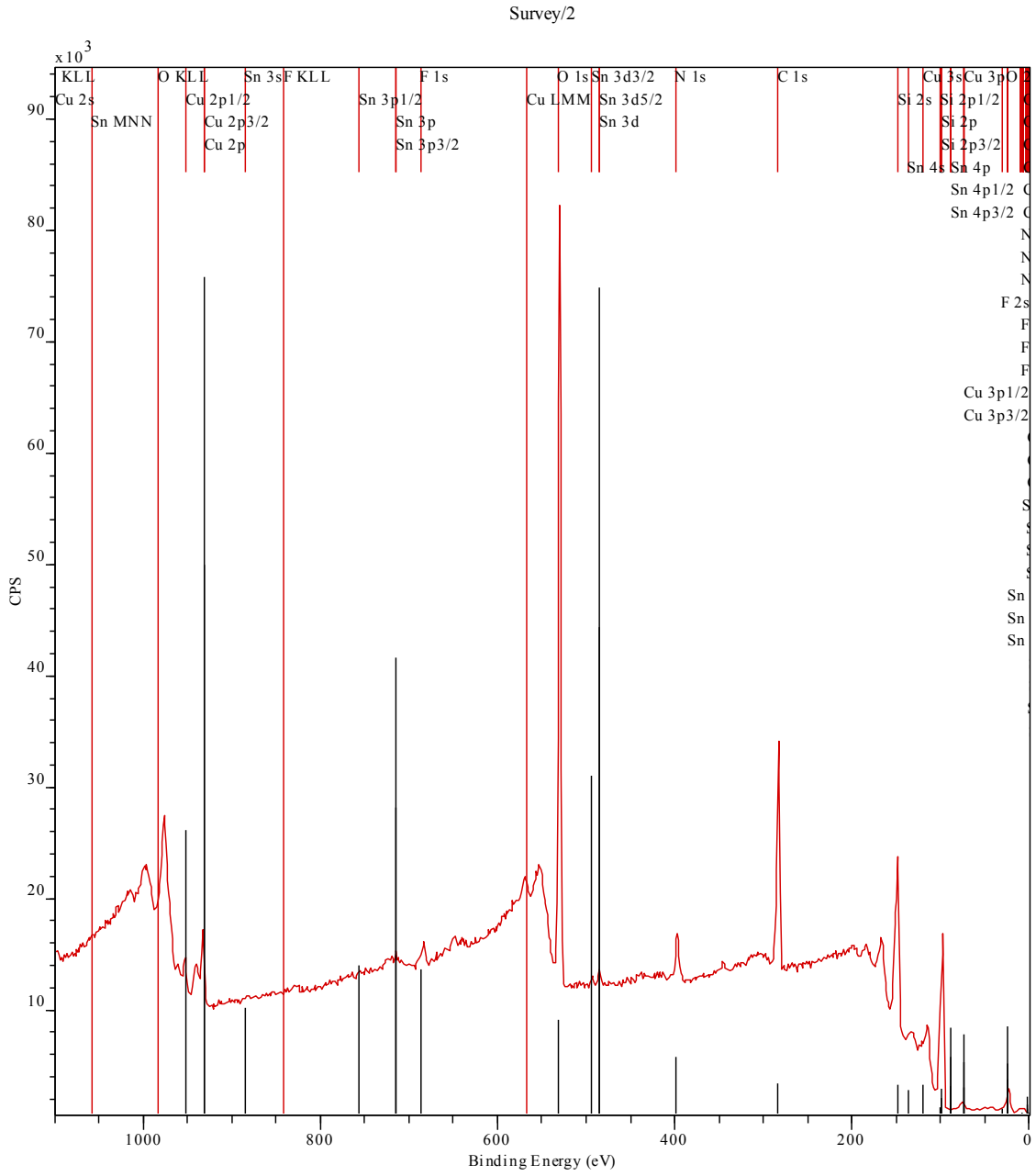

Figure E.10: Experiment 5, Position 8

E.5 Experiment 6

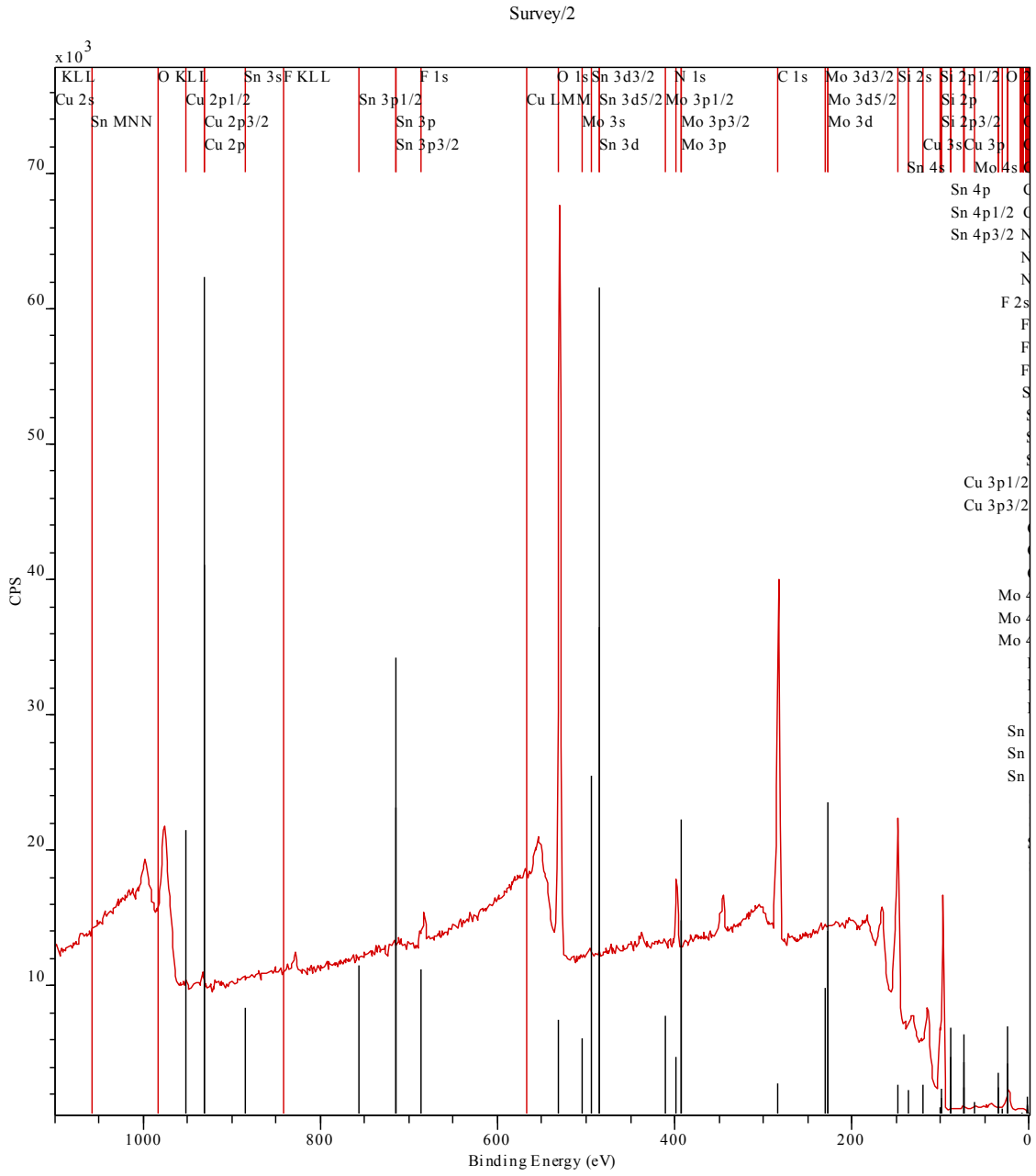

Figure E.11: Experiment 6, Position 8

E.6 Experiment 7

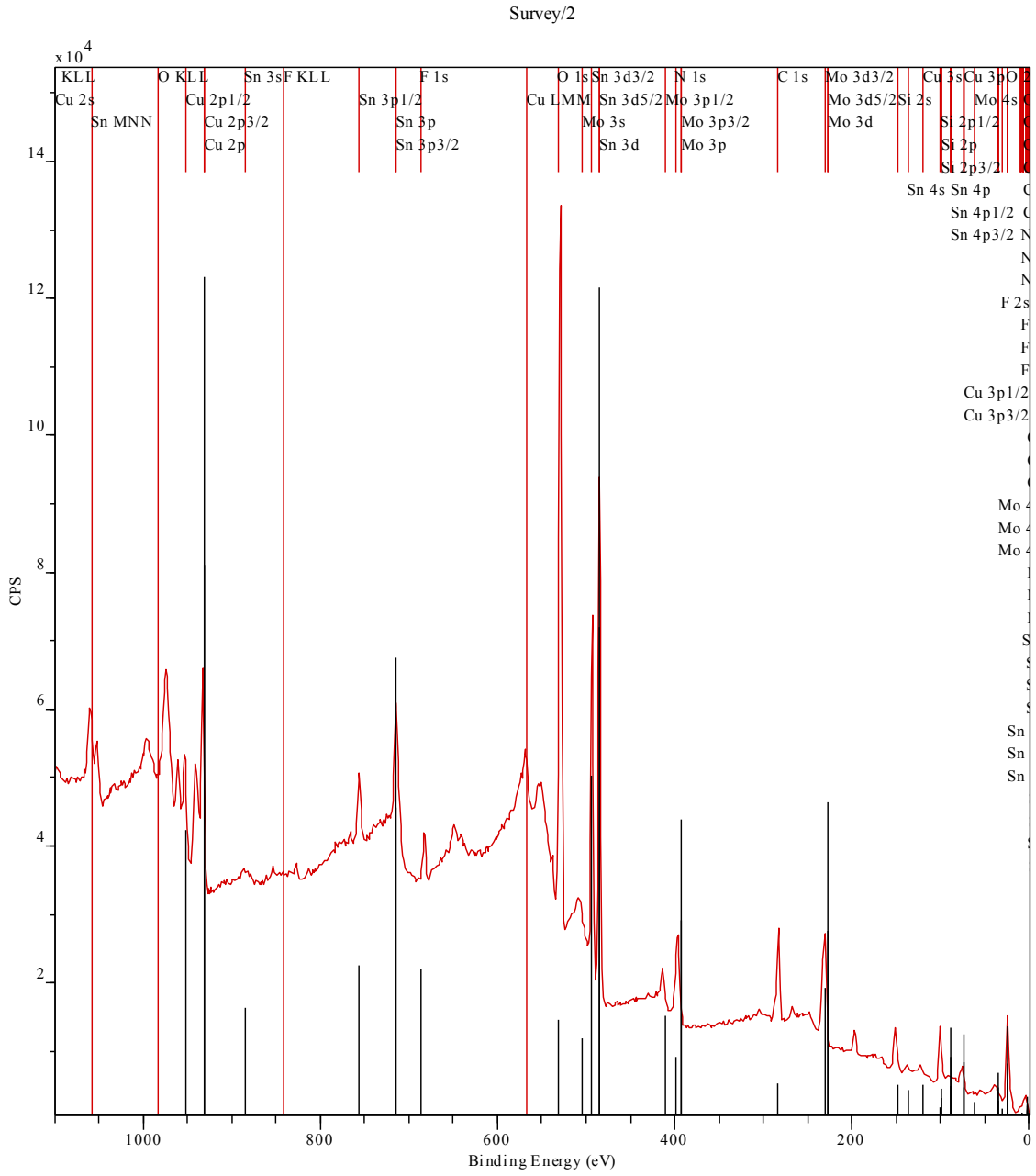

Figure E.12: Experiment 7, Position 8

E.7 Experiment 8

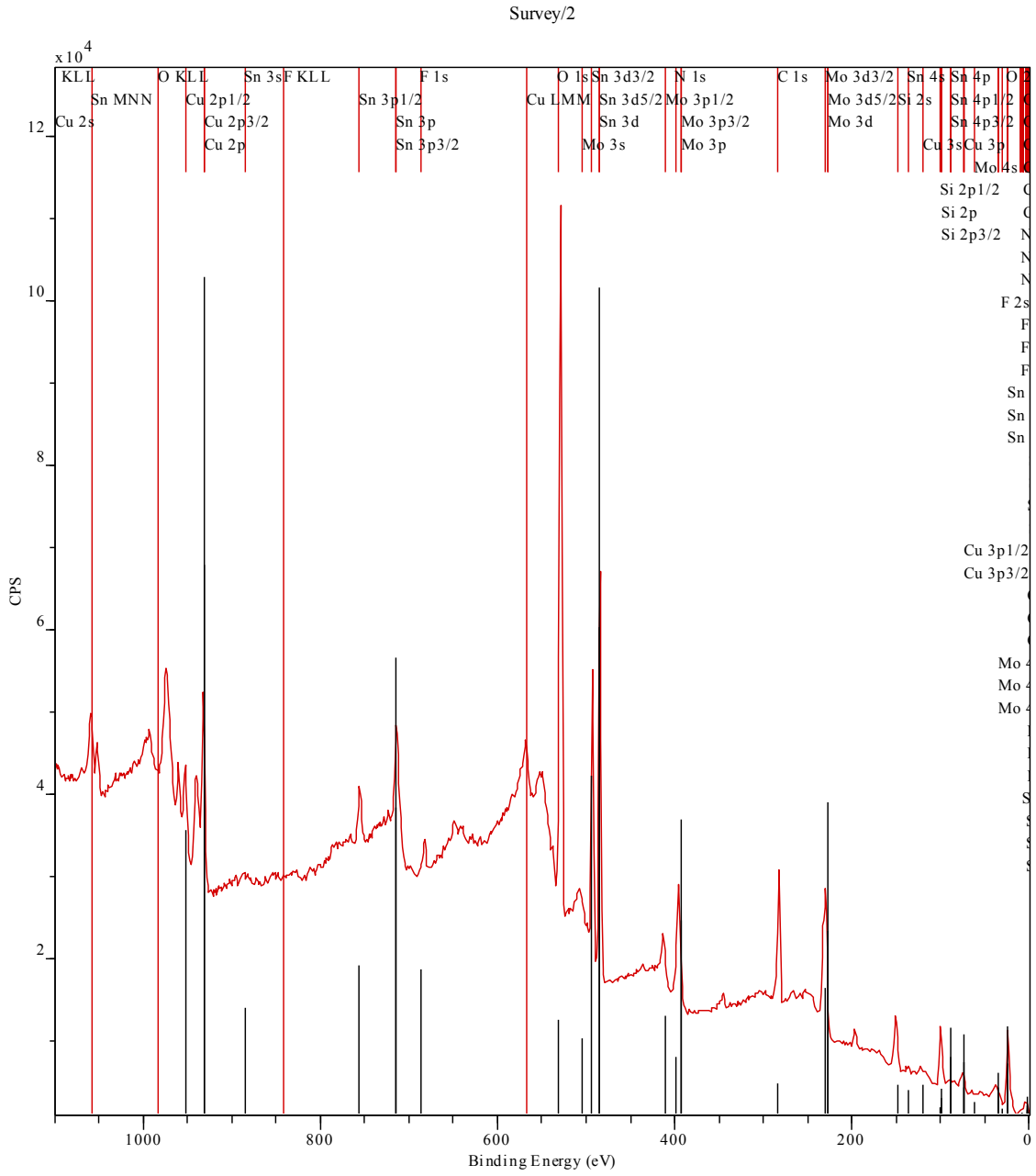

Figure E.13: Experiment 8, Position 8